

Chapter 1

Overview of Aerodynamics

1.1. Introduction and Notation

Flight mechanics is the science of predicting and controlling aircraft motion. From Newton's second law we know that the motion of any body depends on the forces and moments acting on the body. The forces and moments exerted on an aircraft in flight are the aerodynamic forces and moments acting on the aircraft's skin, the propulsive forces and moments created by the aircraft's engine or engines, and the gravitational force between the aircraft and the Earth. Because aerodynamic forces and moments are central to the study of aircraft motion, an understanding of the fundamentals of aerodynamics is a prerequisite to the study of flight mechanics. In this text it will be assumed that the reader has gained this prerequisite knowledge, either through the completion of at least one engineering course on aerodynamics or through independent study. In this chapter we review briefly some of the more important concepts that the reader should understand before proceeding with the material in the remainder of the book.

The aerodynamic forces and moments acting on any body moving through the atmosphere originate from only two sources,

1. The pressure distribution over the body surface.
2. The shear stress distribution over the body surface.

A resultant aerodynamic force, \mathbf{F}_a , and a resultant aerodynamic moment, \mathbf{M}_a , are the net effects of the pressure and shear stress distributions integrated over the entire surface of the body. To express these two vectors in terms of components, we must define a coordinate system. While several different coordinate systems will be used in our study of flight mechanics, the coordinate system commonly used in the study of aerodynamics is referred to here as *Cartesian aerodynamic coordinates*. When considering flow over a body such as an airfoil, wing, or airplane, the x -axis of this particular coordinate system is aligned with the body axis or *chord line*, pointing in the general direction of relative air-flow. The origin is typically located at the front of the body or *leading edge*. The y -axis is chosen normal to the x -axis in an upward direction. Choosing a conventional right-handed coordinate system requires the z -axis to be pointing in the spanwise direction from right to left, as shown in Fig. 1.1.1. Here, the components of the resultant aerodynamic force and moment, described in this particular coordinate system, are denoted as

$$\mathbf{F}_a = A\mathbf{i}_x + N\mathbf{i}_y + B\mathbf{i}_z$$

$$\mathbf{M}_a = -\ell\mathbf{i}_x - n\mathbf{i}_y - m\mathbf{i}_z$$

where \mathbf{i}_x , \mathbf{i}_y , and \mathbf{i}_z are the unit vectors in the x -, y -, and z -directions, respectively. The terminology that describes these components is

2 Chapter 1 Overview of Aerodynamics

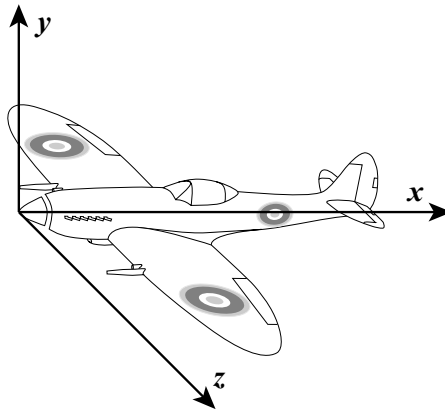


Figure 1.1.1. Cartesian aerodynamic coordinate system used in the study of aerodynamics.

- A \equiv aftward axial force $\equiv x$ -component of \mathbf{F}_a (parallel to the chord)
- N \equiv upward normal force $\equiv y$ -component of \mathbf{F}_a (normal to the chord and span)
- B \equiv leftward side force $\equiv z$ -component of \mathbf{F}_a (parallel with the span)
- ℓ \equiv rolling moment (positive right wing down)
- n \equiv yawing moment (positive nose right)
- m \equiv pitching moment (positive nose up)

The traditional definitions for the moments in roll, pitch, and yaw do not follow the right-hand rule in this coordinate system. It is often convenient to split the resultant aerodynamic force into only two components,

- D \equiv drag \equiv the component of \mathbf{F}_a parallel to \mathbf{V}_∞ ($D = \mathbf{F}_a \cdot \mathbf{i}_\infty$)
- L \equiv lift \equiv the component of \mathbf{F}_a perpendicular to \mathbf{V}_∞ ($L = |\mathbf{F}_a - D\mathbf{i}_\infty|$)

where \mathbf{V}_∞ is the freestream velocity or *relative wind* far from the body and \mathbf{i}_∞ is the unit vector in the direction of the freestream.

For two-dimensional flow, it is often advantageous to define the *section force* and *section moment* to be the force and moment per unit span. For these definitions the notation used in this book will be

- \tilde{D} \equiv section drag \equiv drag force per unit span (parallel to \mathbf{V}_∞)
- \tilde{L} \equiv section lift \equiv lift force per unit span (perpendicular to \mathbf{V}_∞)
- \tilde{A} \equiv section axial force \equiv axial force per unit span (parallel to chord)
- \tilde{N} \equiv section normal force \equiv normal force per unit span (perpendicular to chord)
- \tilde{m} \equiv section moment \equiv pitching moment per unit span (positive nose up)

where the chord is a line extending from the leading edge to the trailing edge of the body. The chord length, c , is the length of this chord line.

The aerodynamic forces and moments are usually expressed in terms of dimensionless force and moment coefficients. For example,

$$C_D \equiv \text{drag coefficient} \equiv \frac{D}{\frac{1}{2}\rho_\infty V_\infty^2 S_{\text{ref}}}$$

$$C_L \equiv \text{lift coefficient} \equiv \frac{L}{\frac{1}{2}\rho_\infty V_\infty^2 S_{\text{ref}}}$$

$$C_A \equiv \text{axial force coefficient} \equiv \frac{A}{\frac{1}{2}\rho_\infty V_\infty^2 S_{\text{ref}}}$$

$$C_N \equiv \text{normal force coefficient} \equiv \frac{N}{\frac{1}{2}\rho_\infty V_\infty^2 S_{\text{ref}}}$$

$$C_m \equiv \text{pitching moment coefficient} \equiv \frac{m}{\frac{1}{2}\rho_\infty V_\infty^2 S_{\text{ref}} l_{\text{ref}}}$$

where ρ_∞ is the freestream density, S_{ref} is the reference area, and l_{ref} is the reference length. For a streamlined body such as a wing, S_{ref} is the planform area and l_{ref} is a reference chord length. For a bluff body, the frontal area is used as the reference. For two-dimensional flow, the section aerodynamic coefficients per unit span are defined:

$$\tilde{C}_D \equiv \text{section drag coefficient} \equiv \frac{\tilde{D}}{\frac{1}{2}\rho_\infty V_\infty^2 c}$$

$$\tilde{C}_L \equiv \text{section lift coefficient} \equiv \frac{\tilde{L}}{\frac{1}{2}\rho_\infty V_\infty^2 c}$$

$$\tilde{C}_A \equiv \text{section axial force coefficient} \equiv \frac{\tilde{A}}{\frac{1}{2}\rho_\infty V_\infty^2 c}$$

$$\tilde{C}_N \equiv \text{section normal force coefficient} \equiv \frac{\tilde{N}}{\frac{1}{2}\rho_\infty V_\infty^2 c}$$

$$\tilde{C}_m \equiv \text{section moment coefficient} \equiv \frac{\tilde{m}}{\frac{1}{2}\rho_\infty V_\infty^2 c^2}$$

where c is the section chord length defined in Fig. 1.1.2.

The resultant aerodynamic force acting on a two-dimensional airfoil section is completely specified in terms of either lift and drag or axial and normal force. These two equivalent descriptions of the resultant aerodynamic force are related to each other through the angle of attack, as shown in Fig. 1.1.2,

$$\alpha \equiv \text{angle of attack} \equiv \text{the angle from } \mathbf{V}_\infty \text{ to the chord line (positive nose up)}$$

If the normal and axial coefficients are known, the lift and drag coefficients can be found from the relations

4 Chapter 1 Overview of Aerodynamics

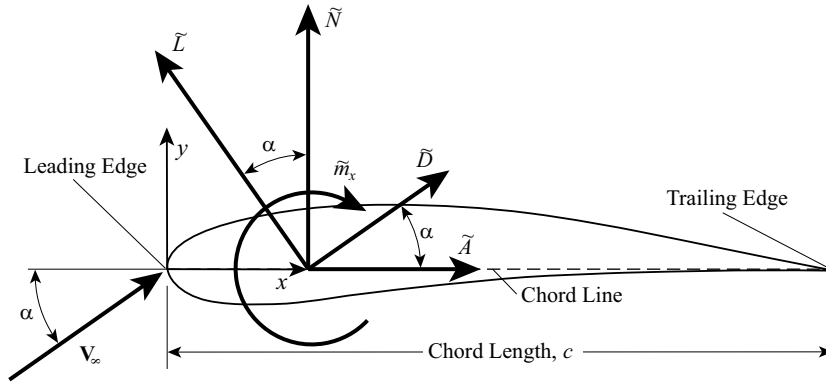


Figure 1.1.2. Section forces and moment.

$$\tilde{C}_L = \tilde{C}_N \cos \alpha - \tilde{C}_A \sin \alpha \quad (1.1.1)$$

$$\tilde{C}_D = \tilde{C}_A \cos \alpha + \tilde{C}_N \sin \alpha \quad (1.1.2)$$

and when the lift and drag coefficients are known, the normal and axial coefficients are found from

$$\tilde{C}_N = \tilde{C}_L \cos \alpha + \tilde{C}_D \sin \alpha \quad (1.1.3)$$

$$\tilde{C}_A = \tilde{C}_D \cos \alpha - \tilde{C}_L \sin \alpha \quad (1.1.4)$$

Because the lift is typically much larger than the drag, from Eq. (1.1.4) we see why the axial force is often negative even though the angle of attack is small.

The resultant aerodynamic force and moment acting on a body must have the same effect as the distributed loads. Thus, the resultant moment will depend on where the resultant force is placed on the body. For example, let x be the coordinate measured along the chord line of an airfoil, from the leading edge toward the trailing edge. If we place the resultant force and moment on the chord line, the value of the resultant moment will depend on the x -location of the resultant force. The resultant moment about some arbitrary point on the chord line a distance x from the leading edge, \tilde{m}_x , is related to the resultant moment about the leading edge, \tilde{m}_{le} , according to

$$\tilde{m}_{le} = \tilde{m}_x - x\tilde{N}$$

or in terms of dimensionless coefficients,

$$\tilde{C}_{m_{le}} = \tilde{C}_{m_x} - \frac{x}{c}\tilde{C}_N \quad (1.1.5)$$

Two particular locations along the chord line are of special interest:

x_{cp} \equiv center of pressure \equiv the point about which the resultant moment is zero.

x_{ac} \equiv aerodynamic center \equiv the point about which the change in the resultant moment with respect to the angle of attack is zero.

Using the definition of center of pressure in Eq. (1.1.5), the section pitching moment coefficient about the leading edge can be written as

$$\tilde{C}_{m_{le}} = \tilde{C}_{m_x} - \frac{x}{c} \tilde{C}_N = -\frac{x_{cp}}{c} \tilde{C}_N$$

Solving for the **center of pressure** yields

$$\frac{x_{cp}}{c} = \frac{x}{c} - \frac{\tilde{C}_{m_x}}{\tilde{C}_N} \quad (1.1.6)$$

From this relation, the location of the center of pressure at any given angle of attack can be determined from the normal force coefficient and the moment coefficient about any point on the airfoil chord line. In general, the position of the center of pressure can vary significantly with angle of attack.

In a similar manner, using the aerodynamic center in Eq. (1.1.5) we can write

$$\tilde{C}_{m_{le}} = \tilde{C}_{m_x} - \frac{x}{c} \tilde{C}_N = \tilde{C}_{m_{ac}} - \frac{x_{ac}}{c} \tilde{C}_N$$

or after solving for the moment about the aerodynamic center, we have

$$\tilde{C}_{m_{ac}} = \tilde{C}_{m_x} + \left(\frac{x_{ac}}{c} - \frac{x}{c} \right) \tilde{C}_N \quad (1.1.7)$$

From the definition of the aerodynamic center, Eq. (1.1.7) requires

$$\frac{\partial \tilde{C}_{m_{ac}}}{\partial \alpha} = \frac{\partial \tilde{C}_{m_x}}{\partial \alpha} + \left(\frac{x_{ac}}{c} - \frac{x}{c} \right) \frac{\partial \tilde{C}_N}{\partial \alpha} = 0 \quad (1.1.8)$$

Solving Eq. (1.1.8) for the location of the **aerodynamic center** results in

$$\frac{x_{ac}}{c} = \frac{x}{c} - \frac{\partial \tilde{C}_{m_x}}{\partial \alpha} / \frac{\partial \tilde{C}_N}{\partial \alpha} \quad (1.1.9)$$

The location of the aerodynamic center can be determined according to Eq. (1.1.9) from knowledge of how the normal force coefficient and the moment coefficient about any point on the chord line vary with angle of attack. For most airfoils, the position of the aerodynamic center is very nearly independent of angle of attack.

6 Chapter 1 Overview of Aerodynamics

The concept of an aerodynamic center is extremely important in the study of flight mechanics. We see from Eq. (1.1.9) that the location of the aerodynamic center does not depend on the magnitude of the aerodynamic coefficients, as the center of pressure does; rather, it depends only on derivatives of the aerodynamic coefficients with respect to angle of attack. As we proceed with our study of flight mechanics, we shall discover many other such derivatives that are important. To avoid the somewhat cumbersome notation used in Eq. (1.1.9), here we shall use a shorthand notation for such derivatives. **In this text, a subscript preceded by a comma will be used to signify differentiation.** For example,

$$\tilde{C}_{L,\alpha} \equiv \frac{\partial \tilde{C}_L}{\partial \alpha}, \quad \tilde{C}_{D,\alpha} \equiv \frac{\partial \tilde{C}_D}{\partial \alpha}, \quad \tilde{C}_{N,\alpha} \equiv \frac{\partial \tilde{C}_N}{\partial \alpha}, \quad \tilde{C}_{m_x,\alpha} \equiv \frac{\partial \tilde{C}_{m_x}}{\partial \alpha}, \quad \text{etc.}$$

Using this shorthand notation, Eq. (1.1.9) is written as

$$\frac{x_{ac}}{c} = \frac{x}{c} - \frac{\tilde{C}_{m_x,\alpha}}{\tilde{C}_{N,\alpha}} \quad (1.1.9)$$

EXAMPLE 1.1.1. An airfoil has section lift, drag, and quarter-chord moment coefficients given by the following equations:

$$\tilde{C}_L = 6.0\alpha + 0.2, \quad \tilde{C}_D = 0.2\alpha^2 + 0.006, \quad \tilde{C}_{m_{c/4}} = -0.05 - 0.01\alpha$$

where α is the angle of attack in radians. Find the center of pressure and the aerodynamic center of the airfoil for angles of attack of $-5, 0, 5,$ and 10 degrees.

Solution. Using Eq. (1.1.3) in Eq. (1.1.6), the center of pressure can be expressed in terms of the section lift, drag, and quarter-chord moment coefficients,

$$\begin{aligned} \frac{x_{cp}}{c} &= 0.25 - \frac{\tilde{C}_{m_{c/4}}}{\tilde{C}_L \cos \alpha + \tilde{C}_D \sin \alpha} \\ &= 0.25 - \frac{-0.05 - 0.01\alpha}{(6.0\alpha + 0.2)\cos \alpha + (0.2\alpha^2 + 0.006)\sin \alpha} \end{aligned}$$

From Eq. (1.1.3), the change in the normal force coefficient with respect to angle of attack is

$$\tilde{C}_{N,\alpha} = \tilde{C}_{L,\alpha} \cos \alpha - \tilde{C}_L \sin \alpha + \tilde{C}_{D,\alpha} \sin \alpha + \tilde{C}_D \cos \alpha$$

Using this result in Eq. (1.1.9) and rearranging yields

$$\frac{x_{ac}}{c} = \frac{x}{c} - \frac{\tilde{C}_{m_x,\alpha}}{(\tilde{C}_{L,\alpha} + \tilde{C}_D)\cos \alpha - (\tilde{C}_L - \tilde{C}_{D,\alpha})\sin \alpha}$$

and for this particular airfoil we have

$$\begin{aligned}\frac{x_{ac}}{c} &= 0.25 - \frac{\tilde{C}_{m_{c/4},\alpha}}{(\tilde{C}_{L,\alpha} + \tilde{C}_D) \cos \alpha - (\tilde{C}_L - \tilde{C}_{D,\alpha}) \sin \alpha} \\ &= 0.25 - \frac{-0.01}{(6.0 + 0.2\alpha^2 + 0.006) \cos \alpha - (6.0\alpha + 0.2 - 0.4\alpha) \sin \alpha}\end{aligned}$$

At angles of attack of -5 , 0 , 5 , and 10 degrees, these relations result in

α (deg)	α (rad)	x_{cp}/c	x_{ac}/c
-5.0	-0.08727	0.09791	0.25168
0.0	0.00000	0.50000	0.25167
5.0	0.08727	0.32051	0.25169
10.0	0.17453	0.29206	0.25175

Note that although the position of the center of pressure varies considerably with angle of attack, the position of the aerodynamic center is nearly independent of angle of attack. This result is typical for cambered airfoils, which are commonly used in the construction of aircraft wings.

Body-Fixed Stability and Control Coordinates

Although the Cartesian aerodynamic coordinate system shown in Fig. 1.1.1 is commonly used in the study of aerodynamics, there are several disadvantages to using this reference frame in the study of flight mechanics. Some of these disadvantages may not become apparent until later in our development of the aircraft equations of motion. However, we have already noted that the conventional definitions for the aerodynamic moments in roll, pitch, and yaw do not follow the usual right-hand rule in this traditional aerodynamic coordinate system.

Historically, the aerodynamic coordinate system originated with the development of airfoil theory. When formulating this two-dimensional problem in Cartesian coordinates, a conventional x - y coordinate system was chosen and it was convenient to have the x -axis aligned with the chord line pointing in the general direction of flow, with the origin at the leading edge. The y -axis was naturally chosen normal to the x -axis in the upward direction, as shown in Fig. 1.1.2. It was also quite natural to choose the angle of attack to be positive with a positive y -component of relative wind, because increasing the angle of attack in this direction increases the lift produced on the airfoil. Once the sign convention for angle of attack was established, a nose-up pitching moment was defined to be positive, because this is the direction of increasing angle of attack. When the study of aerodynamics was later extended to three-dimensional flow about finite wings, it was convenient to align the x - and y -axes with the airfoil sections as was done for the two-dimensional airfoil analysis. With this orientation of the x - and y -axes, choosing a conventional right-handed coordinate system requires the z -axis to be pointing in the spanwise direction to the pilot's left, as shown in Fig. 1.1.1. Retaining the original airfoil sign convention for pitch, the positive nose-up pitching moment is a left-hand moment

8 Chapter 1 Overview of Aerodynamics

about the z -axis. Thus, the left-handed moment convention in the Cartesian aerodynamic coordinate system was established.

There are significant advantages to using the traditional aerodynamic coordinate system for the study of lift and drag. Furthermore, the disadvantages of the left-handed moment convention for roll, pitch, and yaw were probably not fully recognized until early in the development of the theory of aircraft dynamics. By then, the convention was well established in the aerodynamics literature.

To avoid the left-handed moment convention while retaining the traditional sign convention for roll, pitch and yaw, the body-fixed coordinate system shown in Fig. 1.1.3 is commonly used in the study of flight mechanics. In this text, the notation (x_b, y_b, z_b) will always be used in reference to this particular body-fixed coordinate system. The origin of this Cartesian system is always located at the aircraft center of gravity. The x_b -axis points forward along some convenient fuselage reference line in the aircraft's plane of symmetry. The y_b -axis is normal to the plane of symmetry pointing in the direction of the right wing. The z_b -axis then points downward in the aircraft plane of symmetry, completing the right-handed Cartesian system. In this coordinate system, a positive angle of attack corresponds to a positive z_b -component of the airplane's velocity vector relative to the surrounding atmosphere. Similarly, a positive sideslip angle is defined to correspond to a positive y_b -component of the airplane's velocity relative to the air. With this coordinate system, the traditional sign conventions for roll, pitch, and yaw follow the right-hand rule relative to the x_b -, y_b -, and z_b -axes, respectively. The components of the resultant aerodynamic force and moment in this coordinate system are denoted throughout this textbook as

$$\mathbf{F}_a = X \mathbf{i}_{x_b} + Y \mathbf{i}_{y_b} + Z \mathbf{i}_{z_b}$$

$$\mathbf{M}_a = \ell \mathbf{i}_{x_b} + m \mathbf{i}_{y_b} + n \mathbf{i}_{z_b}$$

where \mathbf{i}_{x_b} , \mathbf{i}_{y_b} , and \mathbf{i}_{z_b} are the unit vectors in the x_b -, y_b -, and z_b -directions, respectively.

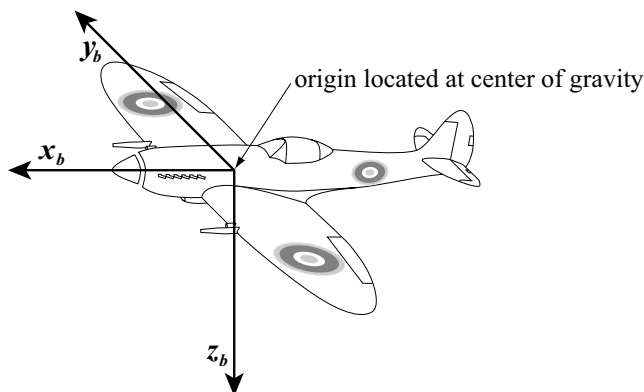


Figure 1.1.3. Body-fixed stability and control coordinates used in the study of flight mechanics.

The sign convention used in this textbook for control surface deflection also follows the right-hand rule relative to the (x_b, y_b, z_b) coordinate system shown in Fig. 1.1.3. As shown in Fig. 1.1.4, the control surfaces commonly used on a conventional airplane consist of ailerons, elevator, and rudder. The ailerons are used to control the rolling moment, the elevator is used to control the pitching moment, and the rudder is used to control the yawing moment. Downward deflection of the elevator is positive, deflection of the rudder to the left is positive, and aileron deflection is positive when the right aileron is deflected down and the left aileron is deflected up. Thus, positive elevator deflection is a right-hand rotation of the elevator relative to the y_b -axis. Similarly, positive rudder deflection corresponds to a right-hand rotation of the rudder relative to the z_b -axis. Positive aileron deflection can also be thought of as a right-hand rotation relative to the y_b -axis. For positive deflection of the ailerons, the aileron on the positive (right) wing has positive (right-hand) rotation and the aileron on the negative (left) wing has negative (left-hand) rotation.

For a positive deflection of the ailerons, the downward deflection of the right aileron increases lift on the right wing and the upward deflection of the left aileron decreases lift on the left wing. This produces a rolling moment to the left (negative ℓ). In a similar manner, a positive deflection of the elevator (downward) increases lift on the horizontal tail, producing a nose-down increment in the pitching moment (negative m). Likewise, a positive rudder deflection (to the left) produces a lift force to the right on the vertical tail and creates a nose-left yawing moment (negative n). In this text, angular deflections of the ailerons, elevator, and rudder are designated as δ_a , δ_e , and δ_r , respectively.

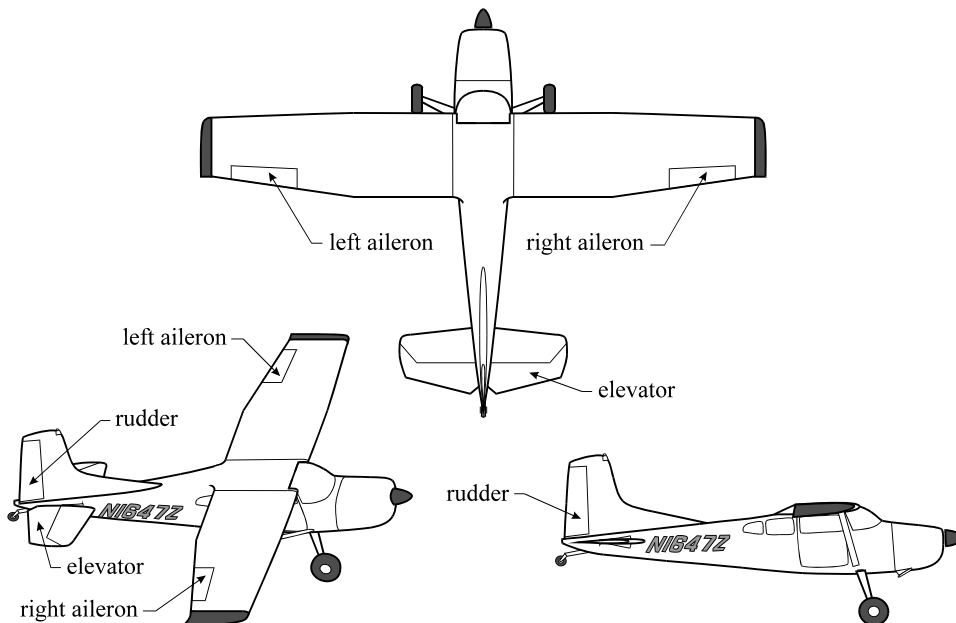


Figure 1.1.4. Typical control surfaces of a conventional airplane.

10 Chapter 1 Overview of Aerodynamics

1.2. Fluid Statics and the Atmosphere

The lift and drag acting on a moving aircraft are strong functions of air density. Thus, to predict aircraft motion, we must be able to determine the density of the air at the aircraft's altitude. For this purpose, the atmosphere can be regarded as a static fluid.

In a static fluid, the change in pressure, p , with respect to geometric altitude, H , is

$$\frac{dp}{dH} = -\rho g \quad (1.2.1)$$

where ρ is the fluid density and g is the acceleration of gravity. For all practical purposes, the atmosphere can be assumed to behave as an ideal gas, which gives

$$\rho = \frac{p}{RT} \quad (1.2.2)$$

where R is the ideal gas constant for the gas and T is the absolute temperature. Thus, the pressure variation in the atmosphere is governed by

$$\frac{dp}{dH} = -\frac{g}{R} \frac{p}{T} \quad (1.2.3)$$

From Newton's law of gravitation, g varies with altitude according to the relation

$$g = g_o \left(\frac{R_E}{R_E + H} \right)^2$$

where g_o is the standard acceleration of gravity at sea level, $g_o = 9.806645 \text{ m/s}^2$, and R_E is the radius of the Earth at sea level, $R_E = 6,356,766 \text{ m}$. Using Newton's law of gravitation in Eq. (1.2.3) gives

$$\left(\frac{R_E + H}{R_E} \right)^2 \frac{dp}{dH} = -\frac{g_o}{R} \frac{p}{T} \quad (1.2.4)$$

The integration of Eq. (1.2.4) is simplified by introducing the change of variables

$$Z \equiv \frac{R_E H}{R_E + H} \quad (1.2.5)$$

With this change of variables, Eq. (1.2.4) can be written as

$$\frac{1}{p} \frac{dp}{dZ} = -\frac{g_o}{R} \frac{1}{T} \quad (1.2.6)$$

The new variable that is defined in Eq. (1.2.5), Z , is called the *geopotential altitude*. The difference between the geopotential and geometric altitudes is small in the first several thousand feet above sea level. However, at higher altitudes the difference is significant.

1.2. Fluid Statics and the Atmosphere 11

Since the temperature and pressure variations in the atmosphere are different from day to day, aircraft instruments make use of the concept of a *standard atmosphere*. Many different “standard” atmospheres have been defined. However, most are essentially indistinguishable below 100,000 feet, which encloses the domain of most aircraft.

The standard atmosphere commonly used in the calibration of aircraft instruments is divided into several regions, each of which is assumed to have a constant temperature gradient with respect to geopotential altitude. The temperature gradients defined for this standard atmosphere are given in Table 1.2.1. This information completely defines the temperature throughout the standard atmosphere. Other atmosphere definitions are quite commonly used for special area environments. These include the *polar atmosphere*, the *desert atmosphere*, and the *10 percent hot day*.

Since the temperature gradient is constant in each of the altitude ranges defined in Table 1.2.1, the temperature in each range is linear,

$$T(Z) = T(Z_i) + T'_i(Z - Z_i) \quad (1.2.7)$$

where Z_i is the minimum geopotential altitude in the range and T'_i is the temperature gradient for the range, defined as the change in temperature with respect to geopotential altitude, dT/dZ . The negative of this temperature gradient is commonly referred to as the *lapse rate*. Applying Eq. (1.2.7), the integration of Eq. (1.2.6) subject to the boundary condition, $p(Z_i) = p_i$, yields

$$p(Z) = \begin{cases} p_i \exp\left[-\frac{g_o(Z - Z_i)}{RT_i}\right], & T'_i = 0 \\ p_i \left[\frac{T_i + T'_i(Z - Z_i)}{T_i}\right]^{\frac{-g_o}{RT'_i}}, & T'_i \neq 0 \end{cases} \quad (1.2.8)$$

From Eqs. (1.2.7) and (1.2.8), combined with the information given in Table 1.2.1, the temperature and pressure throughout the atmosphere can be determined from the ideal

Geopotential Altitude Range		Initial Temperature	Temperature Gradient
Z_i (m)	Z_{i+1} (m)	T_i (K)	T'_i (K/km)
0	11,000	288.150	-6.5
11,000	20,000	216.650	0.0
20,000	32,000	216.650	1.0
32,000	47,000	228.650	2.8
47,000	52,000	270.650	0.0
52,000	61,000	270.650	-2.0
61,000	79,000	252.650	-4.0
79,000	~90,000	180.650	0.0

Table 1.2.1. Temperature gradients with respect to geopotential altitude for the standard atmosphere commonly used in the calibration of aircraft instruments.

12 Chapter 1 Overview of Aerodynamics

gas constant and the temperature and pressure at standard sea level. The gas constant for the standard atmosphere is defined to be $287.0528 \text{ N}\cdot\text{m}/\text{kg}\cdot\text{K}$. The standard atmosphere is defined to have a temperature at sea level of 288.150 K , and standard atmospheric pressure at sea level is defined as $101,325 \text{ N}/\text{m}^2$.

Once the temperature and pressure are known at any altitude the density can be determined from Eq. (1.2.2) and the speed of sound can be computed from

$$a = \sqrt{\gamma RT} \quad (1.2.9)$$

where γ is the ratio of constant pressure to constant volume specific heat, which is 1.4 for the standard atmosphere. Remember that since a newton is $1 \text{ kg}\cdot\text{m}/\text{s}^2$, the ideal gas constant for the standard atmosphere can also be written as $287.0528 \text{ m}^2/\text{s}^2\cdot\text{K}$.

EXAMPLE 1.2.1. Compute the absolute temperature, pressure, density, and speed of sound for the standard atmosphere defined in Table 1.2.1 at a geometric altitude of 30,000 meters.

Solution. We start by determining geopotential altitude from the known geometric altitude. From Eq. (1.2.5),

$$Z \equiv \frac{R_E H}{R_E + H} = \frac{6,356,766 \text{ m}(30,000 \text{ m})}{6,356,766 \text{ m} + 30,000 \text{ m}} = 29,859 \text{ m}$$

Since this is in the third of altitude ranges given in Table 1.2.1, we must first integrate across the first two ranges. At the boundary between the first and the second range ($Z_1 = 11 \text{ km}$), from Eqs. (1.2.7) and (1.2.8) we obtain

$$T_1 = T_0 + T'_0(Z_1 - Z_0) = 288.150 \text{ K} + (-6.5 \text{ K}/\text{km})(11 - 0) \text{ km} = 216.650 \text{ K}$$

$$\begin{aligned} p_1 &= p_0 \left[\frac{T_0 + T'_0(Z_1 - Z_0)}{T_0} \right]^{\frac{-g_0}{RT'_0}} = p_0 \left(\frac{T_1}{T_0} \right)^{\frac{-g_0}{RT'_0}} \\ &= 101,325 \text{ N}/\text{m}^2 \left(\frac{216.650 \text{ K}}{288.150 \text{ K}} \right)^{\frac{-9.806645 \text{ m}/\text{s}^2}{287.0528 \text{ m}^2/\text{s}^2\cdot\text{K}(-0.0065 \text{ K}/\text{m})}} = 22,632 \text{ N}/\text{m}^2 \end{aligned}$$

and at the boundary between the second and the third range ($Z_2 = 20 \text{ km}$),

$$T_2 = T_1 + T'_1(Z_2 - Z_1) = 216.650 \text{ K} + (0.0 \text{ K}/\text{km})(20 - 11) \text{ km} = 216.650 \text{ K}$$

$$\begin{aligned} p_2 &= p_1 \exp \left[-\frac{g_0(Z_2 - Z_1)}{RT_1} \right] = 22,632 \text{ N}/\text{m}^2 \exp \left[-\frac{9.806645(20 - 11) \times 10^3}{287.0528(216.650)} \right] \\ &= 5,474.9 \text{ N}/\text{m}^2 \end{aligned}$$

1.2. Fluid Statics and the Atmosphere 13

Integrating from this point to the specified geopotential altitude of 29,859 meters, Eqs. (1.2.7) and (1.2.8) yield

$$T = T_2 + T_2'(Z - Z_2) = 216.650 \text{ K} + (1.0 \text{ K/km})(29.859 - 20) \text{ km} = \underline{226.509 \text{ K}}$$

$$\begin{aligned} p &= p_2 \left[\frac{T_2 + T_2'(Z - Z_2)}{T_2} \right]^{\frac{-g_0}{RT_2'}} = p_2 \left(\frac{T}{T_2} \right)^{\frac{-g_0}{RT_2'}} \\ &= 5,474.9 \text{ N/m}^2 \left(\frac{226.509 \text{ K}}{216.650 \text{ K}} \right)^{\frac{-9.806645 \text{ m/s}^2}{287.0528 \text{ m}^2/\text{s}^2 \cdot \text{K}(0.0010 \text{ K/m})}} = \underline{1,197.0 \text{ N/m}^2} \end{aligned}$$

From Eq. (1.2.2), the density is

$$\rho = \frac{p}{RT} = \frac{1,197.0 \text{ N/m}^2}{287.0528 \text{ N} \cdot \text{m/kg} \cdot \text{K} (226.509 \text{ K})} = \underline{0.018410 \text{ kg/m}^3}$$

and from Eq. (1.2.9), the speed of sound is

$$a = \sqrt{\gamma RT} = \sqrt{1.4 (287.0528 \text{ m}^2/\text{s}^2 \cdot \text{K}) 226.509 \text{ K}} = \underline{301.71 \text{ m/s}}$$

EXAMPLE 1.2.2. Compute the absolute temperature, pressure, density, and speed of sound, in English engineering units, for the standard atmosphere that is defined in Table 1.2.1 at a geometric altitude of 100,000 feet.

Solution. Since this standard atmosphere is defined in SI units, we start by converting the given geometric altitude to meters:

$$H = 100,000 \text{ ft} (0.304800 \text{ m/ft}) = 30,480 \text{ m}$$

Following the procedure used in Example 1.2.1, we obtain

$$Z = 30,335 \text{ m} / 0.3048 \text{ m/ft} = 99,523 \text{ ft}$$

$$T = 226.985 \text{ K} (1.80000^\circ \text{R/K}) = \underline{408.572^\circ \text{R}}$$

$$p = 1,114.3 \text{ N/m}^2 (0.02088543 \text{ lbf/ft}^2 / \text{N/m}^2) = 23.272 \text{ lbf/ft}^2 = \underline{0.16161 \text{ psi}}$$

$$\rho = 0.017102 \text{ kg/m}^3 (0.001940320 \text{ slug/ft}^3 / \text{kg/m}^3) = \underline{0.000033182 \text{ slug/ft}^3}$$

$$a = 302.03 \text{ m/s} / 0.3048 \text{ m/ft} = \underline{990.90 \text{ ft/sec}}$$

14 Chapter 1 Overview of Aerodynamics

Atmospheric temperature and pressure vary substantially with time and location on the Earth. Nevertheless, for the correlation of test data taken at different times and locations and for the calibration of aircraft flight instruments, it is important to have an agreed-upon standard for atmospheric properties. From the assumption of an ideal gas, pressure, density, and the speed of sound can be determined directly from a defined temperature profile. The standard atmosphere, based on the temperature profile defined in Table 1.2.1 and tabulated in Appendices A and B, is commonly used for the purposes mentioned above. Slightly different temperature profiles have also been used to define other standard atmospheres, but the variation is small below 100,000 feet.

1.3. The Boundary Layer Concept

As pointed out in Sec. 1.1, there are only two types of aerodynamic forces acting on a body moving through the atmosphere: pressure forces and viscous shear forces. The Reynolds number provides a measure of the relative magnitude of the pressure forces in relation to the viscous shear forces. For the airspeeds typically encountered in flight, Reynolds numbers are quite high and viscous forces are usually small compared to pressure forces. This does not mean that viscous forces can be neglected. However, it does allow us to apply the simplifying concept of boundary layer theory.

For flow over a streamlined body at low angle of attack and high Reynolds number, the effects of viscosity are essentially confined to a thin layer adjacent to the surface of the body, as shown in Fig. 1.3.1. Outside the boundary layer, the shear forces can be neglected and since the boundary layer is thin, the change in pressure across the thickness of this layer is insignificant. With this flow model, the pressure forces can be determined from the inviscid flow outside the boundary layer, and the shear forces can be obtained from a solution to the boundary layer equations.

While boundary layer theory provides a tremendous simplification over the complete Navier-Stokes equations, solutions to the boundary layer equations are far from trivial, especially for the complex geometry that is often encountered in an aircraft. A thorough review of boundary layer theory is beyond the intended scope of this chapter and is not prerequisite to an understanding of the fundamental principles of flight mechanics. However, there are some important results of boundary layer theory that the reader should know and understand.

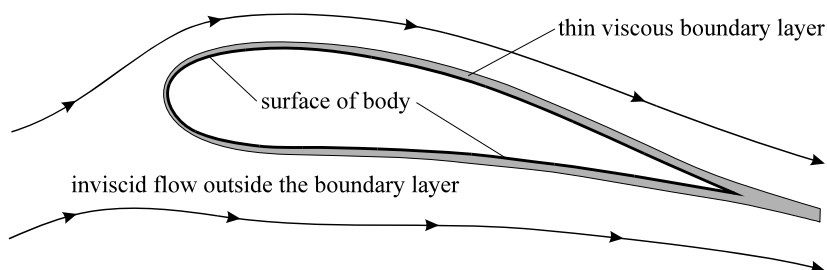


Figure 1.3.1. Boundary layer flow over a streamlined body at a low angle of attack.

1.3. The Boundary Layer Concept 15

1. For the high-Reynolds-number flows typically encountered in flight, the viscous shear forces are small compared to the pressure forces.
2. For flow at high Reynolds number, the pressure forces acting on a body can be closely approximated from an inviscid flow analysis, outside the boundary layer.
3. For two-dimensional flow about streamlined bodies at high Reynolds numbers and low angles of attack, pressure forces do not contribute significantly to drag.
4. For bluff bodies and streamlined bodies at high angles of attack, boundary layer separation occurs, as shown in Fig. 1.3.2, and pressure forces dominate the drag.

Boundary layer separation in the flow over airfoils and wings is commonly referred to as *stall*. An understanding of stall and its effect on lift and drag is critical in the study of flight mechanics. As the angle of attack for a wing is increased from zero, at first the boundary layer remains attached, as shown in Fig. 1.3.1, the lift coefficient increases as a nearly linear function of angle of attack, and the drag coefficient increases approximately with the angle of attack squared. As angle of attack continues to increase, the positive pressure gradient on the aft portion of the upper surface of the wing also increases. At some angle of attack this adverse pressure gradient may result in local boundary layer separation and the increase in lift with angle of attack will begin to diminish. At a slightly higher angle of attack, boundary layer separation becomes complete, as shown

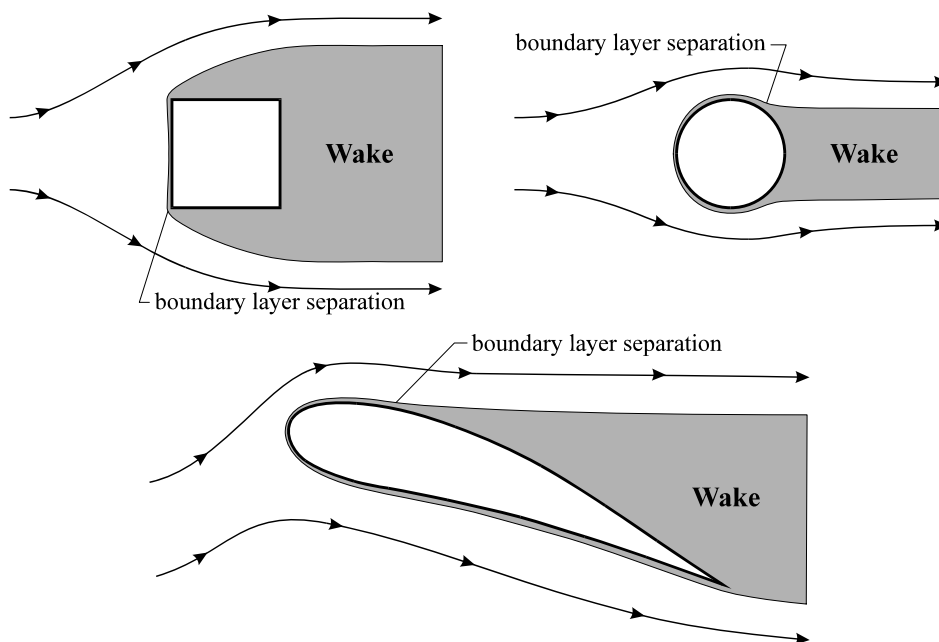


Figure 1.3.2. Examples of boundary layer separation.

16 Chapter 1 Overview of Aerodynamics

in Fig. 1.3.2, and the lift rapidly decreases as the angle of attack is increased further. Boundary layer separation also greatly accelerates the increase in drag with angle of attack. The maximum lift coefficient and the exact shape of the lift curve for angles of attack near stall depend substantially on the airfoil section geometry. As the angle of attack increases beyond stall, the lift and drag coefficients become less sensitive to section geometry and for angles of attack beyond about 25 degrees, the lift and drag coefficients are nearly independent of the airfoil section.

The maximum lift coefficient that can be attained on a given wing before stall is quite important in flight mechanics. This parameter not only determines the maximum weight that can be carried by a given wing at a particular airspeed, it also affects takeoff distance, turning radius, and other measures of airplane performance.

1.4. Inviscid Aerodynamics

Since the pressure forces acting on an aircraft at high Reynolds number can be closely estimated from an inviscid analysis of the flow outside the boundary layer, inviscid aerodynamics is an important tool used in the estimation of the forces acting on an aircraft in flight. Written in vector notation, the general equations that govern inviscid fluid flow are the continuity equation

$$\frac{\partial \rho}{\partial t} + (\mathbf{V} \cdot \nabla) \rho + \rho \nabla \cdot \mathbf{V} = 0 \quad (1.4.1)$$

and the momentum equation

$$\frac{\partial \mathbf{V}}{\partial t} + (\mathbf{V} \cdot \nabla) \mathbf{V} = -\frac{\nabla p}{\rho} - g \nabla H \quad (1.4.2)$$

where \mathbf{V} is the fluid velocity vector and t is time. Using the important mathematical identity

$$(\mathbf{V} \cdot \nabla) \mathbf{V} = \nabla \left(\frac{1}{2} V^2 \right) - \mathbf{V} \times (\nabla \times \mathbf{V})$$

the momentum equation for inviscid flow can be written

$$\frac{\partial \mathbf{V}}{\partial t} + \nabla \left(\frac{1}{2} V^2 \right) + \frac{\nabla p}{\rho} + g \nabla H = \mathbf{V} \times \boldsymbol{\Omega} \quad (1.4.3)$$

where $\boldsymbol{\Omega}$ is the curl of the velocity vector, traditionally called the *vorticity*:

$$\boldsymbol{\Omega} \equiv \nabla \times \mathbf{V} \quad (1.4.4)$$

It can be shown from the application of vector calculus to Eqs. (1.4.1) and (1.4.3) that vorticity cannot be generated in an inviscid flow. In the aerodynamics problem

1.4. Inviscid Aerodynamics 17

associated with flow over an aircraft in flight, the fluid velocity far upstream from the aircraft is uniform. From the definition of vorticity given in Eq. (1.4.4), this means that the vorticity far upstream from the aircraft is zero. Since vorticity cannot be generated in an inviscid flow, the vorticity must be zero everywhere in the inviscid flow outside the boundary layer. Vorticity is generated in the viscous boundary layer next to the skin of the aircraft and thus there is also vorticity in the boundary layer wake that trails behind an aircraft in flight. However, outside the boundary layer and trailing wake, the flow can be assumed to be inviscid and free of vorticity. Thus, for this flow, the right-hand side of Eq. (1.4.3) will be zero. This type of flow is called *inviscid irrotational flow*.

In summary, inviscid irrotational flow can be assumed to exist outside the boundary layer and trailing wake of an aircraft in flight. For this flow, the continuity and momentum equations are

$$\frac{\partial \rho}{\partial t} + (\mathbf{V} \cdot \nabla) \rho + \rho \nabla \cdot \mathbf{V} = 0 \quad (1.4.5)$$

$$\frac{\partial \mathbf{V}}{\partial t} + \nabla \left(\frac{1}{2} V^2 \right) + \frac{\nabla p}{\rho} + g \nabla H = 0 \quad (1.4.6)$$

For the important special case of an aircraft in steady flight, the time derivatives are zero and Eq. (1.4.6) reduces to

$$\nabla \left(\frac{1}{2} V^2 \right) + \frac{\nabla p}{\rho} + g \nabla H = 0 \quad (1.4.7)$$

For the freestream flow far from the aircraft, Eq. (1.4.7) gives

$$\nabla \left(\frac{1}{2} V_\infty^2 \right) + \frac{\nabla p_\infty}{\rho_\infty} + g \nabla H = 0$$

Since the freestream velocity is uniform, the gradient of V_∞^2 is zero, which gives

$$g \nabla H = - \frac{\nabla p_\infty}{\rho_\infty} \quad (1.4.8)$$

This is simply a form of the hydrostatic equation, which is given by Eq. (1.2.1). Using Eq. (1.4.8) in Eq. (1.4.7) to eliminate the geometric altitude gradient, **the momentum equation for the inviscid flow about an aircraft in steady flight is**

$$\nabla \left(\frac{1}{2} V^2 \right) + \frac{\nabla p}{\rho} - \frac{\nabla p_\infty}{\rho_\infty} = 0 \quad (1.4.9)$$

where p_∞ and ρ_∞ are evaluated at the same altitude as p and ρ .

18 Chapter 1 Overview of Aerodynamics

A special case of Eq. (1.4.9) that is of particular interest is the case of flow with negligible variation in air density. This approximation can be applied to flight at low Mach numbers. Assuming that ρ is constant, Eq. (1.4.9) reduces to

$$\nabla \left(\frac{1}{2} V^2 + \frac{p - p_\infty}{\rho} \right) = 0 \quad (1.4.10)$$

Integrating this result from the freestream to some arbitrary point in the flow and solving for the local static pressure, **the momentum equation for incompressible inviscid flow about an aircraft in steady flight yields**

$$p = p_\infty + \frac{1}{2} \rho (V_\infty^2 - V^2) \quad (1.4.11)$$

Once the velocity field has been determined in some manner, Eq. (1.4.11) can be used to determine the pressure at any point in the flow. The net contribution that these pressure forces make to the resultant aerodynamic force is then computed from

$$\mathbf{F}_p = - \iint_{\mathcal{S}} p \mathbf{n} d\mathcal{S} = - \iint_{\mathcal{S}} p_\infty \mathbf{n} d\mathcal{S} + \frac{1}{2} \rho V_\infty^2 \iint_{\mathcal{S}} [(V/V_\infty)^2 - 1] \mathbf{n} d\mathcal{S} \quad (1.4.12)$$

where \mathbf{n} is the unit outward normal and \mathcal{S} is the surface area. The first integral on the far right-hand side of Eq. (1.4.12) is the buoyant force, and the second integral is the vector sum of the pressure contribution to the lift and drag. For most conventional airplanes the buoyant force is small and can be neglected.

From Eq. (1.4.5), the continuity equation for incompressible flow is

$$\nabla \cdot \mathbf{V} = 0 \quad (1.4.13)$$

Because the curl of the gradient of any scalar function is zero, a flow field is irrotational if the velocity field is written as the gradient of a scalar function

$$\mathbf{V} = \nabla \phi \quad (1.4.14)$$

where ϕ is normally called the *velocity potential* and could be any scalar function of space and time that satisfies the continuity equation and the required boundary conditions. Using Eq. (1.4.14) in Eq. (1.4.13), this requires that

$$\nabla \cdot \mathbf{V} = \nabla \cdot \nabla \phi = \nabla^2 \phi = 0 \quad (1.4.15)$$

Thus the incompressible velocity potential must satisfy Laplace's equation and some appropriate boundary conditions. The far-field boundary condition is uniform flow. At the surface of the aircraft the normal component of velocity must go to zero. However, since the flow is inviscid, we do not require zero tangential velocity at the surface.

1.4. Inviscid Aerodynamics 19

For flight at higher Mach numbers the result predicted by Eq. (1.4.9) is more complex. When the density of a fluid changes with pressure, the temperature changes as well. Thus, in a compressible fluid, the pressure gradients that accompany velocity gradients also produce temperature gradients. In general, temperature gradients result in heat transfer. However, the thermal conductivity of air is extremely low. Thus, it is commonly assumed that the flow outside the boundary layer is adiabatic as well as inviscid. Inviscid adiabatic flow is isentropic. From the fundamentals of thermodynamics recall that for isentropic flow of an ideal gas, density is related to pressure according to the relation

$$\rho = \rho_{\infty} \left(\frac{p}{p_{\infty}} \right)^{\frac{1}{\gamma}} \quad (1.4.16)$$

where again γ is the ratio of specific heats ($\gamma = 1.4$ for air). Substituting Eq. (1.4.16) into Eq. (1.4.9) and neglecting the gradients of p_{∞} and ρ_{∞} yields

$$\nabla \left(\frac{1}{2} V^2 + \frac{\gamma}{\gamma-1} \frac{p}{\rho} \right) = 0 \quad (1.4.17)$$

Integrating Eq. (1.4.17) gives

$$\frac{1}{2} V^2 + \frac{\gamma}{\gamma-1} \frac{p}{\rho} = \text{constant} \quad (1.4.18)$$

Equation (1.4.18) must apply at the stagnation state, where $V=0$. Thus, the constant in Eq. (1.4.18) can be expressed in terms of the stagnation pressure and density, p_0 and ρ_0 ,

$$\frac{1}{2} V^2 + \frac{\gamma}{\gamma-1} \frac{p}{\rho} = \frac{\gamma}{\gamma-1} \frac{p_0}{\rho_0} \quad (1.4.19)$$

For an ideal gas $p/\rho = RT$ and $a^2 = \gamma RT$, where R is the gas constant and a is the speed of sound. Thus, Eqs. (1.4.16) and (1.4.19) written in terms of Mach number, M , require that

$$T = T_0 \left(1 + \frac{\gamma-1}{2} M^2 \right)^{-1} \quad (1.4.20)$$

$$p = p_0 \left(1 + \frac{\gamma-1}{2} M^2 \right)^{\frac{-\gamma}{\gamma-1}} \quad (1.4.21)$$

$$\rho = \rho_0 \left(1 + \frac{\gamma-1}{2} M^2 \right)^{\frac{-1}{\gamma-1}} \quad (1.4.22)$$

20 Chapter 1 Overview of Aerodynamics

Stagnation conditions are readily evaluated by applying Eqs. (1.4.20) through (1.4.22) to the freestream flow:

$$T_0 = T_\infty \left(1 + \frac{\gamma - 1}{2} M_\infty^2 \right) \quad (1.4.23)$$

$$p_0 = p_\infty \left(1 + \frac{\gamma - 1}{2} M_\infty^2 \right)^{\frac{\gamma}{\gamma - 1}} \quad (1.4.24)$$

$$\rho_0 = \rho_\infty \left(1 + \frac{\gamma - 1}{2} M_\infty^2 \right)^{\frac{1}{\gamma - 1}} \quad (1.4.25)$$

Equation (1.4.14) applies to compressible flow as well as to incompressible flow. **For any irrotational flow, the velocity vector field can always be expressed as the gradient of a scalar potential field.** All such flows are called *potential flows*. The only requirement for potential flow is that the flow be irrotational. There are no further restrictions. It can be shown mathematically that the curl of the gradient of any scalar function is zero. Thus, it follows that **every potential flow is an irrotational flow.** It can also be shown mathematically that if the curl of any vector field is zero, that vector field can be expressed as the gradient of some scalar function. Therefore, **every irrotational flow is a potential flow.** For this reason the terms *potential flow* and *irrotational flow* are used synonymously.

1.5. Review of Elementary Potential Flows

Since the governing equations for incompressible potential flow are linear, solutions are additive. That is, if two or more solutions each satisfy the incompressible potential flow equations independently, their sum will satisfy these equations as well. As a result, the solution for incompressible potential flow over a body of complex geometry can be obtained by combining a number of elementary solutions.

In this section we review some of the more commonly used elementary solutions for incompressible potential flows. In your introductory classes on fluid mechanics and aerodynamics you probably developed at least some of these elementary solutions. Here, only the final results will be presented in summary form.

Uniform Flow

A uniform flow with constant but completely arbitrary velocity components will satisfy the potential flow equations and can be expressed as

$$\phi = V_x x + V_y y + V_z z + C \quad (1.5.1)$$

$$\mathbf{V} = \nabla \phi = V_x \mathbf{i}_x + V_y \mathbf{i}_y + V_z \mathbf{i}_z \quad (1.5.2)$$

Two-Dimensional Source Flow

For a two-dimensional (2-D) source located at the origin and having strength A , the scalar velocity potential and velocity vector fields in polar coordinates (r, θ) are given by

$$\phi = \frac{A}{2\pi} \ln r + C \quad (1.5.3)$$

$$\mathbf{V} = \nabla\phi = \frac{A}{2\pi r} \mathbf{i}_r \quad (1.5.4)$$

where C is an arbitrary constant and \mathbf{i}_r is the unit vector in the r -direction.

Two-Dimensional Vortex Flow

A 2-D vortex with circulation Γ located at the origin is described by

$$\phi = -\frac{\Gamma}{2\pi} \theta + C \quad (1.5.5)$$

$$\mathbf{V} = \nabla\phi = -\frac{\Gamma}{2\pi r} \mathbf{i}_\theta \quad (1.5.6)$$

Two-Dimensional Doublet Flow

Combining a positive source with a negative source (called a *sink*) forms a doublet. This potential flow is described according to

$$\phi = \frac{\kappa}{2\pi} \frac{\cos\theta}{r} + C \quad (1.5.7)$$

$$\mathbf{V} = \nabla\phi = -\frac{\kappa \cos\theta}{2\pi r^2} \mathbf{i}_r - \frac{\kappa \sin\theta}{2\pi r^2} \mathbf{i}_\theta \quad (1.5.8)$$

Two-Dimensional Stagnation Flow

The flow near a 2-D stagnation point can be described as a potential flow. For the case where the freestream velocity is in the x -direction, the solid surface is coincident with the y -axis, and the stagnation point is located at the origin, the potential field and velocity field can be expressed as

$$\phi = \frac{B}{2} (x^2 - y^2) + C \quad (1.5.9)$$

$$\mathbf{V} = \nabla\phi = Bx\mathbf{i}_x - By\mathbf{i}_y \quad (1.5.10)$$

22 Chapter 1 Overview of Aerodynamics

Two-Dimensional Source Panels

The source sheet is an important elementary potential flow that is not included in many introductory aerodynamics textbooks. While it is possible to synthesize flow over some bodies of very specific shape by combining a finite number of sources and sinks with a uniform flow, to synthesize flow over a body of arbitrary shape, greater flexibility is required. The 2-D source sheet helps provide such increased flexibility. Combining an infinite number of infinitesimally weak 2-D sources in side-by-side fashion as shown in Fig. 1.5.1 forms this potential flow.

While a source sheet with a completely arbitrary curved shape, such as that shown in Fig. 1.5.1, is required to synthesize flow exactly over a body of arbitrary shape, such a sheet can be closely approximated using a series of planar segments. A planar source sheet is usually referred to as a *source panel*. Approximating a source sheet with a series of source panels significantly simplifies the solution process.

Consider the differential segment of a 2-D source panel that lies on the x -axis at the location $x = x_o$, as shown in Fig. 1.5.2. The velocity induced by this differential source panel at an arbitrary point with coordinates (x,y) is given by

$$dV_x = dV_r \cos \theta = \frac{\lambda(x_o)}{2\pi r} \cos \theta dx_o = \frac{(x-x_o)\lambda(x_o)}{2\pi[(x-x_o)^2 + y^2]} dx_o$$

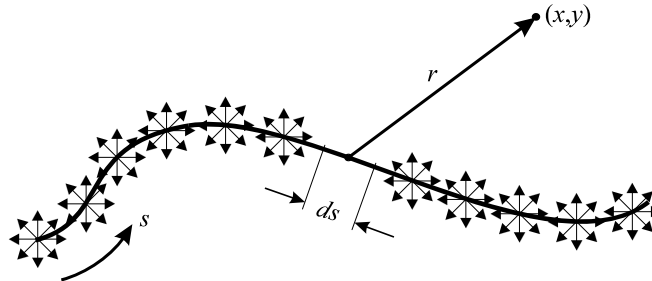


Figure 1.5.1. Edge view of a 2-D source sheet.

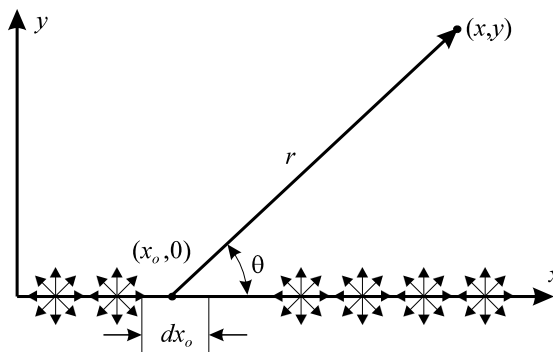


Figure 1.5.2. Edge view of a 2-D source panel on the x -axis.

and

$$dV_y = dV_r \sin \theta = \frac{\lambda(x_o)}{2\pi r} \sin \theta dx_o = \frac{y \lambda(x_o)}{2\pi [(x-x_o)^2 + y^2]} dx_o$$

where $\lambda(x_o)$ is the strength per unit length at x_o and the remaining notation is defined in Fig. 1.5.2. Integrating over a panel with a linear strength distribution that extends from $x_o = 0$ to $x_o = l$, the velocity induced at the point (x,y) by the entire source panel is

$$\begin{Bmatrix} V_x \\ V_y \end{Bmatrix} = \frac{1}{2\pi l} \begin{bmatrix} [-y\Phi + (l-x)\Psi + l] & (y\Phi + x\Psi - l) \\ [(l-x)\Phi + y\Psi] & (x\Phi - y\Psi) \end{bmatrix} \begin{Bmatrix} \lambda(0) \\ \lambda(l) \end{Bmatrix} \quad (1.5.11)$$

$$\Phi \equiv \text{atan2}(yl, y^2 + x^2 - xl) \quad (1.5.12)$$

$$\Psi \equiv \frac{1}{2} \ln \left[\frac{x^2 + y^2}{(x-l)^2 + y^2} \right] \quad (1.5.13)$$

As can be seen in Fig. 1.5.3, the angle Φ can take any value between $-\pi$ and π . Note that when the point (x,y) is either left or right of the panel ($x < 0$ or $x > l$) the angle Φ is positive when y is above the axis, negative when y is below the axis, and approaches zero as y approaches zero from either side. However, when the point (x,y) is directly above the panel ($0 < x < l$ and $y > 0$) and y approaches zero from above, Φ approaches π . On the other hand, when the point (x,y) is directly below the panel ($0 < x < l$ and $y < 0$) and y approaches zero from below, Φ approaches $-\pi$. Thus we see that there is a step discontinuity of 2π in the angle Φ as we cross the panel itself,

$$\Phi(x, \pm 0) = \pm \pi, \quad 0 < x < l$$

where $y = +0$ indicates a point just above the surface and $y = -0$ indicates a point just below the surface.

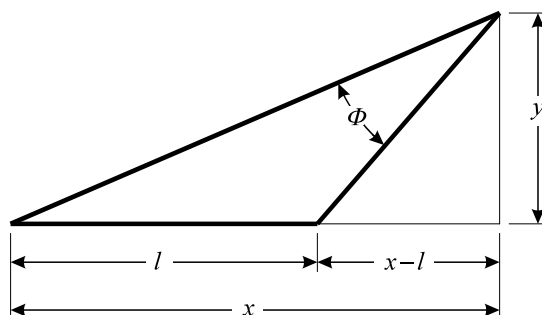


Figure 1.5.3. Geometry for a finite 2-D source panel.

24 Chapter 1 Overview of Aerodynamics

Single-argument arctangent functions like the Fortran or C intrinsic function “atan” will always return values between $-\pi/2$ and $\pi/2$. Such functions cannot be used to compute the angle Φ from Eq. (1.5.12) for all values of x and y . To obtain the correct result over the full range of x and y , the angle Φ must always be computed using a two-argument arctangent function, such as the Fortran or C intrinsic function “atan2.”

Two-Dimensional Vortex Panels

While 2-D source panels can be used to synthesize nonlifting flow over a 2-D body of arbitrary cross-section, a source panel produces no circulation. No potential flow that includes circulation can be synthesized from source panels alone. In addition, the Kutta-Joukowski law requires that for any closed 2-D body of arbitrary shape, the lift per unit span is always proportional to the circulation. Thus, no lifting potential flow can be synthesized from source panels alone.

For the synthesis of 2-D lifting flows, vortex panels are commonly used. A 2-D vortex panel is formed from 2-D vortices in the same way that a 2-D source panel is formed from 2-D sources. An infinite number of infinitesimally weak vortices are combined in side-by-side fashion as shown in Fig. 1.5.4. In this figure we are again looking at an edge view of the panel with the vortices all perpendicular to the page.

Now consider a differential segment of a vortex panel that lies on the x -axis at the location $x = x_o$ and has length dx_o . The velocity induced at any point (x,y) by this differential vortex panel is normal to a line drawn between the point (x,y) and the point $(x_o,0)$ and has a magnitude inversely proportional to the distance between the two points. The x - and y -components of the velocity induced at the point (x,y) by this infinitesimally small section of the vortex panel are then given by

$$dV_x = -dV_\theta \sin \theta = \frac{\gamma(x_o)}{2\pi r} \sin \theta dx_o = \frac{y\gamma(x_o)}{2\pi[(x-x_o)^2 + y^2]} dx_o$$

$$dV_y = dV_\theta \cos \theta = -\frac{\gamma(x_o)}{2\pi r} \cos \theta dx_o = -\frac{(x-x_o)\gamma(x_o)}{2\pi[(x-x_o)^2 + y^2]} dx_o$$

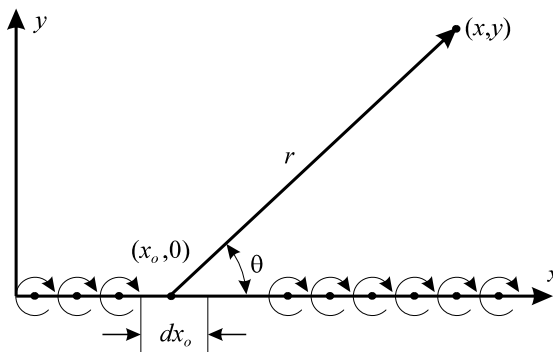


Figure 1.5.4. Edge view of a 2-D vortex panel on the x -axis.

1.5. Review of Elementary Potential Flows 25

where $\gamma(x_o)$ is the vortex strength per unit length at x_o and the remaining notation is defined in Fig. 1.5.4. For a linear vortex strength distribution on a panel extending from $x = 0$ to $x = l$, the total induced velocity at the point (x, y) is

$$\begin{Bmatrix} V_x \\ V_y \end{Bmatrix} = \frac{1}{2\pi l} \begin{bmatrix} [(l-x)\Phi + y\Psi] & (x\Phi - y\Psi) \\ [y\Phi - (l-x)\Psi - l] & (-y\Phi - x\Psi + l) \end{bmatrix} \begin{Bmatrix} \gamma(0) \\ \gamma(l) \end{Bmatrix} \quad (1.5.14)$$

$$\Phi \equiv \text{atan2}(yl, y^2 + x^2 - xl) \quad (1.5.15)$$

$$\Psi \equiv \frac{1}{2} \ln \left[\frac{x^2 + y^2}{(x-l)^2 + y^2} \right] \quad (1.5.16)$$

At any point along a vortex panel, there is a local jump in tangential velocity across the panel that is equal to the local vortex strength. There is no normal velocity jump across a vortex panel.

Three-Dimensional Vortex Line Segments

Vortex filaments can be used to synthesize potential flow over finite wings and other lifting surfaces. Since the vortex filaments used for this purpose cannot be straight over their entire length, these vortex filaments are often broken up into finite segments. As a fundamental building block, consider an arbitrary straight segment of a vortex filament that extends from point 1 to point 2, as shown in Fig. 1.5.5. We wish to express the velocity vector induced at point 3 by this straight vortex segment. Let point 4 be an arbitrary point on the vortex segment between point 1 and point 2. Let $d\mathbf{V}$ be the differential velocity vector induced at point 3 by the directed differential segment of the filament, $d\mathbf{l}$, located at point 4. From the Biot-Savart law, we have

$$d\mathbf{V} = \frac{\Gamma d\mathbf{l} \times \mathbf{r}}{4\pi |\mathbf{r}|^3} \quad (1.5.17)$$

where Γ is the vortex strength and \mathbf{r} is the spatial vector from point 4 to point 3.

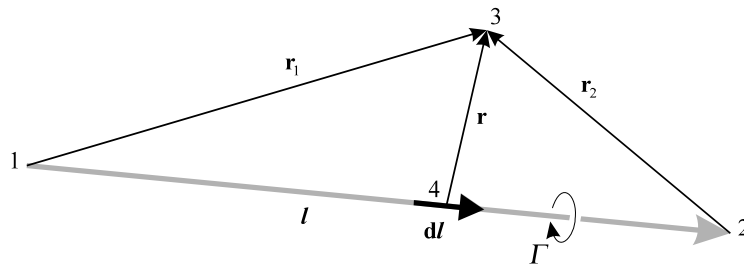


Figure 1.5.5. Geometric relationships for the velocity induced by a straight vortex segment.

26 Chapter 1 Overview of Aerodynamics

After integrating Eq. (1.5.17) from point 1 to point 2, it can be shown that the velocity vector induced at an arbitrary point in space by **any straight vortex segment** is

$$\mathbf{V} = \frac{\Gamma}{4\pi} \frac{(r_1 + r_2)(\mathbf{r}_1 \times \mathbf{r}_2)}{r_1 r_2 (r_1 r_2 + \mathbf{r}_1 \cdot \mathbf{r}_2)} \quad (1.5.18)$$

where Γ is the vortex strength, \mathbf{r}_1 is the spatial vector from the beginning of the segment to the arbitrary point in space, and \mathbf{r}_2 is the spatial vector from the end of the segment to the arbitrary point in space.

The velocity that is induced at an arbitrary point in space by a **straight semi-infinite vortex segment** can be determined as a special case of Eq. (1.5.18), by taking the limit as r_2 approaches infinity. This gives

$$\mathbf{V} = \frac{\Gamma}{4\pi} \frac{\mathbf{u}_\infty \times \mathbf{r}_1}{r_1 (r_1 - \mathbf{u}_\infty \cdot \mathbf{r}_1)} \quad (1.5.19)$$

where Γ is the vortex strength, \mathbf{u}_∞ is the unit vector in the direction from the beginning of the segment toward the end at infinity, and \mathbf{r}_1 is the spatial vector from the beginning of the segment to the arbitrary point in space.

1.6. Incompressible Flow over Airfoils

An airfoil is any 2-D cross-section of a wing or other lifting surface that lies in a plane perpendicular to the spanwise coordinate. An airfoil section is completely defined by the geometric shape of its boundary. However, the aerodynamic properties of an airfoil section are most profoundly affected by the shape of its centerline. This centerline is midway between the upper and lower surfaces of the airfoil and is called the *camber line*. If the airfoil is not symmetric, the camber line is not a straight line but rather a planar curve.

Because the shape of the camber line is such an important factor in airfoil design, it is critical that the student understand exactly how the camber line is defined. In addition, there are several other designations that will be used throughout this and following chapters when referring to the geometric attributes of airfoil sections. The student should be sure that he or she understands the following nomenclature as it applies to airfoil geometry such as that shown in Fig. 1.6.1.

The **camber line** is the locus of points midway between the upper and lower surfaces of an airfoil section as **measured perpendicular to the camber line itself**.

The **leading edge** is the most forward point on the camber line.

The **trailing edge** is the most rearward point on the camber line.

The **chord line** is a straight line connecting the leading edge and the trailing edge.

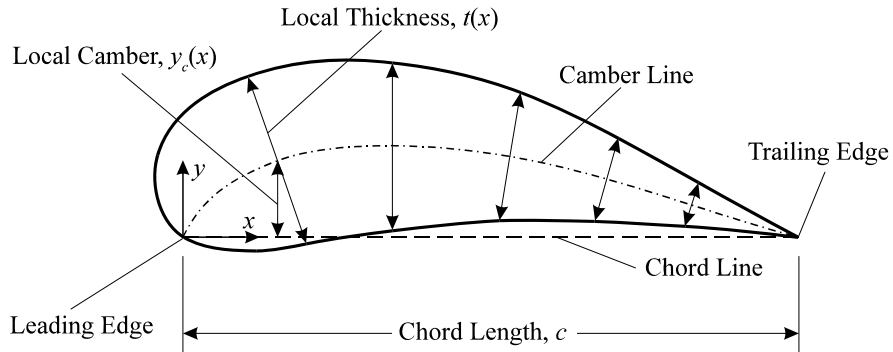


Figure 1.6.1. Airfoil coordinates and nomenclature.

The **chord length**, often referred to simply as the **chord**, is the distance between the leading edge and the trailing edge as measured along the chord line.

The **maximum camber**, often referred to simply as the **camber**, is the maximum distance between the chord line and the camber line as measured perpendicular to the chord line.

The **local thickness**, at any point along the chord line, is the distance between the upper and lower surfaces as **measured perpendicular to the camber line**.

The **maximum thickness**, often referred to simply as the **thickness**, is the maximum distance between the upper and lower surfaces as **measured perpendicular to the camber line**.

The **upper and lower surface coordinates** for an airfoil can be obtained explicitly from the camber line geometry, $y_c(x)$, and the thickness distribution, $t(x)$,

$$x_u(x) = x - \frac{t(x)}{2\sqrt{1+(dy_c/dx)^2}} \frac{dy_c}{dx} \quad (1.6.1)$$

$$y_u(x) = y_c(x) + \frac{t(x)}{2\sqrt{1+(dy_c/dx)^2}} \quad (1.6.2)$$

$$x_l(x) = x + \frac{t(x)}{2\sqrt{1+(dy_c/dx)^2}} \frac{dy_c}{dx} \quad (1.6.3)$$

$$y_l(x) = y_c(x) - \frac{t(x)}{2\sqrt{1+(dy_c/dx)^2}} \quad (1.6.4)$$

28 Chapter 1 Overview of Aerodynamics

Thin Airfoil Theory

For airfoils with a maximum thickness of about 12 percent or less, the inviscid aerodynamic force and moment are only slightly affected by the thickness distribution. The resultant aerodynamic force and moment acting on such an airfoil depend almost exclusively on the angle of attack and the shape of the camber line. For this reason, the inviscid aerodynamics for these airfoils can be closely approximated by assuming that the airfoil thickness is zero everywhere along the camber line. Thus, airfoils with a thickness of about 12 percent or less can be approximated by combining a uniform flow with a vortex sheet placed along the camber line, as shown schematically in Fig. 1.6.2. The strength of this vortex sheet is allowed to vary with the distance, s , measured along the camber line. The variation in this strength, $\gamma(s)$, is determined so that the camber line becomes a streamline for the flow.

In the development of thin airfoil theory it is shown that the vortex strength distribution necessary to make the camber line a streamline is related to the camber line geometry according to

$$\frac{1}{2\pi} \int_{x_o=0}^c \frac{\gamma(x_o)}{x-x_o} dx_o = V_\infty \left(\alpha - \frac{dy_c}{dx} \right) \quad (1.6.5)$$

This is the fundamental equation of thin airfoil theory. Any vortex strength distribution, $\gamma(x_o)$, which satisfies Eq. (1.6.5) will make the camber line a streamline of the flow, at least within the accuracy of the approximations used in thin airfoil theory. For a given airfoil at a given angle of attack, the only unknown in Eq. (1.6.5) is the vortex strength distribution, $\gamma(x_o)$. This equation is subject to a boundary condition known as the *Kutta condition*, which requires that

$$\gamma(c) = 0 \quad (1.6.6)$$

Development of the general solution to Eq. (1.6.5), subject to (1.6.6), is presented in most undergraduate engineering textbooks on aerodynamics. This solution is found by using the change of variables, $x=c(1-\cos\theta)/2$. Only the final result is presented here.

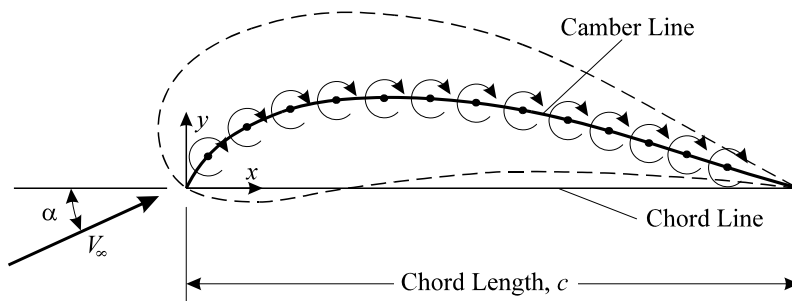


Figure 1.6.2. Synthesis of a thin airfoil section from a uniform flow and a curved vortex sheet distributed along the camber line.

1.6. Incompressible Flow over Airfoils 29

The solution is in the form of an infinite series for the vortex strength distribution,

$$\gamma(\theta) = 2V_\infty \left(A_0 \frac{1+\cos\theta}{\sin\theta} + \sum_{n=1}^{\infty} A_n \sin(n\theta) \right) \quad (1.6.7)$$

$$A_0 = \alpha - \frac{1}{\pi} \int_{\theta=0}^{\pi} \frac{dy_c}{dx} d\theta \quad (1.6.8)$$

$$A_n = \frac{2}{\pi} \int_{\theta=0}^{\pi} \frac{dy_c}{dx} \cos(n\theta) d\theta \quad (1.6.9)$$

$$x(\theta) \equiv \frac{c}{2}(1-\cos\theta) \quad (1.6.10)$$

The aerodynamic force per unit span can be predicted from the **Kutta-Joukowski law**, which applies to all 2-D potential flows. This requires that the net aerodynamic force is always normal to the freestream and equal to

$$\tilde{L} = \rho V_\infty \Gamma \quad (1.6.11)$$

A direct consequence of the Kutta-Joukowski law is that the pressure drag for any 2-D flow without boundary layer separation is zero.

Applying the Kutta-Joukowski law to a differential segment of the vortex sheet that is used to synthesize a thin airfoil gives

$$d\tilde{L} = \rho V_\infty d\Gamma = \rho V_\infty \gamma(x_o) dx_o = \frac{\rho V_\infty c}{2} \gamma(\theta_o) \sin\theta_o d\theta_o$$

Applying Eq. (1.6.7) for the vortex strength distribution, this result can be used to evaluate the lift and moment coefficients as well as the center of pressure.

$$\tilde{C}_L = 2\pi(A_0 + \frac{1}{2}A_1) = 2\pi \left(\alpha - \frac{1}{\pi} \int_{\theta=0}^{\pi} \frac{dy_c}{dx} (1-\cos\theta) d\theta \right) = 2\pi(\alpha - \alpha_{L0}) \quad (1.6.12)$$

$$\tilde{C}_{m_{c/4}} = -\frac{\tilde{C}_L}{4} + \frac{\pi}{4}(A_2 - A_1) = -\frac{\tilde{C}_L}{4} + \frac{1}{2} \int_{\theta=0}^{\pi} \frac{dy_c}{dx} [\cos(2\theta) - \cos\theta] d\theta \quad (1.6.13)$$

$$\tilde{C}_{m_{c/4}} = \frac{\pi}{4}(A_2 - A_1) = \frac{1}{2} \int_{\theta=0}^{\pi} \frac{dy_c}{dx} [\cos(2\theta) - \cos\theta] d\theta \quad (1.6.14)$$

$$\frac{x_{cp}}{c} = \frac{1}{4} + \frac{\pi}{4\tilde{C}_L}(A_1 - A_2) = \frac{1}{4} + \frac{1}{2\tilde{C}_L} \int_{\theta=0}^{\pi} \frac{dy_c}{dx} [\cos\theta - \cos(2\theta)] d\theta \quad (1.6.15)$$

30 Chapter 1 Overview of Aerodynamics

Note from Eq. (1.6.12) that thin airfoil theory predicts a section lift coefficient that is a linear function of angle of attack, and that the change in lift coefficient with respect to angle of attack is 2π per radian. Also note that the lift coefficient at zero angle of attack is a function only of the shape of the camber line. Thus, for thin airfoils,

$$\text{section lift slope} \equiv \frac{d\tilde{C}_L}{d\alpha} \equiv \tilde{C}_{L,\alpha} = 2\pi$$

$$\text{zero lift angle of attack} \equiv \alpha_{L0} = \frac{1}{\pi} \int_{\theta=0}^{\pi} \frac{dy_c}{dx} (1 - \cos \theta) d\theta$$

Also notice that the leading-edge moment coefficient and center of pressure both depend on lift coefficient and hence on angle of attack. The quarter-chord moment coefficient, on the other hand, is independent of angle of attack and depends only on the shape of the camber line. Since the aerodynamic center is defined to be the point on the airfoil where the moment does not change with angle of attack, **for incompressible flow, the quarter chord is the aerodynamic center of a thin airfoil**. Thus, the quarter chord is usually referred to as the *theoretical* or *ideal aerodynamic center* of the cambered airfoil. Viscous effects and airfoil thickness can cause the quarter-chord moment coefficient to vary slightly with angle of attack, but this variation is small and the aerodynamic center is always close to the quarter chord for subsonic flow. For this reason, airfoil section moment data are usually reported in terms of the quarter-chord moment coefficient. For an airfoil with no camber, Eq. (1.6.15) shows that **the quarter chord is also the center of pressure for incompressible flow about a thin symmetric airfoil**.

As is the case with all 2-D potential flow, thin airfoil theory predicts a net aerodynamic force that is normal to the freestream. Thus, thin airfoil theory predicts a section drag coefficient that is exactly zero. This is not a function of the thin airfoil approximation. Numerical panel methods will also predict zero section drag, including the effects of thickness. Section drag in any 2-D subsonic flow results entirely from viscous effects, which are neglected in the potential flow equations. The viscous forces also have some effect on lift, but this effect is relatively small.

EXAMPLE 1.6.1. For the purpose of demonstrating the application of thin airfoil theory, consider a hypothetical airfoil section that has a parabolic camber line geometry defined by the equation

$$\frac{y_c}{c} = 4 \frac{y_{mc}}{c} \left[\frac{x}{c} - \left(\frac{x}{c} \right)^2 \right]$$

where c is the airfoil chord length and y_{mc} is the maximum camber. Using thin airfoil theory, obtain algebraic expressions for the zero-lift angle of attack and the quarter-chord moment coefficient as a function of maximum camber. For an airfoil of this geometry having 4 percent maximum camber, use this thin airfoil analysis to estimate the section lift coefficients at a 5-degree angle of attack and the section quarter-chord moment coefficient.

1.6. Incompressible Flow over Airfoils 31

Solution. Differentiating the given camber line equation, the camber line slope is

$$\frac{dy_c}{dx} = 4y_{mc} \left(\frac{1}{c} - 2 \frac{x}{c^2} \right) = 4 \frac{y_{mc}}{c} \left(1 - 2 \frac{x}{c} \right)$$

Using the change of variables

$$\frac{x}{c} \equiv \frac{1}{2}(1 - \cos \theta)$$

we have

$$\frac{dy_c}{dx} = 4 \frac{y_{mc}}{c} \left[1 - 2 \frac{1}{2}(1 - \cos \theta) \right] = 4 \frac{y_{mc}}{c} \cos \theta$$

From Eqs. (1.6.8) and (1.6.9), the first three coefficients in the infinite series solution are

$$A_0 = \alpha - \frac{1}{\pi} \int_{\theta=0}^{\pi} \frac{dy_c}{dx} d\theta = \alpha - \frac{4}{\pi} \frac{y_{mc}}{c} \int_{\theta=0}^{\pi} \cos \theta d\theta = \alpha - \frac{4}{\pi} \frac{y_{mc}}{c} [\sin \theta]_{\theta=0}^{\pi} = \alpha$$

$$\begin{aligned} A_1 &= \frac{2}{\pi} \int_{\theta=0}^{\pi} \frac{dy_c}{dx} \cos \theta d\theta = \frac{8}{\pi} \frac{y_{mc}}{c} \int_{\theta=0}^{\pi} \cos^2 \theta d\theta = \frac{8}{\pi} \frac{y_{mc}}{c} \left[\frac{1}{2} \theta + \frac{1}{4} \sin(2\theta) \right]_{\theta=0}^{\pi} \\ &= 4 \frac{y_{mc}}{c} \end{aligned}$$

$$\begin{aligned} A_2 &= \frac{2}{\pi} \int_{\theta=0}^{\pi} \frac{dy_c}{dx} \cos(2\theta) d\theta = \frac{8}{\pi} \frac{y_{mc}}{c} \int_{\theta=0}^{\pi} \cos \theta \cos(2\theta) d\theta \\ &= \frac{8}{\pi} \frac{y_{mc}}{c} \int_{\theta=0}^{\pi} \cos \theta (2 \cos^2 \theta - 1) d\theta = \frac{8}{\pi} \frac{y_{mc}}{c} \int_{\theta=0}^{\pi} (2 \cos^3 \theta - \cos \theta) d\theta \\ &= \frac{8}{\pi} \frac{y_{mc}}{c} \left[\frac{2}{3} \sin \theta (\cos^2 \theta + 2) - \sin \theta \right]_{\theta=0}^{\pi} = 0 \end{aligned}$$

From Eq. (1.6.12), the section lift coefficient is

$$\tilde{C}_L = 2\pi(A_0 + \frac{1}{2}A_1) = 2\pi \left(\alpha + 2 \frac{y_{mc}}{c} \right) = 2\pi(\alpha - \alpha_{L0})$$

Thus, the zero-lift angle of attack can be expressed as

$$\alpha_{L0} = \underline{\underline{-2 \frac{y_{mc}}{c}}}$$

32 Chapter 1 Overview of Aerodynamics

Similarly, from Eq. (1.6.14), the quarter-chord moment coefficient is

$$\tilde{C}_{m_{c/4}} = \frac{\pi}{4}(A_2 - A_1) = \frac{\pi}{4}\left(0 - 4\frac{y_{mc}}{c}\right) = \underline{-\pi\frac{y_{mc}}{c}}$$

For this airfoil with 4 percent maximum camber and a 5-degree angle of attack,

$$\tilde{C}_L = 2\pi(\alpha - \alpha_{L0}) = 2\pi\left[\alpha - \left(-2\frac{y_{mc}}{c}\right)\right] = 2\pi\left[\frac{5\pi}{180} + 2(0.04)\right] = \underline{1.05}$$

$$\tilde{C}_{m_{c/4}} = -\pi\frac{y_{mc}}{c} = -\pi(0.04) = \underline{-0.126}$$

The Vortex Panel Method

Potential flow over an airfoil of arbitrary shape can be synthesized by combining uniform flow with a curved vortex sheet wrapped around the surface of the airfoil, as shown in Fig. 1.6.3. The vortex strength must vary along the surface such that the normal component of velocity induced by the entire sheet and the uniform flow is zero everywhere along the surface of the airfoil. In most cases, the strength distribution necessary to satisfy this condition is very difficult or impossible to determine analytically. However, for numerical computations, such a sheet can be approximated as a series of flat vortex panels wrapped around the surface of the airfoil. In the limit as the panel size becomes very small, the panel solution approaches that for the curved vortex sheet.

To define the vortex panels, a series of nodes is placed on the airfoil surface. For best results the nodes should be clustered more tightly near the leading and trailing edges. The most popular method for attaining this clustering is called *cosine clustering*. For this method we use the change of variables

$$\frac{x}{c} = \frac{1}{2}(1 - \cos\theta)$$

which is the same change of variables as that used in thin airfoil theory. Distributing the nodes uniformly in θ will provide the desired clustering in x . For best results near the

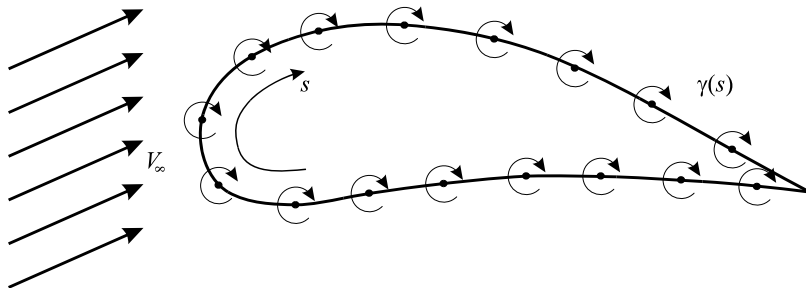


Figure 1.6.3. Synthesis of an arbitrary airfoil section from a uniform flow and a vortex sheet.

1.6. Incompressible Flow over Airfoils 33

leading edge, an even number of nodes should always be used. For this particular distribution, the nodal coordinates are computed from the algorithm

$$\delta\theta = \frac{2\pi}{n-1} \quad (1.6.16)$$

$$\begin{cases} x_N(n/2+i) \\ y_N(n/2+i) \\ x_N(n/2+1-i) \\ y_N(n/2+1-i) \end{cases} = \begin{cases} x_u \\ y_u \\ x_l \\ y_l \end{cases}, \quad \frac{x}{c} = 0.5\{1 - \cos[(i-0.5)\delta\theta]\}, \quad i=1, n/2 \quad (1.6.17)$$

where n is the total number of nodes and the upper and lower surface coordinates are computed from Eqs. (1.6.1) through (1.6.4). A nodal distribution using cosine clustering with 12 nodes is shown in Fig. 1.6.4. Notice that both the first and last nodes are placed at the trailing edge. Between 50 and 200 nodes should be used for computation.

We can now synthesize an airfoil using $n-1$ vortex panels placed between these n nodes on the airfoil surface. The panels start at the trailing edge, are spaced forward along the lower surface, are wrapped up around the leading edge, and then run back along the upper surface to the trailing edge. The last panel ends at the trailing edge where the first panel began. The strength of each vortex panel is assumed to be linear along the panel and is required to be continuous from one panel to the next, i.e., the strength at the end of one panel must equal the strength at the beginning of the next panel. The strength is not required to be continuous across the trailing edge, i.e., $\gamma_1 \neq \gamma_n$. Each panel is assigned a local panel coordinate system (ξ, η) , as shown in Fig. 1.6.5. The velocity induced by each of these panels is expressed in panel coordinates using Eq. (1.5.14), and the induced velocity components are then transformed to airfoil coordinates.

To solve for the n unknown nodal vortex strengths, control points are placed at the center of each of the $n-1$ panels. The coordinates of these control points are given by

$$\begin{cases} x_C(i) \\ y_C(i) \end{cases} = \begin{cases} \frac{x_N(i) + x_N(i+1)}{2} \\ \frac{y_N(i) + y_N(i+1)}{2} \end{cases}, \quad i=1, n-1 \quad (1.6.18)$$

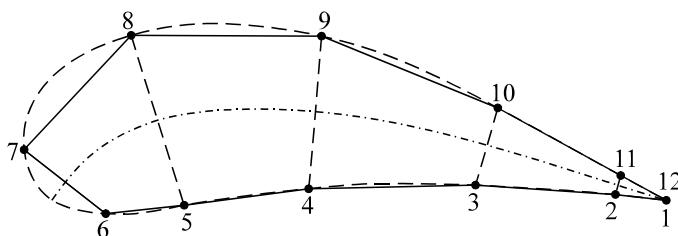


Figure 1.6.4. Vortex panel distribution with cosine clustering and an even number of nodes.

34 Chapter 1 Overview of Aerodynamics

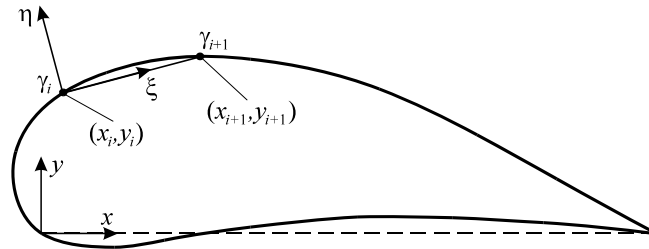


Figure 1.6.5. A vortex panel on the surface of an arbitrary airfoil section.

The normal velocity at each control point, induced by all $n-1$ panels and the uniform flow, must be zero. This gives $n-1$ equations for the n unknown nodal vortex strengths.

For the remaining equation, we know that the flow must leave the airfoil from the trailing edge. This means that the velocity just above the trailing edge must equal the velocity just below the trailing edge. If the angle between the upper and lower surfaces at the trailing edge is nonzero, the trailing edge is a stagnation point. If the angle between the upper and lower surfaces at the trailing edge is zero, the velocity at the trailing edge can be finite but the velocity must be continuous across the trailing edge. Since there is discontinuity in tangential velocity across a vortex sheet, we know that at the trailing edge, the discontinuity across the upper surface is equal and opposite to the discontinuity across the lower surface. Thus, the net discontinuity across both surfaces will be zero. Because the discontinuity in tangential velocity across any vortex sheet is equal to the local strength of the sheet, at the trailing edge, the strength of the upper surface must be exactly equal and opposite to the strength of the lower surface. That is,

$$\gamma_1 + \gamma_n = 0$$

This is called the *Kutta condition* and it provides the remaining equation necessary to solve for the n unknown nodal strengths.

The 2×2 panel coefficient matrix in airfoil coordinates, $[\mathbf{P}]_{i(x,y)}$, for the velocity induced at the arbitrary point (x,y) by panel i , extending from the node at (x_i, y_i) to the node at (x_{i+1}, y_{i+1}) , is computed from the algorithm

$$l_i = \sqrt{(x_{i+1} - x_i)^2 + (y_{i+1} - y_i)^2} \quad (1.6.19)$$

$$\begin{Bmatrix} \xi \\ \eta \end{Bmatrix} = \frac{1}{l_i} \begin{bmatrix} (x_{i+1} - x_i) & (y_{i+1} - y_i) \\ -(y_{i+1} - y_i) & (x_{i+1} - x_i) \end{bmatrix} \begin{Bmatrix} (x - x_i) \\ (y - y_i) \end{Bmatrix} \quad (1.6.20)$$

$$\Phi = \text{atan2}(\eta l_i, \eta^2 + \xi^2 - \xi l_i) \quad (1.6.21)$$

$$\Psi = \frac{1}{2} \ln \left[\frac{\xi^2 + \eta^2}{(\xi - l_i)^2 + \eta^2} \right] \quad (1.6.22)$$

and

$$[\mathbf{P}]_{i(x,y)} = \frac{1}{2\pi l_i^2} \begin{bmatrix} (x_{i+1} - x_i) & -(y_{i+1} - y_i) \\ (y_{i+1} - y_i) & (x_{i+1} - x_i) \end{bmatrix} \begin{bmatrix} [(l_i - \xi)\Phi + \eta\Psi] & (\xi\Phi - \eta\Psi) \\ [\eta\Phi - (l_i - \xi)\Psi - l_i] & (-\eta\Phi - \xi\Psi + l_i) \end{bmatrix} \quad (1.6.23)$$

The $n \times n$ airfoil coefficient matrix, $[\mathbf{A}]$, is generated from the 2×2 panel coefficient matrix in airfoil coordinates, $[\mathbf{P}]_{ji}$, for the velocity induced at control point i by panel j , extending from node j to node $j + 1$, using the algorithm

$$A_{ij} = 0.0, \quad i = 1, n; \quad j = 1, n \quad (1.6.24)$$

$$\left. \begin{aligned} A_{ij} &= A_{ij} + \frac{x_{i+1} - x_i}{l_i} P_{21ji} - \frac{y_{i+1} - y_i}{l_i} P_{11ji} \\ A_{ij+1} &= A_{ij+1} + \frac{x_{i+1} - x_i}{l_i} P_{22ji} - \frac{y_{i+1} - y_i}{l_i} P_{12ji} \end{aligned} \right\}, \quad i = 1, n-1; \quad j = 1, n-1 \quad (1.6.25)$$

$$A_{n1} = 1.0 \quad (1.6.26)$$

$$A_{nn} = 1.0 \quad (1.6.27)$$

The n nodal vortex strengths, γ_1 through γ_n , are then obtained by numerically solving the $n \times n$ linear system

$$[\mathbf{A}] \begin{Bmatrix} \gamma_1 \\ \gamma_2 \\ \vdots \\ \gamma_{n-1} \\ \gamma_n \end{Bmatrix} = V_\infty \begin{Bmatrix} [(y_2 - y_1) \cos \alpha - (x_2 - x_1) \sin \alpha] / l_1 \\ [(y_3 - y_2) \cos \alpha - (x_3 - x_2) \sin \alpha] / l_2 \\ \vdots \\ [(y_n - y_{n-1}) \cos \alpha - (x_n - x_{n-1}) \sin \alpha] / l_{n-1} \\ 0.0 \end{Bmatrix} \quad (1.6.28)$$

Once the nodal strengths are known, the velocity and pressure at any point in space can be computed by adding the velocity induced by all $n - 1$ vortex panels to the free-stream velocity,

$$\begin{Bmatrix} V_x \\ V_y \end{Bmatrix} = V_\infty \begin{Bmatrix} \cos \alpha \\ \sin \alpha \end{Bmatrix} + \sum_{i=1}^{n-1} [\mathbf{P}]_{i(x,y)} \begin{Bmatrix} \gamma_i \\ \gamma_{i+1} \end{Bmatrix} \quad (1.6.29)$$

$$V^2 = V_x^2 + V_y^2 \quad (1.6.30)$$

$$C_p \equiv \frac{p - p_\infty}{\frac{1}{2} \rho V_\infty^2} = 1 - \frac{V^2}{V_\infty^2} \quad (1.6.31)$$

36 Chapter 1 Overview of Aerodynamics

The lift and moment coefficients for the entire airfoil are the sum of those induced by all of the $n - 1$ vortex panels,

$$\tilde{C}_L = \sum_{i=1}^{n-1} \frac{l_i}{c} \frac{\gamma_i + \gamma_{i+1}}{V_\infty} \quad (1.6.32)$$

$$\tilde{C}_{m_{lc}} = -\frac{1}{3} \sum_{i=1}^{n-1} \frac{l_i}{c} \left[\frac{2x_i\gamma_i + x_i\gamma_{i+1} + x_{i+1}\gamma_i + 2x_{i+1}\gamma_{i+1}}{cV_\infty} \cos(\alpha) + \frac{2y_i\gamma_i + y_i\gamma_{i+1} + y_{i+1}\gamma_i + 2y_{i+1}\gamma_{i+1}}{cV_\infty} \sin(\alpha) \right] \quad (1.6.33)$$

Comparison with Experimental Data

Section lift and moment coefficients predicted by thin airfoil theory and panel codes are in good agreement with experimental data for low Mach numbers and small angles of attack. In Fig. 1.6.6, the inviscid lift coefficient for a NACA 2412 airfoil, as predicted by thin airfoil theory, is compared with the inviscid lift coefficient predicted by the vortex panel method and with experimental data for total lift coefficient as reported by Abbott and Von Doenhoff (1949). Thin airfoil theory predicts a section lift coefficient

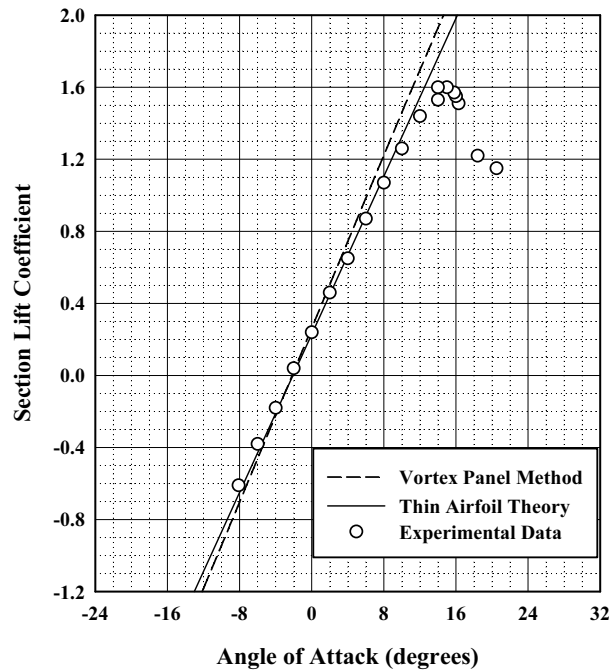


Figure 1.6.6. Section lift coefficient comparison among thin airfoil theory, the vortex panel method, and experimental data based on total lift, for the NACA 2412 airfoil.

that is independent of the thickness distribution and dependent only on angle of attack and camber line shape. At small angles of attack, the thin airfoil approximation agrees closely with experimental data based on total lift, for airfoils as thick as about 12 percent. The agreement seen in Fig. 1.6.6 is quite typical. For airfoils much thicker than about 12 percent, viscous effects become increasingly important, even at fairly low angles of attack, and the inviscid lift coefficient predicted by thin airfoil theory begins to deviate more from experimental observations based on total lift. This can be seen in Fig. 1.6.7.

The reason why thin airfoil theory predicts total lift so well over such a wide range of thickness is that thickness tends to increase the lift slope slightly, while viscous effects tend to decrease the lift slope. Since both thickness effects and viscous effects are neglected in thin airfoil theory, the resulting errors tend to cancel, giving the theory a broader range of applicability than would otherwise be expected. Coincidentally, because of these opposing errors, thin airfoil theory actually predicts a lift slope that agrees more closely with experimental data for total lift than does that predicted by the more elaborate vortex panel method. The vortex panel method accurately predicts the pressure distribution around the airfoil, including the effects of thickness. However, since the vortex panel method provides a potential flow solution, it does not account for viscous effects in any way.

After seeing that thin airfoil theory predicts total section lift better than the vortex panel method, one may wonder why we should ever be interested in the vortex panel

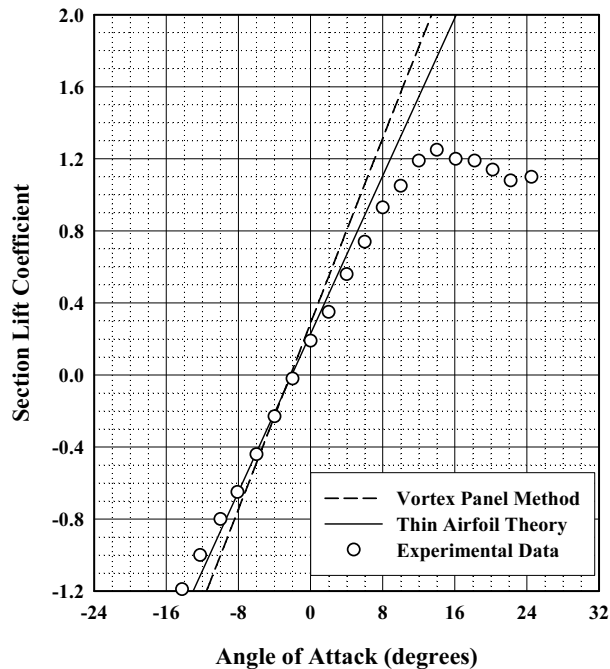


Figure 1.6.7. Section lift coefficient comparison among thin airfoil theory, the vortex panel method, and experimental data based on total lift, for the NACA 2421 airfoil.

38 Chapter 1 Overview of Aerodynamics

method. For the answer, we must remember that both the vortex panel solution and the thin airfoil solution come from potential flow theory. Thus, neither of these two solutions can be expected to predict viscous forces. However, potential flow solutions are often used as boundary conditions for viscous flow analysis. Potential flow is used to predict the pressure distribution around the airfoil. The viscous forces are then computed from boundary layer theory. However, since boundary layer flow is greatly affected by the pressure distribution around the airfoil, our potential flow solution must accurately predict the section pressure distribution. Because thin airfoil theory does not account for airfoil thickness, it cannot be used to predict the surface pressure distribution on an airfoil section with finite thickness. The vortex panel method, on the other hand, accurately predicts the inviscid pressure distribution for airfoils of any thickness.

While the experimental data shown in Figs. 1.6.6 and 1.6.7 are based on total section lift, section lift data have been obtained that are based on pressure forces only. This is usually accomplished by spacing a large number of static pressure taps around the circumference of an airfoil. The net pressure force acting on the airfoil section is derived by numerically integrating the forces obtained from these pressure measurements. The lift coefficient predicted by thin airfoil theory and that predicted by the vortex panel method are compared with experimental data of this type in Fig. 1.6.8. Notice that the vortex panel method agrees very closely with these experimental data, while thin airfoil theory predicts a lift coefficient that is somewhat low.

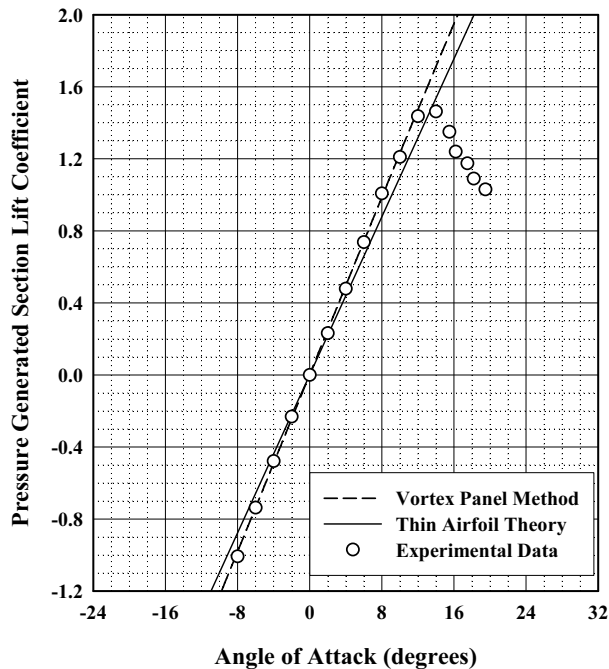


Figure 1.6.8. Section lift coefficient comparison among thin airfoil theory, the vortex panel method, and experimental data based on pressure lift, for the NACA 0015 airfoil.

In summary, thin airfoil theory can be used to obtain a first approximation for the total section lift coefficient, at small angles of attack, produced by airfoils of thickness less than about 12 percent. Thin airfoil theory gives no prediction for the section drag.

To improve on the results obtained from thin airfoil theory, we can combine a boundary layer solution with the velocity and pressure distribution obtained from the vortex panel method. Since this analytical procedure accounts for both thickness and viscous effects, it produces results that agree closely with experimental data for total lift and drag over a broad range of section thickness. Another alternative available with today's high-speed computers is the use of computational fluid dynamics (CFD). However, a CFD solution will increase the required computation time by several orders of magnitude.

In Figs. 1.6.6 through 1.6.8 it should be noticed that at angles of attack near the zero-lift angle of attack, the result predicted by thin airfoil theory agrees very well with that predicted by the vortex panel method and with that observed from all experimental data. Thus, we see that the thickness distribution has little effect on the lift produced by an airfoil at angles of attack near the zero-lift angle of attack. The thickness distribution does, however, have a significant effect on the maximum lift coefficient and on the stall characteristics of the airfoil section. This is seen by comparing Fig. 1.6.6 with Fig. 1.6.7. The two airfoils described in these two figures have exactly the same camber line. They differ only in thickness. Notice that the NACA 2412 section has a maximum lift coefficient of about 1.6, while the NACA 2421 airfoil produces a maximum lift coefficient of only about 1.2. Also notice that the thinner section has a sharper and more abrupt stall than that displayed by the thicker section.

1.7. Trailing-Edge Flaps and Section Flap Effectiveness

An attached trailing-edge flap is formed by hinging some aft portion of the airfoil section so that it can be deflected, either downward or upward, by rotating the flap about the hinge point as shown in Fig. 1.7.1. The deflection of a trailing-edge flap effectively changes the camber of the airfoil section, and in so doing changes the aerodynamic characteristics of the section. A downward deflection of the flap increases the effective camber and is thus usually considered to be a positive deflection.

For small angles of attack and small flap deflections, thin airfoil theory can be applied to an airfoil section with a deflected trailing-edge flap. Let y_d be the y -position

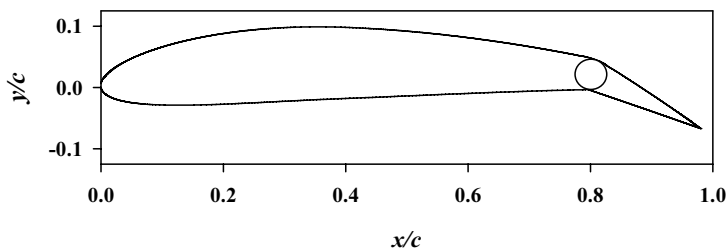


Figure 1.7.1. NACA 4412 airfoil section with a 20 percent trailing-edge flap.

40 Chapter 1 Overview of Aerodynamics

of the section camber line with the trailing-edge flap deflected as shown in Fig. 1.7.2. All of the results obtained from thin airfoil theory must apply to this modified camber line geometry. Thus from Eq. (1.6.12), we can write

$$\tilde{C}_L = 2\pi(\alpha - \alpha_{L0}) = 2\pi \left(\alpha - \frac{1}{\pi} \int_{\theta=0}^{\pi} \frac{dy_d}{dx} (1 - \cos\theta) d\theta \right) \quad (1.7.1)$$

However, within the small-angle approximation, the slope of the deflected camber line geometry can be related to the slope of the undeflected geometry according to

$$\frac{dy_d}{dx} = \begin{cases} \frac{dy_c}{dx}, & x \leq c - c_f \\ \frac{dy_c}{dx} - \delta, & x \geq c - c_f \end{cases} \quad (1.7.2)$$

where y_c is the undeflected camber line ordinate, c_f is the flap chord length, and δ is the deflection of the flap in radians, with positive deflection being downward.

Using Eq. (1.7.2) in Eq. (1.7.1), we have

$$\tilde{C}_L = 2\pi(\alpha - \alpha_{L0}) = 2\pi \left(\alpha - \frac{1}{\pi} \int_{\theta=0}^{\pi} \frac{dy_c}{dx} (1 - \cos\theta) d\theta + \frac{\delta}{\pi} \int_{\theta=\theta_f}^{\pi} (1 - \cos\theta) d\theta \right) \quad (1.7.3)$$

or

$$\alpha_{L0} = \frac{1}{\pi} \int_{\theta=0}^{\pi} \frac{dy_c}{dx} (1 - \cos\theta) d\theta - \frac{\delta}{\pi} \int_{\theta=\theta_f}^{\pi} (1 - \cos\theta) d\theta \quad (1.7.4)$$

where α_{L0} is the zero-lift angle of attack for the airfoil section with the flap deflected and θ_f is given by

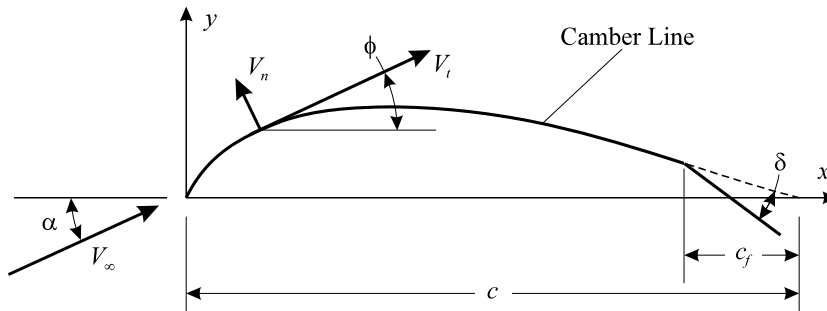


Figure 1.7.2. Camber line geometry for an airfoil section with attached trailing-edge flap and positive flap deflection.

1.7. Trailing-Edge Flaps and Section Flap Effectiveness 41

$$\theta_f = \cos^{-1}\left(2\frac{c_f}{c} - 1\right) \quad (1.7.5)$$

From Eqs. (1.7.3) and (1.7.4), we see that the thin airfoil lift coefficient is affected by flap deflection only through a change in the zero-lift angle of attack. The lift coefficient is still a linear function of the angle of attack and the lift slope is not affected by the flap deflection. The first integral on the right-hand side of Eq. (1.7.4) is simply the zero-lift angle of attack with no flap deflection. The second integral in this equation is readily evaluated to yield what is commonly called the *ideal section flap effectiveness*,

$$\varepsilon_{fi} \equiv -\frac{\partial \alpha_{L0}}{\partial \delta} = \frac{1}{\pi} \int_{\theta=\theta_f}^{\pi} (1 - \cos \theta) d\theta = 1 - \frac{\theta_f - \sin \theta_f}{\pi} \quad (1.7.6)$$

Notice that the ideal section flap effectiveness depends only on the ratio of flap chord to total chord and is independent of both camber line geometry and flap deflection. Using this definition in Eq. (1.7.4), the zero-lift angle of attack for a thin airfoil with an ideal trailing-edge flap is found to vary linearly with flap deflection,

$$\alpha_{L0}(\delta) = \alpha_{L0}(0) - \varepsilon_{fi} \delta \quad (1.7.7)$$

In a similar manner we can predict the quarter-chord moment coefficient for a thin airfoil with a deflected trailing-edge flap. From Eq. (1.6.14), we have

$$\tilde{C}_{m_{c/4}} = \frac{1}{2} \int_{\theta=0}^{\pi} \frac{dy_d}{dx} [\cos(2\theta) - \cos \theta] d\theta \quad (1.7.8)$$

Using Eq. (1.7.2) in Eq. (1.7.8) gives

$$\tilde{C}_{m_{c/4}} = \frac{1}{2} \int_{\theta=0}^{\pi} \frac{dy_c}{dx} [\cos(2\theta) - \cos \theta] d\theta - \frac{\delta}{2} \int_{\theta=\theta_f}^{\pi} [\cos(2\theta) - \cos \theta] d\theta \quad (1.7.9)$$

From Eq. (1.7.9) we see that the section quarter-chord moment coefficient for a thin airfoil is also a linear function of flap deflection. The first integral on the right-hand side of Eq. (1.7.9) is the quarter-chord moment coefficient for the airfoil section with no flap deflection, and the second integral can be evaluated to yield the section quarter-chord moment slope with respect to flap deflection. Thus, the quarter-chord moment coefficient for a thin airfoil section with an ideal trailing-edge flap can be written as

$$\tilde{C}_{m_{c/4}}(\delta) = \tilde{C}_{m_{c/4}}(0) + \tilde{C}_{m,\delta} \delta \quad (1.7.10)$$

where the change in the section quarter-chord moment coefficient with respect to flap deflection is given by

42 Chapter 1 Overview of Aerodynamics

$$\tilde{C}_{m,\delta} \equiv \frac{\partial \tilde{C}_{m,c/4}}{\partial \delta} = -\frac{1}{2} \int_{\theta=\theta_f}^{\pi} [\cos(2\theta) - \cos\theta] d\theta = \frac{\sin(2\theta_f) - 2\sin\theta_f}{4} \quad (1.7.11)$$

Notice that the change in moment coefficient with respect to flap deflection depends only on the ratio of flap chord to total chord. Thus, as was the case with the ideal section flap effectiveness, the ideal section quarter-chord moment slope with respect to flap deflection is independent of both camber line geometry and flap deflection.

In summary, at angles of attack below stall, the lift coefficient for an airfoil section with a deflected trailing-edge flap is found to be very nearly a linear function of both the airfoil angle of attack, α , and the flap deflection, δ . This linear relation can be written

$$\tilde{C}_L(\alpha, \delta) = \tilde{C}_{L,\alpha}[\alpha - \alpha_{L0}(0) + \varepsilon_f \delta] \quad (1.7.12)$$

where $\tilde{C}_{L,\alpha}$ is the section lift slope, $\alpha_{L0}(0)$ is the zero-lift angle of attack with no flap deflection, and ε_f is called the *section flap effectiveness*. Previously we found that thin airfoil theory predicts a section lift slope of 2π . However, solutions obtained using the vortex panel method and experimental measurements have shown that the actual section lift slope can vary somewhat from this value. The zero-lift angle of attack with no flap deflection, as predicted by thin airfoil theory, was previously shown to be in excellent agreement with both the vortex panel method and experimental data. As we shall see, the section flap effectiveness predicted by thin airfoil theory agrees with results predicted using the vortex panel method, but deviates somewhat from experimental observation.

The actual section flap effectiveness is always less than the ideal section flap effectiveness given by Eq. (1.7.6). The hinge mechanism in a real trailing-edge flap always reduces the flap effectiveness. This reduction results from local boundary layer separation and from flow leakage through the hinge from the high-pressure side to the low-pressure side. In addition, at flap deflections greater than about ± 10 degrees, the error associated with the small-angle approximation used to obtain Eq. (1.7.6) begins to become significant. This results in an additional decrease in the section flap effectiveness for larger flap deflections. A comparison among the section flap effectiveness predicted by thin airfoil theory, typical results predicted by the vortex panel method, and results observed experimentally is shown in Fig. 1.7.3. The data shown in this figure are from Abbott and Von Doenhoff (1949).

The discrepancy between the theoretical results and the experimental data shown in Fig. 1.7.3 is only about 7 percent with a flap chord fraction of 0.4, but at a flap chord fraction of 0.1 this discrepancy is nearly 25 percent. The deviation between actual section flap effectiveness and the ideal section flap effectiveness continues to increase as the flap chord fraction becomes smaller. The poor agreement at low flap chord fraction is attributed to the thickness of the boundary layer, which is much larger near the trailing edge. The trailing-edge flaps used to generate the data shown in Fig. 1.7.3 all had flap hinges that were sealed to prevent leakage from the high-pressure side to the low-pressure side. For unsealed trailing-edge flaps, an additional decrease in section flap effectiveness of about 20 percent is observed.

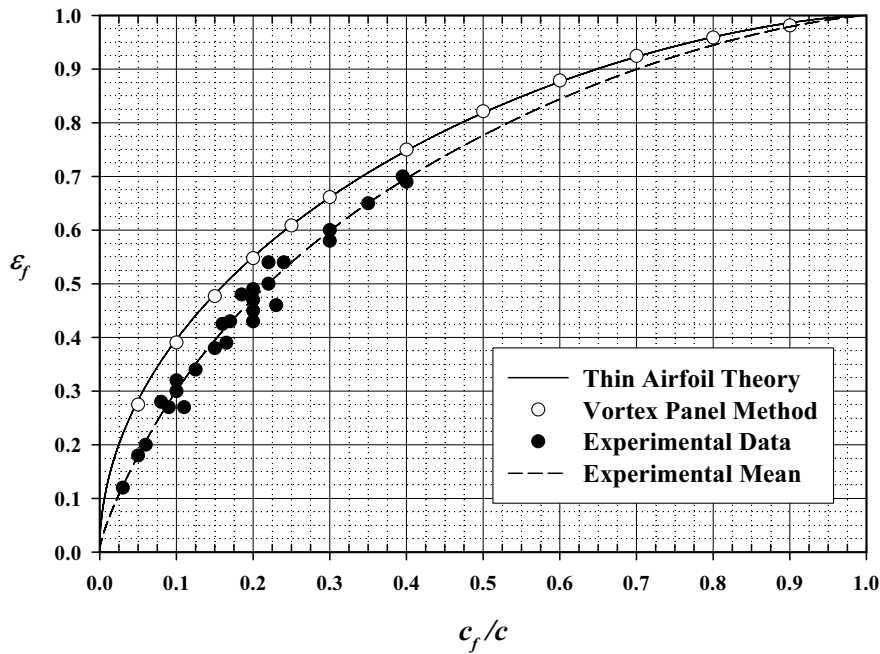


Figure 1.7.3. Section flap effectiveness comparison among thin airfoil theory, the vortex panel method, and experimental data.

The data shown in Fig. 1.7.3 were all taken at flap deflections of less than 10 degrees. For larger deflections, actual flap effectiveness deviates even more from the ideal, as a result of errors associated with the small-angle approximation. The actual section flap effectiveness for a trailing-edge flap can be expressed in terms of the ideal section flap effectiveness, ϵ_{fi} , given by Eq. (1.7.6), according to

$$\epsilon_f = \eta_h \eta_d \epsilon_{fi} \tag{1.7.13}$$

where η_h and η_d are, respectively, the section flap hinge efficiency and the section flap deflection efficiency.

For well-designed sealed flaps, the section hinge efficiency can be approximated from Fig. 1.7.4. This figure is based on the mean line for the experimental data shown in Fig. 1.7.3. If the gap between the main wing and the trailing-edge flap is not sealed, it is recommended that the values found from Fig. 1.7.4 be reduced by 20 percent. Remember that the result given in this figure represents a mean experimental efficiency. The actual hinge efficiency for a specific trailing-edge flap installed in a particular airfoil section may deviate significantly from the value found in this figure. For flap deflections of more than ± 10 degrees, Perkins and Hage (1949) recommend the flap deflection efficiency shown in Fig. 1.7.5. For flap deflections of less than ± 10 degrees, a flap deflection efficiency of 1.0 should be used.

44 Chapter 1 Overview of Aerodynamics

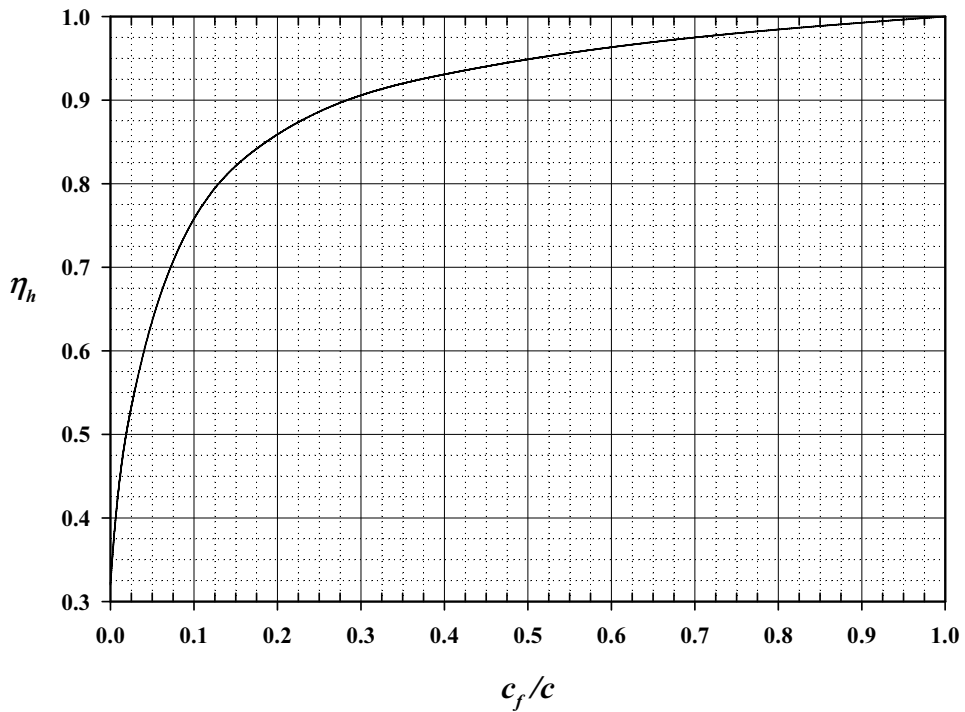


Figure 1.7.4. Section flap hinge efficiency for well-designed and sealed trailing-edge flaps. For unsealed flaps this hinge efficiency should be decreased by about 20 percent.

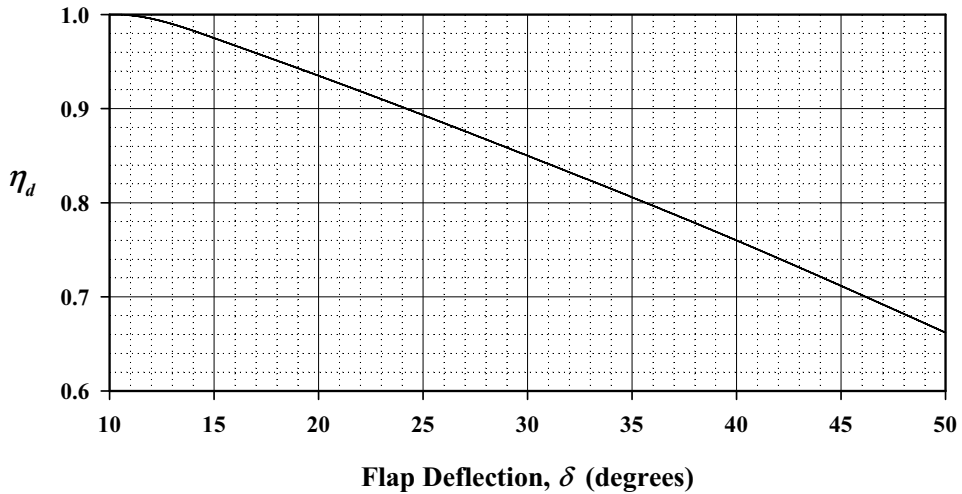


Figure 1.7.5. Section flap deflection efficiency for trailing-edge flaps with flap deflections of more than ± 10 degrees. For flap deflections of less than ± 10 degrees a deflection efficiency of 1.0 should be used.

1.7. Trailing-Edge Flaps and Section Flap Effectiveness 45

At angles of attack below stall, the pitching moment coefficient for an airfoil section with a deflected trailing-edge flap is also found to be very nearly a linear function of both angle of attack, α , and flap deflection, δ . This linear relation can be written in the form

$$\tilde{C}_{m_{c/4}}(\alpha, \delta) = \tilde{C}_{m_{c/4}}(0,0) + \tilde{C}_{m,\alpha} \alpha + \tilde{C}_{m,\delta} \delta \quad (1.7.14)$$

where $\tilde{C}_{m_{c/4}}(0,0)$, $\tilde{C}_{m,\alpha}$, and $\tilde{C}_{m,\delta}$ are, respectively, the section pitching moment coefficient at zero angle of attack and zero flap deflection, the moment slope with angle of attack, and the moment slope with flap deflection.

Thin airfoil theory predicts that the quarter chord is the aerodynamic center of an airfoil section. Thus, thin airfoil theory predicts a zero quarter-chord moment slope with respect to angle of attack. In reality, solutions obtained from the vortex panel method and experimental observations have shown that the quarter chord is not exactly the aerodynamic center of all airfoil sections. Thus, in general, we should allow for a finite quarter-chord moment slope with angle of attack. However, for preliminary design, the quarter-chord moment slope with angle of attack is usually taken to be zero.

The section quarter-chord moment slope with respect to flap deflection is shown in Fig. 1.7.6. In this figure the ideal quarter-chord moment slope, as predicted by thin airfoil theory in Eq. (1.7.11), is compared with typical results predicted from the vortex panel method and with limited experimental data. Airfoil section thickness tends to increase the magnitude of the negative quarter-chord moment slope with respect to flap deflection. The hinge effects, on the other hand, tend to lessen the magnitude of this moment slope. The result from thin airfoil theory is often used for preliminary design.

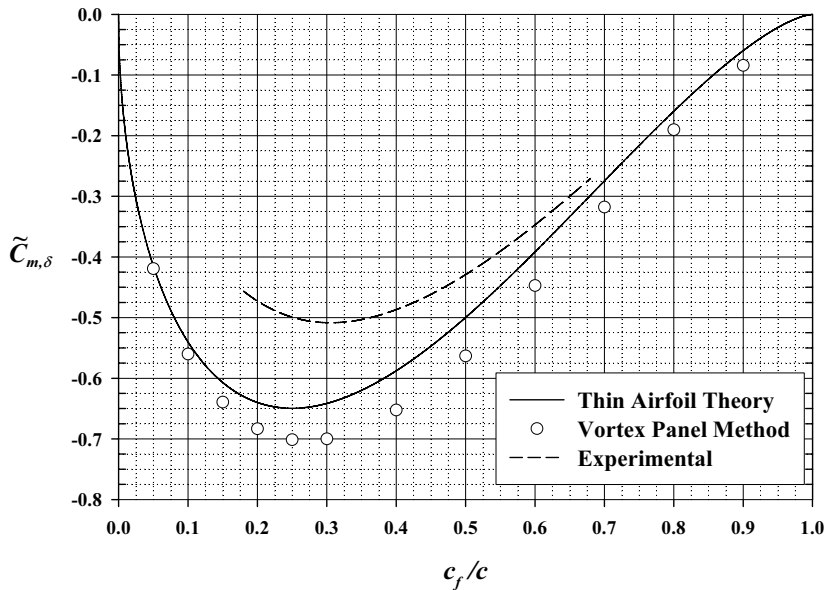


Figure 1.7.6. Quarter-chord moment slope with respect to flap deflection.

46 Chapter 1 Overview of Aerodynamics

EXAMPLE 1.7.1. The airfoil section with 4 percent maximum camber, which is described in Example 1.6.1, has a sealed 20 percent trailing-edge flap. Estimate the section flap effectiveness and the section lift coefficient for a 5-degree flap deflection and a 0-degree angle of attack relative to the undeflected chord line.

Solution. From Eq. (1.7.5), a flap fraction of 0.20 gives

$$\theta_f = \cos^{-1}\left(2\frac{c_f}{c} - 1\right) = \cos^{-1}[2(0.20) - 1] = 2.214297$$

Using this in Eq. (1.7.6) yields an ideal section flap effectiveness of

$$\varepsilon_{fi} = 1 - \frac{\theta_f - \sin \theta_f}{\pi} = 1 - \frac{2.214297 - \sin(2.214297)}{\pi} = 0.55$$

Applying this and results from Figs. 1.7.4 and 1.7.5 to Eq. (1.7.13) yields

$$\varepsilon_f = \eta_h \eta_d \varepsilon_{fi} = (0.86)(1.00)(0.55) = \underline{0.47}$$

With this and the value of α_{L0} from Example 1.6.1, Eq. (1.7.12) results in

$$\tilde{C}_L = \tilde{C}_{L,\alpha}[\alpha - \alpha_{L0}(0) + \varepsilon_f \delta] = 2\pi[0.0 - (-0.08) + 0.47(5\pi/180)] = \underline{0.76}$$

1.8. Incompressible Flow over Finite Wings

In Sec. 1.6 we reviewed the aerodynamic properties of airfoils, which are the same as the aerodynamic properties of wings with infinite span. A wing of constant cross-section and infinite span would have no variation in aerodynamic forces in the spanwise direction. The aerodynamic forces per unit span acting on such a wing, at any point along the span, would be the same as those for an airfoil of the same cross-section. An airfoil or wing of infinite span is synthesized using vortex sheets that are made up of straight vortex filaments that extend to $\pm\infty$ in the direction of span. The vortex strength can vary over the sheet as we move in a chordwise direction from one vortex filament to another. However, there is no variation in vortex strength as we move along a vortex filament in the direction of span.

Any real wing, of course, must have finite span. At the tips of a finite wing, the air on the lower surface of the wing comes in direct contact with the air on the upper surface of the wing. Thus, at the tips of a finite wing, the pressure difference between the upper and lower surfaces must always go to zero. As a result, the lift on any finite wing must go to zero at the wingtips, as shown schematically in Fig. 1.8.1.

The pressure difference between the upper and lower surfaces of a finite wing is reduced near the wingtips, because some of the air from the high-pressure region below the wing spills outward, around the wingtip, and back inward toward the low-pressure region above the wing. Thus, while the flow around an infinite wing is entirely in the plane of the airfoil section, the flow around a finite wing is three-dimensional.

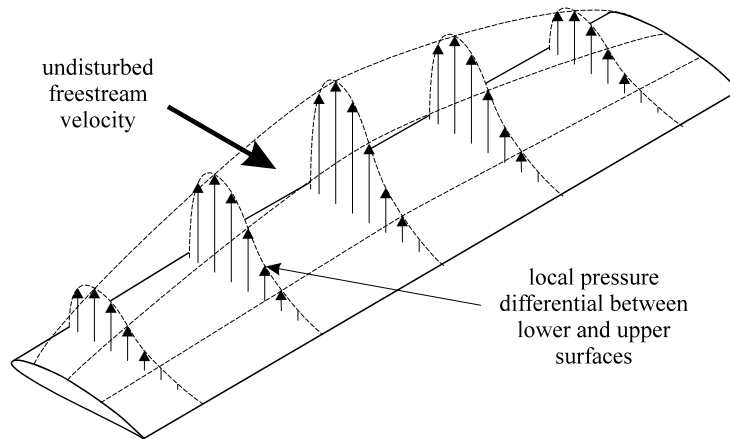


Figure 1.8.1. Lift distribution on a finite wing.

As air flows over a finite wing, the air below the wing moves outward toward the wingtip and the air above the wing moves inward toward the root, as shown in Fig. 1.8.2. Where the flows from the upper and lower surfaces combine at the trailing edge, the difference in spanwise velocity generates a trailing vortex sheet. Because this vortex sheet is free and not bound to the wing's surface, the flow field induced by the sheet tends to change the shape of the sheet as it moves downstream from the wing. As can be seen in Fig. 1.8.3, this vortex sheet rolls up around an axis trailing slightly inboard from each wingtip. At some distance behind the wing, the sheet becomes completely rolled up to form two large vortices, one trailing aft of each wingtip. For this reason,

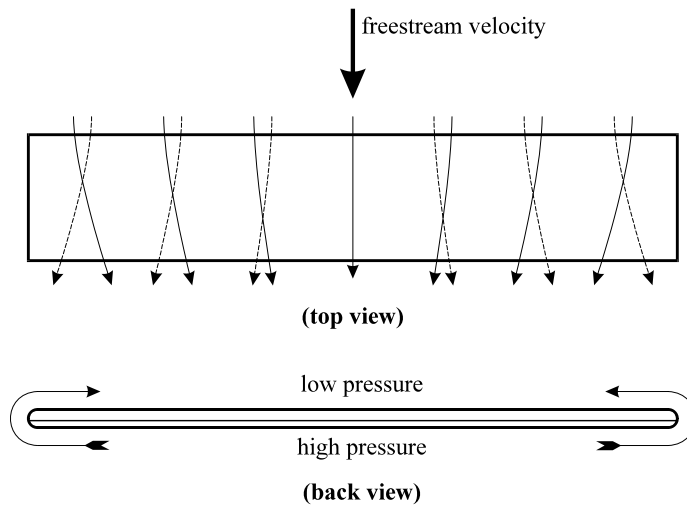


Figure 1.8.2. Airflow around a finite wing.

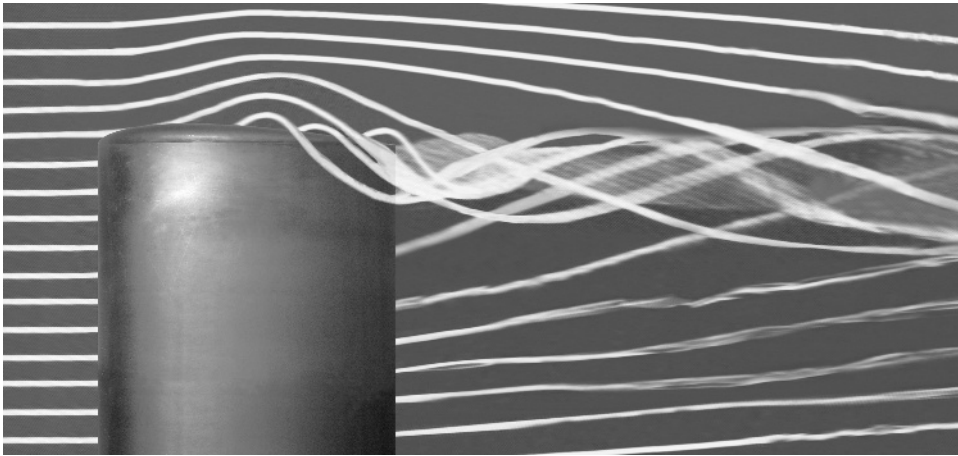


Figure 1.8.3. Vorticity trailing aft of a finite wing.

these vortices are referred to as *wingtip vortices*, even though they are generated over the full span of the wing. The downward velocity component that is induced between the wingtip vortices is called *downwash*. Potential flow theory predicts that the wingtip vortices must trail behind the wing for an infinite distance with no reduction in strength. In reality, viscous effects will eventually dissipate the energy in these vortices, but this is a slow process. These vortices will still have significant energy several miles behind a large aircraft and are of sufficient strength to cause control loss or structural damage to other aircraft following too closely.

From the discussion above, we see that a wing of finite span cannot be synthesized with a vortex sheet made up of vortex filaments that are always perpendicular to the airfoil sections of the wing. We can, however, still synthesize a finite wing with a vortex sheet, but the sheet must be made up of horseshoe-shaped vortex filaments. These filaments run out along the wing in the direction of span, curving back and eventually leaving the wing from the trailing edge at some point inboard of the wingtip. This is seen schematically in the plan view of the elliptic wing shown in Fig. 1.8.4. Because the strength of a vortex filament cannot vary along its length, the decrease in the circulation about the wing as we move out from the root toward the tip must result entirely from the vorticity that leaves the wing in the trailing vortex sheet.

The classical lifting-line theory developed by Prandtl (1918) was the first analytical method to satisfactorily predict the performance of a finite wing. While a general 3-D vortex lifting law was not available at the time of Prandtl's development, the 2-D vortex lifting law of Kutta (1902) and Joukowski (1906) was well known. Prandtl's lifting-line theory is based on the hypothesis that each spanwise section of a finite wing has a section lift that is equivalent to that acting on a similar section of an infinite wing having the same section circulation. However, to reconcile this theory with reality, the undisturbed freestream velocity in the Kutta-Joukowski law was intuitively replaced with the vector sum of the freestream velocity and the velocity induced by the trailing vortex sheet.

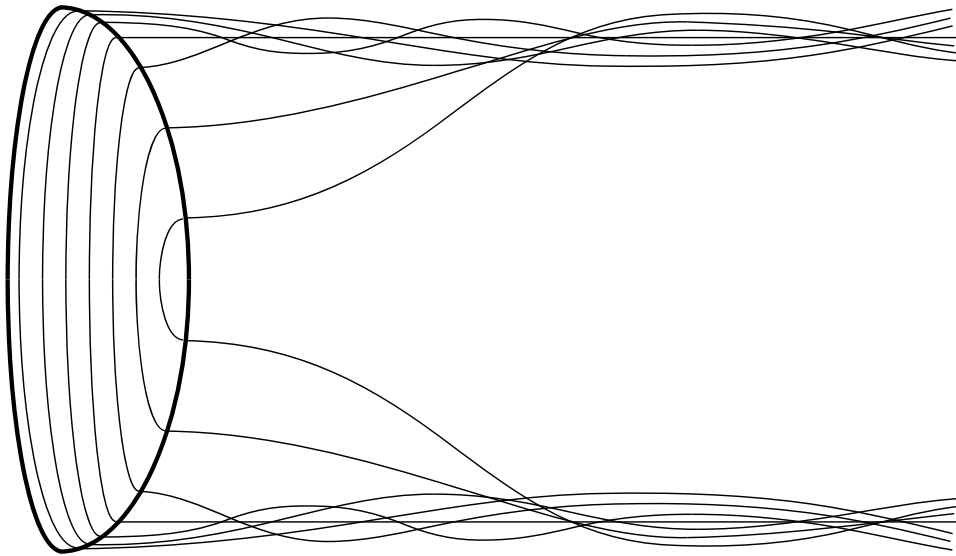


Figure 1.8.4. Schematic of the vorticity distribution on a finite wing with elliptic planform shape.

Today we know that Prandtl's hypothesis was correct. This can be shown as a direct consequence of the **vortex lifting law**, which is a three-dimensional counterpart to the two-dimensional Kutta-Joukowski law. This vortex lifting law states that for any potential flow containing vortex filaments, the force per unit length exerted on the surroundings at any point along a vortex filament is given by

$$\mathbf{dF} = \rho \Gamma \mathbf{V} \times \mathbf{dl} \quad (1.8.1)$$

where \mathbf{dF} is the differential aerodynamic force vector and ρ , Γ , \mathbf{V} , and \mathbf{dl} are, respectively, the fluid density, vortex strength, local fluid velocity, and the directed differential vortex length vector (see Saffman 1992).

The force computed from Eq. (1.8.1) is called the *vortex force* or *Kutta lift*. The vortex lifting law is a very useful tool in the study of aerodynamics and flight mechanics. It provides the basis for much of finite wing theory. There are two important consequences of Eq. (1.8.1). First, **for a bound vortex filament, the vortex force is always perpendicular to both the local velocity vector and the vortex filament**. Second, since a free vortex filament can support no force, **free vortex filaments must be aligned everywhere with the streamlines of the flow**.

Prandtl's Classical Lifting-Line Theory

Prandtl's lifting-line theory gives good agreement with experimental data for straight wings of aspect ratio greater than about 4. Development of this theory is presented in any undergraduate engineering textbook on aerodynamics and will not be repeated here. Only summary results are presented in this section.

50 Chapter 1 Overview of Aerodynamics

The model used by Prandtl to approximate the bound vorticity and trailing vortex sheet is shown in Fig. 1.8.5. All bound vortex filaments are assumed to follow the wing quarter-chord line, and all trailing vortex filaments are assumed to be straight and parallel with the freestream. Rollup of the trailing vortex sheet is ignored.

The foundation of lifting-line theory is the requirement that for each cross-section of the wing, the lift predicted from the vortex lifting law must be equal to that predicted from airfoil section theory, i.e.,

$$\tilde{C}_L(z) = \tilde{C}_{L,\alpha}[\alpha_{\text{eff}}(z) - \alpha_{L0}(z)]$$

where α_{eff} is the local section angle of attack, including the effects of velocity induced by the trailing vortex sheet. Because of the downwash induced on the wing by the trailing vortex sheet, the local relative wind is inclined at an angle, α_i , to the freestream, as shown in Fig. 1.8.6. This angle is called the *induced angle of attack*. Since the lift is always perpendicular to the local relative wind, the downwash tilts the lift vector back, creating a component of lift parallel to the freestream. This is called *induced drag*.

When the downwash is accounted for, Prandtl's hypothesis requires that

$$\frac{2\Gamma(z)}{V_\infty c(z)} + \frac{\tilde{C}_{L,\alpha}}{4\pi V_\infty} \int_{\zeta=-b/2}^{b/2} \frac{1}{z-\zeta} \left(\frac{d\Gamma}{dz} \right)_{z=\zeta} d\zeta = \tilde{C}_{L,\alpha}[\alpha(z) - \alpha_{L0}(z)] \quad (1.8.2)$$

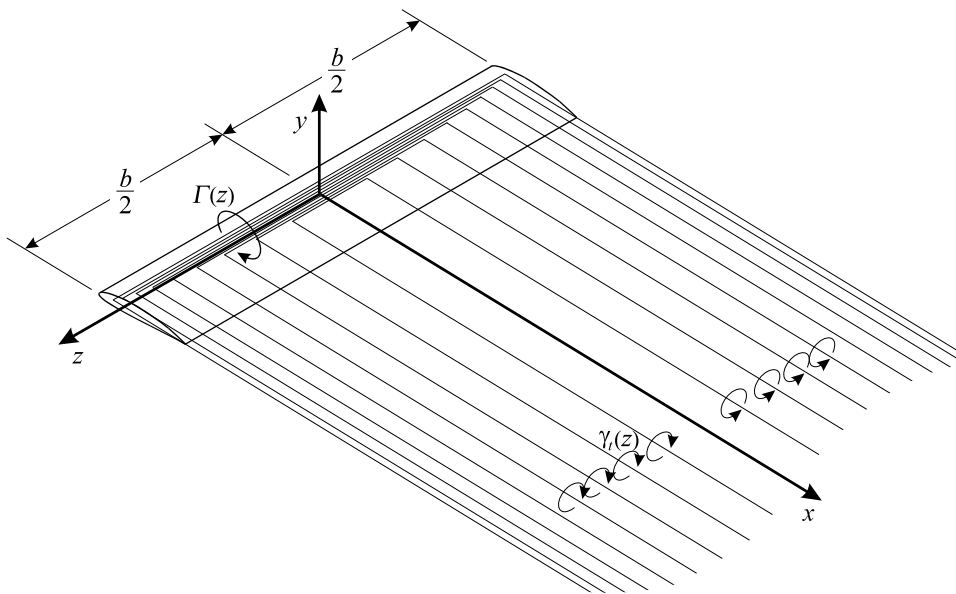


Figure 1.8.5. Prandtl's model for the bound vorticity and the trailing vortex sheet generated by a wing of finite span.

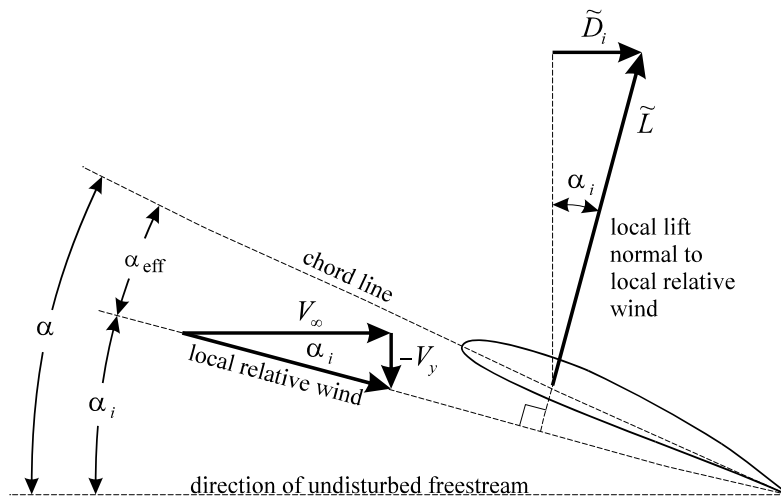


Figure 1.8.6. Induced angle of attack.

Equation (1.8.2) is the fundamental equation of Prandtl's lifting-line theory. It is a non-linear integrodifferential equation that involves only one unknown, the local section circulation as a function of the spanwise position, $\Gamma(z)$. All other parameters are known for a given wing design at a given geometric angle of attack and a given freestream velocity. Remember that the chord length, c , the geometric angle of attack, α , and the zero-lift angle of attack, α_{L0} , are all allowed to vary in the spanwise direction. The section lift slope could also vary with z but is usually assumed to be constant.

There is certain terminology associated with spanwise variation in wing geometry with which the reader should be familiar. If a wing has spanwise variation in geometric angle of attack as shown in Fig. 1.8.7, the wing is said to have *geometric twist*. The tip is commonly at a lower angle of attack than the root, in which case the geometric twist is referred to as *washout*. A spanwise variation in zero-lift angle of attack, like that shown in Fig. 1.8.8, is called *aerodynamic twist*. Deflecting a trailing-edge flap that extends over only part of the span is another form of aerodynamic twist (see Fig. 1.8.9).

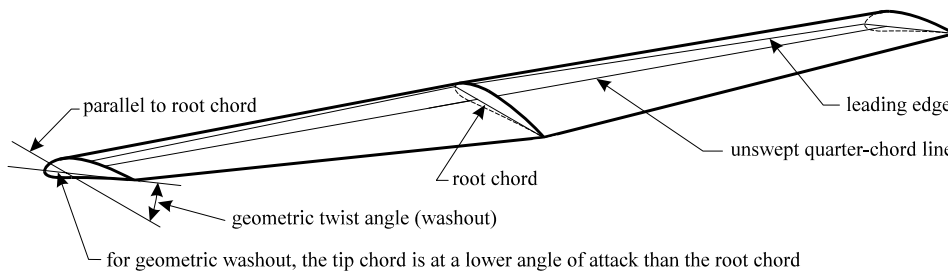


Figure 1.8.7. Geometric twist in an unswept rectangular wing.

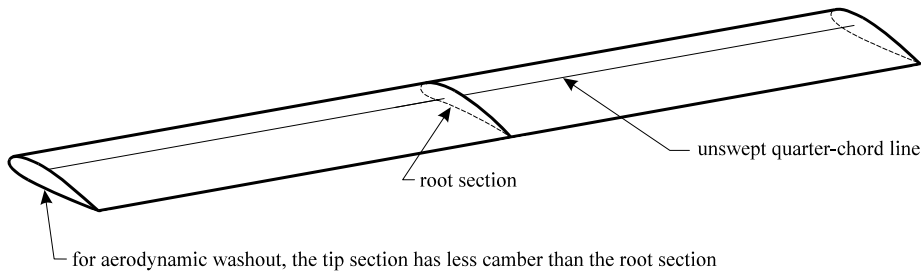


Figure 1.8.8. Aerodynamic twist in an unswept rectangular wing.

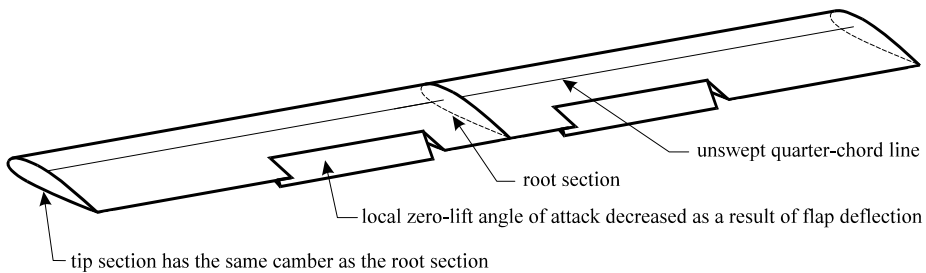


Figure 1.8.9. Aerodynamic twist resulting from deflection of a trailing-edge flap spanning only a portion of the wing.

For a single finite wing with no sweep or dihedral, an analytical solution to Prandtl’s lifting-line equation can be obtained in terms of a Fourier sine series. For a given wing design, at a given angle of attack, the planform shape, $c(z)$, the geometric twist, $\alpha(z)$, and the aerodynamic twist, $\alpha_{L0}(z)$, are all known as functions of spanwise position. The circulation distribution is written as a Fourier series, the series is truncated to a finite number of terms (N), and the Fourier coefficients are determined by forcing the lifting-line equation to be satisfied at N specific sections along the span of the wing. From this solution the circulation distribution is given by

$$\Gamma(\theta) = 2bV_\infty \sum_{n=1}^N A_n \sin(n\theta); \quad \theta = \cos^{-1}(-2z/b) \quad (1.8.3)$$

where the Fourier coefficients, A_n , are obtained from

$$\sum_{n=1}^N A_n \left[\frac{4b}{\tilde{C}_{L,\alpha} c(\theta)} + \frac{n}{\sin(\theta)} \right] \sin(n\theta) = \alpha(\theta) - \alpha_{L0}(\theta) \quad (1.8.4)$$

Once the circulation distribution has been determined, the section lift distribution can be obtained from the vortex lifting law. The resulting lift and induced drag coefficients for the finite wing are

$$C_L = \pi R_A A_1, \quad R_A \equiv \frac{b^2}{S} \quad (1.8.5)$$

$$C_{D_i} = \pi R_A \sum_{n=1}^N n A_n^2 = \frac{C_L^2}{\pi R_A e_s}, \quad e_s \equiv \frac{1}{1+\sigma}, \quad \sigma \equiv \sum_{n=2}^N n \left(\frac{A_n}{A_1} \right)^2 \quad (1.8.6)$$

The wingspan squared divided by the planform area, R_A , is called the *aspect ratio* and the parameter e_s is called the *span efficiency factor*.

Lifting-line theory predicts that an elliptic wing with no geometric or aerodynamic twist produces minimum possible induced drag for a given lift coefficient and aspect ratio. This planform has a chord that varies with the spanwise coordinate according to

$$c(z) = \frac{4b}{\pi R_A} \sqrt{1 - (2z/b)^2} \quad \text{or} \quad c(\theta) = \frac{4b}{\pi R_A} \sin(\theta)$$

As shown in Fig. 1.8.10, an unswept elliptic wing has a straight quarter-chord line. This gives the leading edge less curvature and the trailing edge more curvature than a conventional ellipse, which has a straight half-chord line. Several aircraft have been designed and built with elliptic wings. One of the best known is the British Spitfire, shown in Fig. 1.8.11.

The lift and induced drag coefficients predicted from Eqs. (1.8.5) and (1.8.6) for an **elliptic wing with no geometric or aerodynamic twist** are

$$C_L = C_{L,\alpha}(\alpha - \alpha_{L0}), \quad C_{L,\alpha} = \frac{\tilde{C}_{L,\alpha}}{1 + \tilde{C}_{L,\alpha}/(\pi R_A)} \quad (1.8.7)$$

$$C_{D_i} = \frac{C_L^2}{\pi R_A} \quad (1.8.8)$$

where $C_{L,\alpha}$ is the lift slope for the finite wing. Equation (1.8.7) shows that the lift slope for an untwisted elliptic wing is less than the section lift slope for the airfoil from which the wing was generated. However, as the aspect ratio for the wing becomes large, the

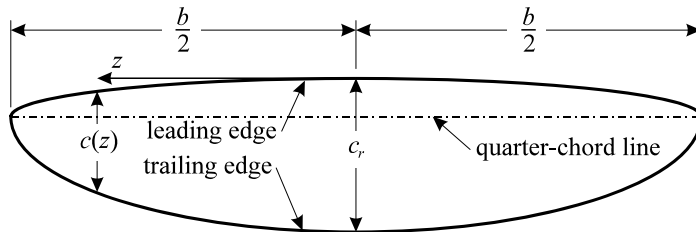


Figure 1.8.10. Planform shape of an unswept elliptic wing with an aspect ratio of 6.

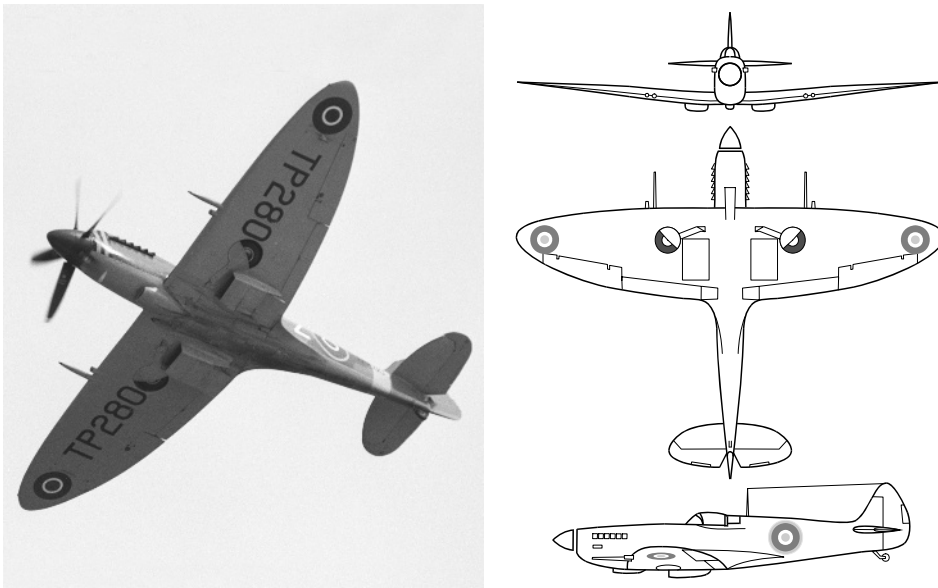


Figure 1.8.11. Elliptic wing used on the famous British Spitfire. (Photograph by Barry Santana)

lift slope for the finite wing approaches that of the airfoil section and the induced drag becomes small. At a given angle of attack, the untwisted elliptic wing produces more lift than any other untwisted wing of the same aspect ratio. Planform shape affects both the induced drag and the lift slope of a finite wing. However, the effect of planform shape is small compared to that of aspect ratio.

While untwisted elliptic wings produce minimum possible induced drag, they are more expensive to manufacture than simple rectangular wings. Untwisted rectangular wings are easy to manufacture, but they generate induced drag at a level that is less than optimum. The untwisted tapered wing, shown in Fig. 1.8.12, has commonly been used as a compromise. Tapered wings have a chord length that varies linearly from the root to the tip. They are nearly as easy to manufacture as rectangular wings, and they can be designed to produce induced drag close to the optimum value of an elliptic wing.

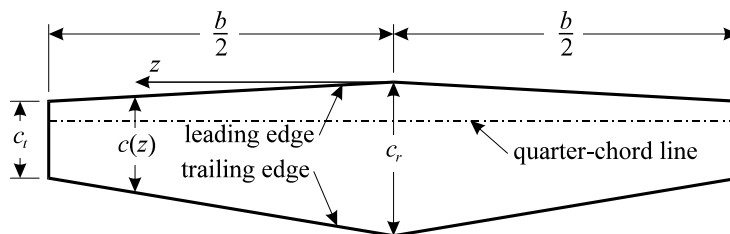


Figure 1.8.12. Planform shape of an unswept tapered wing with a taper ratio of 0.5 and an aspect ratio of 6.

1.8. Incompressible Flow over Finite Wings 55

The chord length for a tapered wing varies with the spanwise coordinate according to the relation

$$c(z) = \frac{2b}{R_A(1+R_T)} [1 - (1-R_T)|2z/b|] \quad \text{or} \quad c(\theta) = \frac{2b}{R_A(1+R_T)} [1 - (1-R_T)|\cos\theta|]$$

where R_T is the taper ratio, related to the root chord, c_r , and the tip chord, c_t , by

$$R_T \equiv c_t/c_r$$

For a wing of any planform having no sweep, dihedral, geometric twist, or aerodynamic twist, the circulation distribution predicted from Prandtl's lifting-line theory can be written in terms of a Fourier series with coefficients, a_n , that are independent of angle of attack. Under these conditions, Eq. (1.8.3) can be rearranged to give

$$\Gamma(\theta) = 2bV_\infty(\alpha - \alpha_{L0}) \sum_{n=1}^N a_n \sin(n\theta); \quad \theta = \cos^{-1}(-2z/b) \quad (1.8.9)$$

where the Fourier coefficients are obtained from

$$\sum_{n=1}^N a_n \left[\frac{4b}{\tilde{C}_{L,\alpha} c(\theta)} + \frac{n}{\sin(\theta)} \right] \sin(n\theta) = 1 \quad (1.8.10)$$

The lift and induced drag coefficients predicted from Eqs. (1.8.5) and (1.8.6) for a **wing with no geometric or aerodynamic twist** can be written as

$$C_L = C_{L,\alpha}(\alpha - \alpha_{L0}), \quad C_{L,\alpha} = \frac{\tilde{C}_{L,\alpha}}{[1 + \tilde{C}_{L,\alpha}/(\pi R_A)](1 + \kappa_L)} \quad (1.8.11)$$

$$C_{D_i} = \frac{C_L^2}{\pi R_A e_s}, \quad e_s = \frac{1}{1 + \kappa_D} \quad (1.8.12)$$

where the lift slope factor, κ_L , and the induced drag factor, κ_D , are given by

$$\kappa_L = \frac{1 - (1 + \pi R_A / \tilde{C}_{L,\alpha}) a_1}{(1 + \pi R_A / \tilde{C}_{L,\alpha}) a_1} \quad (1.8.13)$$

$$\kappa_D = \sum_{n=2}^N n \left(\frac{a_n}{a_1} \right)^2 \quad (1.8.14)$$

For untwisted tapered wings, numerical results obtained for these two factors are shown in Figs. 1.8.13 and 1.8.14. These results were generated using a section lift slope of 2π .

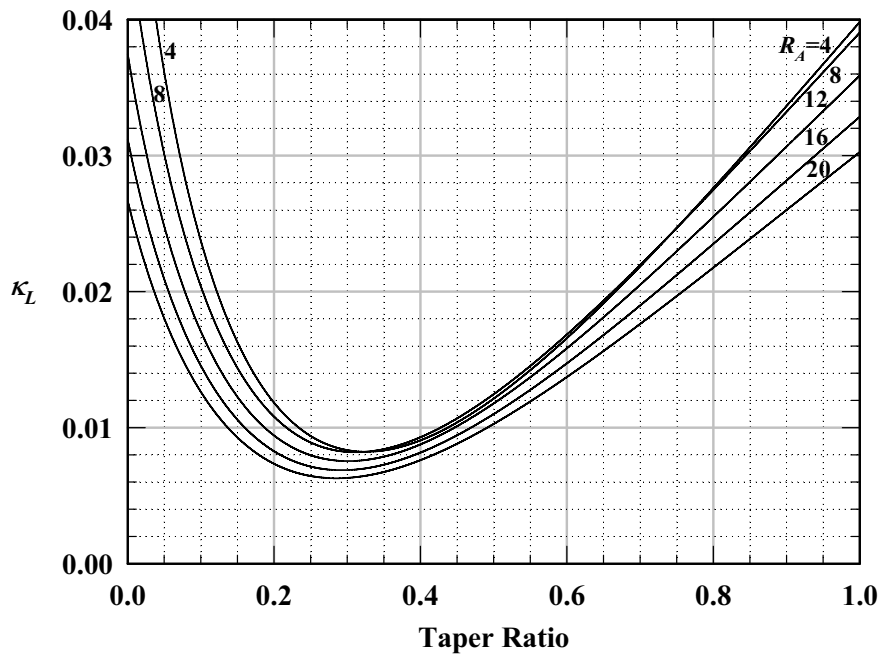


Figure 1.8.13. Lift slope factor for untwisted tapered wings from Prandtl's lifting-line theory.

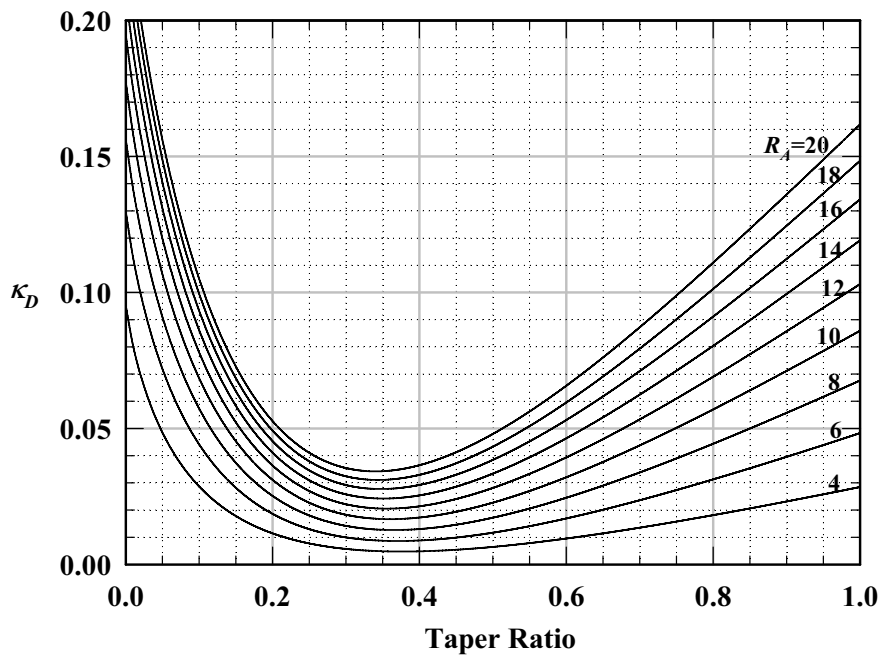


Figure 1.8.14. Induced drag factor for untwisted tapered wings from Prandtl's lifting-line theory.

Glauert (1926) first presented results similar to those shown in Fig. 1.8.14. Such results have sometimes led to the conclusion that a tapered wing with a taper ratio of about 0.4 always produces significantly less induced drag than a rectangular wing of the same aspect ratio developing the same lift. As a result, tapered wings are often used as a means of reducing induced drag. However, this reduction in drag usually comes at a price. Because a tapered wing has a lower Reynolds number at the wingtips than at the root, a tapered wing with no geometric or aerodynamic twist tends to stall first in the region of the wingtips. This wingtip stall commonly leads to poor handling qualities during stall recovery.

The results shown in Fig. 1.8.14 can be misleading if one loses sight of the fact that these results apply only for the special case of wings with no geometric or aerodynamic twist. This is only one of many possible twist distributions that could be used for a wing of any given planform. Furthermore, it is not the twist distribution that produces minimum induced drag with finite lift, except for the case of an elliptic wing. When the effects of twist are included, it can be shown that the conclusions sometimes reached from consideration of only those results shown in Fig. 1.8.14 are erroneous.

Effects of Wing Twist

For a wing with geometric and/or aerodynamic twist, the solution expressed in the form of Eqs. (1.8.3) through (1.8.6) is cumbersome for the evaluation of traditional wing properties, because the Fourier coefficients depend on angle of attack and must be reevaluated for each operating point studied. Furthermore, the definition of σ that is given in Eq. (1.8.6) is not practical for use at an arbitrary angle of attack, because the value becomes singular for a twisted wing when the lift coefficient approaches zero. A more useful form of the solution can be obtained by using the change of variables

$$\alpha(\theta) - \alpha_{L0}(\theta) \equiv (\alpha - \alpha_{L0})_{\text{root}} - \Omega \omega(\theta) \quad (1.8.15)$$

where Ω is defined to be the maximum total washout, geometric plus aerodynamic,

$$\Omega \equiv (\alpha - \alpha_{L0})_{\text{root}} - (\alpha - \alpha_{L0})_{\text{max}} \quad (1.8.16)$$

and $\omega(\theta)$ is the local washout distribution function, which is normalized with respect to maximum total washout

$$\omega(\theta) \equiv \frac{\alpha(\theta) - \alpha_{L0}(\theta) - (\alpha - \alpha_{L0})_{\text{root}}}{(\alpha - \alpha_{L0})_{\text{max}} - (\alpha - \alpha_{L0})_{\text{root}}} \quad (1.8.17)$$

The normalized washout distribution function, $\omega(\theta)$, is independent of angle of attack and always varies from 0.0 at the root to 1.0 at the point of maximum washout, which is commonly at the wingtips.

Using Eq. (1.8.15) in Eq. (1.8.4) gives

$$\sum_{n=1}^N A_n \left[\frac{4b}{\tilde{C}_{L,\alpha} c(\theta)} + \frac{n}{\sin(\theta)} \right] \sin(n\theta) = (\alpha - \alpha_{L0})_{\text{root}} - \Omega \omega(\theta) \quad (1.8.18)$$

58 Chapter 1 Overview of Aerodynamics

The Fourier coefficients in Eq. (1.8.18) for a **wing with geometric and/or aerodynamic twist** can be written conveniently as

$$A_n \equiv a_n(\alpha - \alpha_{L0})_{\text{root}} - b_n \Omega \quad (1.8.19)$$

where

$$\sum_{n=1}^N a_n \left[\frac{4b}{\tilde{C}_{L,\alpha} c(\theta)} + \frac{n}{\sin(\theta)} \right] \sin(n\theta) = 1 \quad (1.8.20)$$

$$\sum_{n=1}^N b_n \left[\frac{4b}{\tilde{C}_{L,\alpha} c(\theta)} + \frac{n}{\sin(\theta)} \right] \sin(n\theta) = \omega(\theta) \quad (1.8.21)$$

Comparing Eq. (1.8.20) with Eq. (1.8.10), we see that the Fourier coefficients defined by Eq. (1.8.20) are those corresponding to the solution for a wing of the same planform shape but with no geometric or aerodynamic twist. The solution to Eq. (1.8.21) can be obtained in a similar manner and is also independent of angle of attack.

Using Eq. (1.8.19) in Eq. (1.8.5), the lift coefficient for a wing with washout can be expressed as

$$C_L = \pi R_A A_1 = \pi R_A [a_1(\alpha - \alpha_{L0})_{\text{root}} - b_1 \Omega] \quad (1.8.22)$$

Using Eq. (1.8.19) in Eq. (1.8.6), the induced drag coefficient is given by

$$C_{D_i} = \pi R_A \sum_{n=1}^N n A_n^2 = \pi R_A [a_1(\alpha - \alpha_{L0})_{\text{root}} - b_1 \Omega]^2 + \pi R_A \sum_{n=2}^N n [a_n(\alpha - \alpha_{L0})_{\text{root}} - b_n \Omega]^2$$

or after using Eq. (1.8.22) to express the first term on the right-hand side in terms of the lift coefficient,

$$C_{D_i} = \frac{C_L^2}{\pi R_A} + \pi R_A \sum_{n=2}^{\infty} n [a_n^2 (\alpha - \alpha_{L0})_{\text{root}}^2 - 2a_n b_n (\alpha - \alpha_{L0})_{\text{root}} \Omega + b_n^2 \Omega^2] \quad (1.8.23)$$

Equations (1.8.22) and (1.8.23) can be algebraically rearranged to yield a convenient expression for the lift and induced drag developed by a **finite wing with geometric and/or aerodynamic twist**:

$$C_L = C_{L,\alpha} [(\alpha - \alpha_{L0})_{\text{root}} - \varepsilon_{\Omega} \Omega] \quad (1.8.24)$$

$$C_{D_i} = \frac{C_L^2 (1 + \kappa_D) - \kappa_{DL} C_L C_{L,\alpha} \Omega + \kappa_{D\Omega} (C_{L,\alpha} \Omega)^2}{\pi R_A} \quad (1.8.25)$$

where

$$C_{L,\alpha} = \pi R_A a_1 = \frac{\tilde{C}_{L,\alpha}}{[1 + \tilde{C}_{L,\alpha}/(\pi R_A)](1 + \kappa_L)} \quad (1.8.26)$$

$$\kappa_L \equiv \frac{1 - (1 + \pi R_A/\tilde{C}_{L,\alpha})a_1}{(1 + \pi R_A/\tilde{C}_{L,\alpha})a_1} \quad (1.8.27)$$

$$\varepsilon_\Omega \equiv \frac{b_1}{a_1} \quad (1.8.28)$$

$$\kappa_D \equiv \sum_{n=2}^N n \frac{a_n^2}{a_1^2} \quad (1.8.29)$$

$$\kappa_{DL} \equiv 2 \frac{b_1}{a_1} \sum_{n=2}^N n \frac{a_n}{a_1} \left(\frac{b_n}{b_1} - \frac{a_n}{a_1} \right) \quad (1.8.30)$$

$$\kappa_{D\Omega} \equiv \left(\frac{b_1}{a_1} \right)^2 \sum_{n=2}^N n \left(\frac{b_n}{b_1} - \frac{a_n}{a_1} \right)^2 \quad (1.8.31)$$

Comparing Eqs. (1.8.24) through (1.8.31) with Eqs. (1.8.11) and (1.8.14), we see that washout increases the zero-lift angle of attack for any wing but the lift slope for a wing of arbitrary planform shape is not affected by washout. Notice that the induced drag for a wing with washout is not zero at zero lift. In addition to the usual component of induced drag, which is proportional to the lift coefficient squared, a wing with washout produces a component of induced drag that is proportional to the washout squared, and this results in induced drag at zero lift. There is also a component of induced drag that varies with the product of the lift coefficient and the washout.

A commonly used washout distribution that is easy to implement is linear washout. For the special case of a linear variation in washout from the root to the tip, the normalized washout distribution function is simply

$$\omega(z) = |2z/b| \quad \text{or} \quad \omega(\theta) = |\cos(\theta)| \quad (1.8.32)$$

For tapered wings, the variation in chord length is also linear:

$$c(z) = \frac{2b}{R_A(1+R_T)} [1 - (1-R_T)|2z/b|] \quad \text{or} \quad c(\theta) = \frac{2b}{R_A(1+R_T)} [1 - (1-R_T)|\cos(\theta)|] \quad (1.8.33)$$

Using Eqs. (1.8.32) and (1.8.33) in Eqs. (1.8.20) and (1.8.21) yields the results for a tapered wing with linear washout,

60 Chapter 1 Overview of Aerodynamics

$$\sum_{n=1}^N a_n \left[\frac{2R_A(1+R_T)}{\tilde{C}_{L,\alpha} [1-(1-R_T)|\cos(\theta)]} + \frac{n}{\sin(\theta)} \right] \sin(n\theta) = 1 \quad (1.8.34)$$

$$\sum_{n=1}^N b_n \left[\frac{2R_A(1+R_T)}{\tilde{C}_{L,\alpha} [1-(1-R_T)|\cos(\theta)]} + \frac{n}{\sin(\theta)} \right] \sin(n\theta) = |\cos(\theta)| \quad (1.8.35)$$

The solution obtained from Eq. (1.8.34) for the Fourier coefficients, a_n , is the familiar result that was used to produce Figs. 1.8.13 and 1.8.14. Induced drag for a wing with washout is readily predicted from Eq. (1.8.25) with the definitions given in Eqs. (1.8.29) through (1.8.31). For tapered wings with linear washout, the Fourier coefficients, b_n , can be obtained from Eq. (1.8.35) in exactly the same manner as the coefficients, a_n , are obtained from Eq. (1.8.34). Using the Fourier coefficients so obtained in Eqs. (1.8.28), (1.8.30), and (1.8.31) produces the results shown in Figs. 1.8.15 through 1.8.17. Notice from examining either Eq. (1.8.31) or Fig. 1.8.17 that $\kappa_{D\Omega}$ is always positive. Thus, the third term in the numerator on the right-hand side of Eq. (1.8.25) always contributes to an increase in induced drag. However, from the results shown in Fig. 1.8.16, we see that the second term in the numerator on the right-hand side of Eq. (1.8.25) can either increase or decrease the induced drag, depending on the signs of κ_{DL} and Ω . This raises an important question regarding wing efficiency. What level and distribution of washout will result in minimum induced drag for a given wing planform and lift coefficient?

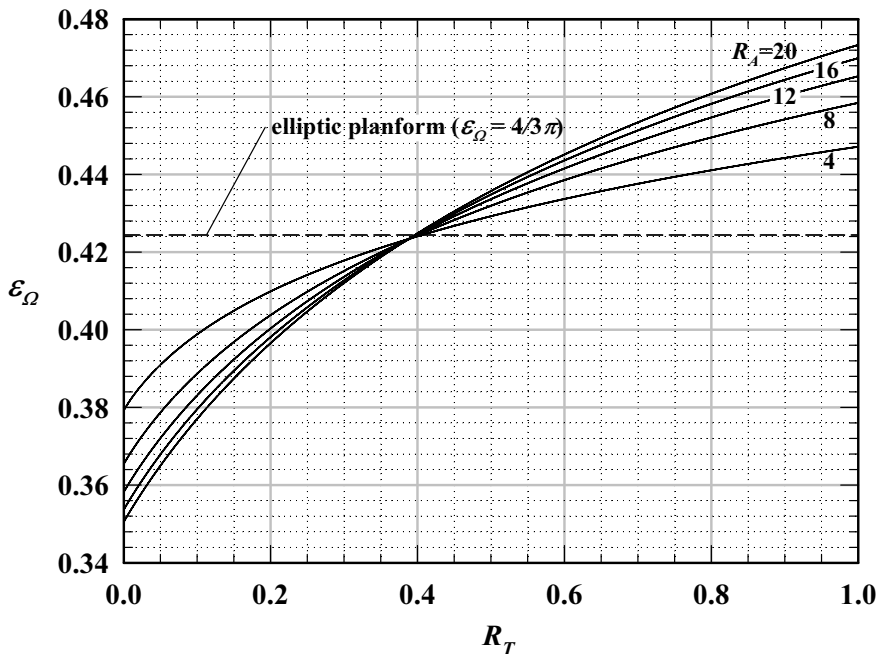


Figure 1.8.15. Washout effectiveness for tapered wings with linear washout.

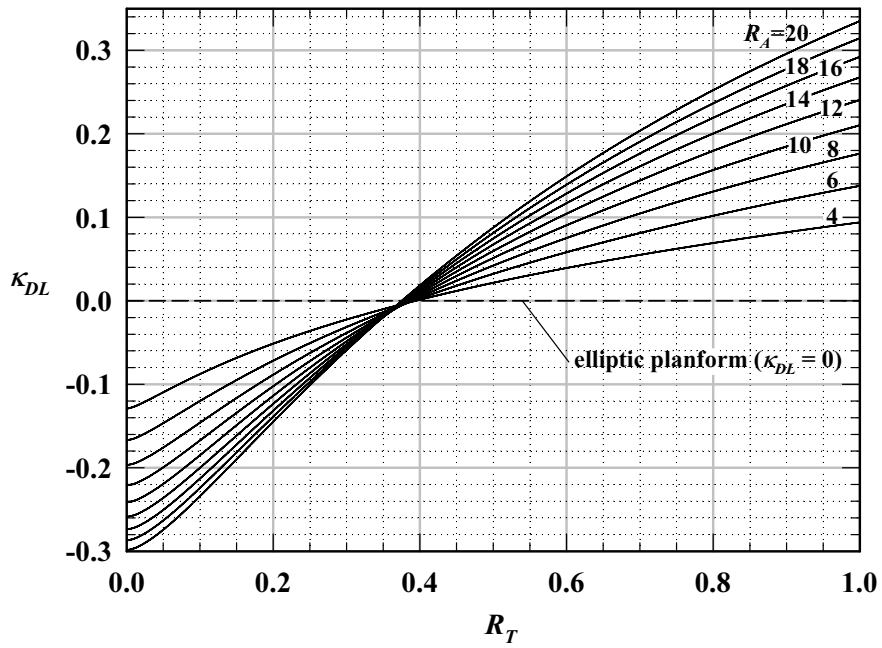


Figure 1.8.16. Lift-washout contribution to induced drag for tapered wings with linear washout.

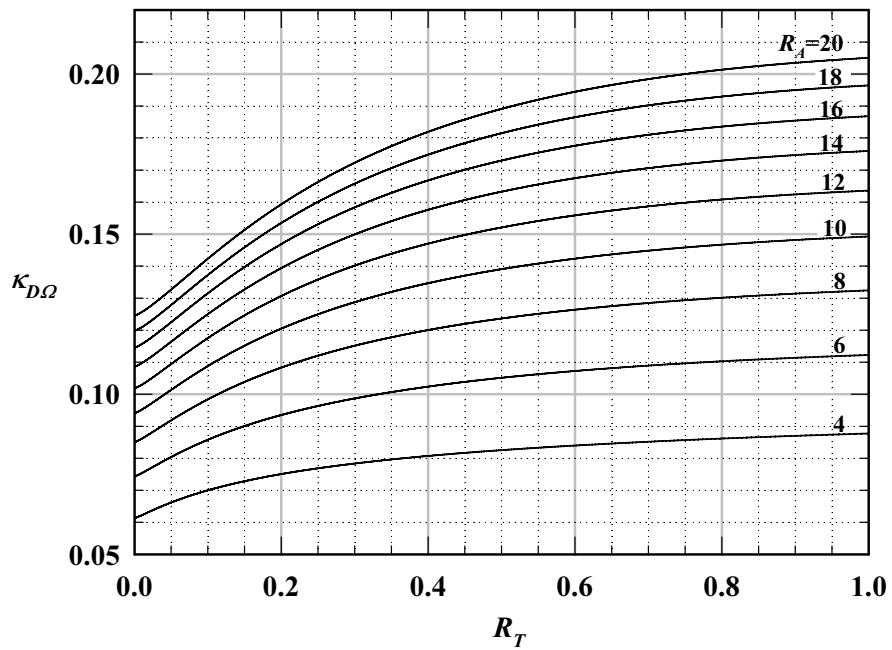


Figure 1.8.17. Washout contribution to induced drag for tapered wings with linear washout.

62 Chapter 1 Overview of Aerodynamics

Minimizing Induced Drag with Washout

For a wing of any given planform shape having a fixed washout distribution, induced drag can be minimized with washout as a result of the trade-off between the second and third terms in the numerator on the right-hand side of Eq. (1.8.25). Thus, Eq. (1.8.25) can be used to determine the optimum value of total washout, which will result in minimum induced drag for any washout distribution function and any specified lift coefficient. Differentiating Eq. (1.8.25) with respect to Ω at constant lift coefficient gives

$$\frac{\partial C_{D_i}}{\partial \Omega} = \frac{-\kappa_{DL} C_L C_{L,\alpha} + 2\kappa_{D\Omega} C_{L,\alpha}^2 \Omega}{\pi R_A} \quad (1.8.36)$$

Setting the right-hand side of Eq. (1.8.36) to zero and solving for Ω , it can be seen that minimum induced drag is attained for any given wing planform, $c(z)$, any given washout distribution, $\omega(z)$, and any given design lift coefficient, C_{Ld} , by using an optimum total amount of washout, Ω_{opt} , which is given by the relation

$$\Omega_{\text{opt}} = \frac{\kappa_{DL} C_{Ld}}{2\kappa_{D\Omega} C_{L,\alpha}} \quad (1.8.37)$$

For the elliptic planform, all of the Fourier coefficients, a_n , are zero for n greater than 1. Thus, Eq. (1.8.30) shows that κ_{DL} is zero for an elliptic wing. As a result, elliptic wings are always optimized with no washout. From consideration of Eq. (1.8.37) together with the results shown in Figs. 1.8.16 and 1.8.17, we see that tapered wings with linear washout and taper ratios greater than 0.4 are optimized with positive washout, whereas those with taper ratios less than about 0.4 are optimized with negative washout.

Using the value of optimum washout from Eq. (1.8.37) in the expression for induced drag coefficient given by Eq. (1.8.25), we find that the induced drag coefficient for a wing of arbitrary planform with a fixed washout distribution and optimum total washout is given by

$$(C_{D_i})_{\text{opt}} = \frac{C_L^2}{\pi R_A} \left[1 + \kappa_D - \frac{\kappa_{DL}^2}{4\kappa_{D\Omega}} \left(2 - \frac{C_{Ld}}{C_L} \right) \frac{C_{Ld}}{C_L} \right] \quad (1.8.38)$$

From Eq. (1.8.38) it can be seen that a wing with optimum washout will always produce less induced drag than a wing with no washout having the same planform and aspect ratio, provided that the actual lift coefficient is greater than one-half the design lift coefficient. When the actual lift coefficient is equal to the design lift coefficient, the induced drag coefficient for a wing with optimum washout is

$$(C_{D_i})_{\text{opt}} = \frac{C_L^2}{\pi R_A} (1 + \kappa_{D_o}), \quad \kappa_{D_o} \equiv \kappa_D - \frac{\kappa_{DL}^2}{4\kappa_{D\Omega}} \quad (1.8.39)$$

For tapered wings with linear washout, the variations in κ_{D_o} with aspect ratio and taper ratio are shown in Fig. 1.8.18. For comparison, the dashed lines in this figure show the

same results for wings with no washout. Notice that when linear washout is used to further optimize tapered wings, taper ratios near 0.4 correspond closely to a maximum in induced drag, not to a minimum.

The choice of a linear washout distribution, which was used to generate the results shown in Fig. 1.8.18, is as arbitrary as the choice of no washout. While a linear variation in washout is commonly used and simple to implement, it is not the optimum washout distribution for wings with linear taper. Minimum possible induced drag for a finite lift coefficient always occurs when the local section lift varies with the spanwise coordinate in proportion to $\sin(\theta)$. This results in uniform downwash and requires that the product of the local chord length and local aerodynamic angle of attack, $\alpha - \alpha_{L0}$, varies elliptically with the spanwise coordinate, i.e.,

$$\frac{c(z)[\alpha(z) - \alpha_{L0}(z)]}{\sqrt{1 - (2z/b)^2}} = \frac{c(\theta)[\alpha(\theta) - \alpha_{L0}(\theta)]}{\sin(\theta)} = \text{constant} \quad (1.8.40)$$

There are many possibilities for wing geometry that will satisfy this condition. The elliptic planform with no geometric or aerodynamic twist is only one such geometry. Since the local aerodynamic angle of attack decreases along the span in direct proportion to the increase in washout, Eq. (1.8.40) can only be satisfied if the washout distribution satisfies the relation

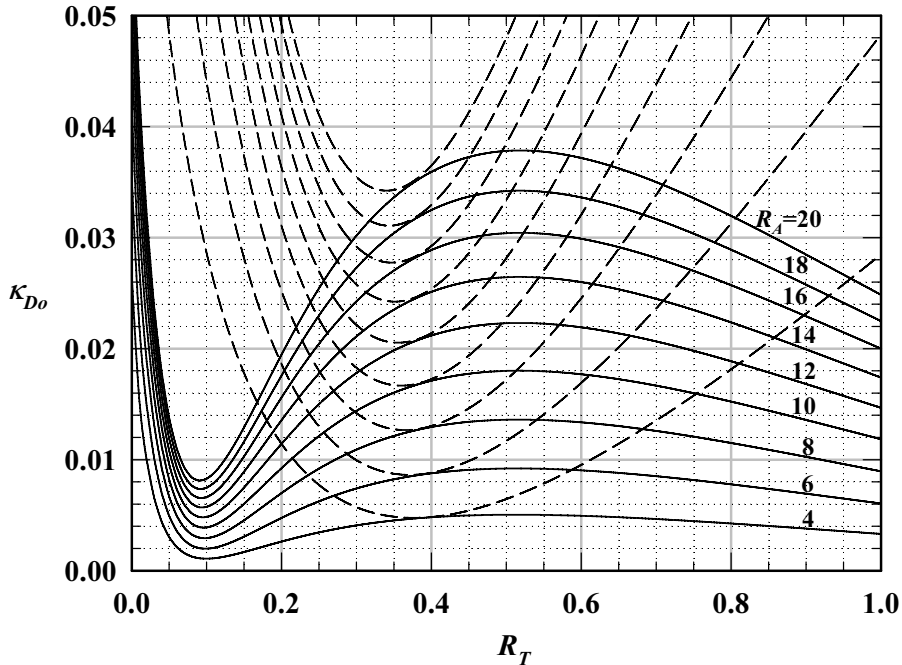


Figure 1.8.18. Optimum induced drag factor for tapered wings with linear washout.

64 Chapter 1 Overview of Aerodynamics

$$\frac{c(z)[1-\omega(z)]}{\sqrt{1-(2z/b)^2}} = \frac{c(\theta)[1-\omega(\theta)]}{\sin(\theta)} = \text{constant} \quad (1.8.41)$$

Equation (1.8.41) is satisfied by the **optimum washout distribution**

$$\omega_{\text{opt}} = 1 - \frac{\sqrt{1-(2z/b)^2}}{c(z)/c_{\text{root}}} = 1 - \frac{\sin(\theta)}{c(\theta)/c_{\text{root}}}, \quad \Omega_{\text{opt}} = \frac{4b C_L}{\pi R_A \tilde{C}_{L,\alpha} c_{\text{root}}} \quad (1.8.42)$$

For wings with linear taper, this gives

$$\omega_{\text{opt}} = 1 - \frac{\sqrt{1-(2z/b)^2}}{1-(1-R_T)|2z/b|} = 1 - \frac{\sin(\theta)}{1-(1-R_T)|\cos(\theta)|}, \quad \Omega_{\text{opt}} = \frac{2(1+R_T)C_L}{\pi \tilde{C}_{L,\alpha}} \quad (1.8.43)$$

This optimum washout distribution is shown in Fig. 1.8.19 for several values of taper ratio. Results obtained for tapered wings having this washout distribution are presented in Figs. 1.8.20 through 1.8.22. It should be noted that computing Ω_{opt} from Eq. (1.8.42) or (1.8.43) is only valid for wings having the optimum washout distribution, ω_{opt} . On the other hand, Eq. (1.8.37) is valid for any washout distribution. For $\omega = \omega_{\text{opt}}$, Eq. (1.8.37) produces exactly the same result as Eq. (1.8.42) or (1.8.43).

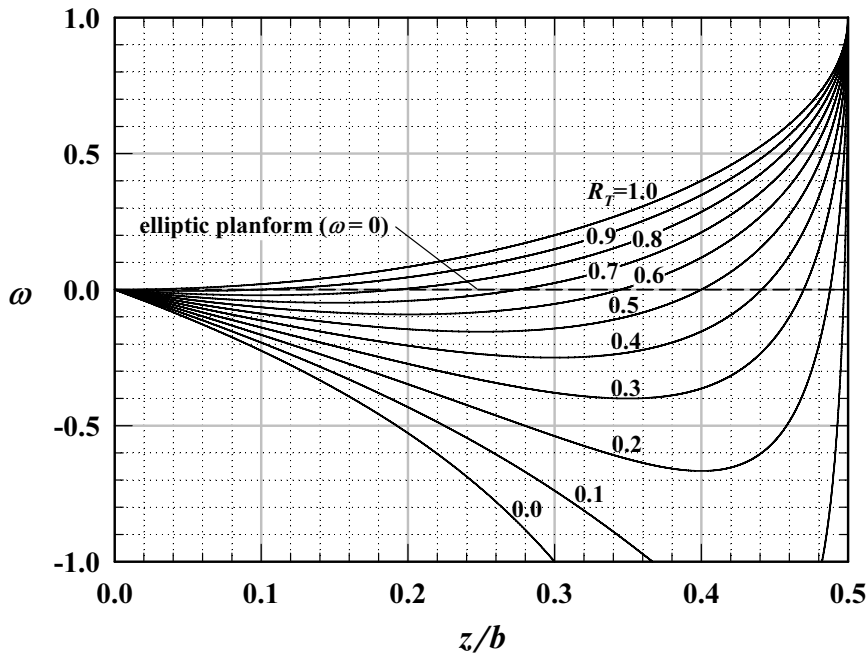


Figure 1.8.19. Optimum washout distribution that results in production of minimum induced drag for wings with linear taper, as defined in Eq. (1.8.43).

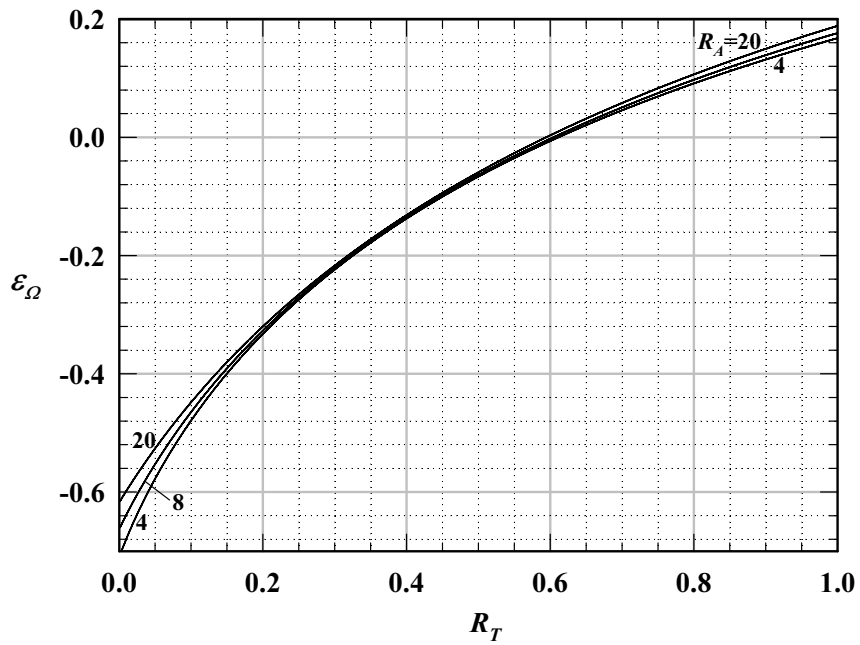


Figure 1.8.20. Washout effectiveness for wings with linear taper and optimum washout.

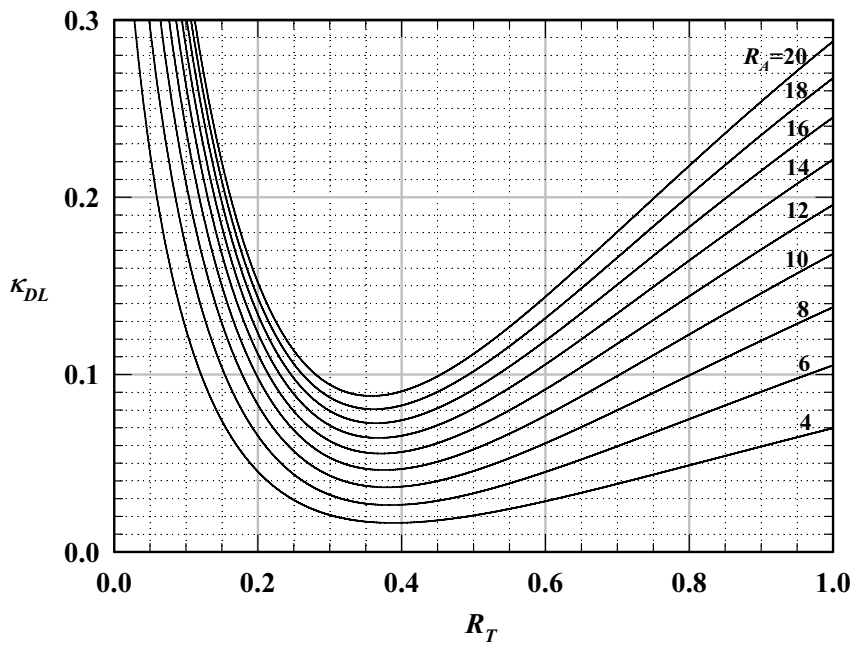


Figure 1.8.21. Lift-washout contribution to the induced drag factor for wings with linear taper and the optimum washout distribution specified by Eq. (1.8.43).

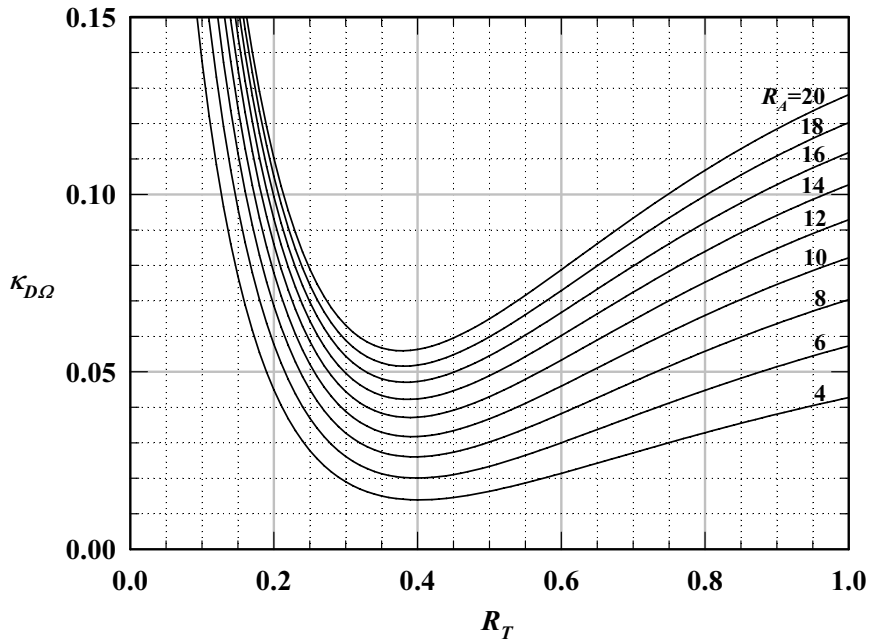


Figure 1.8.22. Washout contribution to the induced drag factor for wings with linear taper and the optimum washout distribution specified by Eq. (1.8.43).

When an unswept wing of arbitrary planform has the washout distribution specified by Eq. (1.8.42), the value of κ_{D_o} as defined in Eq. (1.8.39) is always identically zero. With the washout distribution set to ω_{opt} and the total amount washout set to Ω_{opt} , an unswept wing of any planform shape can be designed to operate at a given lift coefficient with the same induced drag as that produced by an untwisted elliptic wing with the same aspect ratio and lift coefficient. This is demonstrated in the following examples.

EXAMPLE 1.8.1. When results similar to those shown in Fig. 1.8.14 were first published by Glauert (1926), all calculations were made without the aid of a computer. For this reason, only a few terms were retained in the Fourier series. For a rectangular planform with an aspect ratio of 8.0 and the optimum washout distribution specified by Eq. (1.8.42), solve Eqs. (1.8.20) and (1.8.21) by retaining only seven terms in the Fourier series and forcing Eqs. (1.8.20) and (1.8.21) to be satisfied at only seven sections along the span of the wing. Locate the first and last sections at the wingtips and space the intermediate sections equally in θ , i.e.,

$$\theta_i = \frac{(i-1)\pi}{N-1}, \quad i = 1, N$$

where N is 7. Assume an airfoil lift slope of 2π and use the solution to compute κ_D , κ_{DL} , $\kappa_{D\Omega}$, and κ_{D_o} . Compare the results with those obtained for $N = 99$.

1.8. Incompressible Flow over Finite Wings 67

Solution. In order to obtain N independent equations for the N unknown Fourier coefficients, a_n , Eq. (1.8.20) can be written for each of N spanwise sections of the wing. With the first and last sections located at the wingtips and the intermediate sections spaced equally in θ , this gives the system of equations

$$\begin{bmatrix} C_{11} & C_{12} & C_{13} & \cdots & C_{1N} \\ C_{21} & C_{22} & C_{23} & \cdots & C_{2N} \\ C_{31} & C_{32} & C_{33} & \cdots & C_{3N} \\ \vdots & \vdots & \vdots & \ddots & \vdots \\ C_{N1} & C_{N2} & C_{N3} & \cdots & C_{NN} \end{bmatrix} \begin{Bmatrix} a_1 \\ a_2 \\ a_3 \\ \vdots \\ a_N \end{Bmatrix} = \begin{Bmatrix} 1 \\ 1 \\ 1 \\ \vdots \\ 1 \end{Bmatrix}$$

where

$$C_{ij} = \left[\frac{4b}{\tilde{C}_{L,\alpha} c(\theta_i)} + \frac{j}{\sin(\theta_i)} \right] \sin(j\theta_i), \quad \theta_i = \frac{(i-1)\pi}{N-1}, \quad \begin{cases} i=1, N \\ j=1, N \end{cases}$$

The components of the matrix, $[\mathbf{C}]$, on the left-hand side of this linear system are indeterminate when evaluated at the wingtips, $\theta=0$ and $\theta=\pi$. However, applying *l'Hospital's rule* gives

$$\begin{aligned} \left(\frac{\sin(j\theta_i)}{\sin(\theta_i)} \right)_{\theta_i \rightarrow 0} &= \left(\frac{j \cos(j\theta_i)}{\cos(\theta_i)} \right)_{\theta_i \rightarrow 0} = j \\ \left(\frac{\sin(j\theta_i)}{\sin(\theta_i)} \right)_{\theta_i \rightarrow \pi} &= \left(\frac{j \cos(j\theta_i)}{\cos(\theta_i)} \right)_{\theta_i \rightarrow \pi} = (-1)^{j+1} j \end{aligned}$$

Thus, for the purpose of numerical evaluation, the matrix $[\mathbf{C}]$ is determined from the algorithm

$$\begin{aligned} C_{1j} &= j^2, \quad j=1, N \\ C_{ij} &= \left[\frac{4b}{\tilde{C}_{L,\alpha} c(\theta_i)} + \frac{j}{\sin(\theta_i)} \right] \sin(j\theta_i), \quad \theta_i = \frac{(i-1)\pi}{N-1}, \quad \begin{cases} i=2, N-1 \\ j=1, N \end{cases} \\ C_{Nj} &= (-1)^{j+1} j^2, \quad j=1, N \end{aligned}$$

For this rectangular planform of aspect ratio of 8.0, the chord is independent of θ and $b/c(\theta)=8$. Thus, for an airfoil section lift slope of 2π and $N=7$, we have

$$C_{ij} = \left[\frac{16}{\pi} + \frac{j}{\sin[(i-1)\pi/6]} \right] \sin[j(i-1)\pi/6], \quad \begin{cases} i=2, 6 \\ j=1, 7 \end{cases}$$

Some example computations give

68 Chapter 1 Overview of Aerodynamics

$$C_{21} = \left[\frac{16}{\pi} + \frac{1}{\sin[(2-1)\pi/6]} \right] \sin\left(\frac{1(2-1)\pi}{6}\right) = \left[\frac{16}{\pi} + \frac{1}{\sin(\pi/6)} \right] \sin\left(\frac{\pi}{6}\right) = 3.5465$$

$$C_{22} = \left[\frac{16}{\pi} + \frac{2}{\sin[(2-1)\pi/6]} \right] \sin\left(\frac{2(2-1)\pi}{6}\right) = \left[\frac{16}{\pi} + \frac{2}{\sin(\pi/6)} \right] \sin\left(\frac{2\pi}{6}\right) = 7.8747$$

$$C_{45} = \left[\frac{16}{\pi} + \frac{5}{\sin[(4-1)\pi/6]} \right] \sin\left(\frac{5(4-1)\pi}{6}\right) = \left[\frac{16}{\pi} + \frac{5}{\sin(3\pi/6)} \right] \sin\left(\frac{15\pi}{6}\right) = 10.093$$

After performing the remaining computations, we have

$$[\mathbf{C}] = \begin{bmatrix} 1 & 4 & 9 & 16 & 25 & 36 & 49 \\ 3.5465 & 7.8747 & 11.093 & 11.339 & 7.5465 & 0 & -9.5465 \\ 5.4106 & 6.4106 & 0 & -8.4106 & -9.4106 & 0 & 11.411 \\ 6.0930 & 0 & -8.0930 & 0 & 10.093 & 0 & -12.093 \\ 5.4106 & -6.4106 & 0 & 8.4106 & -9.4106 & 0 & 11.411 \\ 3.5465 & -7.8747 & 11.093 & -11.339 & 7.5465 & 0 & -9.5465 \\ 1 & -4 & 9 & -16 & 25 & -36 & 49 \end{bmatrix}$$

The inverse of this matrix is

$$[\mathbf{C}]^{-1} = \begin{bmatrix} 0.00005 & 0.02061 & 0.04702 & 0.05661 & 0.04702 & 0.02061 & 0.00005 \\ 0.00000 & 0.03027 & 0.04081 & 0.00000 & -0.04081 & -0.03027 & 0.00000 \\ 0.00019 & 0.03016 & 0.00298 & -0.04047 & 0.00298 & 0.03016 & 0.00019 \\ 0.00000 & 0.02307 & -0.02834 & 0.00000 & 0.02834 & -0.02307 & 0.00000 \\ 0.00764 & 0.00286 & -0.01725 & 0.02481 & -0.01725 & 0.00286 & 0.00764 \\ 0.01389 & -0.01362 & 0.00806 & 0.00000 & -0.00806 & 0.01362 & -0.01389 \\ 0.00627 & -0.00742 & 0.00729 & -0.00638 & 0.00729 & -0.00742 & 0.00627 \end{bmatrix}$$

which yields

$$\begin{Bmatrix} a_1 \\ a_2 \\ a_3 \\ a_4 \\ a_5 \\ a_6 \\ a_7 \end{Bmatrix} = [\mathbf{C}]^{-1} \begin{Bmatrix} 1 \\ 1 \\ 1 \\ 1 \\ 1 \\ 1 \\ 1 \end{Bmatrix} = \begin{Bmatrix} 0.191966 \\ 0 \\ 0.026191 \\ 0 \\ 0.011287 \\ 0 \\ 0.005921 \end{Bmatrix}$$

Comparing Eqs. (1.8.20) and (1.8.21), we see that the Fourier coefficients, b_n , can be obtained from a linear system of equations that is almost identical to that used

1.8. Incompressible Flow over Finite Wings 69

to obtain the Fourier coefficients, a_n . The matrices on the left-hand sides of these two systems are identical. The only difference is that the right-hand side of the system used to obtain a_n is a vector having all components equal to 1, whereas the right-hand side of the system used to obtain b_n is a vector obtained from the washout distribution function,

$$\begin{bmatrix} C_{11} & C_{12} & C_{13} & \cdots & C_{1N} \\ C_{21} & C_{22} & C_{23} & \cdots & C_{2N} \\ C_{31} & C_{32} & C_{33} & \cdots & C_{3N} \\ \vdots & \vdots & \vdots & \ddots & \vdots \\ C_{N1} & C_{N2} & C_{N3} & \cdots & C_{NN} \end{bmatrix} \begin{bmatrix} b_1 \\ b_2 \\ b_3 \\ \vdots \\ b_N \end{bmatrix} = \begin{bmatrix} \omega(\theta_1) \\ \omega(\theta_2) \\ \omega(\theta_3) \\ \vdots \\ \omega(\theta_N) \end{bmatrix}$$

Using the optimum washout distribution function from Eq. (1.8.42) yields

$$\omega(\theta_i) = 1 - \frac{\sin(\theta_i)}{c(\theta_i)/c_{\text{root}}}, \quad \theta_i = \frac{(i-1)\pi}{N-1}, \quad i = 1, N$$

For this rectangular planform, the chord is constant, so $c(\theta)/c_{\text{root}} = 1$. Thus, for $N=7$, the Fourier coefficients, b_n , are found to be

$$\begin{Bmatrix} b_1 \\ b_2 \\ b_3 \\ b_4 \\ b_5 \\ b_6 \\ b_7 \end{Bmatrix} = [\mathbf{C}]^{-1} \begin{Bmatrix} 1 \\ 1 - \sin(\pi/6) \\ 1 - \sin(2\pi/6) \\ 1 - \sin(3\pi/6) \\ 1 - \sin(4\pi/6) \\ 1 - \sin(5\pi/6) \\ 1 - \sin(6\pi/6) \end{Bmatrix} = [\mathbf{C}]^{-1} \begin{Bmatrix} 1 \\ 0.5 \\ 0.133975 \\ 0 \\ 0.133975 \\ 0.5 \\ 1 \end{Bmatrix} = \begin{Bmatrix} 0.033309 \\ 0 \\ 0.031334 \\ 0 \\ 0.013504 \\ 0 \\ 0.007084 \end{Bmatrix}$$

Using these results in Eqs. (1.8.29), (1.8.30), (1.8.31), and (1.8.39) yields

$$\kappa_D \equiv \sum_{n=2}^N n \frac{a_n^2}{a_1^2} = \underline{0.079791}$$

$$\kappa_{DL} \equiv 2 \frac{b_1}{a_1} \sum_{n=2}^N n \frac{a_n}{a_1} \left(\frac{b_n}{b_1} - \frac{a_n}{a_1} \right) = \underline{0.163225}$$

$$\kappa_{D\Omega} \equiv \left(\frac{b_1}{a_1} \right)^2 \sum_{n=2}^N n \left(\frac{b_n}{b_1} - \frac{a_n}{a_1} \right)^2 = \underline{0.083476}$$

$$\kappa_{Do} \equiv \kappa_D - \frac{\kappa_{DL}^2}{4\kappa_{D\Omega}} = \underline{0.000000}$$

70 Chapter 1 Overview of Aerodynamics

For comparison, repeating these computations with $N=99$ gives

$$\begin{pmatrix} a_1 \\ a_2 \\ a_3 \\ a_4 \\ a_5 \\ a_6 \\ a_7 \\ \vdots \\ a_{98} \\ a_{99} \end{pmatrix} = \begin{pmatrix} 0.19248612 \\ 0 \\ 0.02740767 \\ 0 \\ 0.00656477 \\ 0 \\ 0.00202851 \\ \vdots \\ 0 \\ 0.00000144 \end{pmatrix}, \quad \begin{pmatrix} b_1 \\ b_2 \\ b_3 \\ b_4 \\ b_5 \\ b_6 \\ b_7 \\ \vdots \\ b_{98} \\ b_{99} \end{pmatrix} = \begin{pmatrix} 0.03393114 \\ 0 \\ 0.03278916 \\ 0 \\ 0.00785376 \\ 0 \\ 0.00242681 \\ \vdots \\ 0 \\ 0.00000172 \end{pmatrix}$$

$$\kappa_D = \underline{0.067611}, \quad \kappa_{DL} = \underline{0.137937}, \quad \kappa_{D\Omega} = \underline{0.070353}, \quad \kappa_{D\sigma} = \underline{0.000000}$$

EXAMPLE 1.8.2. We wish to repeat the computations in Example 1.8.1 for a wing of tapered planform with an aspect ratio of 8.0 and a taper ratio of 0.5.

Solution. For a wing planform having linear taper, the section chord length varies with the spanwise coordinate as specified in Eq. (1.8.33). With an aspect ratio of 8.0 and a taper ratio of 0.5, this gives

$$\frac{c(\theta)}{b} = \frac{2}{R_A(1+R_T)} [1 - (1-R_T)|\cos(\theta)|] = \frac{1}{6} [1 - 0.5|\cos(\theta)|]$$

Thus, following Example 1.8.1, for this wing geometry and an airfoil section lift slope of 2π , the components of the matrix $[\mathbf{C}]$ are determined from

$$\begin{aligned} C_{1j} &= j^2, \quad j=1, N \\ C_{ij} &= \left[\frac{12}{\pi[1-0.5|\cos(\theta_i)]} + \frac{j}{\sin(\theta_i)} \right] \sin(j\theta_i), \quad \theta_i = \frac{(i-1)\pi}{N-1}, \quad \begin{cases} i=2, N-1 \\ j=1, N \end{cases} \\ C_{Nj} &= (-1)^{j+1} j^2, \quad j=1, N \end{aligned}$$

For example, with $N=7$,

$$C_{45} = \left[\frac{12}{\pi[1-0.5|\cos(3\pi/6)]} + \frac{5}{\sin(3\pi/6)} \right] \sin(15\pi/6) = 8.8197$$

After performing the remaining computations, we have

1.8. Incompressible Flow over Finite Wings 71

$$[\mathbf{C}] = \begin{bmatrix} 1 & 4 & 9 & 16 & 25 & 36 & 49 \\ 4.3684 & 9.2984 & 12.7369 & 12.7625 & 8.3684 & 0 & -10.3684 \\ 5.4106 & 6.4106 & 0 & -8.4106 & -9.4106 & 0 & 11.4106 \\ 4.8197 & 0 & -6.8197 & 0 & 8.8197 & 0 & -10.8197 \\ 5.4106 & -6.4106 & 0 & 8.4106 & -9.4106 & 0 & 11.4106 \\ 4.3684 & -9.2984 & 12.7369 & -12.7625 & 8.3684 & 0 & -10.3684 \\ 1 & -4 & 9 & -16 & 25 & -36 & 49 \end{bmatrix}$$

$$[\mathbf{C}]^{-1} = \begin{bmatrix} 0.00010 & 0.01798 & 0.04785 & 0.06742 & 0.04785 & 0.01798 & 0.00010 \\ 0.00000 & 0.02628 & 0.03988 & 0.00000 & -0.03988 & -0.02628 & 0.00000 \\ 0.00003 & 0.02619 & 0.00055 & -0.04872 & 0.00055 & 0.02619 & 0.00003 \\ 0.00000 & 0.02003 & -0.02905 & 0.00000 & 0.02905 & -0.02003 & 0.00000 \\ 0.00767 & 0.00251 & -0.01663 & 0.02962 & -0.01663 & 0.00251 & 0.00767 \\ 0.01389 & -0.01182 & 0.00848 & 0.00000 & -0.00848 & 0.01182 & -0.01389 \\ 0.00628 & -0.00646 & 0.00741 & -0.00754 & 0.00741 & -0.00646 & 0.00628 \end{bmatrix}$$

$$\begin{Bmatrix} a_1 \\ a_2 \\ a_3 \\ a_4 \\ a_5 \\ a_6 \\ a_7 \end{Bmatrix} = [\mathbf{C}]^{-1} \begin{Bmatrix} 1 \\ 1 \\ 1 \\ 1 \\ 1 \\ 1 \\ 1 \end{Bmatrix} = \begin{Bmatrix} 0.199278 \\ 0 \\ 0.004824 \\ 0 \\ 0.016713 \\ 0 \\ 0.006928 \end{Bmatrix}$$

For this planform with linear taper and a taper ratio of 0.5, the optimum washout distribution function from Eq. (1.8.43) is

$$\omega(\theta_i) = 1 - \frac{\sin(\theta_i)}{1 - 0.5|\cos(\theta_i)|}, \quad \theta_i = \frac{(i-1)\pi}{N-1}, \quad i = 1, N$$

$$\begin{Bmatrix} b_1 \\ b_2 \\ b_3 \\ b_4 \\ b_5 \\ b_6 \\ b_7 \end{Bmatrix} = [\mathbf{C}]^{-1} \begin{Bmatrix} \omega(0) \\ \omega(\pi/6) \\ \omega(2\pi/6) \\ \omega(3\pi/6) \\ \omega(4\pi/6) \\ \omega(5\pi/6) \\ \omega(\pi) \end{Bmatrix} = [\mathbf{C}]^{-1} \begin{Bmatrix} 1 \\ 0.118146 \\ -0.154701 \\ 0 \\ -0.154701 \\ 0.118146 \\ 1 \end{Bmatrix} = \begin{Bmatrix} -0.010351 \\ 0 \\ 0.006087 \\ 0 \\ 0.021088 \\ 0 \\ 0.008742 \end{Bmatrix}$$

72 Chapter 1 Overview of Aerodynamics

Using these results in Eqs. (1.8.29), (1.8.30), (1.8.31), and (1.8.39) yields

$$\kappa_D = \underline{0.045387}, \quad \kappa_{DL} = \underline{0.119253}, \quad \kappa_{D\Omega} = \underline{0.078334}, \quad \kappa_{D\sigma} = \underline{0.000000}$$

With $N=99$ we obtain

$$\begin{pmatrix} a_1 \\ a_2 \\ a_3 \\ a_4 \\ a_5 \\ a_6 \\ a_7 \\ \vdots \\ a_{98} \\ a_{99} \end{pmatrix} = \begin{pmatrix} 0.19751337 \\ 0 \\ 0.00837113 \\ 0 \\ 0.00918923 \\ 0 \\ 0.00142163 \\ \vdots \\ 0 \\ 0.00000164 \end{pmatrix}, \quad \begin{pmatrix} b_1 \\ b_2 \\ b_3 \\ b_4 \\ b_5 \\ b_6 \\ b_7 \\ \vdots \\ b_{98} \\ b_{99} \end{pmatrix} = \begin{pmatrix} -0.01257714 \\ 0 \\ 0.01056269 \\ 0 \\ 0.01159497 \\ 0 \\ 0.00179381 \\ \vdots \\ 0 \\ 0.00000207 \end{pmatrix}$$

$$\kappa_D = \underline{0.017190}, \quad \kappa_{DL} = \underline{0.045569}, \quad \kappa_{D\Omega} = \underline{0.030200}, \quad \kappa_{D\sigma} = \underline{0.000000}$$

From Examples 1.8.1 and 1.8.2 it should be observed that all of the even Fourier coefficients, in both a_n and b_n , were identically zero for both the rectangular and tapered wings. This was realized regardless of how many terms were carried in the Fourier series and was a direct result of the spanwise symmetry of these two wings. If we were always willing to restrict our analysis to spanwise symmetric wing geometry, the computation time could be reduced by forcing all even coefficients to be zero and solving for the odd coefficients using sections distributed over only one side of the wing, i.e., $0 \leq \theta \leq \pi/2$. The requirement for a spanwise symmetric wing planform is not too restrictive. Most wings exhibit this symmetry. However, restricting our analysis to wings having a spanwise symmetric distribution in geometric and aerodynamic twist would eliminate the possibility of using lifting-line theory for the analysis of asymmetric control surface deflection. Such control surface deflection is almost always used in the wing of an airplane to provide roll control.

Solution with Control Surface Deflection and Rolling Rate

Trailing-edge flaps extending over only some portion of the wingspan are commonly used as control surfaces on an airplane wing. A spanwise symmetric control surface deflection can be used to provide pitch control, and spanwise asymmetric control surface deflection can be used to provide roll control. The control surfaces commonly used to provide roll control are called *aileron*s. These are small trailing-edge flaps located in the outboard sections of the wing. The ailerons are deflected asymmetrically to change the rolling moment. One aileron is deflected downward and the other is deflected upward, as

shown in Fig. 1.8.23. This increases lift on the semispan with the downward-deflected aileron and decreases lift on the semispan with the upward-deflected aileron. Aileron deflection is given the symbol δ_a , and the rolling moment is denoted as ℓ . The sign convention that is commonly used for aileron deflection is shown in Fig. 1.8.23. Aileron deflection is assumed positive when the right aileron is deflected downward and the left aileron is deflected upward. The traditional sign convention used for the rolling moment is positive to the right (i.e., a moment that would roll the right wing down). With these two sign conventions, a positive aileron deflection produces a rolling moment to the left (i.e., negative ℓ). The two ailerons are not necessarily deflected the same magnitude. The aileron angle, δ_a , is usually defined to be the average of the two angular deflections.

The rolling moment produced by aileron deflection results in a rolling acceleration, which in turn produces a rolling rate. This rolling rate changes the spanwise variation in geometric angle of attack as shown in Fig. 1.8.24. The symbol traditionally used to

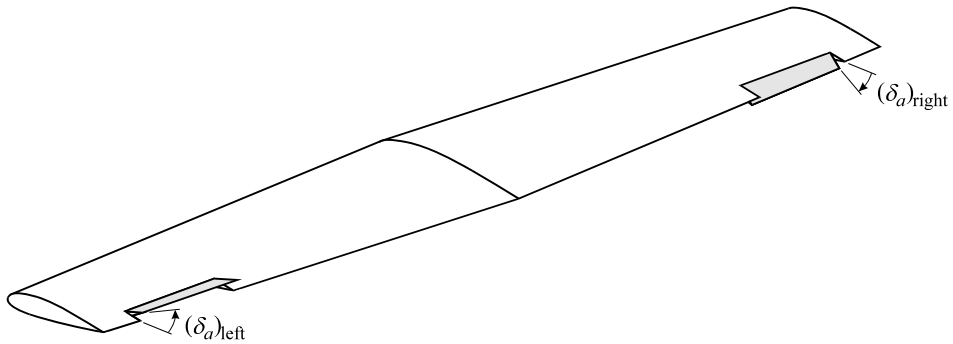


Figure 1.8.23. Asymmetric aileron deflection typically used for roll control.

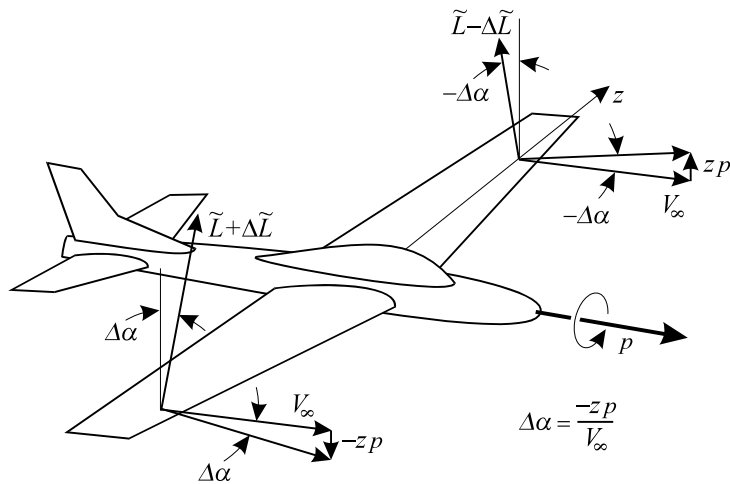


Figure 1.8.24. Change in local section angle of attack resulting from a rolling rate.

74 Chapter 1 Overview of Aerodynamics

represent rolling rate is p . As shown in Fig. 1.8.24, p is taken to be positive when the right semispan is moving downward and the left semispan is moving upward. Thus, a positive rolling rate increases the local geometric angle of attack on the right semispan and decreases the local geometric angle of attack on the left semispan. This produces a negative rolling moment, which opposes the rolling rate.

When a small positive aileron deflection is first initiated, a negative rolling moment is produced by the asymmetric change in the wing's local aerodynamic angle of attack. This rolling moment imbalance results in negative rolling acceleration, which produces a negative rolling rate. As the magnitude of the rolling rate increases, an opposing rolling moment develops as a result of the asymmetric change in the local geometric angle of attack. This reduces the moment imbalance and slows the rolling acceleration. At some point, the positive rolling moment produced by the negative rolling rate will just balance the negative rolling moment produced by the positive aileron deflection, and a constant rolling rate will develop that is proportional to the aileron deflection.

As we will learn in Chapter 9, roll in a conventional airplane is what is referred to as *heavily damped motion*. This means that when a typical fixed-wing aircraft responds to aileron input, the period of rolling acceleration is very short and the airplane quickly approaches a steady rolling rate, which is proportional to aileron deflection. This gives the pilot the perception that aileron input commands the airplane's rolling rate. Thus, analysis of an airplane's roll response must include consideration of the rolling moment produced by the rolling rate as well as that produced by aileron deflection. Lifting-line theory provides the capability to do just that.

In general, a wing's spanwise variation in local aerodynamic angle of attack can be expressed as the value at the wing root plus the changes due to washout, control surface deflection, and rolling rate,

$$\alpha(z) - \alpha_{L0}(z) \equiv (\alpha - \alpha_{L0})_{\text{root}} - \Omega \omega(z) + \delta_a \chi(z) - pz/V_\infty \quad (1.8.44)$$

where Ω is defined to be the maximum total symmetric washout for the wing, geometric plus aerodynamic,

$$\Omega \equiv [(\alpha - \alpha_{L0})_{\text{root}} - (\Delta\alpha - \Delta\alpha_{L0})_{\text{max}}]_{\text{washout}} \quad (1.8.45)$$

$\omega(z)$ is the symmetric washout distribution function,

$$\omega(z) \equiv \left[\frac{\Delta\alpha(z) - \Delta\alpha_{L0}(z) - (\alpha - \alpha_{L0})_{\text{root}}}{(\Delta\alpha - \Delta\alpha_{L0})_{\text{max}} - (\alpha - \alpha_{L0})_{\text{root}}} \right]_{\text{washout}} \quad (1.8.46)$$

and $\chi(z)$ is the control surface distribution function,

$$\chi(z) \equiv \left[\frac{\Delta\alpha(z) - \Delta\alpha_{L0}(z) - (\alpha - \alpha_{L0})_{\text{root}}}{\delta_a} \right]_{\text{control}} \quad (1.8.47)$$

For example, ailerons extending from the spanwise coordinate z_{ar} to z_{at} give

$$\chi(z) \equiv \begin{cases} 0, & z < -z_{at} \\ \mathcal{E}_f(z), & -z_{at} < z < -z_{ar} \\ 0, & -z_{ar} < z < z_{ar} \\ -\mathcal{E}_f(z), & z_{ar} < z < z_{at} \\ 0, & z > z_{at} \end{cases} \quad (1.8.48)$$

where \mathcal{E}_f is the local section flap effectiveness.

Using the definition of θ from Eq. (1.8.3) together with Eq. (1.8.44) in the relation for the Fourier coefficients, A_n , specified by Eq. (1.8.4), gives

$$\sum_{n=1}^N A_n \left[\frac{4b}{\tilde{C}_{L,\alpha} c(\theta)} + \frac{n}{\sin(\theta)} \right] \sin(n\theta) = (\alpha - \alpha_{L0})_{\text{root}} - \Omega \omega(\theta) + \delta_a \chi(\theta) + \bar{p} \cos(\theta) \quad (1.8.49)$$

where \bar{p} is a dimensionless rolling rate defined as $\bar{p} = pb/2V_\infty$. The Fourier coefficients in Eq. (1.8.49) can be conveniently written as

$$A_n = a_n (\alpha - \alpha_{L0})_{\text{root}} - b_n \Omega + c_n \delta_a + d_n \bar{p} \quad (1.8.50)$$

where

$$\sum_{n=1}^N a_n \left[\frac{4b}{\tilde{C}_{L,\alpha} c(\theta)} + \frac{n}{\sin(\theta)} \right] \sin(n\theta) = 1 \quad (1.8.51)$$

$$\sum_{n=1}^N b_n \left[\frac{4b}{\tilde{C}_{L,\alpha} c(\theta)} + \frac{n}{\sin(\theta)} \right] \sin(n\theta) = \omega(\theta) \quad (1.8.52)$$

$$\sum_{n=1}^N c_n \left[\frac{4b}{\tilde{C}_{L,\alpha} c(\theta)} + \frac{n}{\sin(\theta)} \right] \sin(n\theta) = \chi(\theta) \quad (1.8.53)$$

$$\sum_{n=1}^N d_n \left[\frac{4b}{\tilde{C}_{L,\alpha} c(\theta)} + \frac{n}{\sin(\theta)} \right] \sin(n\theta) = \cos(\theta) \quad (1.8.54)$$

Equations (1.8.51) and (1.8.52) are exactly Eqs. (1.8.20) and (1.8.21) and their solutions are obtained following Examples 1.8.1 and 1.8.2. The solutions to Eqs. (1.8.53) and (1.8.54) can be obtained in a similar manner and are both independent of angle of attack and rolling rate.

Once the Fourier coefficients are determined from Eqs. (1.8.50) through (1.8.54), the spanwise circulation distribution is known from Eq. (1.8.3) and the spanwise section lift distribution is given by

76 Chapter 1 Overview of Aerodynamics

$$\tilde{L}(z) = \rho V_\infty \Gamma(z)$$

Thus, in view of Eq. (1.8.3), the rolling moment coefficient can be evaluated from

$$C_\ell = \frac{1}{\frac{1}{2} \rho V_\infty^2 S b} \int_{z=-b/2}^{b/2} \tilde{L}(z) z dz = \frac{2}{V_\infty S b} \int_{z=-b/2}^{b/2} \Gamma(z) z dz = -\frac{b^2}{S} \sum_{n=1}^N A_n \int_{\theta=0}^{\pi} \sin(n\theta) \cos(\theta) \sin(\theta) d\theta$$

or after applying the trigonometric identity, $\sin(2\theta) = 2\sin(\theta)\cos(\theta)$, along with the definition of aspect ratio

$$C_\ell = -\frac{R_A}{2} \sum_{n=1}^N A_n \int_{\theta=0}^{\pi} \sin(n\theta) \sin(2\theta) d\theta \quad (1.8.55)$$

The integral in Eq. (1.8.55) is evaluated from

$$\int_{\theta=0}^{\pi} \sin(m\theta) \sin(n\theta) d\theta = \begin{cases} 0, & n \neq m \\ \pi/2, & n = m \end{cases} \quad (1.8.56)$$

After applying Eqs. (1.8.50) and (1.8.56), Eq. (1.8.55) becomes

$$C_\ell = -\frac{\pi R_A}{4} A_2 = -\frac{\pi R_A}{4} [a_2(\alpha - \alpha_{L0})_{\text{root}} - b_2 \Omega + c_2 \delta_a + d_2 \bar{p}] \quad (1.8.57)$$

For a wing with a **spanwise symmetric planform and spanwise symmetric washout**, the solutions to Eqs. (1.8.51) and (1.8.52) give

$$a_n = b_n = 0, \quad n \text{ even} \quad (1.8.58)$$

and Eq. (1.8.57) reduces to

$$C_\ell = C_{\ell, \delta_a} \delta_a + C_{\ell, \bar{p}} \bar{p} \quad (1.8.59)$$

where

$$C_{\ell, \delta_a} = -\frac{\pi R_A}{4} c_2 \quad (1.8.60)$$

$$C_{\ell, \bar{p}} = -\frac{\pi R_A}{4} d_2 \quad (1.8.61)$$

The Fourier coefficients obtained from Eq. (1.8.53) depend on control surface geometry as well as the planform shape of the wing. Thus, the change in rolling moment coefficient with respect to aileron deflection depends on the size and shape of the ailerons

1.8. Incompressible Flow over Finite Wings 77

and the wing planform. On the other hand, the Fourier coefficients that are evaluated from Eq. (1.8.54) are functions of only wing planform. For an elliptic planform, the spanwise variation in chord length is given by

$$c(y) = \frac{4b}{\pi R_A} \sqrt{1 - (2y/b)^2} \quad \text{or} \quad c(\theta) = \frac{4b}{\pi R_A} \sin(\theta)$$

and Eq. (1.8.54) reduces to

$$\sum_{n=1}^N d_n \left(\frac{\pi R_A}{\tilde{C}_{L,\alpha}} + n \right) \sin(n\theta) = \sin(\theta) \cos(\theta) \quad (1.8.62)$$

The solution to Eq. (1.8.62) is given by the Fourier integral

$$d_n \left(\frac{\pi R_A}{\tilde{C}_{L,\alpha}} + n \right) = \frac{2}{\pi} \int_0^\pi \sin(\theta) \cos(\theta) \sin(n\theta) d\theta = \frac{1}{\pi} \int_0^\pi \sin(2\theta) \sin(n\theta) d\theta \quad (1.8.63)$$

which is readily evaluated from Eq. (1.8.56) to give

$$d_n = \begin{cases} \frac{\tilde{C}_{L,\alpha}}{2(\pi R_A + 2\tilde{C}_{L,\alpha})}, & n = 2 \\ 0, & n \neq 2 \end{cases} \quad (1.8.64)$$

Using Eq. (1.8.64) in Eq. (1.8.61) gives

$$C_{\ell, \bar{p}} = \frac{-\tilde{C}_{L,\alpha}}{8(1 + 2\tilde{C}_{L,\alpha}/\pi R_A)}$$

Thus, in view of Eq. (1.8.7), **the change in rolling moment coefficient with respect to dimensionless rolling rate for an elliptic wing** can be written as

$$C_{\ell, \bar{p}} = -\frac{\kappa_{\ell \bar{p}} C_{L,\alpha}}{8}, \quad \kappa_{\ell \bar{p}} \equiv \frac{1 + \tilde{C}_{L,\alpha}/\pi R_A}{1 + 2\tilde{C}_{L,\alpha}/\pi R_A} \quad (1.8.65)$$

Similarly, in the general case of **a wing with arbitrary planform**,

$$C_{\ell, \bar{p}} = -\frac{\kappa_{\ell \bar{p}} C_{L,\alpha}}{8}, \quad \kappa_{\ell \bar{p}} \equiv \frac{2d_2}{a_1} \quad (1.8.66)$$

Using an airfoil lift slope of 2π to determine a_1 and d_2 from Eqs. (1.8.51) and (1.8.54), the results shown in Fig. 1.8.25 are obtained for tapered wings.

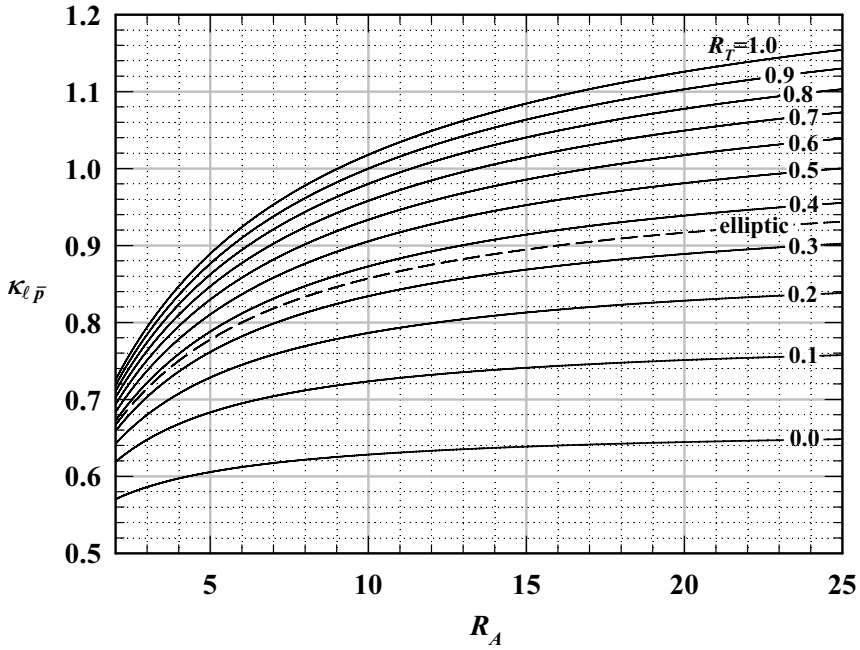


Figure 1.8.25. Roll damping factor for wings with linear taper from Eq. (1.8.66).

The asymmetric spanwise variations in aerodynamic angle of attack, which result from aileron deflection and roll, can also produce a yawing moment. The aerodynamic yawing moment is given the symbol n , and the traditional sign convention for yaw is positive to the right (i.e., a moment that would yaw the airplane’s nose to the right). The yawing moment develops as a direct result of an asymmetric spanwise variation in drag. Thus, the yawing moment coefficient can be written as

$$C_n \equiv \frac{n}{\frac{1}{2} \rho V_\infty^2 S b} = \frac{1}{\frac{1}{2} \rho V_\infty^2 S b} \int_{z=-b/2}^{b/2} (-z) \tilde{D}(z) dz \quad (1.8.67)$$

As shown in Figs. 1.8.6 and 1.8.24, the asymmetric section drag results from tilting the section lift vector through the induced angle, α_i , and the roll angle, zp/V_∞ . Thus, after expressing the section lift in terms of the section circulation, we have

$$\tilde{D}(z) = \tilde{L} \sin(\alpha_i + zp/V_\infty) \cong \tilde{L}(\alpha_i + zp/V_\infty) = \rho V_\infty \Gamma(z) [\alpha_i(z) + zp/V_\infty] \quad (1.8.68)$$

The induced angle of attack as predicted by lifting-line theory is

$$\alpha_i(z) = \frac{1}{4\pi V_\infty} \int_{\zeta=-b/2}^{b/2} \frac{1}{z-\zeta} \left(\frac{d\Gamma}{dz} \right)_{z=\zeta} d\zeta \quad (1.8.69)$$

Using Eqs. (1.8.68) and (1.8.69) in Eq. (1.8.67) gives

$$C_n = \int_{z=-b/2}^{b/2} \frac{-2z\Gamma(z)}{V_\infty^2 S b} \left[\frac{1}{4\pi} \int_{\zeta=-b/2}^{b/2} \frac{1}{z-\zeta} \left(\frac{d\Gamma}{dz} \right)_{z=\zeta} d\zeta + zp \right] dz \quad (1.8.70)$$

From Eq. (1.8.3) we have

$$\Gamma(\theta) = 2bV_\infty \sum_{n=1}^N A_n \sin(n\theta), \quad \cos(\theta) = -\frac{2z}{b}, \quad \frac{d\Gamma}{dz} = 4V_\infty \sum_{n=1}^N A_n \frac{n \cos(n\theta)}{\sin(\theta)}$$

and Eq. (1.8.70) can be written as

$$C_n = R_A \int_{\theta=0}^{\pi} \cos(\theta) \left[\sum_{n=1}^N A_n \sin(n\theta) \right] \left[\sum_{n=1}^N \frac{nA_n}{\pi} \int_{\phi=0}^{\pi} \frac{\cos(n\phi)d\phi}{\cos(\phi) - \cos(\theta)} \right] \sin(\theta) d\theta \\ - R_A \bar{p} \sum_{n=1}^N A_n \int_{\theta=0}^{\pi} \cos^2(\theta) \sin(\theta) \sin(n\theta) d\theta$$

Integrating in ϕ and using the trigonometric relation $\sin(2\theta) = 2\cos(\theta)\sin(\theta)$ yields

$$C_n = R_A \sum_{n=1}^N \sum_{m=1}^N nA_n A_m \int_{\theta=0}^{\pi} \cos(\theta) \sin(n\theta) \sin(m\theta) d\theta \\ - R_A \bar{p} \sum_{n=1}^N A_n \frac{1}{2} \int_{\theta=0}^{\pi} \cos(\theta) \sin(2\theta) \sin(n\theta) d\theta \quad (1.8.71)$$

Since m and n are positive integers, the integrals with respect to θ are evaluated from

$$\int_{\theta=0}^{\pi} \cos(\theta) \sin(n\theta) \sin(m\theta) d\theta = \begin{cases} \pi/4, & m = n \pm 1 \\ 0, & m \neq n \pm 1 \end{cases}$$

and after some rearranging, we obtain

$$C_n = \frac{\pi R_A}{4} \sum_{n=2}^N (2n-1) A_{n-1} A_n - \frac{\pi R_A \bar{p}}{8} (A_1 + A_3) \quad (1.8.72)$$

After applying Eq. (1.8.5), we find that the **yawing moment coefficient for a wing of arbitrary geometry** is given by

$$C_n = \frac{C_L}{8} (6A_2 - \bar{p}) + \frac{\pi R_A}{8} (10A_2 - \bar{p}) A_3 + \frac{\pi R_A}{4} \sum_{n=4}^N (2n-1) A_{n-1} A_n \quad (1.8.73)$$

where the Fourier coefficients, A_n , are related to Ω , δ_a , and \bar{p} through Eq. (1.8.50).

80 Chapter 1 Overview of Aerodynamics

If the wing planform and washout distribution are both spanwise symmetric, all even coefficients in both a_n and b_n are zero. The change in aerodynamic angle of attack that results from roll is always a spanwise odd function. Thus, all odd coefficients in d_n are zero for a spanwise symmetric wing. If the ailerons produce an equal and opposite change on each semispan, the control surface distribution function is a spanwise odd function as well and all odd coefficients in c_n are also zero. With this **wing symmetry** the Fourier coefficients must satisfy the relations $a_n = b_n = 0$ for n even and $c_n = d_n = 0$ for n odd. Thus, Eq. (1.8.50) reduces to

$$A_n = \begin{cases} a_n(\alpha - \alpha_{L0})_{\text{root}} - b_n\Omega, & n \text{ odd} \\ c_n\delta_a + d_n\bar{p}, & n \text{ even} \end{cases} \quad (1.8.74)$$

Using the Fourier coefficients from Eq. (1.8.74) in Eq. (1.8.73), the **yawing moment coefficient with the wing symmetry described above** is given by

$$C_n = \frac{C_L}{8}[6c_2\delta_a - (1 - 6d_2)\bar{p}] + \frac{\pi R_A}{8}[10c_2\delta_a - (1 - 10d_2)\bar{p}][a_3(\alpha - \alpha_{L0})_{\text{root}} - b_3\Omega] \\ + \frac{\pi R_A}{4} \left[\sum_{n=4}^N (2n-1)[a_{n-1}(\alpha - \alpha_{L0})_{\text{root}} - b_{n-1}\Omega](c_n\delta_a + d_n\bar{p}) \right]_{n \text{ even}} \quad (1.8.75) \\ + \frac{\pi R_A}{4} \left[\sum_{n=5}^N (2n-1)(c_{n-1}\delta_a + d_{n-1}\bar{p})[a_n(\alpha - \alpha_{L0})_{\text{root}} - b_n\Omega] \right]_{n \text{ odd}}$$

For the special case of a **symmetric wing operating with optimum washout**, which is specified by Eq. (1.8.42), $a_n(\alpha - \alpha_{L0})_{\text{root}} - b_n\Omega$ is always zero for $n > 1$ and

$$C_n = C_{n,\delta_a}\delta_a + C_{n,\bar{p}}\bar{p}, \quad C_{n,\delta_a} = \frac{3C_L}{4}c_2, \quad C_{n,\bar{p}} = -\frac{C_L}{8}(1 - 6d_2) \quad (1.8.76)$$

For wings without optimum washout, the higher-order terms in Eq. (1.8.75) are not too large and the linear relation from Eq. (1.8.76) can be used as a rough approximation.

By comparing Eq. (1.8.59) with Eq. (1.8.76) we find that **within the accuracy of Eq. (1.8.76)**, the yawing moment can be expressed in terms of the rolling moment and the rolling rate,

$$C_n = -\frac{3C_L}{\pi R_A}C_\ell - \frac{C_L}{8}\bar{p} \quad (1.8.77)$$

When an airplane responds to aileron input, the rolling rate quickly reaches the steady-state value, which results in no rolling moment. Thus, we see from Eq. (1.8.77) that the magnitude of the steady yawing moment produced by aileron deflection is proportional to the lift coefficient developed by the wing and the steady rolling rate that develops as a

result of the aileron deflection. From Eq. (1.8.77), we can also see that the sign of the yawing moment, which is induced on a wing by aileron deflection, is opposite to that of the rolling moment induced by the same aileron deflection. Positive aileron deflection induces a wing rolling moment to the left and a wing yawing moment to the right. For this reason, the yawing moment induced on the wing by aileron deflection is commonly called *adverse yaw*. We can also see from Eq. (1.8.77) that adverse yaw is more pronounced at low airspeeds, which require higher values of C_L .

EXAMPLE 1.8.3. The rectangular wing of aspect ratio 8.0, which was described in Example 1.8.1, has ailerons with sealed hinges that extend from the spanwise coordinate $z/b = \pm 0.25$ to $z/b = \pm 0.45$. The aileron chord length is constant and equal to 18 percent of the wing chord. Estimate the rolling and yawing moment coefficients that would be induced on this wing by a 5-degree deflection of these ailerons when the wing is operating at the design lift coefficient of 0.4 and there is no rolling rate. What steady dimensionless rolling rate could be sustained by this aileron deflection?

Solution. Since $c_f/c = 0.18$, from Fig. 1.7.4, the hinge efficiency for these sealed flaps is estimated to be 0.85. Because the flap deflection is less than 10 degrees, from Fig. 1.7.5, a deflection efficiency of 1.0 is used. Thus, by using Eqs. (1.7.5) and (1.7.6) in Eq. (1.7.13), the section flap effectiveness for these ailerons is constant and given by

$$\theta_f = \cos^{-1}\left(2\frac{c_f}{c} - 1\right) = 2.265, \quad \varepsilon_f = (0.85)(1.0)\left[1 - \frac{\theta_f - \sin(\theta_f)}{\pi}\right] = 0.445$$

With this result, the control surface distribution function from Eq. (1.8.48) is

$$\chi(z) \equiv \begin{cases} 0.000, & z/b < -0.45 \\ 0.445, & -0.45 < z/b < -0.25 \\ 0.000, & -0.25 < z/b < 0.25 \\ -0.445, & 0.25 < z/b < 0.45 \\ 0.000, & z/b > 0.45 \end{cases}$$

In view of Eq. (1.8.53), the Fourier coefficients, c_n , are obtained from

$$\begin{bmatrix} C_{11} & C_{12} & C_{13} & \cdots & C_{1N} \\ C_{21} & C_{22} & C_{23} & \cdots & C_{2N} \\ C_{31} & C_{32} & C_{33} & \cdots & C_{3N} \\ \vdots & \vdots & \vdots & \ddots & \vdots \\ C_{N1} & C_{N2} & C_{N3} & \cdots & C_{NN} \end{bmatrix} \begin{bmatrix} c_1 \\ c_2 \\ c_3 \\ \vdots \\ c_N \end{bmatrix} = \begin{bmatrix} \chi(\theta_1) \\ \chi(\theta_2) \\ \chi(\theta_3) \\ \vdots \\ \chi(\theta_N) \end{bmatrix}$$

where $[C]$ is the same matrix as that used in Example 1.8.1. For $N = 99$, this gives

82 Chapter 1 Overview of Aerodynamics

$$\begin{Bmatrix} c_1 \\ c_2 \\ c_3 \\ c_4 \\ \vdots \\ c_{98} \\ c_{99} \end{Bmatrix} = [\mathbf{C}]^{-1} \begin{Bmatrix} \chi(\theta_1) \\ \chi(\theta_2) \\ \chi(\theta_3) \\ \chi(\theta_4) \\ \vdots \\ \chi(\theta_{98}) \\ \chi(\theta_{99}) \end{Bmatrix} = \begin{Bmatrix} 0 \\ 0.03853294 \\ 0 \\ 0.00335119 \\ \vdots \\ -0.00001777 \\ 0 \end{Bmatrix}$$

From Eq. (1.8.60), the change in the rolling moment coefficient with respect to aileron deflection is

$$C_{\ell, \delta_a} = -\frac{\pi R_A}{4} c_2 = -\frac{\pi(8.0)}{4} 0.0385 = -0.242$$

and from Eq. (1.8.59) with no rolling rate,

$$C_\ell = C_{\ell, \delta_a} \delta_a = -0.242 \frac{5.0\pi}{180} = \underline{-0.0211}$$

Since this wing has optimum washout for this lift coefficient, from Eq. (1.8.77),

$$C_n = -\frac{3C_L}{\pi R_A} C_\ell = -\frac{3(0.4)}{\pi(8.0)} (-0.0211) = \underline{0.00101}$$

This result applies only for the case of optimum washout, which in this case requires 4.64 degrees of elliptic washout. For the same wing planform with no washout, carrying the higher-order terms using either Eq. (1.8.73) or (1.8.75) gives $C_n = 0.00123$, and with 4.5 degrees of linear washout we get $C_n = 0.00087$.

Similarly, the coefficients, d_n , are evaluated from Eq. (1.8.54) and the change in the rolling moment with respect to rolling rate is found from Eq. (1.8.61):

$$\begin{Bmatrix} d_1 \\ d_2 \\ d_3 \\ d_4 \\ \vdots \\ d_{98} \\ d_{99} \end{Bmatrix} = [\mathbf{C}]^{-1} \begin{Bmatrix} \cos(\theta_1) \\ \cos(\theta_2) \\ \cos(\theta_3) \\ \cos(\theta_4) \\ \vdots \\ \cos(\theta_{98}) \\ \cos(\theta_{99}) \end{Bmatrix} = \begin{Bmatrix} 0 \\ 0.09411716 \\ 0 \\ 0.01326130 \\ \vdots \\ 0.00000241 \\ 0 \end{Bmatrix}, \quad C_{\ell, \bar{p}} = -\frac{\pi R_A}{4} d_2 = -0.591$$

Setting the net rolling moment coefficient to zero, Eq. (1.8.59) is solved for the steady dimensionless rolling rate:

$$\bar{p}_{\text{steady}} = -(C_{\ell, \delta_a} / C_{\ell, \bar{p}}) \delta_a = -(-0.242 / -0.591)(5.0\pi / 180) = \underline{-0.0357}$$

Wing Aspect Ratio and Geometric Mean Chord Length

We have seen that the aspect ratio of a finite wing has a profound effect on the wing’s performance. As defined in Eq. (1.8.5), the aspect ratio for a wing of arbitrary planform can be computed as the square of the wingspan divided by the planform area,

$$R_A \equiv \frac{b^2}{S} \tag{1.8.78}$$

In a more general sense, aspect ratio is defined to be the ratio of the longer to the shorter dimension for any two-dimensional shape. The aspect ratio of a rectangle is simply the length of the long side divided by the length of the short side. Thus, the **aspect ratio of a rectangular wing** having a constant chord, c , and wingspan, b , can be defined as

$$R_A \equiv \frac{b}{c} \tag{1.8.79}$$

Because the planform area of a rectangular wing is simply the wingspan multiplied by the chord length, $S = bc$, the definitions given in Eqs. (1.8.78) and (1.8.79) are equivalent. For the more general case of a wing having a chord length that varies with the spanwise coordinate, z , the aspect ratio can be written as the ratio of the wingspan to the average or *mean chord length*, \bar{c} ,

$$R_A \equiv \frac{b}{\bar{c}} \tag{1.8.80}$$

where, by equating the definitions of aspect ratio in Eqs. (1.8.78) and (1.8.80), we see that the **mean chord length** is defined as

$$\bar{c} \equiv \frac{S}{b} = \frac{1}{b} \int_{z=-b/2}^{b/2} c(z) dz \tag{1.8.81}$$

Because the wing aspect ratio defined by Eq. (1.8.78) has such a profound effect on wing performance, **both the wingspan and the mean chord length defined by Eq. (1.8.81) are important characteristic length scales for a finite wing.**

For a wing with linear taper, the planform area is one half the sum of the root chord and the tip chord multiplied by the wingspan. Thus, the mean chord length for a **wing with linear taper** is

$$\bar{c} = \frac{1}{b} \int_{z=-b/2}^{b/2} \left[c_{\text{root}} - (c_{\text{root}} - c_{\text{tip}}) \left| \frac{2z}{b} \right| \right] dz = \frac{c_{\text{root}} + c_{\text{tip}}}{2} = \frac{1 + R_T}{2} c_{\text{root}} \tag{1.8.82}$$

For an **elliptic wing** the mean chord length is

$$\bar{c} = \frac{1}{b} \int_{z=-b/2}^{b/2} c_{\text{root}} \sqrt{1 - \left(\frac{2z}{b} \right)^2} dz = \frac{\pi}{4} c_{\text{root}} \tag{1.8.83}$$

84 Chapter 1 Overview of Aerodynamics

Wing Camber and Mean Aerodynamic Chord

Because section lift does not contribute to the pitching moment about the lifting line of an unswept wing, the pitching moment coefficient about the wing's lifting line depends only on wing camber. From the definitions of wing and airfoil moment coefficients, the pitching moment coefficient about the origin of the coordinate system in Fig. 1.8.5 is

$$C_{m_0} = \frac{1}{S c_{ref}} \int_{z=-b/2}^{b/2} \tilde{C}_{mac} c^2 dz \quad (1.8.84)$$

where \tilde{C}_{mac} is the section moment coefficient about the section aerodynamic center and c_{ref} is the reference chord length used to define the wing pitching moment coefficient. For **wings with no control surface deflection or any other form of aerodynamic twist**, the section moment coefficient is constant over the wingspan and Eq. (1.8.84) becomes

$$C_{m_0} = \frac{\tilde{C}_{mac}}{S c_{ref}} \int_{z=-b/2}^{b/2} c^2 dz \quad (1.8.85)$$

Equation (1.8.85) leads to the definition of a characteristic length scale associated with wing camber, which is typically referred to as the **mean aerodynamic chord**

$$\bar{c}_{mac} \equiv \frac{1}{S} \int_{z=-b/2}^{b/2} c^2 dz \quad (1.8.86)$$

For **wings with linear taper** the mean aerodynamic chord and its location are given by

$$\bar{c}_{mac} = \frac{2}{3} \frac{1 + R_T + R_T^2}{1 + R_T} c_{root}, \text{ located at } \frac{z_{mac}}{b} = \frac{1}{6} \frac{1 + 2R_T}{1 + R_T} \quad (1.8.87)$$

For **wings of elliptic planform** Eq. (1.8.86) results in

$$\bar{c}_{mac} = \frac{8}{3\pi} c_{root}, \text{ located at } \frac{z_{mac}}{b} = \frac{1}{6\pi} \sqrt{9\pi^2 - 64} \quad (1.8.88)$$

Both \bar{c} and \bar{c}_{mac} are commonly used as the reference length for defining the wing pitching moment coefficient. In this textbook \bar{c} is used for this purpose. This choice is completely arbitrary. To convert any moment coefficient based on \bar{c} to that based on \bar{c}_{mac} , we simply multiply by the ratio \bar{c}/\bar{c}_{mac} , which is typically slightly less than unity. For example, the geometric relations for **wings with linear taper** produce the result

$$\bar{c}/\bar{c}_{mac} = 3(1 + R_T)^2 / [4(1 + R_T + R_T^2)] \quad (1.8.89)$$

which for taper ratios of 1.0 and 0.5 yields $\bar{c}/\bar{c}_{mac} = 1.00$ and $\bar{c}/\bar{c}_{mac} \cong 0.96$, respectively. For the **elliptic planform** the ratio \bar{c}/\bar{c}_{mac} is

$$\bar{c}/\bar{c}_{mac} = 3\pi^2/32 \cong 0.93 \quad (1.8.90)$$

The Basic and Additional Section Lift Distributions

For many applications in aircraft design it is important to know how the lift is distributed over the span of a wing. From Eq. (1.8.3) combined with the vortex lifting law, lifting-line theory predicts that the spanwise variation in section lift for an unswept wing is

$$\tilde{L}(\theta) = \rho V_\infty \Gamma(\theta) = 2b\rho V_\infty^2 \sum_{n=1}^{\infty} A_n \sin(n\theta), \quad \theta = \cos^{-1}(-2z/b) \quad (1.8.91)$$

Thus, the spanwise variation in local section lift coefficient is given by

$$\tilde{C}_L(\theta) \equiv \frac{\tilde{L}(\theta)}{\frac{1}{2}\rho V_\infty^2 c(\theta)} = \frac{4b}{c(\theta)} \sum_{n=1}^{\infty} A_n \sin(n\theta) \quad (1.8.92)$$

The Fourier coefficients, A_n , in Eq. (1.8.92) can be written using the change of variables given by Eq. (1.8.19),

$$A_n \equiv a_n(\alpha - \alpha_{L0})_{\text{root}} - b_n \Omega$$

Furthermore, after applying Eqs. (1.8.26) and (1.8.28) to Eq. (1.8.24), we have

$$C_L = \pi R_A [a_1(\alpha - \alpha_{L0})_{\text{root}} - b_1 \Omega]$$

or after solving for the root aerodynamic angle of attack

$$(\alpha - \alpha_{L0})_{\text{root}} = \frac{b_1}{a_1} \Omega + \frac{C_L}{\pi R_A a_1} \quad (1.8.93)$$

Using Eq. (1.8.93) in Eq. (1.8.19) yields

$$A_n = \left(\frac{b_1 a_n}{a_1} - b_n \right) \Omega + \frac{a_n}{\pi R_A a_1} C_L \quad (1.8.94)$$

Using this change of variables, Eq. (1.8.92) can be written as

$$\tilde{C}_L(\theta) = \Omega \sum_{n=1}^{\infty} 4 \left(\frac{b_1 a_n}{a_1} - b_n \right) \frac{\sin(n\theta)}{c(\theta)/b} + C_L \sum_{n=1}^{\infty} \frac{4a_n}{\pi R_A a_1} \frac{\sin(n\theta)}{c(\theta)/b} \quad (1.8.95)$$

We see from Eq. (1.8.95) that the spanwise variation in local section lift coefficient can be divided conveniently into two components. The first term on the right-hand side of Eq. (1.8.95) is called the *basic section lift coefficient* and the second term is called the *additional section lift coefficient*. The basic section lift coefficient is independent of C_L and directly proportional to the total amount of wing twist, Ω . The additional section lift coefficient at any section of the wing is independent of wing twist and directly proportional to the net wing lift coefficient, C_L .

As can be seen from Eq. (1.8.95), **the basic section lift coefficient is the spanwise variation in local section lift coefficient that occurs when the total net lift developed by the wing is zero.** Examination of the first term on the right-hand side of Eq. (1.8.95) reveals that the basic section lift coefficient depends on all of the Fourier coefficients a_n and b_n . From Eq. (1.8.20) we see the Fourier coefficients a_n depend only on the wing planform. Equation (1.8.21) shows that the Fourier coefficients b_n depend on both the wing planform and the dimensionless twist distribution function, $\omega(\theta)$. Thus, **the spanwise variation in the basic section lift coefficient depends on wing planform and wing twist but is independent of the wing's angle of attack.**

Examination of the second term on the right-hand side of Eq. (1.8.95) discloses that the additional section lift coefficient depends only on the wing planform and the Fourier coefficients a_n . From Eq. (1.8.20) we have seen that the coefficients a_n do not depend on wing twist. Thus, for an unswept wing, Eq. (1.8.95) exposes the important fact that **the additional section lift coefficient is independent of wing twist.** Because the basic section lift coefficient is zero for an untwisted wing, we see that **the additional section lift coefficient is equivalent to the spanwise variation in local section lift coefficient that would be developed on an untwisted wing of the same planform operating at the same wing lift coefficient.**

Figure 1.8.26 shows how the net section lift coefficient and its two components obtained from Eq. (1.8.95) vary along the span of an unswept wing with linear taper of aspect ratio 8.0 and taper ratio 0.5. This figure shows the spanwise variation in wing section lift coefficient for several values of total linear twist with the net wing lift coefficient held constant at 1.0. Similar results are shown in Fig. 1.8.27 for three different values of wing lift coefficient with total linear twist held constant at 6 degrees. Notice that whereas the center of total lift on each semispan of this wing moves inboard

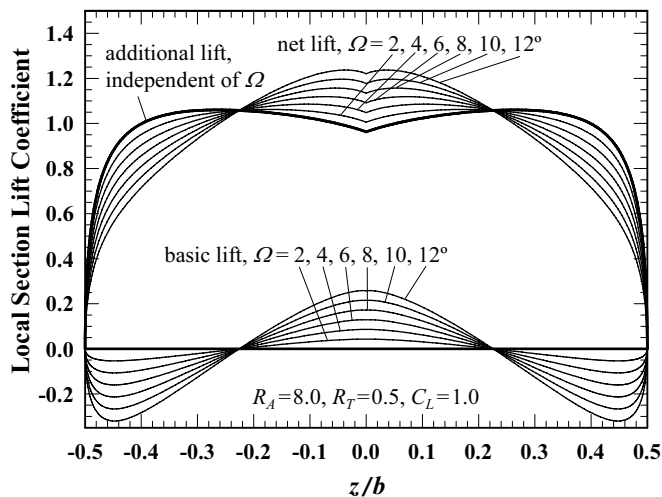


Figure 1.8.26. Spanwise variation in local section lift coefficient as a function of the total amount of linear twist with the net wing lift coefficient held constant at $C_L = 1.0$.

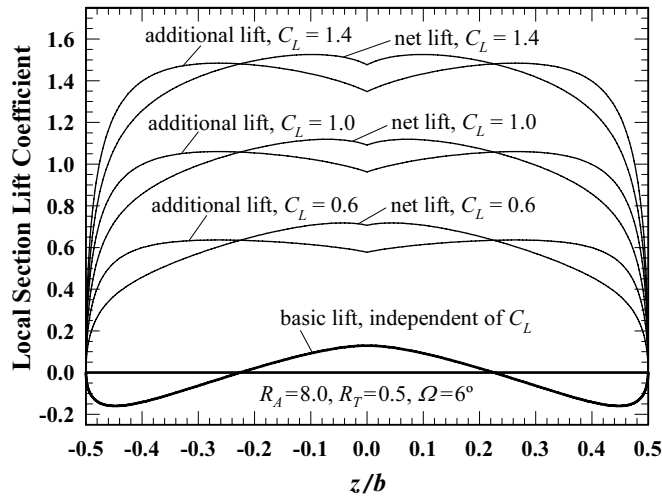


Figure 1.8.27. Spanwise variation in local section lift coefficient as a function of the net wing lift coefficient with the total amount of linear twist held constant at $\Omega = 6^\circ$.

as washout is increased, the center of additional lift on each semispan does not change with either the amount of wing twist or the net wing lift coefficient.

Here \tilde{C}_{L_b} will be used to signify the **basic section lift coefficient**,

$$\tilde{C}_{L_b}(\theta) \equiv \Omega \sum_{n=1}^{\infty} 4 \left(\frac{b_1 a_n}{a_1} - b_n \right) \frac{\sin(n\theta)}{c(\theta)/b} \quad (1.8.96)$$

and \tilde{C}_{L_a} will be used to denote the **additional section lift coefficient**,

$$\tilde{C}_{L_a}(\theta) \equiv C_L \sum_{n=1}^{\infty} \frac{4a_n}{\pi R_A a_1} \frac{\sin(n\theta)}{c(\theta)/b} \quad (1.8.97)$$

The total section lift coefficient at any spanwise section of the wing is simply the sum of the basic and additional section lift coefficients,

$$\tilde{C}_L(\theta) = \tilde{C}_{L_b}(\theta) + \tilde{C}_{L_a}(\theta) \quad (1.8.98)$$

The important points to remember regarding these two components of lift are:

1. *The basic section lift coefficient is independent of angle of attack.*
2. *The additional section lift coefficient is independent of wing twist.*
3. *Both the basic and additional section lift coefficients depend on wing planform.*

88 Chapter 1 Overview of Aerodynamics

Semispan Aerodynamic Center and Moment Components

The spanwise distribution of section aerodynamic loads acting on each semispan of a finite wing can be replaced with a resultant force acting at the aerodynamic center of the semispan and a resultant moment that does not change with angle of attack. Because drag is typically small compared with the lift, drag is commonly neglected in estimating the position of the aerodynamic center. This traditional approximation is presented here. The effect of drag on the position of the aerodynamic center is considered in Chapter 4.

As a first approximation, the aerodynamic center of each wing semispan is sometimes assumed to be located at the section aerodynamic center of the airfoil section located at the spanwise coordinate of the semispan area centroid. Here the chord line that passes through the semispan area centroid is referred to as the *centroidal chord*. The spanwise coordinate of the wing semispan area centroid is given by

$$\bar{z}_c \equiv \frac{2}{S} \int_{z=0}^{b/2} cz \, dz \quad (1.8.99)$$

For **wings with constant linear taper**, i.e., trapezoidal wings, Eq. (1.8.99) results in

$$\frac{\bar{z}_c}{b} = \frac{1}{6} \frac{1+2R_T}{1+R_T} \quad (1.8.100)$$

For **wings of elliptic planform**, the spanwise coordinate of the semispan centroid is

$$\frac{\bar{z}_c}{b} = \frac{2}{3\pi} \quad (1.8.101)$$

The location specified by Eq. (1.8.100) is commonly referred to as the location of the mean aerodynamic chord. Referring to the centroidal chord of a trapezoidal wing as the mean aerodynamic chord can be misleading, because it could be taken to imply that the location of the mean aerodynamic chord is significant for other wing geometries as well. However, the mean aerodynamic chord passes through the semispan centroid only for the special case of a trapezoidal wing. For example, the mean aerodynamic chord of an elliptic wing is located according to Eq. (1.8.88) at $z_{mac}/b \cong 0.264$, whereas the location of the centroidal chord is given by Eq. (1.8.101) as $\bar{z}_c/b \cong 0.212$.

In general, the semispan aerodynamic center of a wing is not located along either the centroidal chord or the mean aerodynamic chord. For example, Fig. 1.8.28 shows the aerodynamic center, centroidal chord, and mean aerodynamic chord for several different semispan geometries. Equation (1.8.99) gives the true spanwise location of the semispan aerodynamic center only if the additional section lift coefficient is uniform across the wingspan. Because a uniform additional section lift coefficient is produced by an elliptic wing with no sweep or dihedral in the locus of airfoil section aerodynamic centers, the semispan aerodynamic center of such wings is located along the centroidal chord as specified by Eq. (1.8.101). However, wings with linear taper do not produce a uniform additional section lift coefficient. **Thus, Eq. (1.8.100) should be used only as a rough estimate for the semispan aerodynamic center of a trapezoidal wing.**

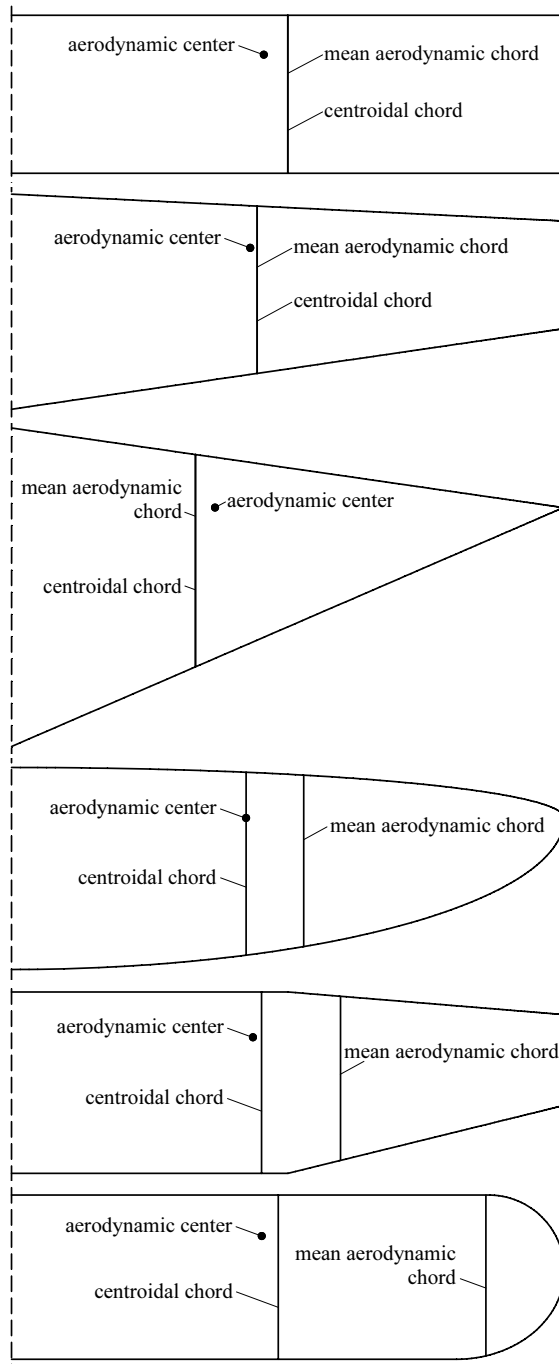


Figure 1.8.28. The aerodynamic center, centroidal chord, and mean aerodynamic chord for six different semispan geometries, all having the same aspect ratio and no quarter-chord sweep.

90 Chapter 1 Overview of Aerodynamics

A more accurate estimate for the location of the semispan aerodynamic center of a wing with no sweep or dihedral in the locus of wing section aerodynamic centers can be obtained from Eqs. (1.8.96) through (1.8.98). Because we are neglecting drag, the resultant aerodynamic moment produced on each semispan of a wing about the origin of the coordinate system shown in Fig. 1.8.5 can be resolved into a pitching component about the z -axis and a rolling component about the freestream velocity vector.

Because section lift does not contribute to the pitching moment about the wing's lifting line, the contribution of the left semispan of an unswept wing to the pitching moment coefficient about the origin of the coordinate system shown in Fig. 1.8.5 is

$$(C_{m_0})_{\text{left}} = \frac{1}{S c_{\text{ref}}} \int_{z=0}^{b/2} \tilde{C}_{m_{ac}} c^2 dz \quad (1.8.102)$$

The moment coefficient specified by Eq. (1.8.102) is also the root twisting moment coefficient resulting from the aerodynamic load on this unswept wing. This moment results only from the effects of wing camber and is independent of geometric twist. For a wing with constant section pitching moment coefficient, Eq. (1.8.102) yields

$$(C_{m_0})_{\text{left}} = \frac{\bar{c}_{m_{ac}}}{c_{\text{ref}}} \frac{\tilde{C}_{m_{ac}}}{2} \quad (1.8.103)$$

In a more general sense, Eq. (1.8.102) could be thought of in terms of a mean section pitching moment coefficient,

$$(C_{m_0})_{\text{left}} = \frac{\bar{c}_{m_{ac}}}{c_{\text{ref}}} \frac{\bar{\tilde{C}}_{m_{ac}}}{2}, \quad \bar{\tilde{C}}_{m_{ac}} \equiv \frac{2}{S \bar{c}_{m_{ac}}} \int_{z=0}^{b/2} \tilde{C}_{m_{ac}} c^2 dz \quad (1.8.104)$$

The contribution of the left wing semispan to the rolling moment coefficient about the origin of the coordinate system shown in Fig. 1.8.5 is

$$(C_{\ell_0})_{\text{left}} = \frac{1}{Sb} \int_{z=0}^{b/2} \tilde{C}_L c z dz = \frac{1}{Sb} \int_{z=0}^{b/2} (\tilde{C}_{L_b} + \tilde{C}_{L_a}) c z dz \quad (1.8.105)$$

It is important to note that within the small-angle approximation, **the moment coefficient specified by Eq. (1.8.105) is the root bending moment coefficient resulting from the aerodynamic load on the wing semispan.** Equating the distributed wing-section loading to a resultant force and moment acting at the aerodynamic center of the wing semispan, we can also write

$$(C_{\ell_0})_{\text{left}} = (C_{\ell_{ac}})_{\text{left}} + \frac{\bar{z}_{ac}}{Sb} \int_{z=0}^{b/2} \tilde{C}_L c dz = (C_{\ell_{ac}})_{\text{left}} + \frac{\bar{z}_{ac}}{b} \frac{C_L}{2} \quad (1.8.106)$$

where $(C_{\ell_{ac}})_{\text{left}}$ is the left wing semispan rolling moment coefficient about the semispan aerodynamic center and \bar{z}_{ac} is the z -coordinate of the semispan aerodynamic center. Combining Eqs. (1.8.105) and (1.8.106) to eliminate the moment about the origin yields

1.8. Incompressible Flow over Finite Wings 91

$$(C_{\ell_{ac}})_{\text{left}} + \frac{\bar{z}_{ac}}{b} \frac{C_L}{2} = \frac{1}{Sb} \int_{z=0}^{b/2} (\tilde{C}_{L_b} + \tilde{C}_{L_a}) cz dz \quad (1.8.107)$$

Because the resultant moment about the aerodynamic center is invariant to small changes in angle of attack, differentiating Eq. (1.8.107) with respect to angle of attack, applying Eqs. (1.8.96) and (1.8.97), and solving for \bar{z}_{ac}/b gives

$$\begin{aligned} \frac{\bar{z}_{ac}}{b} &= \frac{2}{SbC_{L,\alpha}} \frac{\partial}{\partial \alpha} \int_{z=0}^{b/2} (\tilde{C}_{L_b} + \tilde{C}_{L_a}) cz dz = \frac{2}{SbC_{L,\alpha}} \frac{\partial}{\partial \alpha} \int_{z=0}^{b/2} \tilde{C}_{L_a} cz dz \\ &= \frac{-2}{\pi} \sum_{n=1}^{\infty} \frac{a_n}{a_1} \int_{\theta=\pi/2}^{\pi} \sin(n\theta) \cos \theta \sin \theta d\theta = \frac{1}{\pi} \sum_{n=1}^{\infty} \frac{a_n}{a_1} \int_{\theta=\pi}^{\pi/2} \sin(n\theta) \sin(2\theta) d\theta \end{aligned} \quad (1.8.108)$$

Because the additional section lift coefficient is independent of wing twist, Eq. (1.8.108) discloses the important fact that **the spanwise position of the aerodynamic center of the wing semispan is not affected by wing twist**. Recognizing that the even terms in a_n are always zero for spanwise symmetric wings, the integration in Eq. (1.8.108) yields

$$\frac{\bar{z}_{ac}}{b} = \frac{2}{3\pi} + \frac{2}{\pi} \sum_{n=3}^{\infty} \frac{\sin[(n-2)\pi/2]}{n^2-4} \frac{a_n}{a_1} = \frac{2}{3\pi} \left(1 + \sum_{n=1}^{\infty} \frac{(-1)^{n-1} 3}{4n^2 + 4n - 3} \frac{a_{2n+1}}{a_1} \right) \quad (1.8.109)$$

Figure 1.8.29 shows how \bar{z}_{ac}/b varies with taper ratio and aspect ratio for wings with linear taper. The reader should note from Fig. 1.8.29 that except for the special case of trapezoidal wings with a taper ratio near 0.35, **the spanwise location of the mean aerodynamic chord is not the semispan aerodynamic center**, as is commonly stated or implied in the literature. For example, with a linear taper ratio of 0.8 the mean aerodynamic chord is located at $z_{mac}/b \cong 0.24$, whereas the semispan aerodynamic center varies from about $\bar{z}_{ac}/b \cong 0.22$ to $\bar{z}_{ac}/b \cong 0.23$, depending on aspect ratio. Furthermore, the location of the semispan aerodynamic center also varies with wing sweep, whereas the spanwise location of the mean aerodynamic chord does not.

Using Eq. (1.8.97) in Eq. (1.8.108), it can be shown that the spanwise coordinate of the semispan aerodynamic center can also be expressed as

$$\bar{z}_{ac} = \frac{2}{SC_L} \int_{z=0}^{b/2} \tilde{C}_{L_a} cz dz \quad (1.8.110)$$

Using Eq. (1.8.110) in Eq. (1.8.105) yields

$$\begin{aligned} (C_{\ell_0})_{\text{left}} &= \frac{1}{Sb} \int_{z=0}^{b/2} \tilde{C}_{L_a} cz dz + \frac{1}{Sb} \int_{z=0}^{b/2} \tilde{C}_{L_b} cz dz \\ &= \frac{\bar{z}_{ac}}{b} \frac{C_L}{2} + \frac{1}{Sb} \int_{z=0}^{b/2} \tilde{C}_{L_b} cz dz \end{aligned} \quad (1.8.111)$$

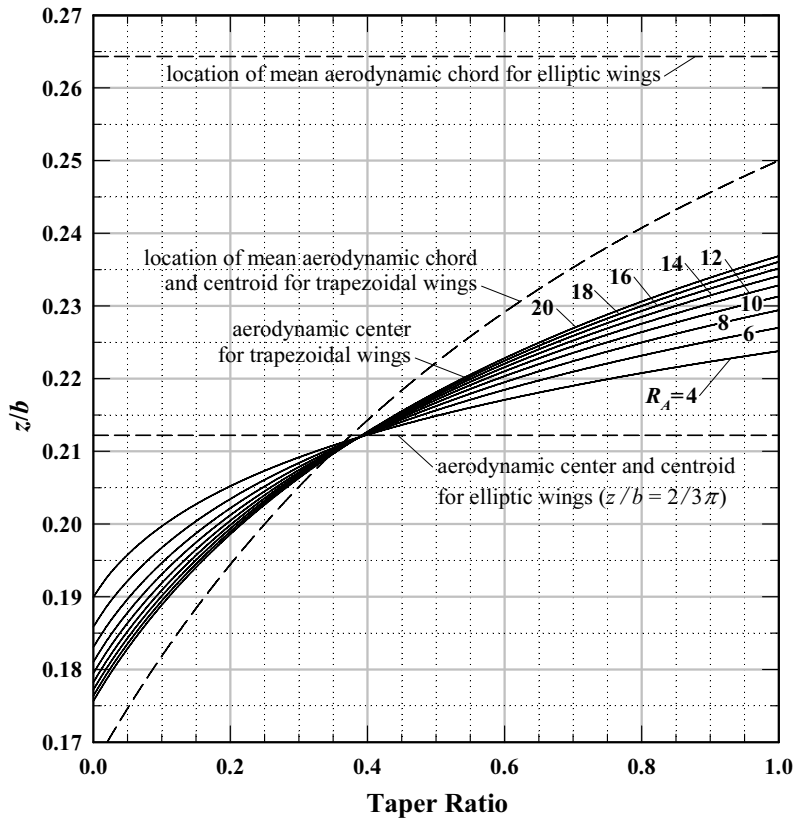


Figure 1.8.29. Aerodynamic center of semispan for unswept wings with linear taper.

For wings with no sweep or dihedral, the integral of the basic section lift coefficient on the right-hand side of Eq. (1.8.111) can be evaluated from Eq. (1.8.96). Following a development similar to that of Eq. (1.8.109) it is readily shown that for spanwise symmetric wings with spanwise symmetric twist, using Eq. (1.8.96) in Eq. (1.8.111) produces a useful relation for the **root wing bending moment coefficient**

$$(C_{\ell_0})_{\text{left}} = \frac{\bar{z}_{ac} C_L}{2b} - \kappa_{M\Omega} \frac{C_{L,\alpha} \Omega}{2} \quad (1.8.112)$$

where

$$\begin{aligned} \kappa_{M\Omega} &\equiv \frac{2}{\pi} \frac{b_1}{a_1} \sum_{n=3}^{\infty} \frac{\sin[(n-2)\pi/2]}{n^2-4} \left(\frac{b_n}{b_1} - \frac{a_n}{a_1} \right) \\ &= \frac{2}{\pi} \frac{b_1}{a_1} \sum_{n=1}^{\infty} \frac{(-1)^{n-1}}{4n^2+4n-3} \left(\frac{b_{2n+1}}{b_1} - \frac{a_{2n+1}}{a_1} \right) \end{aligned} \quad (1.8.113)$$

It is worth noting that the infinite series defined in Eq. (1.8.113) is dominated by the first term. In the case of a rectangular wing of aspect ratio 6.0, carrying only the first term on the right-hand side of Eq. (1.8.113) yields $\kappa_{M\Omega} = 0.024338$, whereas carrying 400 or more terms in this infinite series produces $\kappa_{M\Omega} = 0.024986$. For typical washout distributions $\kappa_{M\Omega}$ is positive. Figure 1.8.30 shows how $\kappa_{M\Omega}$ varies with taper ratio and aspect ratio for wings with constant linear taper and constant linear twist.

As expressed in Eq. (1.8.112), the root wing bending moment coefficient is composed of two components. The first is proportional to the semispan lift acting through a moment arm of \bar{z}_{ac} and the second is proportional to the product of the wing lift slope and the wing twist. For a given wing planform, the value of the proportionality constant $\kappa_{M\Omega}$ depends on the way in which the twist is distributed along the wingspan. This dependence enters into Eq. (1.8.113) through the Fourier coefficients b_n , which depend on the twist distribution through Eq. (1.8.21). For the typical case where washout is greatest near the wingtips, $\kappa_{M\Omega}$ is positive, as shown for the case of linear washout in Fig. 1.8.30. Thus, as might be expected, Eq. (1.8.112) shows that the root bending moment decreases linearly as washout is added at the wingtips. If a twist distribution were used that had the greatest washout near the wing root, then $\kappa_{M\Omega}$ would be negative and the root bending moment would increase in proportion to the amount of twist.

For a given planform and twist distribution, Eq. (1.8.112) shows that the change in bending moment with respect to Ω is directly proportional to the wing lift slope. This should be expected because $C_{L,\alpha}$ is a measure of the wing's lift response to a change in any aerodynamic angle, i.e., α , α_{L0} , or Ω . The lift slope for an unswept wing of arbitrary planform is given by Eq. (1.8.26) and is not affected by wing twist.

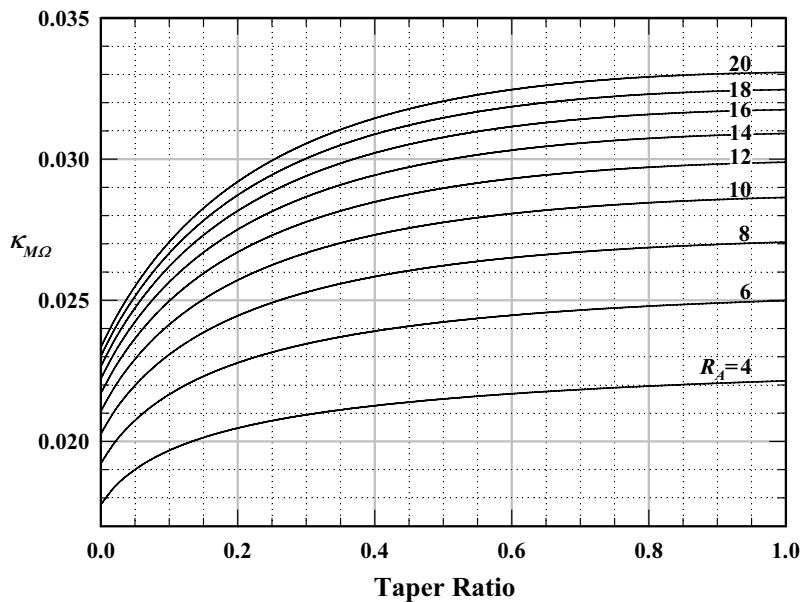


Figure 1.8.30. Twist factor for the root bending moment coefficient on wings with linear twist.

94 Chapter 1 Overview of Aerodynamics

An Alternative View of Downwash

From Prandtl's lifting-line theory we have seen that a finite lifting wing results in the generation of downwash. This downwash has a significant effect on the performance of the wing and other surfaces of an airplane. Mathematically, we have described the downwash and its effects in terms of vorticity and circulation. However, the student may find it easier to understand the physics of downwash when it is described in terms of pressure and momentum.

When an airplane flies overhead, the downwash produced by the lifting wing could be measured on the ground if instruments of sufficient sensitivity were available. This downwash can be viewed as a result of the momentum imparted to the air by the force of the airplane's weight. The weight of the airplane is carried directly by the pressure difference between the upper and lower surfaces of the wing. However, the air also feels this pressure difference. The net effect of the pressure difference on the air is that a force is applied to the air equal to the airplane's weight. From Newton's second law, we know that such a force must result in a downward momentum imparted to the air. As the air directly beneath the airplane moves down, viscous forces from the adjacent air may slow its downward motion. However, these same viscous forces act on the adjacent air to impart downward momentum to that air as well. Newton's second law requires that the total downward momentum of the air cannot change unless acted upon by an external force. Ultimately, the Earth will stop this downward momentum, which began as the downwash from the airplane wing. The final manifestation of the downwash produced by a lifting wing is a very small pressure rise over a very large area of the Earth. The net effect of this pressure rise integrated over the total affected area is a force applied to the surface of the Earth equal to the airplane weight. Whether the airplane is resting on the ground or flying at 40,000 feet, the surface of the Earth must ultimately support the total weight of the aircraft. Because the airplane is moving rapidly over the ground, the downwash is spread over a large area of the Earth and usually goes undetected.

The vortex model that we have used to describe the effects of downwash on a finite wing is based on inviscid flow. This model predicts that the vorticity shed from the wing and the associated downwash will extend an infinite distance behind the wing. In reality, viscous effects in the air will eventually dissipate the wingtip vortices. However, the net downward momentum associated with these vortices does not change as a result of this viscous dissipation. No matter how large the viscosity, this downward momentum will eventually reach the ground, where it produces an aerodynamic force equal to the airplane's weight.

1.9. Flow over Multiple Lifting Surfaces

Prandtl's classical lifting-line equation, expressed in Eq. (1.8.2), applies only to a single lifting surface with no sweep or dihedral. In the development of this relation it was assumed that the only downwash induced on the wing was that induced by the trailing vortex sheet, which is shed from the wing itself. Airplanes are usually designed with more than one lifting surface. A typical configuration could be a wing combined with horizontal and vertical stabilizers. Each of these surfaces can generate lift and vorticity. The vorticity that is generated by one lifting surface will alter the flow about another.

For example, a lifting wing will induce downwash on an aft horizontal stabilizer, and a lifting aft stabilizer will induce upwash on the main wing. Such lifting surface interactions are not accounted for in Eq. (1.8.2).

Even a flying wing cannot be analyzed using Eq. (1.8.2) if the wing has sweep or dihedral. In a wing with sweep and/or dihedral, the quarter-chord line on one semispan makes an angle with the quarter-chord line of the other semispan, as shown in Fig. 1.9.1. A wing is said to have *positive sweep* if the wing is swept back from the root to the tip, with the wingtips being aft of the root. A wing has *positive dihedral* if the wing slopes up from the root to the tip, with the wingtips being above the root. *Negative dihedral* is usually called *anhedral*. Because a wing can also have taper and/or geometric twist, defining the sweep and dihedral angles can be somewhat ambiguous. For a conventional tapered wing, the sweep angle for the leading edge is greater than that for the trailing edge. For a wing with geometric washout, the dihedral angle for the trailing edge is greater than that for the leading edge. Furthermore, neither the sweep nor the dihedral must remain constant over the semispan of a lifting surface. For this reason, local sweep and dihedral angles are defined in terms of the wing quarter-chord line and the orientation of the local streamwise airfoil section, as shown in Fig. 1.9.1.

When constant dihedral is added to a wing, each side of the wing is rotated about the root as a solid body. The rotation of the left-hand side is opposite to that of the right-hand side, so that both wingtips are raised above the root and brought closer together. Since dihedral is a solid-body rotation, the local airfoil sections rotate with the quarter-chord line. For a wing with no dihedral, a vector drawn normal to a local airfoil section is also normal to the aircraft plane of symmetry. As dihedral is added to the wing, both the quarter-chord line and the airfoil section normal are rotated upward, so that the normal to the local airfoil section always forms an angle equal to the dihedral angle with the normal to the aircraft plane of symmetry. For example, the vertical stabilizer of a conventional airplane usually has a dihedral angle of 90 degrees. For the rarely encountered case of an aircraft that does not have a plane of symmetry, the dihedral angle must be defined relative to some other defined reference plane.

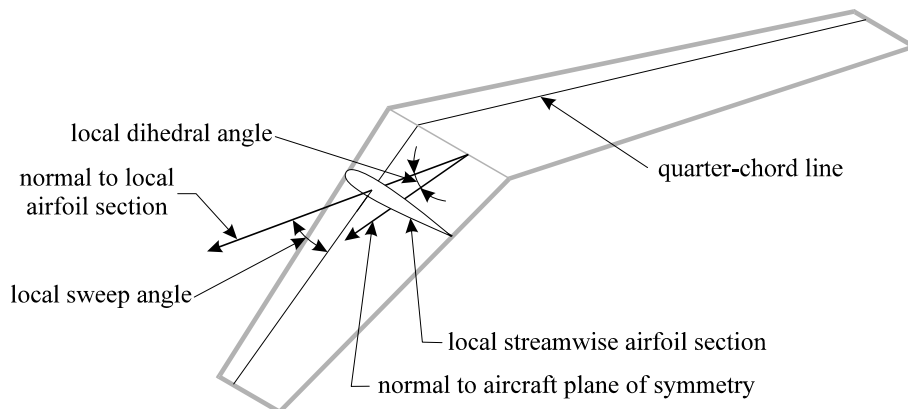


Figure 1.9.1. Local sweep and dihedral angles.

96 Chapter 1 Overview of Aerodynamics

Typically, for an airplane with fixed wings, constant sweep is not a solid-body rotation of each semispan. For a wing with no sweep, the normal to each local airfoil section is aligned with the wing quarter-chord line, and the quarter-chord line is straight. As constant positive sweep is added to a wing, the quarter-chord line for each semispan is rotated back, moving the wingtips aft of the root. However, for constant planform area and aspect ratio, the local airfoil sections are not rotated with the quarter-chord line. Each airfoil section is translated straight back to the new quarter-chord location and the length of the quarter-chord line is increased, so that the distance from wingtip to wingtip does not change. A local sweep angle can be defined as the angle between the normal to the streamwise airfoil section and the quarter-chord line. Thus, the sweep angle for a wing with no dihedral is measured relative to a horizontal line, while the sweep angle for a vertical stabilizer with 90 degrees dihedral is measured relative to a vertical line.

Supersonic airplanes are sometimes designed with wings that can be rotated to vary the sweep angle in flight. This type of sweep variation is solid-body rotation. However, varying sweep in this manner changes not only the sweep but the shape of the streamwise airfoil section, the wingspan, and usually even the planform area of the wing.

Most airplanes are designed with some sweep and/or dihedral in the wing and/or the horizontal and vertical stabilizers. While the reasons for using sweep and dihedral will be left for a later discussion, it is clear from looking at the myriad of airplanes parked at any airport that a means for analyzing the effects of sweep and dihedral is needed. In addition, the downwash created by one lifting surface, such as the wing, has a dramatic effect on the performance of other lifting surfaces, such as the horizontal stabilizer. Thus, a means for predicting the effects of such interactions is also needed.

To predict the aerodynamic forces and moments acting on a complete airplane in flight, three-dimensional panel codes and CFD analysis are often used. However, these methods are very computationally intensive and may not be suitable for use in an undergraduate course on flight mechanics. An alternative method that provides an excellent educational tool at very low computational cost is the numerical lifting-line method, which is presented here.

The Numerical Lifting-Line Method

In developing Prandtl's lifting-line equation, a single lifting surface with no sweep or dihedral was assumed. The lifting line was confined to the z -axis and the trailing vortex sheet was assumed to be in the x - z plane (see Fig. 1.8.5). This significantly simplified the expressions for downwash and induced angle of attack. In order to use lifting-line theory to study the effects of sweep, dihedral, and/or the interactions between lifting surfaces, the theory must be generalized to allow for an arbitrary position and orientation of both the lifting line and the trailing vortex sheet. Here we shall examine a numerical lifting-line method that can be used to obtain a potential flow solution for the forces and moments acting on a system of lifting surfaces, each with arbitrary position and orientation. For a detailed development of this numerical method and a comparison with panel codes, CFD, and experimental data, see Phillips and Snyder (2000).

A first-order numerical lifting-line method can be obtained by synthesizing a system of lifting surfaces using a composite of horseshoe-shaped vortices. The continuous distribution of bound vorticity over the surface of each lifting surface, as well as the

continuous distribution of free vorticity in the trailing vortex sheets, is approximated by a finite number of discrete horseshoe vortices, as shown in Fig. 1.9.2.

The bound portion of each horseshoe vortex is placed coincident with the *locus of wing section aerodynamic centers* called the *lifting line*, which is aligned with the local sweep and dihedral. As a first approximation, the lifting line is usually assumed to be the wing quarter-chord line. The trailing portion of each horseshoe vortex is aligned with the trailing vortex sheet. In Fig. 1.9.2, a small gap is shown between the left-hand trailing segment of one horseshoe vortex and the right-hand trailing segment of the next. This is for display purposes only. In reality, the left-hand corner of one horseshoe and the right-hand corner of the next are both placed at the same point. Thus, except at the wingtips, each trailing vortex segment is coincident with another trailing segment from the adjacent vortex. If two adjacent vortices have exactly the same strength, then the two coincident trailing segments exactly cancel, since one has clockwise rotation and the other has counterclockwise rotation. The net vorticity that is shed from the wing at any internal node is simply the difference in strength of the two adjacent vortices that share the node.

Each horseshoe vortex is composed of three straight segments, a finite bound segment and two semi-infinite trailing segments. From Eqs. (1.5.18) and (1.5.19), we can calculate the velocity induced at an arbitrary point in space (x, y, z) by a general horseshoe vortex. As shown in Fig. 1.9.3, a general horseshoe vortex is completely defined by two nodal points, (x_1, y_1, z_1) and (x_2, y_2, z_2) , a trailing unit vector, \mathbf{u}_∞ , and a vortex strength, Γ . The horseshoe vortex starts at the fluid boundary, an infinite distance downstream. The inbound trailing vortex segment is directed along the vector $-\mathbf{u}_\infty$ to node 1 at (x_1, y_1, z_1) . The bound vortex segment is directed along the wing lifting line from node 1 to node 2 at (x_2, y_2, z_2) . The outbound trailing vortex segment is directed along the vector \mathbf{u}_∞ from node 2 to the fluid boundary, an infinite distance back downstream. The velocity induced by the entire horseshoe vortex is simply the vector sum of the velocities induced by each of the three linear segments that make up the horseshoe.

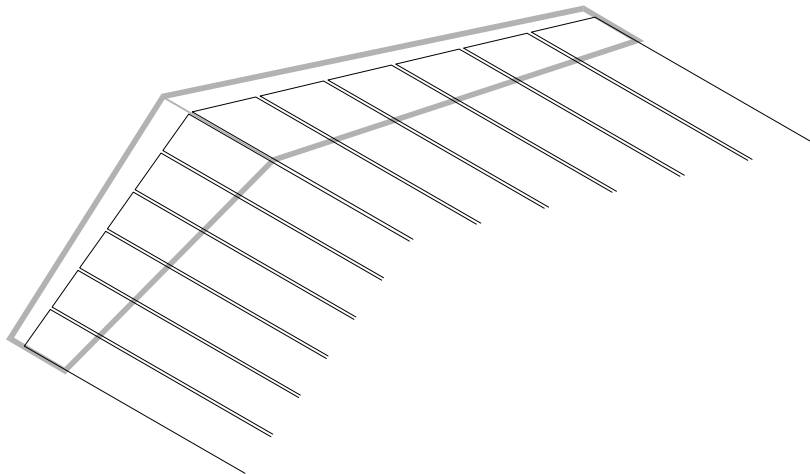


Figure 1.9.2. Horseshoe vortices distributed over the span of a wing with sweep and dihedral.

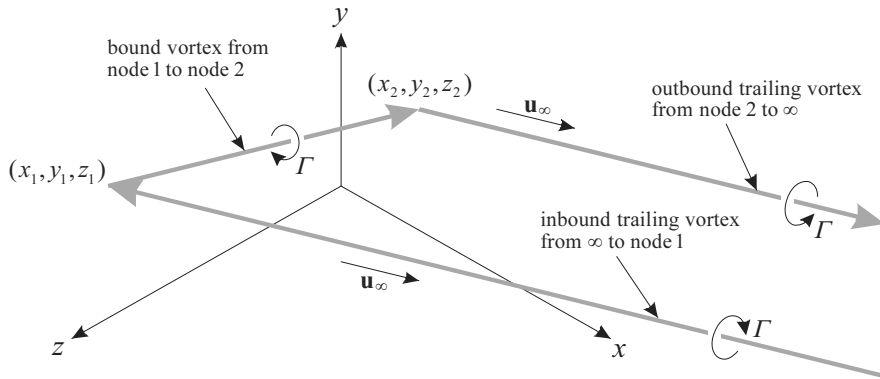


Figure 1.9.3. General horseshoe vortex.

In Eq. (1.5.19) the vorticity vector is assumed to point in the direction of \mathbf{u}_∞ as determined by the right-hand rule. However, the inbound trailing vortex segment can be treated like an outbound segment with negative circulation. Thus, from Eqs. (1.5.18) and (1.5.19), the **velocity vector induced at an arbitrary point in space by a complete horseshoe vortex** is

$$\mathbf{V} = \frac{\Gamma}{4\pi} \left[\frac{\mathbf{u}_\infty \times \mathbf{r}_2}{r_2(r_2 - \mathbf{u}_\infty \cdot \mathbf{r}_2)} + \frac{(r_1 + r_2)(\mathbf{r}_1 \times \mathbf{r}_2)}{r_1 r_2 (r_1 r_2 + \mathbf{r}_1 \cdot \mathbf{r}_2)} - \frac{\mathbf{u}_\infty \times \mathbf{r}_1}{r_1(r_1 - \mathbf{u}_\infty \cdot \mathbf{r}_1)} \right] \quad (1.9.1)$$

where \mathbf{u}_∞ is the unit vector in the direction of the trailing vortex sheet, \mathbf{r}_1 is the spatial vector from (x_1, y_1, z_1) to (x, y, z) , and \mathbf{r}_2 is the spatial vector from (x_2, y_2, z_2) to (x, y, z) ,

$$\mathbf{r}_1 = (x - x_1)\mathbf{i}_x + (y - y_1)\mathbf{i}_y + (z - z_1)\mathbf{i}_z \quad (1.9.2)$$

$$\mathbf{r}_2 = (x - x_2)\mathbf{i}_x + (y - y_2)\mathbf{i}_y + (z - z_2)\mathbf{i}_z \quad (1.9.3)$$

In obtaining the classical lifting-line solution for a single wing without sweep or dihedral, the trailing vortex sheet was assumed to be aligned with the wing chord. This was done to facilitate obtaining an analytical solution. In obtaining a numerical solution, there is little advantage in aligning the trailing vortex sheet with a vehicle axis such as the chord line. More correctly, the trailing vortex sheet should be aligned with the freestream. This is easily done in the numerical solution by setting \mathbf{u}_∞ equal to the unit vector in the direction of the freestream. When using this method to predict the forces and moments on a single lifting surface, there is very little difference between the results obtained from slightly different orientations of the trailing vortex sheet.

When a system of lifting surfaces is synthesized using N of these horseshoe vortices, in a manner similar to that shown in Fig. 1.9.2, Eq. (1.9.1) can be used to determine the resultant velocity induced at any point in space if the vortex strength of each horseshoe

vortex is known. However, these strengths are not known a priori. To compute the strengths of the N vortices, we must have a system of N equations relating these N strengths to some known properties of the wing. For these relations we turn to the three-dimensional vortex lifting law given in Eq. (1.8.1).

If flow over a finite wing is synthesized from a uniform flow combined with horseshoe vortices placed along the locus of wing section aerodynamic centers, from Eq. (1.9.1), the local velocity induced at a control point placed anywhere along the bound segment of horseshoe vortex i is

$$\mathbf{V}_i = \mathbf{V}_\infty + \sum_{j=1}^N \frac{\Gamma_j \mathbf{v}_{ji}}{\bar{c}_j} \quad (1.9.4)$$

where \mathbf{V}_∞ is the velocity of the uniform flow, Γ_j is the strength of horseshoe vortex j , \mathbf{v}_{ji} is a dimensionless velocity that would be induced at control point i by horseshoe vortex j , having a unit strength

$$\mathbf{v}_{ji} = \begin{cases} \frac{\bar{c}_j}{4\pi} \left[\frac{\mathbf{u}_\infty \times \mathbf{r}_{j2i}}{r_{j2i}(r_{j2i} - \mathbf{u}_\infty \cdot \mathbf{r}_{j2i})} + \frac{(r_{j1i} + r_{j2i})(\mathbf{r}_{j1i} \times \mathbf{r}_{j2i})}{r_{j1i}r_{j2i}(r_{j1i}r_{j2i} + \mathbf{r}_{j1i} \cdot \mathbf{r}_{j2i})} - \frac{\mathbf{u}_\infty \times \mathbf{r}_{j1i}}{r_{j1i}(r_{j1i} - \mathbf{u}_\infty \cdot \mathbf{r}_{j1i})} \right], & j \neq i \\ \frac{\bar{c}_j}{4\pi} \left[\frac{\mathbf{u}_\infty \times \mathbf{r}_{j2i}}{r_{j2i}(r_{j2i} - \mathbf{u}_\infty \cdot \mathbf{r}_{j2i})} - \frac{\mathbf{u}_\infty \times \mathbf{r}_{j1i}}{r_{j1i}(r_{j1i} - \mathbf{u}_\infty \cdot \mathbf{r}_{j1i})} \right], & j = i \end{cases} \quad (1.9.5)$$

\mathbf{r}_{j1i} is the spatial vector from node 1 of horseshoe vortex j to the control point of horseshoe vortex i , \mathbf{r}_{j2i} is the spatial vector from node 2 of horseshoe vortex j to the control point of horseshoe vortex i , and \mathbf{u}_∞ is the unit vector in the direction of the freestream. At this point, \bar{c}_j could be any characteristic length associated with the wing section aligned with horseshoe vortex j . This characteristic length is simply used to nondimensionalize Eq. (1.9.5) and has no effect on the induced velocity. An appropriate choice for \bar{c}_j will be addressed at a later point. The bound vortex segment is excluded from Eq. (1.9.5) when $j=i$, because a straight vortex segment induces no downwash along its own length. However, the second term in Eq. (1.9.5), for $j \neq i$, is indeterminate when used with $j=i$, because $r_{j1i}r_{j2i} + \mathbf{r}_{j1i} \cdot \mathbf{r}_{j2i} = 0$.

From Eqs. (1.8.1) and (1.9.4), the aerodynamic force acting on a spanwise differential section of the wing located at control point i is given by

$$d\mathbf{F}_i = \rho \Gamma_i \left(\mathbf{V}_\infty + \sum_{j=1}^N \frac{\Gamma_j}{\bar{c}_j} \mathbf{v}_{ji} \right) \times d\mathbf{l}_i \quad (1.9.6)$$

Allowing for the possibility of flap deflection, the local section lift coefficient for the airfoil section located at control point i is a function of local angle of attack and local flap deflection,

$$\tilde{C}_{Li} = \tilde{C}_{Li}(\alpha_i, \delta_i) \quad (1.9.7)$$

100 Chapter 1 Overview of Aerodynamics

where \tilde{C}_{Li} , α_i , and δ_i are, respectively, the local airfoil section lift coefficient, the local angle of attack, and the local flap deflection, all evaluated for the airfoil section aligned with control point i . Defining \mathbf{u}_{ni} and \mathbf{u}_{ai} to be the local unit normal and axial vectors for the airfoil section located at control point i , as shown in Fig. 1.9.4, the local angle of attack at control point i can be written as

$$\alpha_i = \tan^{-1} \left(\frac{\mathbf{V}_i \cdot \mathbf{u}_{ni}}{\mathbf{V}_i \cdot \mathbf{u}_{ai}} \right) \quad (1.9.8)$$

If the relation implied by Eq. (1.9.7) is known at each section of the wing, the magnitude of the aerodynamic force acting on a spanwise differential section of the wing located at control point i can be written as

$$|\mathbf{dF}_i| = \frac{1}{2} \rho V_\infty^2 \tilde{C}_{Li}(\alpha_i, \delta_i) dS_i \quad (1.9.9)$$

where dS_i is a spanwise differential planform area element located at control point i . Setting the magnitude of the force obtained from Eq. (1.9.6) equal to that obtained from Eq. (1.9.9), applying Eq. (1.9.4) to Eq. (1.9.8), and rearranging, we can write

$$2 \left(\mathbf{u}_\infty + \sum_{j=1}^N \mathbf{v}_{ji} G_j \right) \times \zeta_i \left| G_i - \tilde{C}_{Li}(\alpha_i, \delta_i) \right| = 0 \quad (1.9.10)$$

$$\mathbf{u}_\infty \equiv \frac{\mathbf{V}_\infty}{V_\infty}, \quad \zeta_i \equiv \bar{c}_i \frac{d\mathbf{l}_i}{dS_i}, \quad G_i \equiv \frac{\Gamma_i}{\bar{c}_i V_\infty}$$

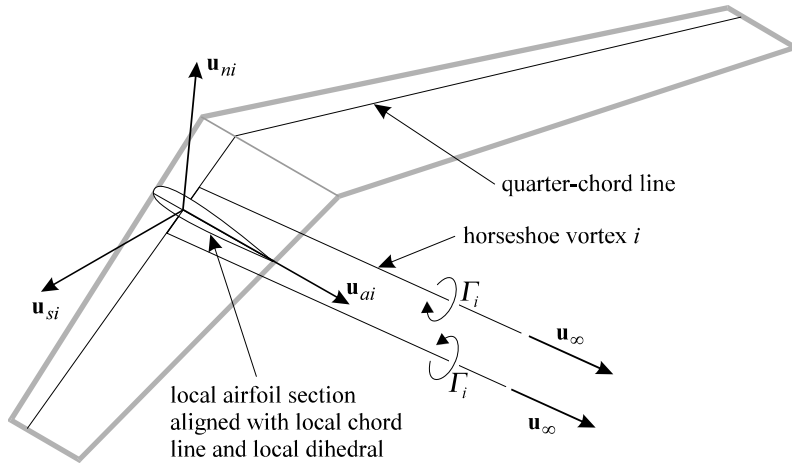


Figure 1.9.4. Unit vectors describing the orientation of the local airfoil section.

1.9. Flow over Multiple Lifting Surfaces 101

where the local section angle of attack is determined from

$$\alpha_i = \tan^{-1} \left[\frac{\left(\mathbf{u}_\infty + \sum_{j=1}^N \mathbf{v}_{ji} G_j \right) \cdot \mathbf{u}_{ni}}{\left(\mathbf{u}_\infty + \sum_{j=1}^N \mathbf{v}_{ji} G_j \right) \cdot \mathbf{u}_{ai}} \right] \quad (1.9.11)$$

Equation (1.9.10) can be written for N different control points, one associated with each of the N horseshoe vortices used to synthesize the lifting surface or system of lifting surfaces. This provides a system of N nonlinear equations relating the N unknown dimensionless vortex strengths, G_i , to known properties of the wing. At angles of attack below stall, this system of nonlinear equations surrenders quickly to Newton's method.

To apply Newton's method, the system of equations is written in the vector form

$$\mathbf{f}(\mathbf{G}) = \mathbf{R} \quad (1.9.12)$$

where

$$f_i(\mathbf{G}) = 2 \left| \mathbf{u}_\infty + \sum_{j=1}^N \mathbf{v}_{ji} G_j \right| \times \zeta_i \left| G_i - \tilde{C}_{Li}(\alpha_i, \delta_i) \right| \quad (1.9.13)$$

and \mathbf{R} is a vector of residuals. We wish to find the vector of dimensionless vortex strengths, \mathbf{G} , that will make all components of the residual vector, \mathbf{R} , go to zero. Thus, we want the change in the residual vector to be $-\mathbf{R}$. We start with some initial estimate for the \mathbf{G} vector and iteratively refine this estimate by applying the Newton corrector equation

$$[\mathbf{J}]\Delta\mathbf{G} = -\mathbf{R} \quad (1.9.14)$$

where $[\mathbf{J}]$ is an $N \times N$ Jacobian matrix of partial derivatives, which is obtained by differentiating Eq. (1.9.13),

$$J_{ij} = \frac{\partial f_i}{\partial G_j} = \begin{cases} \frac{2\mathbf{w}_i \cdot (\mathbf{v}_{ji} \times \zeta_i)}{|\mathbf{w}_i|} G_i - \frac{\partial \tilde{C}_{Li}}{\partial \alpha_i} \frac{v_{ai}(\mathbf{v}_{ji} \cdot \mathbf{u}_{ni}) - v_{ni}(\mathbf{v}_{ji} \cdot \mathbf{u}_{ai})}{v_{ai}^2 + v_{ni}^2}, & j \neq i \\ 2|\mathbf{w}_i| + \frac{2\mathbf{w}_i \cdot (\mathbf{v}_{ji} \times \zeta_i)}{|\mathbf{w}_i|} G_i - \frac{\partial \tilde{C}_{Li}}{\partial \alpha_i} \frac{v_{ai}(\mathbf{v}_{ji} \cdot \mathbf{u}_{ni}) - v_{ni}(\mathbf{v}_{ji} \cdot \mathbf{u}_{ai})}{v_{ai}^2 + v_{ni}^2}, & j = i \end{cases} \quad (1.9.15)$$

$$\mathbf{w}_i \equiv \mathbf{v}_i \times \zeta_i, \quad v_{ni} \equiv \mathbf{v}_i \cdot \mathbf{u}_{ni}, \quad v_{ai} \equiv \mathbf{v}_i \cdot \mathbf{u}_{ai}, \quad \mathbf{v}_i \equiv \mathbf{u}_\infty + \sum_{j=1}^N \mathbf{v}_{ji} G_j$$

102 Chapter 1 Overview of Aerodynamics

Using Eq. (1.9.15) in Eq. (1.9.14), we compute the correction vector, $\Delta \mathbf{G}$. This correction vector is used to obtain an improved estimate for the dimensionless vortex strength vector, \mathbf{G} , according to the relation

$$\mathbf{G} = \mathbf{G} + \Psi \Delta \mathbf{G} \quad (1.9.16)$$

where Ψ is a relaxation factor. The process is repeated until the magnitude of the largest residual is less than some convergence criteria. For angles of attack below stall, this method converges very rapidly using almost any initial estimate for the \mathbf{G} vector with a relaxation factor of unity. At angles of attack beyond stall, the method must be highly underrelaxed and is very sensitive to the initial estimate for the \mathbf{G} vector.

For the fastest convergence of Newton's method, we require an accurate initial estimate for the dimensionless vortex strength vector. For this purpose, a linearized version of Eq. (1.9.10) is useful. Furthermore, for wings of high aspect ratio at small angles of attack, the nonlinear terms in Eq. (1.9.10) are quite small and the linearized system can be used directly to give an accurate prediction of aerodynamic performance.

Applying the small-angle approximation to Eq. (1.9.10) and neglecting all other second-order terms, we obtain

$$2|\mathbf{u}_\infty \times \boldsymbol{\zeta}_i| G_i - \tilde{C}_{Li,\alpha} \sum_{j=1}^N \mathbf{v}_{ji} \cdot \mathbf{u}_{ni} G_j = \tilde{C}_{Li,\alpha} (\mathbf{u}_\infty \cdot \mathbf{u}_{ni} - \alpha_{L0i} + \varepsilon_i \delta_i) \quad (1.9.17)$$

The linearized system of equations given by Eq. (1.9.17) gives good results, at small angles of attack, for wings of reasonably high aspect ratio and little sweep. For larger angles of attack or highly swept wings, the nonlinear system given by Eq. (1.9.10) should be used. However, at angles of attack below stall, Eq. (1.9.17) still provides a reasonable initial estimate for the dimensionless vortex strength vector, to be used with Newton's method for obtaining a solution to the nonlinear system.

Once the vortex strengths are determined from either Eq. (1.9.10) or Eq. (1.9.17), the total aerodynamic force vector can be determined from Eq. (1.9.6). If the lifting surface or surfaces are synthesized from a large number of horseshoe vortices, each covering a small spanwise increment of one lifting surface, we can approximate the aerodynamic force as being constant over each spanwise increment. Then, from Eq. (1.9.6), the total aerodynamic force is given by

$$\mathbf{F}_a = \rho \sum_{i=1}^N \left(\Gamma_i \mathbf{V}_\infty + \sum_{j=1}^N \frac{\Gamma_i \Gamma_j}{\bar{c}_j} \mathbf{v}_{ji} \right) \times \delta \mathbf{l}_i \quad (1.9.18)$$

where $\delta \mathbf{l}_i$ is the spatial vector along the bound segment of horseshoe vortex i from node 1 to node 2. Nondimensionalizing this result, the **total nondimensional aerodynamic force vector** is

$$\frac{\mathbf{F}_a}{\frac{1}{2} \rho V_\infty^2 S_r} = 2 \sum_{i=1}^N \left(G_i \mathbf{u}_\infty + \sum_{j=1}^N G_j G_j \mathbf{v}_{ji} \right) \times \boldsymbol{\zeta}_i \frac{\delta \mathcal{S}_i}{S_r} \quad (1.9.19)$$

1.9. Flow over Multiple Lifting Surfaces 103

where S_r is the global reference area and δS_i is the planform area of the spanwise increment of the lifting surface covered by horseshoe vortex i . If we assume a linear variation in chord length over each spanwise increment, we have

$$\delta S_i \equiv \int_{s=s_1}^{s_2} c \, ds = \frac{c_{i_1} + c_{i_2}}{2} (s_{i_2} - s_{i_1}) \quad (1.9.20)$$

where c is the local chord length and s is the spanwise coordinate.

The aerodynamic moment generated about the center of gravity is

$$\mathbf{M}_a = \rho \sum_{i=1}^N \left\{ \mathbf{r}_i \times \left[\left(\Gamma_i \mathbf{V}_\infty + \sum_{j=1}^N \frac{\Gamma_j \Gamma_j}{\bar{c}_j} \mathbf{v}_{ji} \right) \times \delta \mathbf{l}_i \right] + \delta \mathbf{M}_i \right\} \quad (1.9.21)$$

where \mathbf{r}_i is the spatial vector from the center of gravity to control point i and $\delta \mathbf{M}_i$ is the moment generated about the lifting line by the spanwise increment of the wing covered by horseshoe vortex i . If we assume a constant section moment coefficient over each spanwise increment, then

$$\delta \mathbf{M}_i \cong -\frac{1}{2} \rho V_\infty^2 \tilde{C}_{mi} \int_{s=s_1}^{s_2} c^2 \, ds \, \mathbf{u}_{si} \quad (1.9.22)$$

where \tilde{C}_{mi} is the local section moment coefficient and \mathbf{u}_{si} is the local unit vector in the spanwise direction as shown in Fig. 1.9.4 and defined by

$$\mathbf{u}_{si} = \mathbf{u}_{ai} \times \mathbf{u}_{ni} \quad (1.9.23)$$

Using Eq. (1.9.22) in Eq. (1.9.21) and nondimensionalizing gives

$$\frac{\mathbf{M}_a}{\frac{1}{2} \rho V_\infty^2 S_r l_r} = \sum_{i=1}^N \left\{ 2 \mathbf{r}_i \times \left[\left(G_i \mathbf{u}_\infty + \sum_{j=1}^N G_j G_j \mathbf{v}_{ji} \right) \times \boldsymbol{\zeta}_i \right] - \frac{\tilde{C}_{mi}}{\delta S_i} \int_{s=s_1}^{s_2} c^2 \, ds \, \mathbf{u}_{si} \right\} \frac{\delta S_i}{S_r l_r} \quad (1.9.24)$$

where l_r is the global reference length.

To this point, the local characteristic length, \bar{c}_i , has not been defined. It could be any characteristic length associated with the spanwise increment of the wing covered by horseshoe vortex i . From Eq. (1.9.24), the most natural choice for this local characteristic length is the integral of the chord length squared, with respect to the spanwise coordinate, divided by the incremental area. For a linear variation in chord length over each spanwise increment, this gives

$$\bar{c}_i = \frac{1}{\delta S_i} \int_{s=s_1}^{s_2} c^2 \, ds = \frac{2}{3} \frac{c_{i_1}^2 + c_{i_1} c_{i_2} + c_{i_2}^2}{c_{i_1} + c_{i_2}} \quad (1.9.25)$$

104 Chapter 1 Overview of Aerodynamics

With this definition, the **dimensionless aerodynamic moment vector** is

$$\frac{\mathbf{M}_a}{\frac{1}{2}\rho V_\infty^2 S_r l_r} = \sum_{i=1}^N \left\{ 2\mathbf{r}_i \times \left[\left(G_i \mathbf{u}_\infty + \sum_{j=1}^N G_j G_j \mathbf{v}_{ji} \right) \times \boldsymbol{\zeta}_i \right] - \tilde{C}_{mi} \bar{c}_i \mathbf{u}_{si} \right\} \frac{\delta S_i}{S_r l_r} \quad (1.9.26)$$

Once the dimensionless vortex strengths, G_i , are known, Eqs. (1.9.19) and (1.9.26) are used to evaluate the components of the aerodynamic force and moment.

Each lifting surface must, of course, be divided into spanwise elements, in a manner similar to that shown symbolically in Fig. 1.9.2. In this figure, the wing is divided into elements of equal spanwise increment. However, this is not the most efficient way in which to grid a wing. Since the spanwise derivative of shed vorticity is greater in the region near the wingtips, for best computational efficiency, the nodal points should be clustered more tightly in this region. Conventional cosine clustering has been found to be quite efficient for this purpose. For straight wings, clustering is only needed near the wingtips and the cosine distribution can be applied across the entire span of the wing. However, for wings with sweep or dihedral, there is a step change in the slope of the quarter-chord line at the root of the wing. This step change produces an increase in the spanwise variation of downwash in the region near the root. Thus, in general, it is recommended that cosine clustering be applied independently over each semispan of each lifting surface. This clusters the nodes more tightly at both the tip and root. This clustering is based on the change of variables,

$$\frac{s}{b} = \frac{1 - \cos(\theta)}{4} \quad (1.9.27)$$

where s is the spanwise coordinate and b is twice the semispan. Over each semispan, θ varies from zero to π as s varies from zero to $b/2$. Distributing the nodes uniformly in θ will provide the desired clustering in s . If the total number of horseshoe elements desired on each semispan is n , the spanwise nodal coordinates are computed from

$$\frac{s_i}{b} = \frac{1}{4} \left[1 - \cos\left(\frac{i\pi}{n}\right) \right], \quad 0 \leq i \leq n \quad (1.9.28)$$

where the bound segment of horseshoe vortex i extends from node i to node $i-1$ on any left semispan and from node $i-1$ to node i on any right semispan. Using this nodal distribution with about 40 horseshoe elements per semispan gives the best compromise between speed and accuracy. Figure 1.9.5 shows a system of lifting surfaces overlaid with a grid of this type using 20 elements per semispan.

For maximum accuracy and computational efficiency, some attention must also be paid to the location of control points. At first thought, it would seem most reasonable to place control points on the bound segment of each vortex, midway between the two trailing legs. However, it has been found that this does not give the best accuracy. A significant improvement in accuracy, for a given number of elements, can be achieved by placing the control points midway in θ rather than midway in s . Thus, the spanwise control point coordinates should be computed from

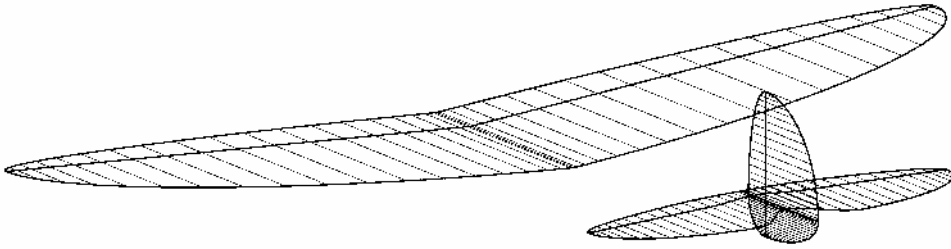


Figure 1.9.5. Lifting-line grid with cosine clustering and 20 elements per semispan.

$$\frac{s_i}{b} = \frac{1}{4} \left[1 - \cos \left(\frac{i\pi}{n} - \frac{\pi}{2n} \right) \right], \quad 1 \leq i \leq n \quad (1.9.29)$$

This distribution places control points very near the spatial midpoint of each bound vortex segment over most of the wing. However, near the root and the tip, these control points are significantly offset from the spatial midpoint.

This numerical lifting-line method can be used to predict the aerodynamic forces and moments acting on a system of lifting surfaces with arbitrary position and orientation. Each lifting surface is synthesized by distributing horseshoe vortices along the lifting line in the manner shown in Fig. 1.9.5. Because all of the horseshoe vortices used to synthesize the complete system of lifting surfaces are combined and forced to satisfy either Eq. (1.9.10) or Eq. (1.9.17) as a single system of coupled equations, all of the interactions between lifting surfaces are accounted for directly.

Unlike the closed-form solution to Prandtl's classical lifting-line theory, the numerical lifting-line method can be applied to wings with sweep and/or dihedral. To examine how well the numerical lifting-line method predicts the effects of sweep, Phillips and Snyder (2000) compared results obtained from this method, a numerical panel method, and an inviscid CFD solution. These results were also compared with experimental data for two different wings. Some of the results from this comparison are shown in Fig. 1.9.6. The solid line and filled symbols correspond to a straight wing of aspect ratio 6.57, with experimental data obtained from McAlister and Takahashi (1991). The dashed line and open symbols are for a 45-degree swept wing of aspect ratio 5.0, having experimental data reported by Weber and Brebner (1958). Both wings have symmetric airfoil sections and constant chord throughout the span, with no geometric twist. The straight wing has a thickness of 15 percent and the swept wing has a thickness of 12 percent. From the results shown in Fig. 1.9.6, we see that the lift coefficient predicted by all four methods is in good agreement with experimental observations for both wings. However, the computational time required to obtain a solution using the numerical panel method was about 2.5×10^4 times that required for the lifting-line method, and the inviscid CFD solutions required approximately 2.7×10^6 times as long as the lifting-line solutions. The accuracy of the numerical lifting-line method for predicting dihedral effects was also investigated by Phillips and Snyder (2000), and the results obtained were similar to those shown in Fig. 1.9.6.

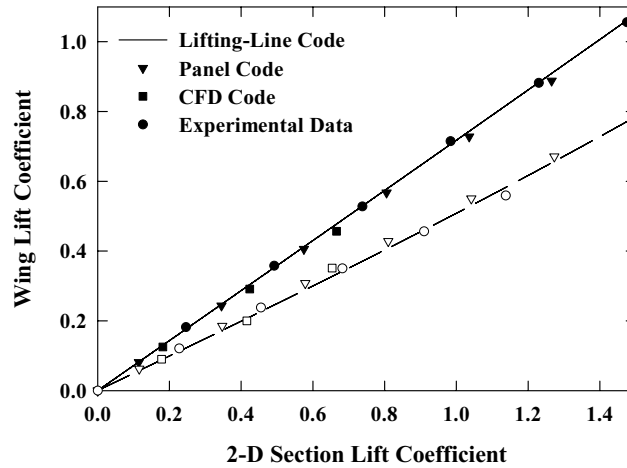


Figure 1.9.6. Comparison between the lift coefficient predicted by the numerical lifting-line method, a numerical panel method, and an inviscid CFD solutions with data obtained from wind tunnel tests for an unswept wing and a wing with 45 degrees of sweep.

The insight of Ludwig Prandtl (1875–1953) was nothing short of astonishing. This was never more dramatically demonstrated than in the development of his classical lifting-line theory, during the period 1911 through 1918. The utility of this simple and elegant theory is so great that it is still widely used today. Furthermore, with a few minor alterations and the use of a modern computer, the model proposed by Prandtl can be used to predict the inviscid forces and moments acting on lifting surfaces of aspect ratio greater than about 4 with an accuracy as good as that obtained from modern panel codes or CFD, but at a small fraction of the computational cost.

Like panel methods, lifting-line theory provides only a potential flow solution. Thus, the forces and moments computed from this method do not include viscous effects. In addition to this restriction, which also applies to panel methods, lifting-line theory imposes an additional restriction, which does not apply to panel methods. For lifting surfaces with low aspect ratio, Prandtl's hypothesis breaks down and the usual relationship between local section lift and local section angle of attack no longer applies. It has long been established that lifting-line theory gives good agreement with experimental data for lifting surfaces of aspect ratio greater than about 4. For lifting surfaces of lower aspect ratio, panel methods or CFD solutions should be used.

The numerical lifting-line method contains no inherent requirement for a linear relationship between section lift and section angle of attack. Thus, the method can be applied, with caution, to account approximately for the effects of stall. The lifting-line method requires a known relationship for the section lift coefficient as a function of section angle of attack. Since such relationships are often obtained experimentally beyond stall, the numerical lifting-line method predicts stall by using a semiempirical correction to an otherwise potential flow solution. For this reason, the method should be used with extreme caution for angles of attack beyond stall.

1.9. Flow over Multiple Lifting Surfaces 107

The effects of viscous parasitic drag can be approximately accounted for in the present numerical lifting-line method through the vector addition of a parasitic drag component to the contribution from each segment in Eqs. (1.9.19) and (1.9.26). The parasitic segment contribution to the net aerodynamic force vector is

$$(\delta \mathbf{F}_i)_{\text{parasite}} \cong \frac{1}{2} \rho V_\infty^2 \tilde{C}_{Di}(\alpha_i) \delta S_i \mathbf{u}_i$$

where $\tilde{C}_{Di}(\alpha_i)$ represents a relation for the local section drag coefficient as a function of angle of attack and \mathbf{u}_i is the unit vector in the direction of the local velocity vector,

$$\mathbf{u}_i \equiv \frac{\mathbf{V}_i}{V_i}$$

A simple polynomial fit to experimental airfoil section data could be used to describe the relation for section drag coefficient as a function of angle of attack. Similarly, the parasitic segment contribution to the net aerodynamic moment vector is

$$(\delta \mathbf{M}_i)_{\text{parasite}} \cong \frac{1}{2} \rho V_\infty^2 \tilde{C}_{Di}(\alpha_i) \delta S_i (\mathbf{r}_i \times \mathbf{u}_i)$$

Thus, the **dimensionless parasitic contributions to the force and moment vectors** are

$$\left(\frac{\mathbf{F}_a}{\frac{1}{2} \rho V_\infty^2 S_r} \right)_{\text{parasite}} = \sum_{i=1}^N \tilde{C}_{Di}(\alpha_i) \frac{\delta S_i}{S_r} \mathbf{u}_i \quad (1.9.30)$$

$$\left(\frac{\mathbf{M}_a}{\frac{1}{2} \rho V_\infty^2 S_r l_r} \right)_{\text{parasite}} = \sum_{i=1}^N \tilde{C}_{Di}(\alpha_i) \frac{\delta S_i}{S_r l_r} (\mathbf{r}_i \times \mathbf{u}_i) \quad (1.9.31)$$

In our study of flight mechanics, we will find it necessary to know how the aerodynamic force and moment components for a complete aircraft vary over a broad range of operating conditions. Ultimately, this information is commonly gathered from wind tunnel testing. However, such testing is very time consuming and expensive. Another alternative that is often used to obtain the required information is CFD computations. Although modern computers are very fast and the CFD algorithms available today are quite accurate, the volume of data needed to define the required aerodynamic parameters is large. Even with the fastest available computers, gathering the desired information from CFD computations requires considerable time. Thus, for preliminary design, it is important to have a more computationally efficient means for the estimation of aerodynamic force and moment components acting on a complete aircraft. When parasitic drag is included, the numerical lifting-line method described in this section provides such an analytical tool. This method reduces computation time by more than four orders of magnitude over that required for inviscid panel codes and by more than six orders of magnitude compared with CFD computations.

1.10. Wing Stall and Maximum Lift Coefficient

Many aspects of aircraft design and performance analysis depend on the maximum lift coefficient that can be attained on a finite wing prior to stall. Because in general the local section lift coefficient is not constant along the span of a finite wing, it is of interest to know the value of the maximum section lift coefficient and the position along the span at which this maximum occurs. Such knowledge allows us to predict the onset of wing stall from known airfoil section properties, including the maximum airfoil section lift coefficient.

From Eqs. (1.8.96) through (1.8.98), lifting-line theory predicts that the spanwise variation in local section lift coefficient for an unswept wing is given by

$$\tilde{C}_L(\theta) = \Omega \sum_{n=1}^{\infty} 4 \left(\frac{b_1 a_n}{a_1} - b_n \right) \frac{\sin(n\theta)}{c(\theta)/b} + C_L \sum_{n=1}^{\infty} \frac{4a_n}{\pi R_A a_1} \frac{\sin(n\theta)}{c(\theta)/b} \quad (1.10.1)$$

where $\theta \equiv \cos^{-1}(-2z/b)$ and Ω is the total amount of wing twist,

$$\Omega \equiv (\alpha - \alpha_{L0})_{\text{root}} - (\alpha - \alpha_{L0})_{\text{max}} \quad (1.10.2)$$

As defined by Eqs. (1.8.20) and (1.8.21) the Fourier coefficients a_n and b_n are obtained from the relations

$$\sum_{n=1}^N a_n \left[\frac{4b}{\tilde{C}_{L,\alpha} c(\theta)} + \frac{n}{\sin(\theta)} \right] \sin(n\theta) = 1 \quad (1.10.3)$$

$$\sum_{n=1}^N b_n \left[\frac{4b}{\tilde{C}_{L,\alpha} c(\theta)} + \frac{n}{\sin(\theta)} \right] \sin(n\theta) = \omega(\theta) \quad (1.10.4)$$

where $\omega(\theta)$ is the dimensionless twist distribution function,

$$\omega(\theta) \equiv \frac{\alpha(\theta) - \alpha_{L0}(\theta) - (\alpha - \alpha_{L0})_{\text{root}}}{(\alpha - \alpha_{L0})_{\text{max}} - (\alpha - \alpha_{L0})_{\text{root}}} \quad (1.10.5)$$

The first term on the right-hand side of Eq. (1.10.1) is the *basic section lift coefficient* and the second term is the *additional section lift coefficient*. The basic section lift coefficient is independent of angle of attack and directly proportional to the total amount of wing twist, Ω . The additional section lift coefficient is independent of wing twist and directly proportional to the net wing lift coefficient, C_L .

In Fig. 1.8.26 we saw how the net section lift coefficient and its two components obtained from Eq. (1.10.1) vary along the span of a linearly tapered wing of aspect ratio 8.0 and taper ratio 0.5. This figure shows the spanwise variation in section lift coefficient for several values of total linear twist with the net wing lift coefficient held constant at 1.0. Similar results were shown in Fig. 1.8.27 for three different values of the net wing lift coefficient with the total linear twist held constant at 6 degrees. Notice that the spanwise coordinates of the maximums in both the basic and additional section lift

1.10. Wing Stall and Maximum Lift Coefficient 109

coefficients do not change with either the amount of wing twist or the net wing lift coefficient. However, the maximum in the net section lift coefficient moves inboard as the total amount of twist is increased, and for wings with positive twist (i.e., washout), this maximum moves outboard as the wing lift coefficient increases. Thus, **the spanwise position of the maximum section lift coefficient on each semispan of a twisted wing varies with both wing twist and angle of attack.**

Combining terms from the basic and additional section lift coefficients on the right-hand side of Eq. (1.10.1) and rearranging, it can be shown that the maximum section lift coefficient occurs at a value of θ that satisfies the relation

$$\begin{aligned} \frac{d\tilde{C}_L}{d\theta} = \frac{4C_L}{\pi R_A} \sum_{n=1}^{\infty} \left(\frac{a_n}{a_1} + \frac{b_1 a_n - a_1 b_n}{a_1^2} \frac{\pi R_A a_1 \Omega}{C_L} \right) \\ \times \left[b \frac{n \cos(n\theta) c(\theta) - \sin(n\theta) dc/d\theta}{c^2(\theta)} \right] = 0 \end{aligned} \quad (1.10.6)$$

Following the development of Phillips and Alley (2007) and applying Eq. (1.8.26), the spanwise location of the airfoil section that supports the largest section lift coefficient is found to be a root of the equation

$$\sum_{n=1}^{\infty} \left(a_n + \frac{b_1 a_n - a_1 b_n}{a_1} \frac{C_{L,\alpha} \Omega}{C_L} \right) \left[n \cos(n\theta) \frac{c(\theta)}{b} - \sin(n\theta) \frac{d(c/b)}{d\theta} \right] = 0 \quad (1.10.7)$$

In the most general case, this root must be found numerically.

After finding the root of Eq. (1.10.7) to obtain the value of θ , which corresponds to the airfoil section that supports the maximum section lift coefficient, this value of θ can be used in Eq. (1.10.1) to determine the maximum section lift coefficient for the wing at the specified operating condition. Dividing Eq. (1.10.1) by C_L and applying Eq. (1.8.26), the ratio of the local section lift coefficient to the total wing lift coefficient is

$$\frac{\tilde{C}_L(\theta)}{C_L} = \frac{4b}{\pi R_A c(\theta)} \left[\sum_{n=1}^{\infty} \frac{a_n}{a_1} \sin(n\theta) + \frac{C_{L,\alpha} \Omega}{C_L} \sum_{n=2}^{\infty} \frac{b_1 a_n - a_1 b_n}{a_1^2} \sin(n\theta) \right] \quad (1.10.8)$$

Examination of Eqs. (1.10.7) and (1.10.8) reveals that for $\Omega=0$, these equations are independent of the net wing lift coefficient. This means that **for an untwisted wing of any planform, the ratio of the maximum section lift coefficient to the total wing lift coefficient and the position along the span at which this maximum occurs are independent of operating conditions and functions of the wing planform only.** Figure 1.10.1 shows how the ratio of total wing lift coefficient to maximum section lift coefficient varies with aspect ratio and taper ratio for untwisted wings with linear taper. The spanwise coordinate of the maximum section lift coefficient for such untwisted wings is shown in Fig. 1.10.2 as a function of aspect ratio and taper ratio. Notice that the spanwise location of the airfoil section that supports the maximum section lift coefficient is quite insensitive to the aspect ratio and nearly a linear function of taper ratio.

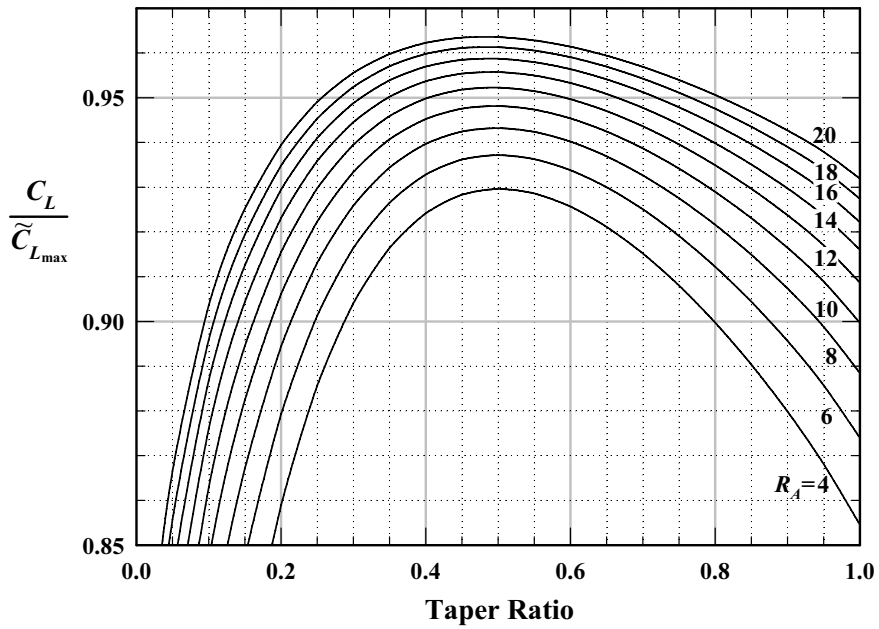


Figure 1.10.1. Maximum lift coefficient for tapered wings with no sweep or twist.

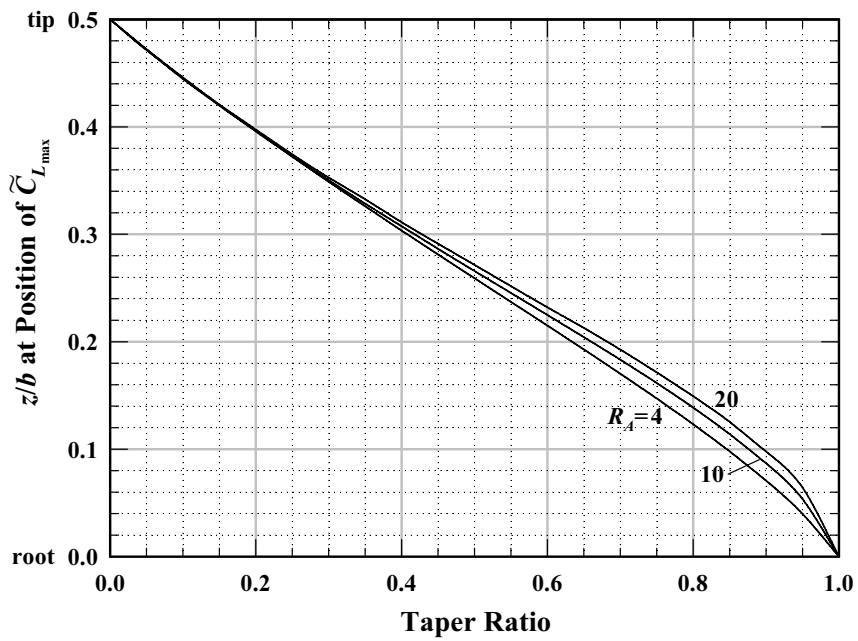


Figure 1.10.2. Spanwise location of maximum section lift coefficient for tapered wings with no sweep or twist.

1.10. Wing Stall and Maximum Lift Coefficient 111

For unswept wings of arbitrary planform and arbitrary twist, the maximum section lift coefficient is obtained by evaluating Eq. (1.10.8) at the value of θ corresponding to the root of Eq. (1.10.7). This result can be algebraically rearranged to obtain a relation for the ratio of the total wing lift coefficient to the maximum section lift coefficient, which yields

$$\left(\frac{C_L}{\tilde{C}_{L_{\max}}} \right)_{A=0} = \left(\frac{C_L}{\tilde{C}_{L_{\max}}} \right)_{\substack{\Omega=0 \\ A=0}} \left(1 - \kappa_{L\Omega} \frac{C_{L,\alpha} \Omega}{\tilde{C}_{L_{\max}}} \right) \quad (1.10.9)$$

where

$$\left(\frac{C_L}{\tilde{C}_{L_{\max}}} \right)_{\substack{\Omega=0 \\ A=0}} = \frac{\pi R_A c(\theta_{\max})}{4b} \bigg/ \sum_{n=1}^{\infty} \frac{a_n}{a_1} \sin(n\theta_{\max}) \quad (1.10.10)$$

$$\kappa_{L\Omega} \equiv \frac{4b}{\pi R_A c(\theta_{\max})} \sum_{n=2}^{\infty} \frac{b_1 a_n - a_1 b_n}{a_1^2} \sin(n\theta_{\max}) \quad (1.10.11)$$

and θ_{\max} is the value of θ at the wing section that supports the maximum airfoil section lift coefficient, which is obtained from the root of Eq. (1.10.7).

For unswept rectangular wings with positive washout ($\Omega \geq 0$), the maximum section lift coefficient occurs at the wing root ($\theta_{\max} = \pi/2$) and the constant chord length is given by $c(\theta) = b/R_A$. Using these results in Eqs. (1.10.10) and (1.10.11) and simplifying, for **unswept rectangular wings with positive washout** we obtain

$$\left(\frac{C_L}{\tilde{C}_{L_{\max}}} \right)_{\substack{\Omega=0 \\ A=0}} = \frac{\pi}{4} \bigg/ \sum_{i=0}^{\infty} (-1)^i \frac{a_{2i+1}}{a_1}, \quad \kappa_{L\Omega} = \frac{4}{\pi} \sum_{i=1}^{\infty} (-1)^i \frac{b_1 a_{2i+1} - a_1 b_{2i+1}}{a_1^2} \quad (1.10.12)$$

For an unswept elliptic wing with $\Omega \geq 0$, the maximum section lift coefficient occurs at the wing root ($\theta_{\max} = \pi/2$), the section chord length is $c(\theta) = [4b/(\pi R_A)] \sin(\theta)$, and the planform Fourier coefficients are $a_1 = \tilde{C}_{L,\alpha} / (\pi R_A + \tilde{C}_{L,\alpha})$ and $a_n = 0$ for $n > 1$. Using these results in Eqs. (1.10.10) and (1.10.11), Phillips and Alley (2007) have shown that for **unswept elliptic wings with positive linear washout**

$$\left(\frac{C_L}{\tilde{C}_{L_{\max}}} \right)_{\substack{\Omega=0 \\ A=0}} = 1, \quad \kappa_{L\Omega} = \frac{1}{\pi} \sum_{i=1}^{\infty} \frac{4}{(2i+1)^2 - 4} \left(\frac{\pi R_A + \tilde{C}_{L,\alpha}}{\pi R_A + (2i+1)\tilde{C}_{L,\alpha}} \right) \quad (1.10.13)$$

Notice that for unswept rectangular and elliptic wings with positive washout, $\kappa_{L\Omega}$ is independent of both Ω and C_L and the ratio of wing lift coefficient to maximum section lift coefficient is a linear function of $C_{L,\alpha} \Omega / \tilde{C}_{L_{\max}}$. Results predicted from Eqs. (1.10.12) and (1.10.13) are shown in Fig. 1.10.3 as a function of aspect ratio.

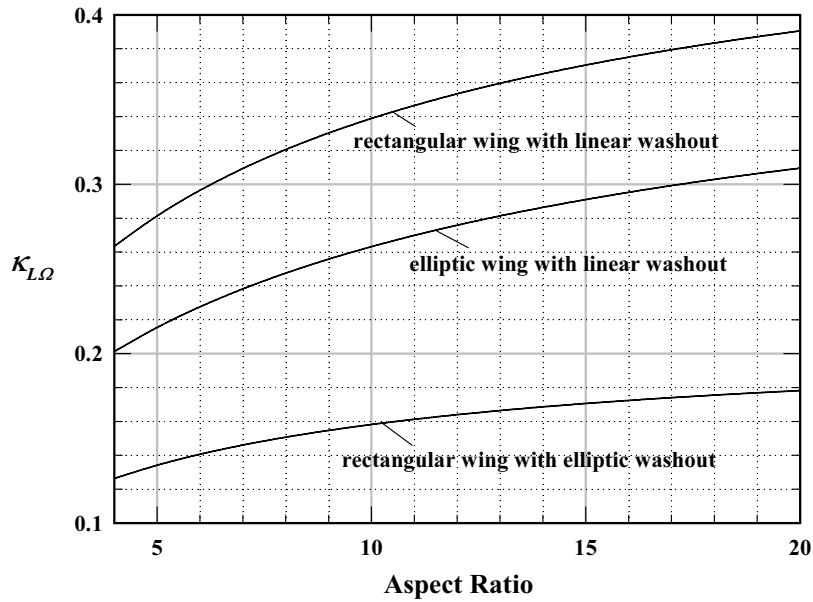


Figure 1.10.3. Effect of wing twist on $\kappa_{L\Omega}$ for elliptic and rectangular wings.

As was seen in Figs. 1.8.26 and 1.8.27, for wings of arbitrary planform the maximum section lift coefficient does not necessarily occur at the wing root. Thus, $\kappa_{L\Omega}$ may vary with $C_{L,\alpha}\Omega/\tilde{C}_{L_{\max}}$ as well as the wing planform. The results plotted in Figs. 1.10.4 and 1.10.5 show how $\kappa_{L\Omega}$ varies with $C_{L,\alpha}\Omega/\tilde{C}_{L_{\max}}$ for wings with linear taper and linear washout.

For **unswept wings with twist optimized to produce minimum induced drag**, the optimum twist distribution and optimum total amount of twist are given in Eq. (1.8.42). For wings with linear taper that are twisted in this manner, Phillips and Alley (2007) obtained a closed-form solution to Eqs. (1.10.7) and (1.10.8). From this solution, we find that the z -coordinate of the wing section that supports the maximum airfoil section lift coefficient is a linear function of the taper ratio and independent of operating conditions,

$$z_{\max} \equiv z(\theta_{\max}) = \pm(1 - R_T)b/2 \tag{1.10.14}$$

The ratio of the total wing lift coefficient to the maximum section lift coefficient for such wings is found to be independent of operating conditions and given by

$$\left(\frac{C_L}{\tilde{C}_{L_{\max}}}\right)_{A=0} = \frac{\pi(2R_T - R_T^2)^{1/2}}{2(1 + R_T)} \tag{1.10.15}$$

The reader is cautioned that results predicted from Eqs. (1.10.14) and (1.10.15) are only valid if the wing twist is maintained in proportion to the wing lift coefficient according to the relations provided by Eq. (1.8.42).

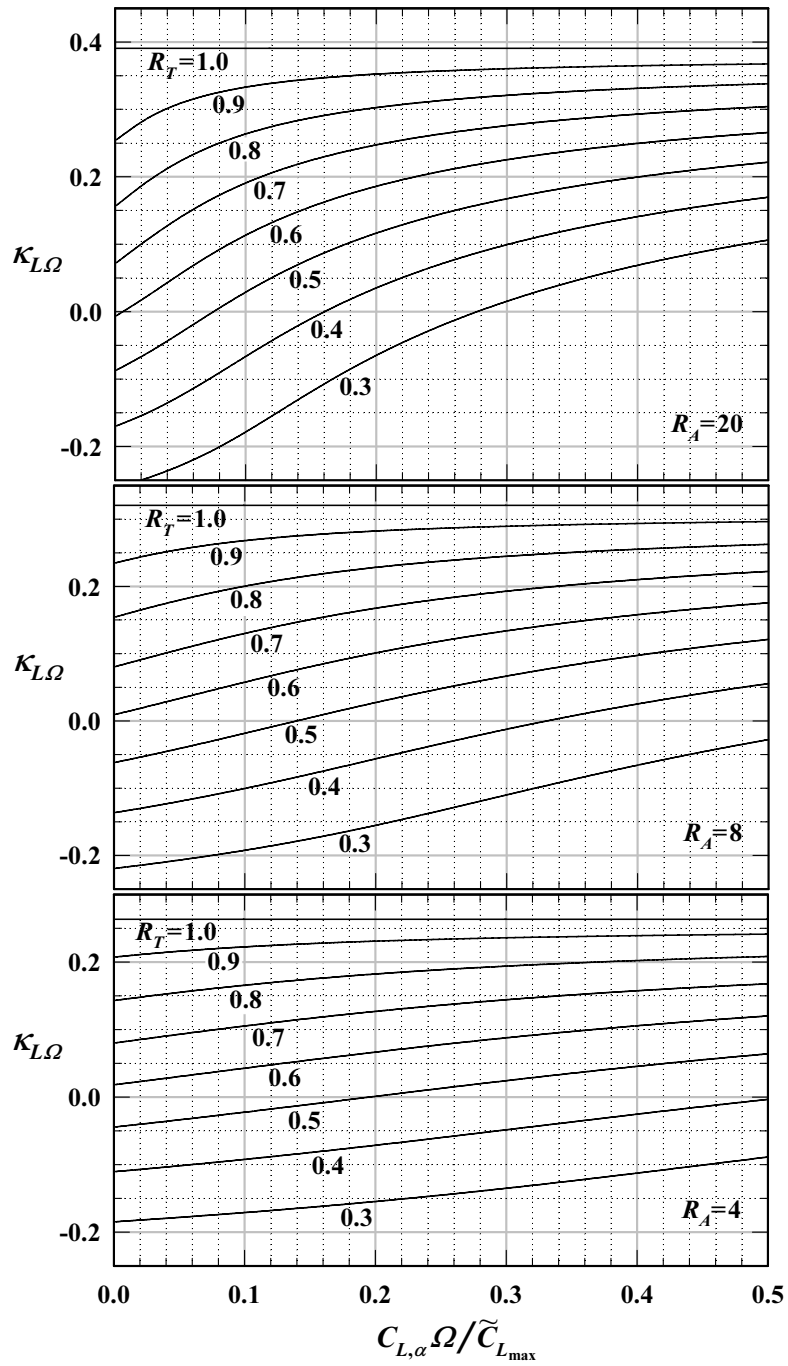


Figure 1.10.4. Effect of wing twist and taper ratio on $\kappa_{L\Omega}$ for wings with linear taper and linear washout.

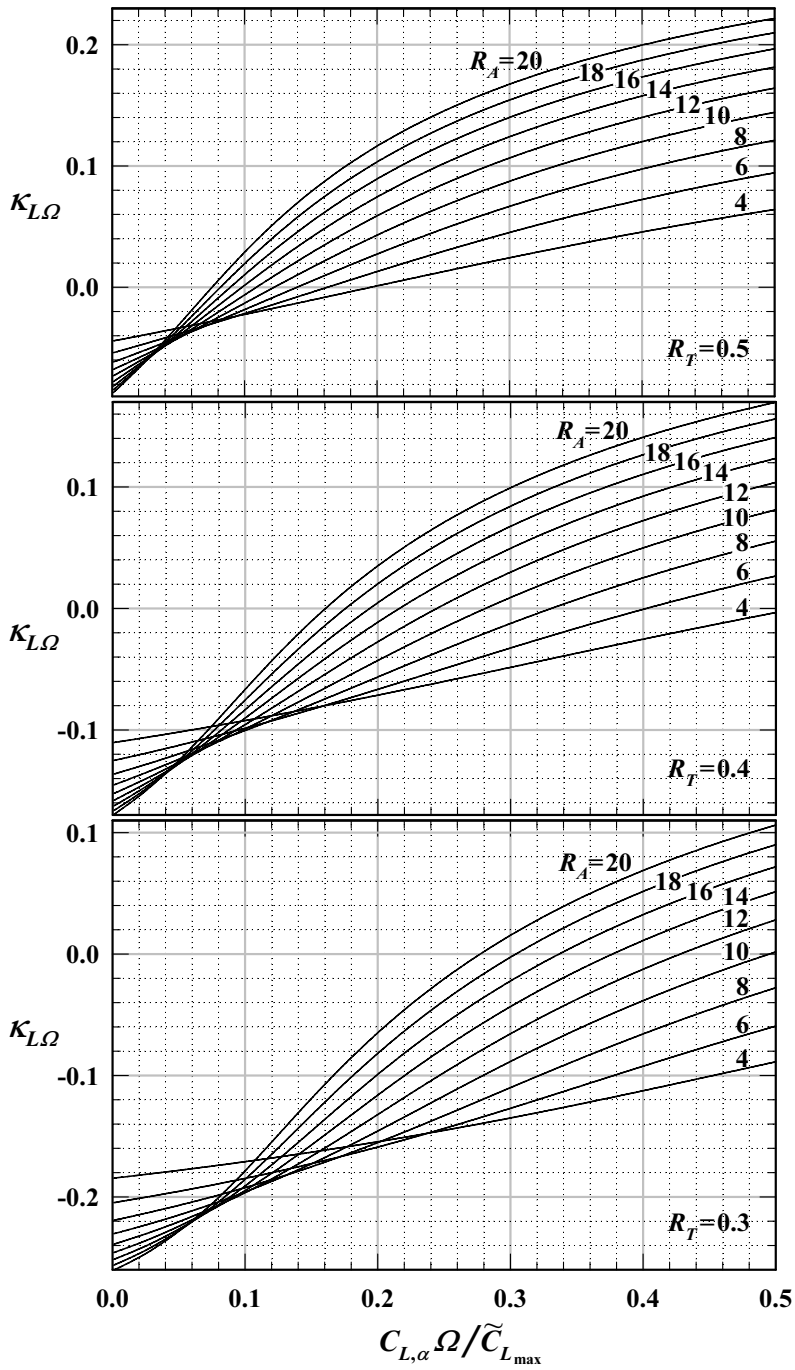


Figure 1.10.5. Effect of wing twist and aspect ratio on $\kappa_{L\Omega}$ for wings with linear taper and linear washout.

1.10. Wing Stall and Maximum Lift Coefficient 115

When Eq. (1.10.9) and Figs. 1.10.1 through 1.10.5 are used to estimate the total wing lift coefficient that corresponds to a given maximum airfoil section lift coefficient, the results apply only to wings without sweep. As a lifting wing of any planform is swept back, the lift near the root of each semispan is reduced as a result of the downwash induced by the bound vorticity generated on the opposite semispan. This tends to move the point of maximum section lift outboard. For wings with significant taper, this outboard shift causes the point of maximum section lift to occur at an airfoil section having a smaller section chord length, which increases the maximum airfoil section lift coefficient that is produced for a given wing lift coefficient. Because the series solution to Prandtl's lifting-line equation applies only to unswept wings, a numerical solution is required to predict the effects of wing sweep. The numerical lifting-line method presented in Sec. 1.9 can be used for this purpose.

The reader should also note that using the maximum airfoil section lift coefficient in Eq. (1.10.9) will give an estimate for the wing lift coefficient at the onset of airfoil section stall. At higher angles of attack, separated flow will exist over some sections of the wing and drag will be substantially increased. However, the wing lift coefficient predicted from Eq. (1.10.9) is not exactly the maximum wing lift coefficient. Viscous interactions between adjacent sections of the wing can initiate flow separation at slightly lower angles of attack than predicted by Eq. (1.10.9). Furthermore, as the angle of attack is increased somewhat beyond that which produces the onset of airfoil section stall, the section lift coefficient on the stalled section of the wing will decrease. However, the section lift coefficient on the unstalled sections of the wing will continue to increase with angle of attack until the maximum section lift coefficient is reached on these sections as well. Thus, the maximum wing lift coefficient could differ slightly from that which is predicted by Eq. (1.10.9). Because boundary layer separation is a viscous phenomenon, the maximum wing lift coefficient for a given wing geometry must be determined from experimental methods or computational fluid dynamics (CFD).

To account for the effects of wing sweep and stall, experimental data and results obtained from CFD computations suggest that predictions from Eq. (1.10.9) can be modified by including sweep and stall correction factors,

$$C_{L_{\max}} = \left(\frac{C_L}{\tilde{C}_{L_{\max}}} \right)_{\substack{\Omega=0 \\ A=0}} \mathcal{K}_{L_s} \mathcal{K}_{L_A} (\tilde{C}_{L_{\max}} - \mathcal{K}_{L\Omega} C_{L,\alpha} \Omega) \quad (1.10.16)$$

The sweep factor \mathcal{K}_{L_A} depends on the wing sweep angle and wing planform. The stall factor \mathcal{K}_{L_s} depends on wing aspect ratio and the wing twist parameter $C_{L,\alpha} \Omega / \tilde{C}_{L_{\max}}$.

For wings with linear taper, Phillips and Alley (2007) presented numerical lifting-line results for the sweep factor, which correlate well with the approximation

$$\mathcal{K}_{L_A} \cong 1 + \mathcal{K}_{A1} A - \mathcal{K}_{A2} A^{1.2} \quad (1.10.17)$$

where A is the wing quarter-chord sweep angle in radians. The empirical coefficients \mathcal{K}_{A1} and \mathcal{K}_{A2} depend on aspect ratio and taper ratio as shown in Figs. 1.10.6 and 1.10.7, respectively.

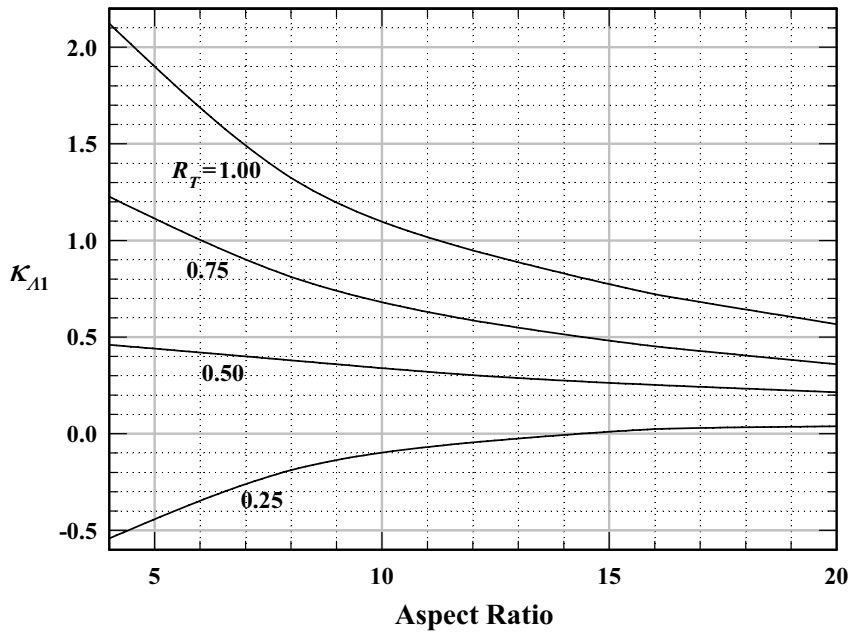


Figure 1.10.6. Wing sweep coefficient K_{A1} to be used in Eq. (1.10.17) for wings with linear taper.

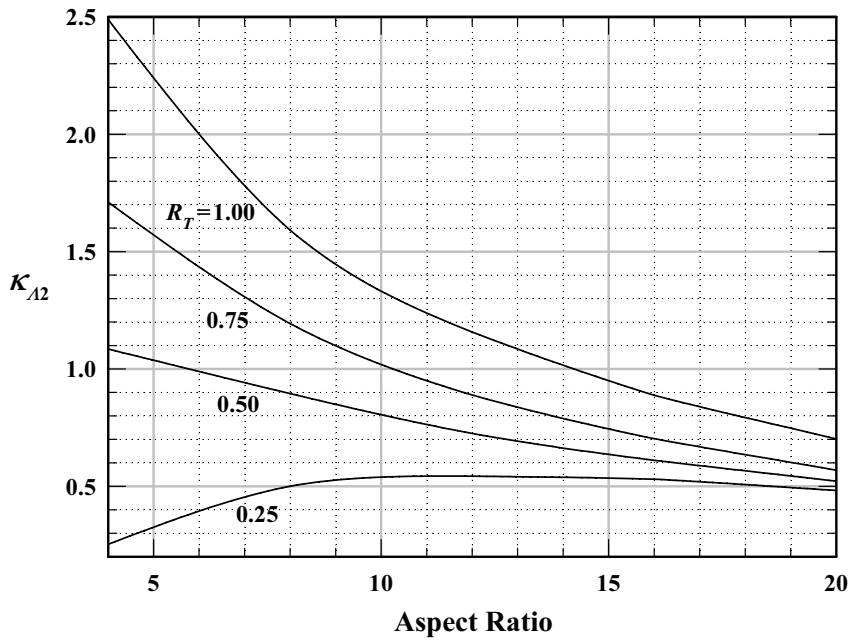


Figure 1.10.7. Wing sweep coefficient K_{A2} to be used in Eq. (1.10.17) for wings with linear taper.

1.10. Wing Stall and Maximum Lift Coefficient 117

For wings with linear taper and linear twist, CFD results obtained by Alley, Phillips, and Spall (2007) for the stall factor in Eq. (1.10.16) were found to correlate well with the approximate algebraic relation

$$\kappa_{L_s} \cong 1 + (0.0042R_A - 0.068) \left(1 + 2.3 \frac{C_{L,\alpha}\Omega}{\bar{C}_{L_{\max}}} \right) \quad (1.10.18)$$

Equation (1.10.18) was obtained from computations of the maximum wing lift coefficient for 25 different wing geometries. These wings had aspect ratios ranging from 4 to 20, taper ratios from 0.5 to 1.0, quarter-chord sweep angles from 0 to 30 degrees, and linear geometric washout ranging from 0 to 8 degrees.

When estimating a maximum wing lift coefficient from Eq. (1.10.16), it is essential that the maximum 2-D airfoil section lift coefficient be evaluated at the same Reynolds number and Mach number as those for the 3-D wing. For the case of a rectangular wing this is rather straightforward. However, for an elliptic or tapered wing the section Reynolds number is not constant across the wingspan. This gives rise to an important question regarding what characteristic length should be used to define the Reynolds number associated with predicting the maximum lift coefficient for a wing of arbitrary planform. The simplest choice would be the mean chord length defined by Eq. (1.8.81) or the mean aerodynamic chord defined by Eq. (1.8.86). However, neither of these chord lengths provides a particularly suitable characteristic length for defining the Reynolds number associated with wing stall. A more appropriate characteristic length for this purpose is the chord length of the wing section supporting the maximum section lift coefficient.

The spanwise coordinate of the maximum airfoil section lift coefficient at the onset of stall depends on wing taper, twist, and sweep. For an untwisted rectangular wing with no sweep, the onset of airfoil section stall always occurs at the wing root. As wing taper ratio is decreased from 1.0, the point of maximum airfoil section lift coefficient moves outboard from the root. Adding sweep to the wing also moves the point of maximum section lift coefficient outboard. On the other hand, adding washout to a wing with taper and/or sweep moves the point of maximum airfoil section lift coefficient inboard. Lifting-line theory can be used to predict the spanwise coordinate of the wing section that supports the maximum airfoil section lift coefficient. For tapered wings with no sweep or twist, the coordinate of the maximum section lift coefficient may be obtained from Fig. 1.10.2.

Results obtained from Fig. 1.10.2 can be modified to account for the effects of twist and sweep. The spanwise coordinate of the wing section that supports the maximum section lift coefficient can be estimated from

$$\frac{z_{\max}}{b} = 0.5 - \kappa_{ZA} \left[0.5 - \kappa_{Z\Omega} \left(\frac{z_{\max}}{b} \right)_{\substack{\Omega=0 \\ A=0}} \right] \quad (1.10.19)$$

For wings with linear taper and linear twist, $\kappa_{Z\Omega}$ and κ_{ZA} are obtained from Figs. 1.10.8 and 1.10.9, respectively.

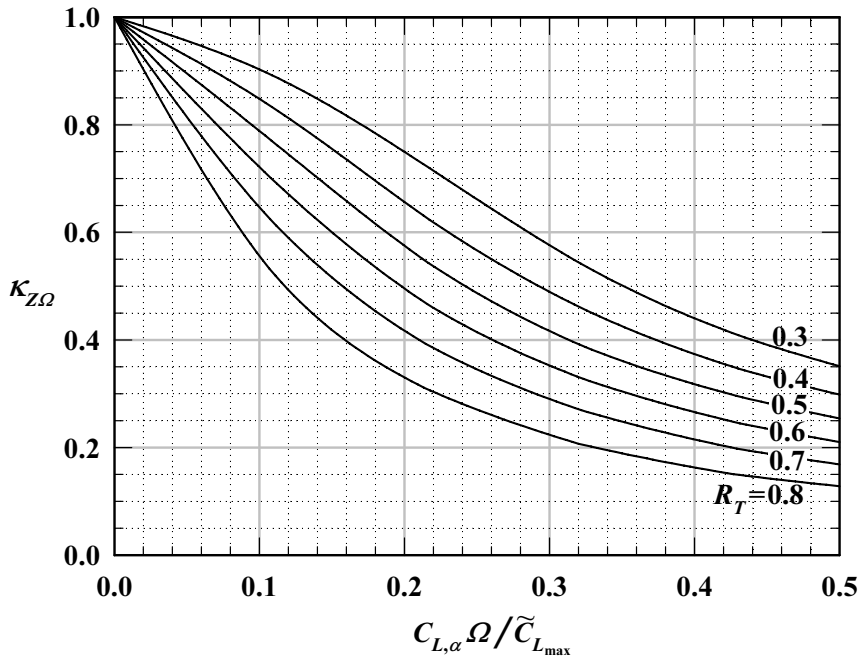


Figure 1.10.8. Twist coefficient $K_{Z\Omega}$ to be used in Eq. (1.10.19) for wings with linear twist.

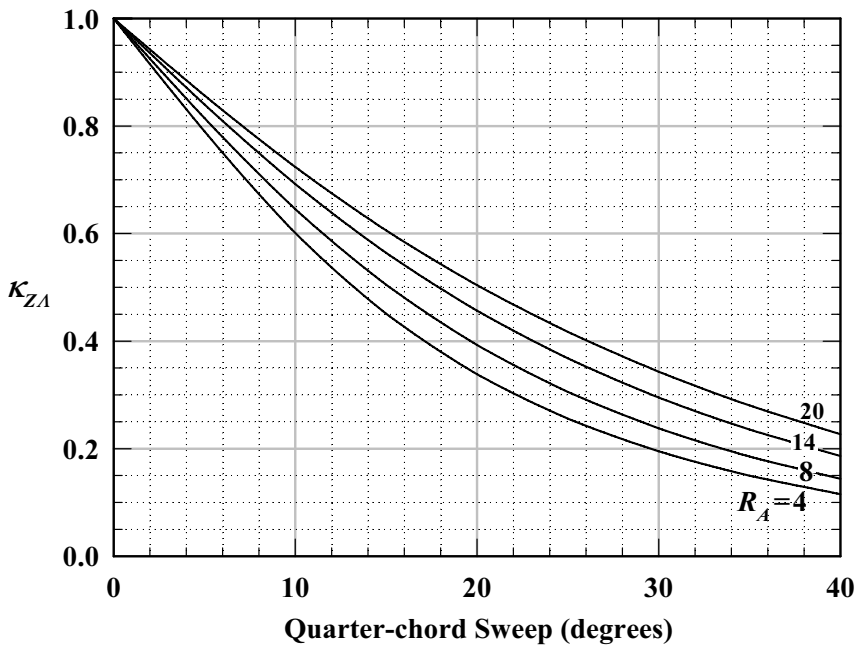


Figure 1.10.9. Sweep coefficient $K_{Z\Lambda}$ to be used in Eq. (1.10.19) for wings with linear taper.

1.10. Wing Stall and Maximum Lift Coefficient 119

EXAMPLE 1.10.1. Consider a wing with linear taper of aspect ratio 8.0 and taper ratio 0.5. The wing has a span of 196 feet and a thin airfoil section having a constant maximum section lift coefficient of 1.6. We wish to estimate the maximum wing lift coefficient and the section chord length at the onset of airfoil section stall for this wing planform with the following amounts of quarter-chord sweep and linear washout:

$$A = 0, \Omega = 0; \quad A = 0, \Omega = 4^\circ; \quad A = 30^\circ, \Omega = 0; \quad A = 30^\circ, \Omega = 4^\circ$$

Solution. Using an airfoil section lift slope of 2π in Eq. (1.8.26) with κ_L obtained from Fig. 1.8.13, for the unswept wing we have

$$\kappa_L = 0.0125, \quad C_{L,\alpha} = \frac{\tilde{C}_{L,\alpha}}{[1 + \tilde{C}_{L,\alpha}/(\pi R_A)](1 + \kappa_L)} = 4.964$$

From Figs. 1.10.1, 1.10.2, 1.10.6, and 1.10.7 we obtain

$$\left(\frac{C_L}{\tilde{C}_{L_{\max}}} \right)_{\substack{\Omega=0 \\ A=0}} = 0.943, \quad \left(\frac{z_{\max}}{b} \right)_{\substack{\Omega=0 \\ A=0}} = 0.264, \quad \kappa_{A1} = 0.38, \quad \kappa_{A2} = 0.89$$

With 4 degrees of linear washout, Figs. 1.10.5 and 1.10.8 and Eq. (1.10.18) yield

$$\frac{C_{L,\alpha} \Omega}{\tilde{C}_{L_{\max}}} = 0.2166, \quad \kappa_{L\Omega} = 0.034, \quad \kappa_{Z\Omega} = 0.54, \quad \kappa_{Ls} = 0.948$$

For 30 degrees sweep and no washout, Eqs. (1.10.17) and (1.10.18) and Fig. 1.10.9 give

$$A = 0.5236, \quad \kappa_{LA} = 0.79, \quad \kappa_{Ls} = 0.966, \quad \kappa_{ZA} = 0.24$$

The maximum wing lift coefficient is obtained from Eq. (1.10.16), the z -coordinate of the wing section supporting the maximum section lift coefficient is estimated from Eq. (1.10.19), and the chord length at the position of the maximum section lift coefficient is found from

$$c_{\max} = \frac{2b}{R_A(1 + R_T)} \left[1 - (1 - R_T) \left| 2z_{\max}/b \right| \right]$$

Thus we obtain

A	Ω	κ_{Ls}	κ_{LA}	$\kappa_{L\Omega}$	$C_{L_{\max}}$	κ_{ZA}	$\kappa_{Z\Omega}$	z_{\max}/b	c_{\max}
0°	0°	0.966	1.00		1.46	1.00	1.00	0.264	24.0
0°	4°	0.948	1.00	0.034	1.42	1.00	0.54	0.143	28.0
30°	0°	0.966	0.79		1.15	0.24	1.00	0.443	18.2
30°	4°	0.948	0.79	0.034	1.12	0.24	0.54	0.414	19.1

1.11. Wing Aerodynamic Center and Pitching Moment

The distribution of section aerodynamic loads acting on a spanwise symmetric wing with spanwise symmetric loading can be replaced with a resultant force vector acting at the aerodynamic center of the wing and a pitching moment that does not vary with small changes in angle of attack. For a spanwise symmetric wing with no sweep in the locus of airfoil section aerodynamic centers, the section aerodynamic center of each airfoil section falls at the same axial coordinate. Thus, for unswept wings, the aerodynamic center of the complete wing lies in the plane of symmetry at the same axial coordinate as the section aerodynamic centers of the root airfoil section, independent of the spanwise section lift distribution. However, for swept wings, the axial coordinate of the section aerodynamic center is a function of the spanwise coordinate, and the axial position of the wing's aerodynamic center is not obvious from simple inspection.

Wing sweep affects the position of the aerodynamic center of a wing in two ways. First and most obvious, when the wing is swept back, the locus of airfoil section aerodynamic centers on the outboard sections of the wing are moved aft of the aerodynamic center of the root airfoil section. Thus, lift developed on a swept wing contributes significantly to the pitching moment about the aerodynamic center of the root airfoil section. In addition, sweep alters the vorticity-induced downwash distribution over the wing planform. Moving the wingtip vortex aft of the wing root tends to reduce the downwash induced on the inboard sections of the wing. On the other hand, the bound vorticity on one semispan of a swept wing induces downwash on the opposite semispan. This tends to increase the wing downwash, more so on the inboard sections of the wing. Thus, not only does sweep alter the geometry of the locus of airfoil section aerodynamic centers, it changes the spanwise section lift distribution as well.

To examine how the aerodynamic center of a swept wing can be located, we first consider the pitching moment developed by an arbitrary wing. From Fig. 1.11.1, the pitching moment about the origin, $x=0, y=0$, for a wing of arbitrary planform and dihedral can be written as

$$m_0 = \int_{z=-b/2}^{b/2} \tilde{m}_{ac} dz - \int_{z=-b/2}^{b/2} (\tilde{L} \cos \alpha + \tilde{D} \sin \alpha) \tilde{x}_{ac} dz - \int_{z=-b/2}^{b/2} (\tilde{L} \sin \alpha - \tilde{D} \cos \alpha) \tilde{y}_{ac} dz \quad (1.11.1)$$

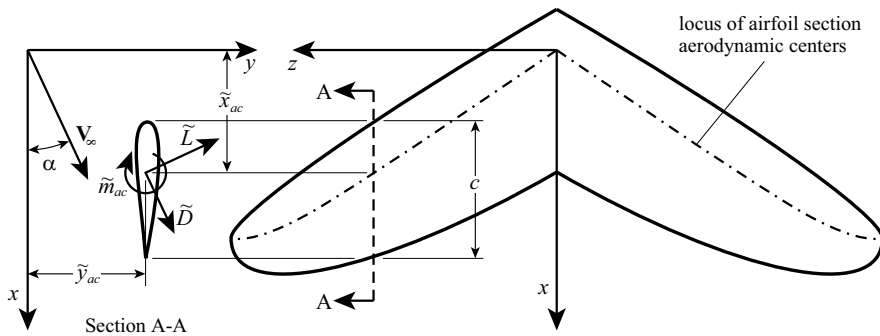


Figure 1.11.1. Section lift, drag, and pitching moment acting on a section of an arbitrary wing.

1.11. Wing Aerodynamic Center and Pitching Moment 121

where \tilde{x}_{ac} and \tilde{y}_{ac} denote the x - and y -coordinates of the locus of airfoil section aerodynamic centers measured relative to the root section aerodynamic center. Note that in Eq. (1.11.1), \tilde{m}_{ac} , \tilde{L} , and \tilde{D} are section moment and force components per unit span, not per unit distance measured parallel with the local dihedral. Dividing Eq. (1.11.1) by the dynamic pressure, planform area, and reference chord length yields

$$C_{m_0} \equiv \frac{m_0}{\frac{1}{2}\rho_\infty V_\infty^2 S c_{\text{ref}}} = \frac{1}{S c_{\text{ref}}} \int_{z=-b/2}^{b/2} \tilde{C}_{m_{ac}} c^2 dz - \frac{1}{S c_{\text{ref}}} \int_{z=-b/2}^{b/2} (\tilde{C}_L \cos \alpha + \tilde{C}_D \sin \alpha) c \tilde{x}_{ac} dz - \frac{1}{S c_{\text{ref}}} \int_{z=-b/2}^{b/2} (\tilde{C}_L \sin \alpha - \tilde{C}_D \cos \alpha) c \tilde{y}_{ac} dz \quad (1.11.2)$$

Because drag is typically small compared with the lift, drag is commonly neglected when estimating the position of the aerodynamic center at small angles of attack. Furthermore, the trigonometric functions that appear in Eq. (1.11.2) are traditionally linearized using the small-angle approximations $\cos(\alpha) \cong 1$ and $\sin(\alpha) \cong \alpha$. Thus, for small angles of attack, Eq. (1.11.2) can be approximated as

$$C_{m_0} \cong \frac{1}{S c_{\text{ref}}} \left(\int_{z=-b/2}^{b/2} \tilde{C}_{m_{ac}} c^2 dz - \int_{z=-b/2}^{b/2} \tilde{C}_L c \tilde{x}_{ac} dz - \int_{z=-b/2}^{b/2} \tilde{C}_L \alpha c \tilde{y}_{ac} dz \right) \quad (1.11.3)$$

The dihedral angle for most wings is small enough so that we can neglect the product of the angle of attack and the y -offset between the outboard airfoil sections and the root airfoil section, i.e., $\alpha \tilde{y}_{ac} \cong 0$. Additionally, for a spanwise symmetric wing with spanwise symmetric lift, each semispan contributes equally to the pitching moment. Thus, for symmetric wings with small dihedral angles operating at small angles of attack, the wing pitching moment coefficient about the root airfoil section aerodynamic center can be approximated as

$$C_{m_0} \cong \frac{2}{S c_{\text{ref}}} \int_{z=0}^{b/2} \tilde{C}_{m_{ac}} c^2 dz - \frac{2}{S c_{\text{ref}}} \int_{z=0}^{b/2} \tilde{C}_L c \tilde{x}_{ac} dz \quad (1.11.4)$$

The distributed aerodynamic loads acting on the wing can be replaced with a resultant force and moment acting at the aerodynamic center of the wing (\bar{x}_{ac} , \bar{y}_{ac}). Thus, the pitching moment about the origin can also be written as

$$m_0 = m_{ac} - \bar{x}_{ac} (L \cos \alpha + D \sin \alpha) - \bar{y}_{ac} (L \sin \alpha - D \cos \alpha) \quad (1.11.5)$$

where m_{ac} is the pitching moment about the aerodynamic center of the wing. Dividing by the dynamic pressure, planform area, and reference chord length, Eq. (1.11.5) can be written in dimensionless form as

122 Chapter 1 Overview of Aerodynamics

$$C_{m_0} = C_{m_{ac}} - \frac{\bar{x}_{ac}}{c_{ref}}(C_L \cos \alpha + C_D \sin \alpha) - \frac{\bar{y}_{ac}}{c_{ref}}(C_L \sin \alpha - C_D \cos \alpha) \quad (1.11.6)$$

We now apply the same small-angle approximations to Eq. (1.11.6) that were used to obtain Eq. (1.11.4) from Eq. (1.11.2). That is, we neglect drag, $C_D \cong 0$, assume small angles of attack, $\cos(\alpha) \cong 1$ and $\sin(\alpha) \cong \alpha$, and assume small dihedral angles, $\alpha \bar{y}_{ac} \cong 0$. Thus, Eq. (1.11.6) is traditionally approximated as

$$C_{m_0} \cong C_{m_{ac}} - \frac{\bar{x}_{ac}}{c_{ref}} C_L \quad (1.11.7)$$

Combining Eqs. (1.11.4) and (1.11.7) to eliminate the pitching moment coefficient about the origin gives

$$C_{m_{ac}} - \frac{\bar{x}_{ac}}{c_{ref}} C_L \cong \frac{2}{S c_{ref}} \int_{z=0}^{b/2} \tilde{C}_{m_{ac}} c^2 dz - \frac{2}{S c_{ref}} \int_{z=0}^{b/2} \tilde{C}_L c \tilde{x}_{ac} dz \quad (1.11.8)$$

By definition, $C_{m_{ac}}$, \bar{x}_{ac} , $\tilde{C}_{m_{ac}}$, and \tilde{x}_{ac} do not vary with small changes in angle of attack. Accordingly, differentiating Eq. (1.11.8) with respect to angle of attack and rearranging yields a relation for the axial position of the wing aerodynamic center in terms of the spanwise section lift distribution. Thus, **for the common case of symmetric wings with small dihedral angles operating at small angles of attack, the axial position of the wing aerodynamic center is traditionally approximated as**

$$\bar{x}_{ac} \cong \frac{1}{C_{L,\alpha}} \frac{\partial}{\partial \alpha} \left(\frac{2}{S} \int_{z=0}^{b/2} \tilde{C}_L c \tilde{x}_{ac} dz \right) \quad (1.11.9)$$

From Eq. (1.11.9) we see that determination of the axial position of the aerodynamic center of a swept wing requires knowledge of the spanwise section lift distribution. Because an analytical solution for the section lift distribution acting on a swept wing does not exist, predictions for the position of the aerodynamic center of swept wings require numerical solutions. Inviscid panel codes and computational fluid dynamics (CFD) are commonly used for this purpose.

As a first approximation, the aerodynamic center of a swept wing is sometimes assumed to be located at the same axial position as the section aerodynamic center of the airfoil section located at the spanwise coordinate of the semispan area centroid. For wings with constant quarter-chord sweep and linear taper, i.e., trapezoidal wings, we have $\bar{x}_c = \bar{z}_c \tan \Lambda$ and from Eq. (1.8.100) this approximation results in

$$\frac{\bar{x}_{ac}}{\bar{c}} \cong \frac{\bar{x}_c}{\bar{c}} = \frac{R_A}{6} \frac{1+2R_T}{1+R_T} \tan \Lambda \quad (1.11.10)$$

The approximation given by Eq. (1.11.10) is equivalent to assuming that the section lift coefficient is constant over the wingspan.

1.11. Wing Aerodynamic Center and Pitching Moment 123

Another commonly used approximation was first suggested by Anderson (1937). **This approximation neglects any changes in the section lift distribution that result from wing sweep.** For wings with constant quarter-chord sweep, $\bar{x}_{ac} = \bar{z}_{ac} \tan \Lambda$, where \bar{z}_{ac} is the z -coordinate of the semispan aerodynamic center. Thus, from Eq. (1.8.109) Anderson's approximation yields

$$\frac{\bar{x}_{ac}}{\bar{c}} \cong \frac{2R_A}{3\pi} \left(1 + \sum_{n=1}^{\infty} \frac{(-1)^{n-1} 3}{4n^2 + 4n - 3} \frac{a_{2n+1}}{a_1} \right) \tan \Lambda \quad (1.11.11)$$

Predictions from Eqs. (1.11.10) and (1.11.11) are compared with CFD solutions in Fig. 1.11.2. Results for 236 wings with constant linear taper and constant quarter-chord sweep are shown in Fig. 1.11.2. Wing aspect ratio was varied from 4.0 to 20 and taper ratios from 0.25 to 1.0 were investigated. For a given taper and aspect ratio, the quarter-chord sweep angle was varied from 0 to 50 degrees. All wings had airfoil sections from the NACA 4-digit airfoil series with camber varied from 0 to 4 percent and thickness ranging from 6 to 18 percent. To investigate the effects of wing twist, linear geometric washout was varied from -4.0 to $+8.0$ degrees. For further details regarding the CFD solutions presented in Fig. 1.11.2, see Phillips, Hunsaker, and Niewoehner (2008).

In Fig. 1.11.2, the location of each aerodynamic center is presented as a deviation from the result predicted by Eq. (1.11.10). This deviation is plotted as a function of the

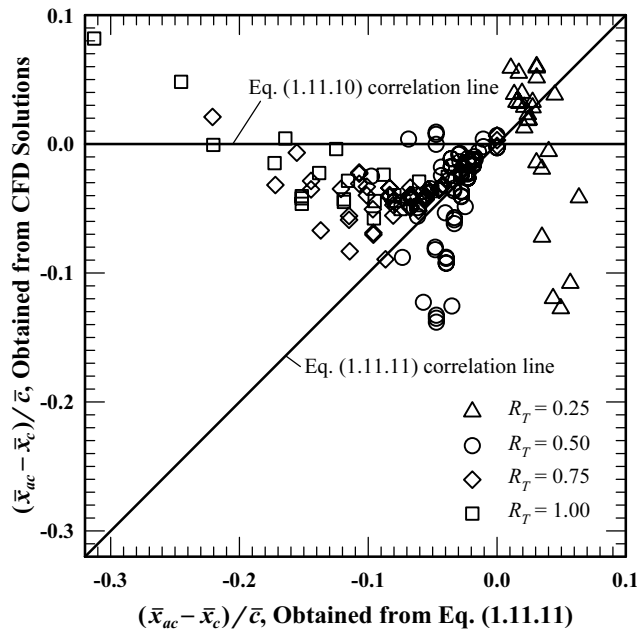


Figure 1.11.2. Deviation of the wing aerodynamic center from the section aerodynamic center of the airfoil located at the semispan centroidal chord as predicted from computational fluid dynamics results vs. the same deviation predicted from Eq. (1.11.11).

124 Chapter 1 Overview of Aerodynamics

same deviation as predicted from Eq. (1.11.11). To see how the data that are plotted in Fig. 1.11.2 are used to assess the accuracy of Eqs. (1.11.10) and (1.11.11), we first recognize that if Eq. (1.11.10) were precise, each aerodynamic center would have the same axial coordinate as the airfoil section aerodynamic center of the semispan centroidal chord. Thus, exact correlation of Eq. (1.11.10) with the CFD results would cause all points in Fig. 1.11.2 to fall along a horizontal line with the vertical ordinate of zero. This is the line denoted as the Eq. (1.11.10) correlation line in Fig. 1.11.2. On the other hand, if Eq. (1.11.11) were to match the CFD predictions exactly, all points in Fig. 1.11.2 would fall along the 45-degree line, which is labeled as the Eq. (1.11.11) correlation line. From the results plotted in Fig. 1.11.2, we see that neither Eq. (1.11.10) nor Eq. (1.11.11) is accurate over a wide range of wing geometry.

Notice from Fig. 1.11.2 that Eq. (1.11.10) seems to be more accurate for the majority of the rectangular wings, whereas the results for many of the wings having a taper ratio of 0.5 agree more closely with Eq. (1.11.11). The reader should particularly notice the heavy concentration of circular symbols just below the intersection of the Eq. (1.11.10) and Eq. (1.11.11) correlation lines. Most of these data are for wings having a taper ratio of 0.5 with quarter-chord sweep angles in the range between 25 and 35 degrees. These results agree closely with Eq. (1.11.11) and show that for such commonly used wing geometries, the lifting-line result presented in Eq. (1.11.11) gives a reasonable first approximation for the position of the aerodynamic center of the wing. However, **for the case of more general wing geometry, neither Eq. (1.11.10) nor Eq. (1.11.11) should be used to predict the aerodynamic center of a swept wing.** These approximations are included here only for historical reasons and because they are likely to be encountered in the literature.

For swept trapezoidal wings, an improved approximation for the axial position of the aerodynamic center is obtained by multiplying the right-hand side of Eq. (1.11.11) by an empirical sweep correction factor

$$\frac{\bar{x}_{ac}}{\bar{c}} \cong \kappa_{ac} \frac{2R_A}{3\pi} \left(1 + \sum_{n=1}^{\infty} \frac{(-1)^{n-1} 3}{4n^2 + 4n - 3} \frac{a_{2n+1}}{a_1} \right) \tan \Lambda = \kappa_{ac} R_A \left(\frac{\bar{z}_{ac}}{b} \right)_{\Lambda=0} \tan \Lambda \quad (1.11.12)$$

where $(\bar{z}_{ac})_{\Lambda=0}$ is the z -coordinate of the semispan aerodynamic center for an unswept wing of the same planform, which can be obtained from Eq. (1.8.109) or Fig. 1.8.29. Results for κ_{ac} , which were presented by Phillips, Hunsaker, and Niewoehner (2008), are shown in Fig. 1.11.3 as a function of wing taper ratio, aspect ratio, and quarter-chord sweep angle. Other results obtained in the same study show that **wing camber, thickness, and twist have no significant effect on the position of the aerodynamic center of a swept wing.** In Fig. 1.11.3 notice that for wings of taper ratio near 0.5, aspect ratios in the range of 6 to 8, and quarter-chord sweep angles near 30 degrees, all values of κ_{ac} are close to unity. This means that the lifting-line solution presented in Eq. (1.11.11) provides a good approximation for this commonly used wing geometry, without using the empirical correction factor. On the other hand, both Fig. 1.11.2 and Fig. 1.11.3 show that **some wing geometries result in very large discrepancies between Eq. (1.11.11) and results obtained from CFD solutions.**

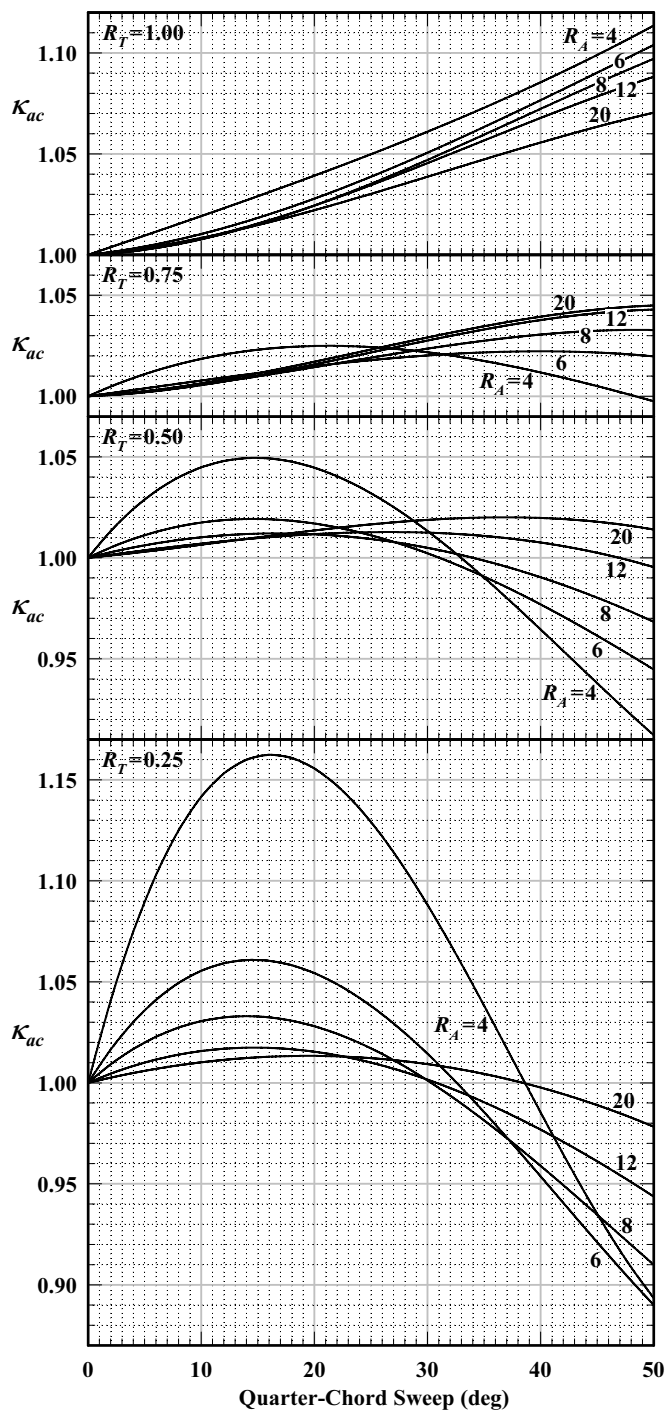


Figure 1.11.3. Effects of wing sweep on the location of the aerodynamic center of a wing.

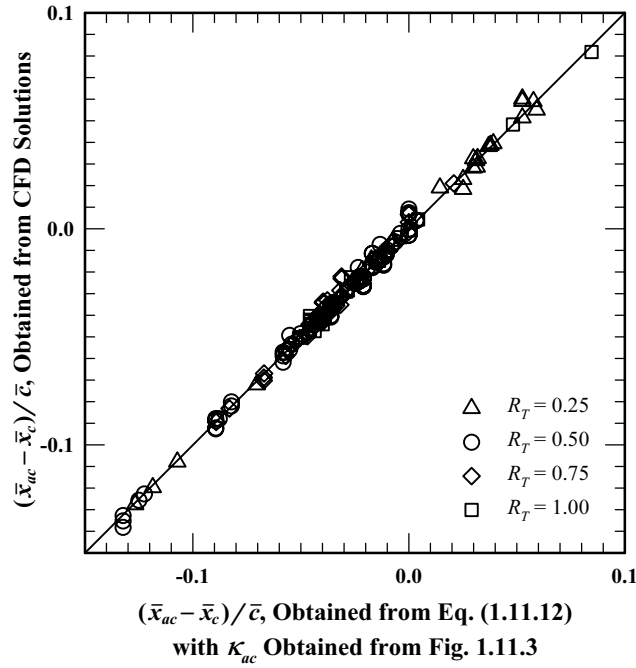


Figure 1.11.4. Deviation of the wing aerodynamic center from the section aerodynamic center of the airfoil located at the semispan centroidal chord as predicted from computational fluid dynamics results vs. the same deviation predicted from Eq. (1.11.12).

Figure 1.11.4 shows the same CFD solutions presented in Fig. 1.11.2 compared with results predicted from Eq. (1.11.12) using the values for κ_{ac} that are plotted in Fig. 1.11.3. Comparing Fig. 1.11.4 with Fig. 1.11.2, we see that using the empirical sweep correction factor plotted in Fig. 1.11.3 provides a very significant improvement over Eq. (1.11.11).

Once the aerodynamic center of a wing is located, the pitching moment coefficient about that aerodynamic center can be determined from the lift coefficient and pitching moment coefficient about the origin. Rearranging Eq. (1.11.7) yields

$$C_{m_{ac}} \cong C_{m_0} + \frac{\bar{x}_{ac}}{c_{ref}} C_L \quad (1.11.13)$$

The pitching moment coefficient about the origin is approximated from Eq. (1.11.4). Using this result in Eq. (1.11.13) we obtain

$$C_{m_{ac}} \cong \frac{2}{S c_{ref}} \int_{z=0}^{b/2} \tilde{C}_{m_{ac}} c^2 dz - \frac{1}{c_{ref}} \left(\frac{2}{S} \int_{z=0}^{b/2} \tilde{C}_L c \tilde{x}_{ac} dz - \bar{x}_{ac} C_L \right) \quad (1.11.14)$$

The total section lift coefficient is the sum of the basic and additional section lift coefficients, $\tilde{C}_L = \tilde{C}_{L_b} + \tilde{C}_{L_a}$, and the axial coordinate of the wing aerodynamic center can

1.11. Wing Aerodynamic Center and Pitching Moment 127

be expressed in terms of the additional section lift coefficient in a manner similar to that used to obtain Eq. (1.8.110),

$$\bar{x}_{ac} \cong \frac{2}{S C_L} \int_{z=0}^{b/2} \tilde{C}_{L_a} c \tilde{x}_{ac} dz \quad (1.11.15)$$

Thus, the pitching moment coefficient about the aerodynamic center of the wing can be expressed in terms of only the airfoil section pitching moment coefficient and the spanwise variation in local section lift coefficient that occurs when the net lift developed by the wing is zero. Using Eq. (1.11.15) in Eq. (1.11.14), **for symmetric wings with small dihedral angles operating at small angles of attack, the pitching moment coefficient about the wing aerodynamic center can be approximated as**

$$C_{m_{ac}} \cong \frac{2}{S c_{ref}} \int_{z=0}^{b/2} \tilde{C}_{m_{ac}} c^2 dz - \frac{2}{S c_{ref}} \int_{z=0}^{b/2} \tilde{C}_{L_b} c \tilde{x}_{ac} dz \quad (1.11.16)$$

The first term on the right-hand side of Eq. (1.11.16) results from the effects of camber and is simply twice the semispan contribution for an unswept wing of the same planform, which is given by Eq. (1.8.102) or Eq. (1.8.104). The second term on the right-hand side of Eq. (1.11.16) results only from wing twist.

For wings with constant quarter-chord sweep, the x -coordinate of the locus of airfoil section aerodynamic centers is proportional to the z -coordinate, $\tilde{x}_{ac} = z \tan \Lambda$, and after using Eq. (1.8.104) in Eq. (1.11.16) we have

$$C_{m_{ac}} \cong \frac{\bar{c}_{mac}}{c_{ref}} \bar{C}_{m_{ac}} - \frac{2 \tan \Lambda}{S c_{ref}} \int_{z=0}^{b/2} \tilde{C}_{L_b} c z dz \quad (1.11.17)$$

For unswept wings the integral on the right-hand side of Eq. (1.11.17) can be evaluated from Eq. (1.8.96). Results presented by Anderson (1937) suggest that this same result can be used in Eq. (1.11.17) as a first approximation for swept wings. Following a procedure similar to that used to develop Eq. (1.11.12), Phillips, Hunsaker, and Niewoehner (2008) have shown that improved results can be obtained from the relation

$$C_{m_{ac}} \cong \frac{\bar{c}_{mac}}{c_{ref}} \bar{C}_{m_{ac}} + \kappa_{M\Omega} \frac{\tan(\kappa_{MA} \Lambda)}{c_{ref}/b} C_{L,\alpha} \Omega \quad (1.11.18)$$

where $\kappa_{M\Omega}$ is the twist factor for an unswept wing of the same planform, which can be evaluated from Eq. (1.8.113) or Fig. 1.8.30. The wing lift slope in Eq. (1.11.18) is that for the swept wing, which can be estimated from

$$C_{L,\alpha} \cong \pi R_A a_1 \kappa_{L\alpha} = (C_{L,\alpha})_{A=0} \kappa_{L\alpha} \quad (1.11.19)$$

where $\kappa_{L\alpha}$ can be obtained from Fig. 1.11.5. The sweep factor κ_{MA} in Eq. (1.11.18) is obtained from Fig. 1.11.6.

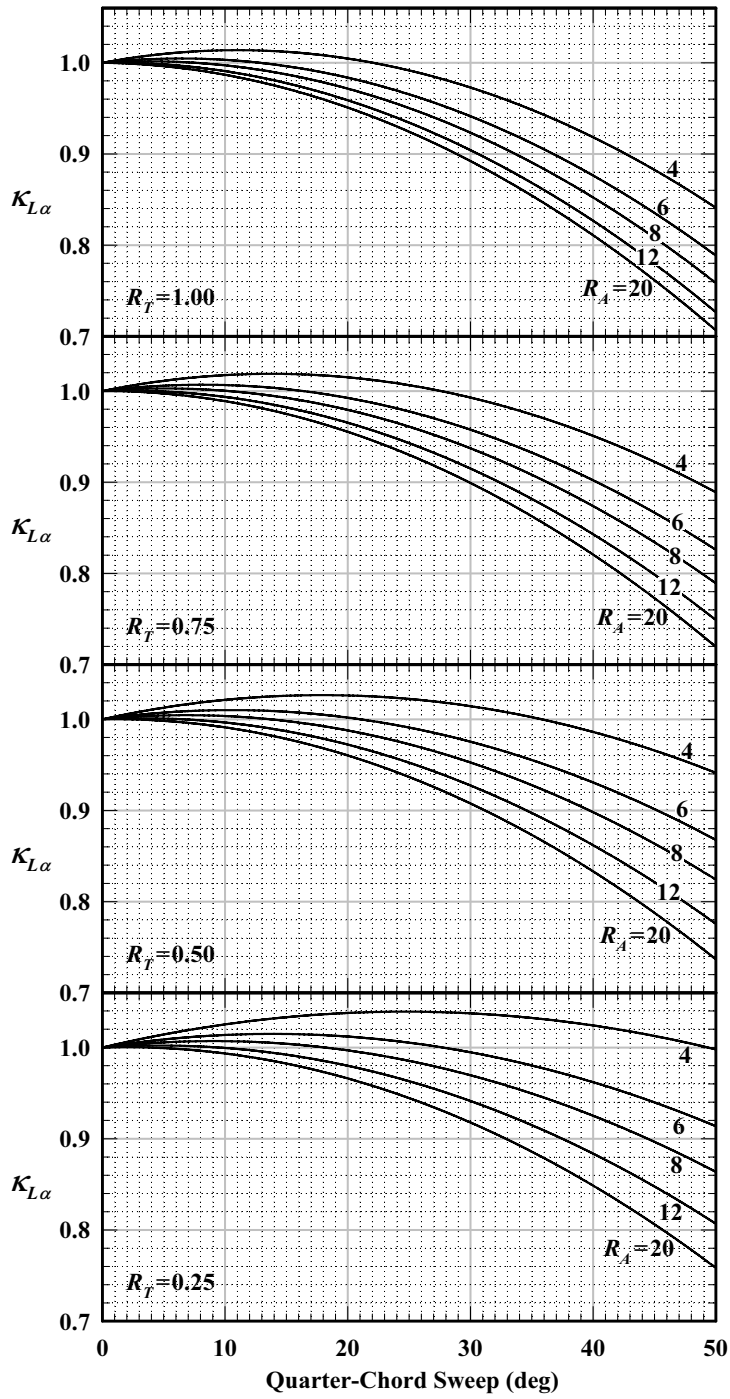


Figure 1.11.5. Effects of wing sweep on the lift slope.

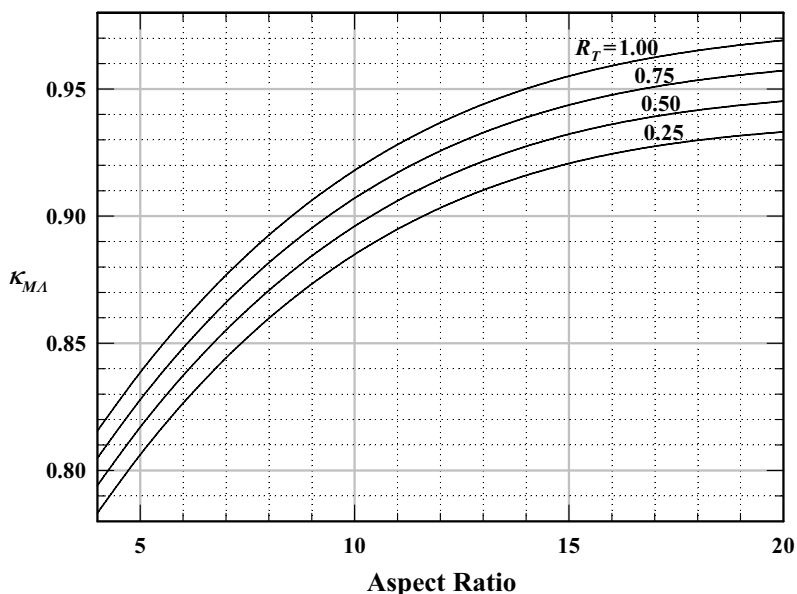


Figure 1.11.6. Sweep factor in the relation for wing pitching moment coefficients about the wing aerodynamic center.

EXAMPLE 1.11.1. Consider a wing with linear taper of aspect ratio 8.0 and taper ratio 0.5. The wing has a span of 196 feet and a thin symmetric airfoil section. We wish to estimate the axial position of the wing aerodynamic center and the pitching moment coefficient about that aerodynamic center for this wing planform with the following amounts of quarter-chord sweep and linear washout:

$$\Lambda = 15^\circ, \Omega = 0; \quad \Lambda = 15^\circ, \Omega = 4^\circ; \quad \Lambda = 30^\circ, \Omega = 0; \quad \Lambda = 30^\circ, \Omega = 4^\circ$$

Solution. Using an airfoil section lift slope of 2π in Eq. (1.8.26) with κ_L obtained from Fig. 1.8.13, for an unswept wing of the same planform we have

$$\kappa_L = 0.0125 \quad \text{and} \quad (C_{L,\alpha})_{\Lambda=0} = \frac{\tilde{C}_{L,\alpha}}{[1 + \tilde{C}_{L,\alpha}/(\pi R_A)](1 + \kappa_L)} = 4.964$$

From Figs. 1.8.29 and 1.8.30 we obtain

$$\left(\frac{\bar{z}_{ac}}{b}\right)_{\Lambda=0} = 0.216 \quad \text{and} \quad \kappa_{M\Omega} = 0.0262$$

With 15 degrees of sweep, Figs. 1.11.3 and 1.11.5 and Eq. (1.11.19) yield

$$\kappa_{ac} = 1.012, \quad \kappa_{L\alpha} = 0.998, \quad \text{and} \quad C_{L,\alpha} \cong (C_{L,\alpha})_{\Lambda=0} \kappa_{L\alpha} = 4.954$$

130 Chapter 1 Overview of Aerodynamics

Similarly, with 30 degrees of sweep

$$\kappa_{ac} = 1.005, \quad \kappa_{L\alpha} = 0.953, \quad \text{and} \quad C_{L,\alpha} \cong (C_{L,\alpha})_{\Lambda=0} \kappa_{L\alpha} = 4.731$$

From Figs. 1.11.6 we obtain

$$\kappa_{MA} = 0.871$$

The axial position of the wing aerodynamic center measured aft of the root quarter chord is estimated from Eq. (1.11.12). This result is independent of wing twist and for 15 degrees of sweep we obtain

$$\begin{aligned} \bar{x}_{ac} &\cong \frac{S}{b} \kappa_{ac} R_A \left(\frac{\bar{z}_{ac}}{b} \right)_{\Lambda=0} \tan \Lambda = \kappa_{ac} b \left(\frac{\bar{z}_{ac}}{b} \right)_{\Lambda=0} \tan \Lambda \\ &= 1.012 \times 196 \times 0.216 \times \tan(15^\circ) = 11.48 \text{ ft} \end{aligned}$$

Similarly, with 30 degrees of sweep

$$\bar{x}_{ac} \cong \kappa_{ac} b \left(\frac{\bar{z}_{ac}}{b} \right)_{\Lambda=0} \tan \Lambda = 1.005 \times 196 \times 0.216 \times \tan(30^\circ) = 24.56 \text{ ft}$$

The pitching moment coefficient about the wing aerodynamic center can be estimated from Eq. (1.11.18). Because this wing has a symmetric airfoil section, the airfoil section pitching moment and the first term in Eq. (1.11.18) are zero. Furthermore, because the second term in Eq. (1.11.18) is proportional to the wing twist, the pitching moment coefficient about the aerodynamic center of the untwisted wings is zero. Using Eq. (1.11.18) and choosing the mean chord as the reference length, for the wing with 15 degrees of sweep and 4 degrees of washout we obtain

$$\begin{aligned} C_{m_{ac}} &\cong \frac{\bar{c}_{mac}}{c_{\text{ref}}} \bar{C}_{m_{ac}} + \kappa_{M\Omega} \frac{\tan(\kappa_{MA} \Lambda)}{\bar{c}/b} C_{L,\alpha} \Omega \\ &= 0.0 + 0.0262 \frac{\tan(0.871 \times 15^\circ)}{1/8} 4.954 (4 \times \pi / 180) = 0.0168 \end{aligned}$$

Similarly, with 30 degrees of sweep and 4 degrees of washout

$$C_{m_{ac}} \cong 0.0 + 0.0262 \frac{\tan(0.871 \times 30^\circ)}{1/8} 4.731 (4 \times \pi / 180) = 0.0340$$

Λ	Ω	κ_{ac}	$(\bar{z}_{ac}/b)_0$	\bar{x}_{ac} (ft)	$\bar{C}_{m_{ac}}$	$C_{L,\alpha}$	$\kappa_{M\Omega}$	κ_{MA}	$C_{m_{ac}}$
15°	0°	1.012	0.216	11.48	0.0000	4.954	0.0262	0.871	0.0000
15°	4°	1.012	0.216	11.48	0.0000	4.954	0.0262	0.871	0.0168
30°	0°	1.005	0.216	24.56	0.0000	4.731	0.0262	0.871	0.0000
30°	4°	1.005	0.216	24.56	0.0000	4.731	0.0262	0.871	0.0340

1.12. Inviscid Compressible Aerodynamics

In the analytical methods that were reviewed in Secs. 1.6 through 1.10, the variation in air density was assumed to be negligible. This is a reasonable approximation for flight Mach numbers less than about 0.3. For higher flight Mach numbers, compressibility effects become increasingly important. For flight speeds near or exceeding the speed of sound, the effects of compressibility vastly alter the airflow about an aircraft in flight. In this and the following sections, we review some of the important concepts associated with compressible aerodynamics.

As discussed in Sec. 1.4, inviscid flow over any body immersed in a uniform flow is irrotational. Any irrotational flow is a potential flow. There is no requirement that the flow be incompressible. Thus, the velocity field for inviscid flow about a body immersed in uniform flow can always be expressed according to Eq. (1.4.14):

$$\mathbf{V} = \nabla\phi \quad (1.12.1)$$

where ϕ is the scalar velocity potential. From Eq. (1.4.5), the continuity equation for steady compressible flow is

$$(\mathbf{V} \cdot \nabla)\rho + \rho \nabla \cdot \mathbf{V} = 0 \quad (1.12.2)$$

Inviscid adiabatic flow is isentropic. For an ideal gas this requires that

$$\frac{p}{p_0} = \left(\frac{\rho}{\rho_0} \right)^\gamma \quad (1.12.3)$$

where p_0 and ρ_0 are the stagnation pressure and density. For steady isentropic flow of an ideal gas, the momentum equation is expressed in Eq. (1.4.19):

$$\frac{1}{2}V^2 + \frac{\gamma}{\gamma-1} \frac{p}{\rho} = \frac{\gamma}{\gamma-1} \frac{p_0}{\rho_0} \quad (1.12.4)$$

For an ideal gas

$$p/\rho = RT \quad (1.12.5)$$

$$a^2 = \gamma RT \quad (1.12.6)$$

Substituting Eqs. (1.12.5) and (1.12.6) into Eq. (1.12.3) gives

$$\frac{p}{p_0} = \frac{RT\rho}{RT_0\rho_0} = \frac{\gamma RT\rho}{\gamma RT_0\rho_0} = \frac{a^2\rho}{a_0^2\rho_0} = \left(\frac{\rho}{\rho_0} \right)^\gamma \quad (1.12.7)$$

Similarly, applying Eqs. (1.12.5) and (1.12.6) to Eq. (1.12.4) yields

132 Chapter 1 Overview of Aerodynamics

$$\frac{1}{2}V^2 + \frac{a^2}{\gamma-1} = \frac{a_0^2}{\gamma-1} \quad (1.12.8)$$

Solving Eq. (1.12.7) for the air density and solving Eq. (1.12.8) for the speed of sound squared results in

$$\rho = \rho_0 \left(\frac{a^2}{a_0^2} \right)^{\frac{1}{\gamma-1}} \quad (1.12.9)$$

$$a^2 = a_0^2 - \frac{\gamma-1}{2} V^2 \quad (1.12.10)$$

Substituting Eq. (1.12.10) into Eq. (1.12.9), we have

$$\rho = \rho_0 \left(1 - \frac{\gamma-1}{2} \frac{V^2}{a_0^2} \right)^{\frac{1}{\gamma-1}} \quad (1.12.11)$$

This specifies the local air density as a function of the local velocity and the stagnation conditions, which are known from the freestream conditions according to Eqs. (1.4.23) through (1.4.25).

Applying Eq. (1.12.1) to express the velocity in Eq. (1.12.11) in terms of the velocity potential, the local air density is found to be a function only of ϕ and known stagnation properties of the flow:

$$\rho = \rho_0 \left(1 - \frac{\gamma-1}{2a_0^2} \mathbf{V} \cdot \mathbf{V} \right)^{\frac{1}{\gamma-1}} = \rho_0 \left(1 - \frac{\gamma-1}{2a_0^2} \nabla \phi \cdot \nabla \phi \right)^{\frac{1}{\gamma-1}} \quad (1.12.12)$$

After using Eqs. (1.12.1) and (1.12.12) in Eq. (1.12.2), the **continuity equation for steady compressible potential flow** can be written as

$$\left(a_0^2 - \frac{\gamma-1}{2} \nabla \phi \cdot \nabla \phi \right) \nabla^2 \phi - \frac{1}{2} (\nabla \phi \cdot \nabla) (\nabla \phi \cdot \nabla \phi) = 0 \quad (1.12.13)$$

This equation contains only one unknown, the velocity potential ϕ . Both γ and a_0 are known constants of the flow. Since Eq. (1.12.13) is a single scalar equation in only one scalar unknown, it provides a tremendous simplification over the more general Navier-Stokes equations. However, like the Navier-Stokes equations but unlike the Laplace equation that governs the velocity potential for incompressible flow, Eq. (1.12.13) is nonlinear. Once the velocity potential has been determined from Eq. (1.12.13), the velocity field can be evaluated from Eq. (1.12.1). With the velocity known, the speed of sound at any point in the flow can be determined from Eq. (1.12.10). Knowing the local velocity and speed of sound at every point in the flow allows us to compute the

1.12. Inviscid Compressible Aerodynamics 133

Mach number and then, using Eqs. (1.4.20) through (1.4.22), to evaluate the pressure, temperature, and air density.

It is sometimes useful to apply a change of variables in Eq. (1.12.13). Here we shall define a new velocity vector to be the difference between the local velocity and the freestream velocity,

$$\mathbf{V}_p \equiv \mathbf{V} - \mathbf{V}_\infty \quad (1.12.14)$$

This is commonly called the *perturbation velocity*. From this definition, we also define the *perturbation velocity potential*,

$$\phi_p \equiv \phi - \phi_\infty \quad (1.12.15)$$

where ϕ_∞ is the velocity potential for the uniform flow, which was presented in Sec. 1.5. For the uniform flow potential we have

$$\nabla \phi_\infty = \mathbf{V}_\infty \quad (1.12.16)$$

$$\nabla \phi_\infty \cdot \nabla \phi_\infty = V_\infty^2 \quad (1.12.17)$$

$$\nabla^2 \phi_\infty = 0 \quad (1.12.18)$$

Using Eqs. (1.12.15) through (1.12.18) in Eq. (1.12.13) results in

$$\begin{aligned} & \left[a_0^2 - \frac{\gamma-1}{2} V_\infty^2 (1 + 2\mathbf{u}_\infty \cdot \nabla \hat{\phi}_p + \nabla \hat{\phi}_p \cdot \nabla \hat{\phi}_p) \right] \nabla^2 \hat{\phi}_p \\ & - \frac{1}{2} V_\infty^2 [(\nabla \hat{\phi}_p + \mathbf{u}_\infty) \cdot \nabla] (2\mathbf{u}_\infty \cdot \nabla \hat{\phi}_p + \nabla \hat{\phi}_p \cdot \nabla \hat{\phi}_p) = 0 \end{aligned} \quad (1.12.19)$$

where \mathbf{u}_∞ is the unit vector in the direction of the freestream

$$\mathbf{u}_\infty \equiv \frac{\mathbf{V}_\infty}{V_\infty} \quad (1.12.20)$$

and

$$\hat{\phi}_p \equiv \frac{\phi_p}{V_\infty} \quad (1.12.21)$$

Equation (1.12.19) is the general equation for the perturbation velocity potential. To this point in the development, no approximation has been made in going from Eq. (1.12.13) to Eq. (1.12.19). This result applies to any irrotational flow.

Equation (1.12.19) can be linearized under the assumption that the perturbation velocity is small compared to the freestream velocity. This approximation results in

134 Chapter 1 Overview of Aerodynamics

$$\left(a_0^2 - \frac{\gamma-1}{2}V_\infty^2\right)\nabla^2\hat{\phi}_p - V_\infty^2(\mathbf{u}_\infty \cdot \nabla)(\mathbf{u}_\infty \cdot \nabla\hat{\phi}_p) = 0 \quad (1.12.22)$$

Applying Eq. (1.12.10) to the freestream gives

$$a_\infty^2 = a_0^2 - \frac{\gamma-1}{2}V_\infty^2 \quad (1.12.23)$$

Substituting Eq. (1.12.23) in Eq. (1.12.22) and dividing through by a_∞^2 , the **linearized equation for the perturbation velocity potential** is

$$\nabla^2\phi_p - M_\infty^2(\mathbf{u}_\infty \cdot \nabla)(\mathbf{u}_\infty \cdot \nabla\phi_p) = 0 \quad (1.12.24)$$

Notice that as the flight Mach number approaches zero this result reduces to Laplace's equation, which applies to incompressible flow. Equation (1.12.24) provides reasonable predictions for slender bodies at low angles of attack with subsonic Mach numbers ($M_\infty < 0.8$) and supersonic Mach numbers ($1.2 < M_\infty < 5$). It is not valid for transonic Mach numbers ($0.8 < M_\infty < 1.2$) or hypersonic Mach numbers ($M_\infty > 5$).

1.13. Compressible Subsonic Flow

The aerodynamic theory of incompressible flow over airfoil sections was reviewed in Secs. 1.6 and 1.7. The analytical methods that have been developed for incompressible flow over airfoils can be applied to subsonic compressible flow through a simple change of variables. However, the reader should recall that subsonic flow does not exist all the way to a flight Mach number of 1.0. For an airfoil section producing positive lift, the flow velocities just outside the boundary layer on the upper surface are greater than the freestream velocity. Thus, at some flight speeds below Mach 1.0, supersonic flow will be encountered in some region above the upper surface of the airfoil. The flight Mach number at which sonic flow is first encountered at some point on the upper surface of the airfoil is called the *critical Mach number*. Here we review the theory of compressible flow over airfoils at flight speeds below the critical Mach number.

The Prandtl-Glauert Compressibility Correction

For thin airfoils at small angles of attack and flight Mach numbers below critical, the linearized potential flow approximation given by Eq. (1.12.24) can be applied. For the special case of two-dimensional flow and a coordinate system having the x -axis aligned with the freestream velocity vector, \mathbf{u}_∞ is simply the unit vector in the x -direction, and the continuity equation as expressed in Eq. (1.12.24) becomes

$$\left(\frac{\partial^2\phi_p}{\partial x^2} + \frac{\partial^2\phi_p}{\partial y^2}\right) - M_\infty^2\left(\frac{\partial}{\partial x}\right)\left(\frac{\partial\phi_p}{\partial x}\right) = 0$$

or after rearranging,

1.13. Compressible Subsonic Flow 135

$$\frac{\partial^2 \phi_p}{\partial x^2} + \frac{1}{1-M_\infty^2} \frac{\partial^2 \phi_p}{\partial y^2} = 0 \quad (1.13.1)$$

The nature of this partial differential equation depends on the sign of $1 - M_\infty^2$. Recall from your introductory course on differential equations that if the flight Mach number is greater than 1.0, Eq. (1.13.1) is hyperbolic. However, for subsonic Mach numbers this partial differential equation is elliptic.

For subsonic flight, Eq. (1.13.1) is simplified by using the change of independent variables

$$\hat{y} \equiv y\sqrt{1-M_\infty^2} \quad (1.13.2)$$

With this change of variables, Eq. (1.13.1) becomes

$$\frac{\partial^2 \phi_p}{\partial x^2} + \frac{\partial^2 \phi_p}{\partial \hat{y}^2} = 0 \quad (1.13.3)$$

which is exactly Laplace's equation that governs incompressible potential flow. Thus, with this coordinate transformation, the incompressible flow solution can be used for compressible flow.

The local pressure coefficient obtained from any solution to Eq. (1.13.3) is given by

$$C_p = \frac{C_{pM0}}{\sqrt{1-M_\infty^2}} \quad (1.13.4)$$

where C_{pM0} is the pressure coefficient for zero Mach number, which is the solution obtained for incompressible flow. Equation (1.13.4) relates the pressure coefficient for subsonic compressible flow to that for incompressible flow and is commonly referred to as the *Prandtl-Glauert compressibility correction*.

For inviscid flow, the section lift and moment coefficients can be found from simple integrals of the pressure distribution over the surface of the airfoil. As a result, the final result for section lift and moment coefficients look much like Eq. (1.13.4):

$$\tilde{C}_L = \frac{\tilde{C}_{LM0}}{\sqrt{1-M_\infty^2}} \quad (1.13.5)$$

$$\tilde{C}_m = \frac{\tilde{C}_{mM0}}{\sqrt{1-M_\infty^2}} \quad (1.13.6)$$

where \tilde{C}_{LM0} and \tilde{C}_{mM0} are the section lift and moment coefficients obtained for incompressible flow. The development of Eqs. (1.13.4) through (1.13.6) can be found in any undergraduate engineering textbook on aerodynamics and will not be repeated here.

136 Chapter 1 Overview of Aerodynamics

Critical Mach Number

For potential flow over an airfoil producing positive lift, the flow velocities along some portion of the upper surface are greater than the freestream velocity. Also recall that for incompressible potential flow, the ratio of local velocity to the freestream velocity at any point in the flow does not vary with the magnitude of the freestream velocity. In other words, if we double the freestream velocity in an incompressible potential flow, the velocity at every point in the flow field will double as well. This is a direct result of the linear nature of the Laplace equation, which governs incompressible potential flow. Thus, within the approximation of Eq. (1.13.1), the position of the point of maximum velocity on the upper surface of the airfoil does not change with freestream velocity.

From the definition of pressure coefficient, we can write

$$\begin{aligned} C_p &\equiv \frac{p - p_\infty}{\frac{1}{2}\rho_\infty V_\infty^2} = \frac{2}{(\rho_\infty/p_\infty)V_\infty^2} \left(\frac{p}{p_\infty} - 1 \right) \\ &= \frac{2}{(\gamma/\gamma RT_\infty)V_\infty^2} \left(\frac{p}{p_\infty} - 1 \right) = \frac{2}{\gamma M_\infty^2} \left(\frac{p}{p_\infty} - 1 \right) \end{aligned} \quad (1.13.7)$$

From Eq. (1.4.21),

$$\frac{p}{p_\infty} = \left(\frac{1 + [(\gamma - 1)/2]M_\infty^2}{1 + [(\gamma - 1)/2]M^2} \right)^{\frac{\gamma}{\gamma - 1}} \quad (1.13.8)$$

Substituting Eq. (1.13.8) into Eq. (1.13.7), the pressure coefficient can be expressed as a function of Mach number,

$$C_p = \frac{2}{\gamma M_\infty^2} \left[\left(\frac{1 + [(\gamma - 1)/2]M_\infty^2}{1 + [(\gamma - 1)/2]M^2} \right)^{\frac{\gamma}{\gamma - 1}} - 1 \right] \quad (1.13.9)$$

This relation allows us to compute the local pressure coefficient at any point in the flow from the local Mach number and the freestream Mach number.

The critical Mach number, M_{cr} , is the freestream Mach number that results in a local Mach number of 1.0 at that point on the upper surface where the pressure coefficient is lowest. Using this fact together with Eqs. (1.13.4) and (1.13.9) gives the relation

$$\frac{(C_{pM0})_{\min}}{\sqrt{1 - M_{cr}^2}} = \frac{2}{\gamma M_{cr}^2} \left[\left(\frac{1 + [(\gamma - 1)/2]M_{cr}^2}{1 + [(\gamma - 1)/2]} \right)^{\frac{\gamma}{\gamma - 1}} - 1 \right] \quad (1.13.10)$$

The minimum pressure coefficient on the airfoil surface for incompressible flow can be evaluated using a panel code. With this pressure coefficient known, Eq. (1.13.10)

contains only one unknown, the critical Mach number. This is easily solved for the value of the critical Mach number by using the secant method. Since the secant method is used frequently in this text for the solution of flight mechanics problems, its use is demonstrated in the following example.

EXAMPLE 1.13.1. For a particular airfoil at a particular angle of attack, a vortex panel code solution predicts that the minimum pressure coefficient on the surface of the airfoil is -0.43 . Estimate the critical Mach number.

Solution. We start by writing Eq. (1.13.10) in residual form, i.e.,

$$R \equiv \frac{2\sqrt{1-M_{cr}^2}}{\gamma M_{cr}^2} \left[\left(\frac{1+[(\gamma-1)/2]M_{cr}^2}{1+[(\gamma-1)/2]} \right)^{\frac{\gamma}{\gamma-1}} - 1 \right] - (C_{pM0})_{\min}$$

where R is the residual. We wish to find the value of M_{cr} that will make R go to zero. We start with some initial estimate for the Mach number, say $M_1 = 0.80$. With $\gamma = 1.4$, this gives a residual value of

$$R_1 = \frac{\sqrt{1-M_1^2}}{0.7M_1^2} \left[\left(\frac{1+0.2M_1^2}{1.2} \right)^{3.5} - 1 \right] - (-0.43) = 0.169216$$

For the secant iteration, we need a second estimate, say $M_2 = 0.70$. This gives

$$R_2 = \frac{\sqrt{1-M_2^2}}{0.7M_2^2} \left[\left(\frac{1+0.2M_2^2}{1.2} \right)^{3.5} - 1 \right] - (-0.43) = -0.126364$$

With these two results we compute our next estimate from the secant algorithm,

$$M_3 = M_2 - R_2 \frac{M_2 - M_1}{R_2 - R_1} = 0.742751, \quad R_3 = 0.017349$$

The process is repeated until the residual is less than some convergence criterion. On each iteration, the oldest estimate is discarded. This gives

$$M_4 = 0.737590, \quad R_4 = 0.001507$$

$$M_5 = 0.737099, \quad R_5 = 0.000020$$

Since this residual is essentially zero, our solution is

$$M_{cr} = \underline{0.74}$$

Drag Divergence

While the lift and pitching moment produced on an airfoil section are generated primarily from pressure forces, at subsonic speeds the drag is attributed almost entirely to viscous forces generated in the boundary layer. Below the critical Mach number, airfoil section drag coefficient does not vary substantially with Mach number. However, beyond the critical Mach number the drag coefficient begins to increase very rapidly with increasing Mach number, reaching a maximum at Mach 1 as shown in Fig. 1.13.1. This figure is intended only to show the general shape of the drag curve that might be expected for some airfoil. The exact shape of this drag curve and the total drag rise for a particular airfoil is quite sensitive to the shape of the airfoil section. There is no simple theory capable of predicting the variation in section drag coefficient with Mach number in the transonic region. At Mach numbers near 1.0, the flow over an airfoil is extremely complex and very sensitive to section shape. In the transonic region we commonly rely on experimental data.

The large increase in drag that occurs at Mach numbers just below 1.0, called *drag divergence*, is due primarily to the shock waves that form in transonic flow and the premature boundary layer separation caused by these shocks. The dramatic increase in drag that is experienced by an airplane as it approaches Mach 1 is what gave rise to the concept and terminology of the *sound barrier*. Some early researchers believed that the drag would become infinite as the speed of sound was approached. Thus, it was thought by some that it would be impossible to exceed the speed of sound in an aircraft. As can be imagined from inspection of Fig. 1.13.1, the speed of sound does present a substantial barrier to an aircraft with limited thrust. Nevertheless, the drag at Mach 1 is finite, and like most things in this universe, the sound barrier will yield to sufficient power. It will yield more easily, however, if finesse is applied with the power.

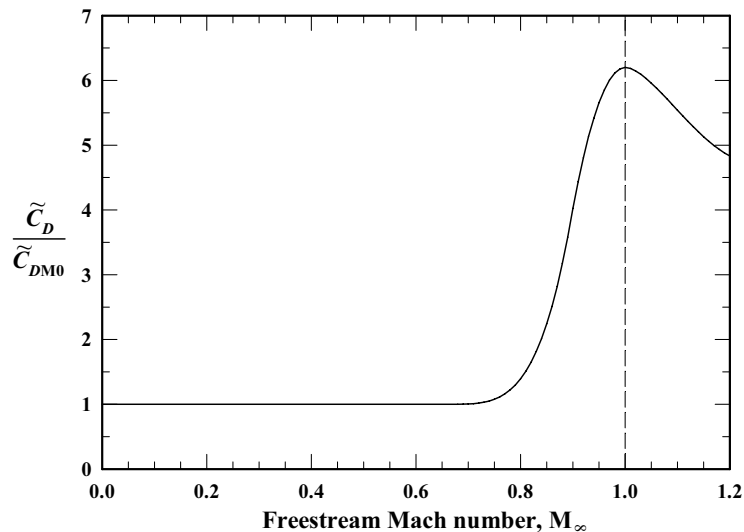


Figure 1.13.1. Sketch of typical variation in section drag coefficient with Mach number.

In the last half-century a great deal of “engineering finesse” has been applied to help “lower the sound barrier” by increasing the critical Mach number and decreasing the peak drag experienced near Mach 1. Contributions that have led to the design of improved supersonic aircraft include the use of thinner airfoils and swept wings, the introduction of the *area rule* in the supersonic design philosophy, and development of the supercritical airfoil. All of these topics are covered in most aerodynamics textbooks and the reader is encouraged to review this material, if necessary.

1.14. Supersonic Flow

In an irrotational supersonic flow where the streamlines make only small angles with the freestream, the linearized potential flow approximation given by Eq. (1.12.24) can be applied. Again consider two-dimensional flow with the x -axis aligned with the free-stream velocity vector. These are exactly the conditions that were used in Sec. 1.13 to study subsonic compressible flow over an airfoil. Thus, Eq. (1.13.1) applies to supersonic flow at small angles as well as to subsonic flow. However, since our interest is now in Mach numbers greater than 1.0, Eq. (1.13.1) is more conveniently written as

$$\frac{\partial^2 \phi_p}{\partial x^2} - \frac{1}{M_\infty^2 - 1} \frac{\partial^2 \phi_p}{\partial y^2} = 0 \quad (1.14.1)$$

Solutions to this hyperbolic partial differential equation are characteristically very different from solution to the elliptic equation encountered for subsonic flow. Thus, we should expect supersonic flow to be very different from subsonic flow.

In obtaining a solution to Eq. (1.14.1), a change of variables is again useful. We wish to find a variable change that will allow us to separate the independent variables, x and y , in Eq. (1.14.1). This is a common technique used in obtaining solutions to partial differential equations. We want to find a change of variables, say $\xi(x, y)$, that will make the perturbation potential a function of ξ only, i.e., $\phi_p(\xi)$. With this in mind, Eq. (1.14.1) can be written as

$$\frac{d^2 \phi_p}{d\xi^2} \left(\frac{\partial \xi}{\partial x} \right)^2 + \frac{d\phi_p}{d\xi} \frac{\partial^2 \xi}{\partial x^2} - \frac{1}{M_\infty^2 - 1} \left[\frac{d^2 \phi_p}{d\xi^2} \left(\frac{\partial \xi}{\partial y} \right)^2 + \frac{d\phi_p}{d\xi} \frac{\partial^2 \xi}{\partial y^2} \right] = 0 \quad (1.14.2)$$

Equation (1.14.2) is satisfied for ϕ_p equal to any function of ξ if

$$\frac{\partial^2 \xi}{\partial x^2} = \frac{1}{M_\infty^2 - 1} \frac{\partial^2 \xi}{\partial y^2} \quad \text{and} \quad \frac{\partial \xi}{\partial x} = \pm \frac{1}{\sqrt{M_\infty^2 - 1}} \frac{\partial \xi}{\partial y}$$

Both of these relations are satisfied if we set both sides of the second relation equal to an arbitrary constant, say C_1 . This gives

$$\frac{\partial \xi}{\partial x} = C_1 \quad \text{and} \quad \frac{\partial \xi}{\partial y} = \pm C_1 \sqrt{M_\infty^2 - 1}$$

140 Chapter 1 Overview of Aerodynamics

These equations are easily integrated to yield

$$\xi(x, y) = C_1 x + f_1(y) \quad \text{and} \quad \xi(x, y) = \pm C_1 \sqrt{M_\infty^2 - 1} y + f_2(x)$$

which require that

$$\xi(x, y) = C_1 \left(x \pm \sqrt{M_\infty^2 - 1} y \right) + C_2$$

Because C_1 and C_2 are arbitrary, we can choose $C_1 = 1$ and $C_2 = 0$, which gives

$$\xi(x, y) = x \pm \sqrt{M_\infty^2 - 1} y \quad (1.14.3)$$

Either of the two solutions for ξ that are given in Eq. (1.14.3) will provide the desired variable change. With either definition, any function $\phi_p(\xi)$ will satisfy Eq. (1.14.1). Thus, any problem associated with small-angle potential flow at supersonic Mach numbers reduces to that of finding the function $\phi_p(\xi)$ that will also satisfy the required boundary conditions.

From Eq. (1.14.3), a great deal can be deduced about supersonic potential flow at small angles without applying any boundary conditions. Since the perturbation potential is a function only of ξ , lines of constant perturbation potential are lines of ξ . Thus, the **constant perturbation potential lines are described by the equation**

$$x \pm \sqrt{M_\infty^2 - 1} y = \text{constant} \quad (1.14.4)$$

Since this is the equation of a straight line, the constant perturbation potential lines are all straight lines. Furthermore, solving Eq. (1.14.4) for y and differentiating with respect to x , we find that **the slope of any constant perturbation potential line is**

$$\left(\frac{\partial y}{\partial x} \right)_{\phi_p = \text{const}} = \mp 1 / \sqrt{M_\infty^2 - 1} \quad (1.14.5)$$

The angle that the constant perturbation potential lines makes with the freestream (i.e., the x -axis) is called the **Mach angle** and is given by

$$\mu = \mp \tan^{-1} \left(1 / \sqrt{M_\infty^2 - 1} \right) \quad (1.14.6)$$

Notice that for supersonic potential flow at small angles, the Mach angle is independent of surface geometry. It depends only on the freestream Mach number. Also notice that there are two solutions for the Mach angle and that the signs in Eqs. (1.14.5) and (1.14.6) are opposite to those in Eqs. (1.14.3) and (1.14.4). Thus, choosing the negative sign in Eq. (1.14.3) results in a positive Mach angle, and vice versa.

From the definition of perturbation potential, given in Eq. (1.12.15), the local fluid velocity vector is given by

$$\mathbf{V} = \nabla\phi = \nabla\phi_\infty + \nabla\phi_p = \mathbf{V}_\infty + \nabla\phi_p = V_\infty\mathbf{i}_x + \nabla\phi_p$$

Using the relation

$$\phi_p = \phi_p(\xi) = \phi_p(x \pm \sqrt{M_\infty^2 - 1} y)$$

we have

$$\mathbf{V} = \left(V_\infty + \frac{d\phi_p}{d\xi} \frac{\partial\xi}{\partial x} \right) \mathbf{i}_x + \frac{d\phi_p}{d\xi} \frac{\partial\xi}{\partial y} \mathbf{i}_y = \left(V_\infty + \frac{d\phi_p}{d\xi} \right) \mathbf{i}_x \pm \sqrt{M_\infty^2 - 1} \frac{d\phi_p}{d\xi} \mathbf{i}_y \quad (1.14.7)$$

The slope of a streamline at any point in the flow can be evaluated from Eq. (1.14.7),

$$\frac{V_y}{V_x} = \pm \sqrt{M_\infty^2 - 1} \frac{d\phi_p}{d\xi} / \left(V_\infty + \frac{d\phi_p}{d\xi} \right)$$

Because we are considering the case of small perturbation velocity, only the first-order term in this result should be retained. Since the streamlines are tangent to the velocity vector, **the slope of the local streamline relative to the x-axis is**

$$\left(\frac{\partial y}{\partial x} \right)_{\text{streamline}} = \pm \frac{\sqrt{M_\infty^2 - 1}}{V_\infty} \frac{d\phi_p}{d\xi} \quad (1.14.8)$$

From Eq. (1.14.7), the local velocity squared is

$$V^2 = \left(V_\infty + \frac{d\phi_p}{d\xi} \right)^2 + (M_\infty^2 - 1) \left(\frac{d\phi_p}{d\xi} \right)^2 = V_\infty^2 + 2V_\infty \frac{d\phi_p}{d\xi} + M_\infty^2 \left(\frac{d\phi_p}{d\xi} \right)^2$$

Again, since we are considering the case of small perturbation velocity, the second-order term should be ignored and the **velocity at any point in the flow** is given by

$$V^2 = V_\infty^2 + 2V_\infty \frac{d\phi_p}{d\xi} \quad (1.14.9)$$

From the momentum equation for a compressible potential flow, which is given by Eq. (1.4.19), we can express the local temperature in terms of the local velocity. Using the ideal gas law in Eq. (1.4.19) at an arbitrary point and the freestream gives

$$\frac{1}{2} V^2 + \frac{\gamma RT}{\gamma - 1} = \frac{1}{2} V_\infty^2 + \frac{\gamma RT_\infty}{\gamma - 1}$$

142 Chapter 1 Overview of Aerodynamics

Solving this for temperature, using Eq. (1.14.9) to eliminate the velocity, and applying the relation $a^2 = \gamma RT$ gives the **temperature at any point in the flow**:

$$T = T_\infty \left[1 - (\gamma - 1) \frac{M_\infty}{a_\infty} \frac{d\phi_p}{d\xi} \right] \quad (1.14.10)$$

From the isentropic relations given in Eqs. (1.4.20) and (1.4.21), the pressure ratio is easily related to the temperature ratio and after applying Eq. (1.14.10), we obtain

$$\frac{p}{p_\infty} = \left(\frac{T}{T_\infty} \right)^{\frac{\gamma}{\gamma-1}} = \left[1 - (\gamma - 1) \frac{M_\infty}{a_\infty} \frac{d\phi_p}{d\xi} \right]^{\frac{\gamma}{\gamma-1}}$$

Expanding this result in a Taylor series and retaining only the first-order term results in an expression for the **pressure at any point in the flow**:

$$p = p_\infty \left(1 - \gamma \frac{M_\infty}{a_\infty} \frac{d\phi_p}{d\xi} \right) \quad (1.14.11)$$

Using Eq. (1.14.11) in the definition of pressure coefficient as expressed in Eq. (1.13.7) results in

$$C_p = \frac{2}{\gamma M_\infty^2} \left(\frac{p}{p_\infty} - 1 \right) = - \frac{2}{V_\infty} \frac{d\phi_p}{d\xi} \quad (1.14.12)$$

Solving Eq. (1.14.8) for the derivative of the perturbation potential and using Eq. (1.14.6) to eliminate the freestream Mach number in favor of the Mach angle gives

$$\frac{d\phi_p}{d\xi} = \pm \frac{V_\infty}{\sqrt{M_\infty^2 - 1}} \left(\frac{\partial y}{\partial x} \right)_{\text{streamline}} = -V_\infty \tan(\mu) \left(\frac{\partial y}{\partial x} \right)_{\text{streamline}} \quad (1.14.13)$$

Substituting Eq. (1.14.13) into Eq. (1.14.12), **the pressure coefficient at any point in a small-angle potential flow at supersonic Mach numbers can be expressed as a function of only the Mach angle and the slope of the local streamline**:

$$C_p = 2 \tan(\mu) \left(\frac{\partial y}{\partial x} \right)_{\text{streamline}} \quad (1.14.14)$$

Remember that the Mach angle can be chosen as either positive or negative as needed to satisfy the required boundary conditions. However, the positive sign in Eq. (1.14.14) holds regardless of the sign chosen for the Mach angle. If the streamline slope has the same sign as the Mach angle, the pressure coefficient is positive. If these signs are opposite, the pressure coefficient is negative.

For those of us interested in computing aerodynamic forces, this is a very simple result in comparison to most solutions that have been obtained for fluid flow. In this respect, supersonic potential flow at small angles is less complex than subsonic flow at small angles. It rivals Bernoulli's equation for raw simplicity. The Mach angle depends only on the freestream Mach number. Furthermore, at the surface of a solid body, the streamlines must be tangent to the surface. Thus, the slope of the surface streamlines depends only on the surface geometry and the angle of attack.

Supersonic Thin Airfoils

The supersonic small-angle potential flow equations can be used to predict the aerodynamic force and moment components acting on a thin airfoil at small angles of attack, provided that the airfoil has a sharp leading edge as shown in Fig. 1.14.1. This type of leading edge is commonly used on supersonic airfoils because a blunt leading edge produces a strong bow shock in supersonic flight.

Consider supersonic flow over the cambered airfoil shown in Fig. 1.14.1. Because the flow must be symmetric for a symmetric airfoil at zero angle of attack, the positive slope is chosen for the Mach lines above the airfoil and the negative slope is chosen for those Mach lines below the airfoil. The slope of the upper surface relative to the freestream can be expressed as the slope of the chord line relative to the freestream, plus the slope of the camber line relative to the chord line, plus the slope of the thickness line relative to the camber line. Thus, for small angles of attack, **the upper surface slope is**

$$\frac{dy_u}{dx} = -\alpha + \frac{dy_c}{dx} + \frac{dy_t}{dx} \tag{1.14.15}$$

where y_c is the local camber and y_t is one-half the local thickness. Similarly, **the lower surface slope is**

$$\frac{dy_l}{dx} = -\alpha + \frac{dy_c}{dx} - \frac{dy_t}{dx} \tag{1.14.16}$$

Since the streamlines must be tangent to the airfoil surface, the results above can be used in Eq. (1.14.14) to evaluate the pressure coefficient on the airfoil surface.

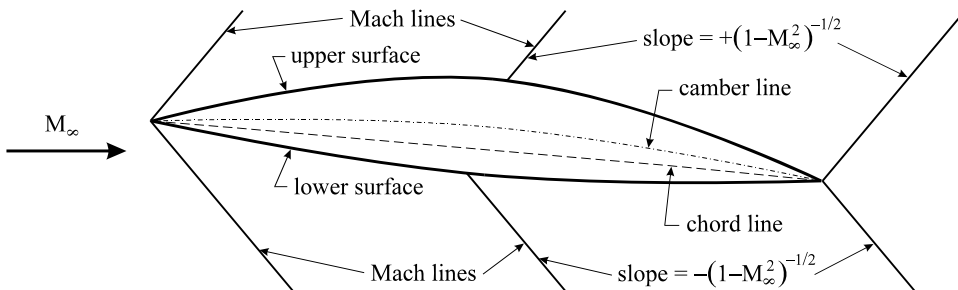


Figure 1.14.1. Small-angle supersonic potential flow over an airfoil.

144 Chapter 1 Overview of Aerodynamics

The contribution of pressure on the lower surface to the section lift is the surface pressure multiplied by a differential area per unit span projected on the x -axis. Similarly, the upper surface contributes to the lift in just the opposite direction. Thus, the section lift coefficient is

$$\tilde{C}_L = \frac{\tilde{L}}{\frac{1}{2}\rho_\infty V_\infty^2 c} = \int_0^c \frac{p_l - p_u}{\frac{1}{2}\rho_\infty V_\infty^2} \frac{dx}{c} = \int_0^c (C_{pl} - C_{pu}) \frac{dx}{c} \quad (1.14.17)$$

The slope of the Mach lines is positive on the upper surface and negative on the lower surface. Thus, from Eq. (1.14.6),

$$\tan(\mu_l) = -1/\sqrt{M_\infty^2 - 1} \quad \text{and} \quad \tan(\mu_u) = +1/\sqrt{M_\infty^2 - 1}$$

Using these results with Eqs. (1.14.14) through (1.14.16) applied to Eq. (1.14.17) gives

$$\begin{aligned} \tilde{C}_L &= \int_0^c \left[2 \frac{-1}{\sqrt{M_\infty^2 - 1}} \left(-\alpha + \frac{dy_c}{dx} - \frac{dy_t}{dx} \right) - 2 \frac{+1}{\sqrt{M_\infty^2 - 1}} \left(-\alpha + \frac{dy_c}{dx} + \frac{dy_t}{dx} \right) \right] \frac{dx}{c} \\ &= \frac{4}{\sqrt{M_\infty^2 - 1}} \int_0^c \left(\alpha - \frac{dy_c}{dx} \right) \frac{dx}{c} = \frac{4}{\sqrt{M_\infty^2 - 1}} \left[\alpha - \frac{y_c(c) - y_c(0)}{c} \right] \end{aligned}$$

By definition, the camber of any airfoil is zero at both the leading and trailing edges. Thus, **the section lift coefficient is**

$$\tilde{C}_L = \frac{4\alpha}{\sqrt{M_\infty^2 - 1}} = \tilde{C}_{L,\alpha} \alpha \quad \text{where} \quad \tilde{C}_{L,\alpha} = \frac{4}{\sqrt{M_\infty^2 - 1}} \quad (1.14.18)$$

From this result, we see that the small-angle potential flow equations predict that neither camber nor thickness makes a contribution to the lift at supersonic airspeeds.

Similarly, the pitching moment coefficient about the leading edge is evaluated from

$$\tilde{C}_{m_{le}} = \frac{\tilde{m}_{le}}{\frac{1}{2}\rho_\infty V_\infty^2 c^2} = \int_0^c (C_{pu} - C_{pl}) \frac{x dx}{c^2}$$

which gives

$$\tilde{C}_{m_{le}} = \frac{-4}{\sqrt{M_\infty^2 - 1}} \int_0^c \left(\alpha - \frac{dy_c}{dx} \right) \frac{x dx}{c^2} = \frac{-2\alpha}{\sqrt{M_\infty^2 - 1}} + \frac{4}{\sqrt{M_\infty^2 - 1}} \left(\int_0^c \frac{dy_c}{dx} \frac{x dx}{c^2} \right)$$

or

$$\tilde{C}_{m_{le}} = -\frac{1}{2} \tilde{C}_L + \tilde{C}_{L,\alpha} \int_0^c \frac{dy_c}{dx} \frac{x dx}{c^2}$$

From this result and the material that was reviewed in Sec. 1.1, it can be seen that **the aerodynamic center is located at the half-chord and the pitching moment coefficient about the aerodynamic center is**

$$\tilde{C}_{m_{ac}} = \tilde{C}_{L,\alpha} \int_0^c \frac{dy_c}{dx} \frac{x}{c^2} dx \quad \text{where} \quad \frac{x_{ac}}{c} = \frac{1}{2} \quad (1.14.19)$$

The moment coefficient about the aerodynamic center depends only on the camber line shape. Since camber does not contribute to lift in small-angle supersonic potential flow, symmetric airfoils are often used for supersonic flight. Notice from Eq. (1.14.19) that a thin symmetric airfoil produces no moment about its half-chord. Thus, **the half-chord is also the center of pressure for a thin symmetric airfoil in supersonic flight.**

The section drag for supersonic potential flow over a thin airfoil is not zero as it is for subsonic flow. This section drag is called *wave drag* and is computed from

$$\tilde{C}_D = \frac{\tilde{D}}{\frac{1}{2} \rho_\infty V_\infty^2 c} = \int_0^c \left(\frac{p_u - p_\infty}{\frac{1}{2} \rho_\infty V_\infty^2} \frac{dy_u}{dx} - \frac{p_l - p_\infty}{\frac{1}{2} \rho_\infty V_\infty^2} \frac{dy_l}{dx} \right) \frac{dx}{c} = \int_0^c \left(C_{pu} \frac{dy_u}{dx} - C_{pl} \frac{dy_l}{dx} \right) \frac{dx}{c}$$

Applying Eqs. (1.14.6) and (1.14.14) through (1.14.16) gives

$$\begin{aligned} \tilde{C}_D &= \frac{2}{\sqrt{M_\infty^2 - 1}} \int_0^c \left[\left(-\alpha + \frac{dy_c}{dx} + \frac{dy_t}{dx} \right)^2 + \left(-\alpha + \frac{dy_c}{dx} - \frac{dy_t}{dx} \right)^2 \right] \frac{dx}{c} \\ &= \frac{4}{\sqrt{M_\infty^2 - 1}} \int_0^c \left[\alpha^2 - 2\alpha \frac{dy_c}{dx} + \left(\frac{dy_c}{dx} \right)^2 + \left(\frac{dy_t}{dx} \right)^2 \right] \frac{dx}{c} \\ &= \frac{4}{\sqrt{M_\infty^2 - 1}} \left\{ \alpha^2 + \int_0^c \left[\left(\frac{dy_c}{dx} \right)^2 + \left(\frac{dy_t}{dx} \right)^2 \right] \frac{dx}{c} \right\} \end{aligned}$$

This result can be written in terms of the lift slope that was evaluated previously and presented in Eq. (1.14.18). Thus, **the section wave drag coefficient is**

$$\tilde{C}_D = \tilde{C}_{L,\alpha} \alpha^2 + \tilde{C}_{L,\alpha} \int_0^c \left[\left(\frac{dy_c}{dx} \right)^2 + \left(\frac{dy_t}{dx} \right)^2 \right] \frac{dx}{c} \quad (1.14.20)$$

From the results presented in Eqs. (1.14.18), (1.14.19), and (1.14.20), we see that small-angle potential flow theory predicts that there is no advantage to using camber in a supersonic airfoil. It only contributes to the pitching moment and the drag, making no predicted contribution to the lift. Furthermore, we see that airfoil thickness makes a predicted contribution to wave drag that is proportional to thickness squared. This is one reason why thin airfoil sections are commonly used on supersonic aircraft. Most modern airplanes that are designed to fly at Mach 1.5 and above use airfoils having a thickness on

146 Chapter 1 Overview of Aerodynamics

the order of 4 percent. This approximate linearized supersonic airfoil theory agrees reasonably well with experimental observations for airfoils as thick as about 10 percent and angles of attack as large as 20 degrees. As should be expected, this inviscid theory underpredicts the drag and moment coefficients and overpredicts the lift coefficient. However, the discrepancy is only a few percent. Most of the discrepancy can be attributed to viscous effects in the boundary layer. The drag that is predicted by this linear theory includes only wave drag. If a contribution for viscous drag is included from boundary layer computations, the predictions are improved. However, the viscous drag is quite small compared to the wave drag and for many purposes can be ignored.

1.15. Problems

- 1.1. The following is a tabulation of the section lift, drag, and quarter-chord moment coefficients taken from test data for a particular airfoil section.

α (deg)	\tilde{C}_L	\tilde{C}_D	$\tilde{C}_{m_{c/4}}$
-6.0	-0.38	0.0077	-0.0446
-5.0	-0.28	0.0071	-0.0440
-4.0	-0.18	0.0066	-0.0434
-3.0	-0.07	0.0063	-0.0428
-2.0	0.04	0.0060	-0.0422
-1.0	0.14	0.0059	-0.0416
0.0	0.24	0.0058	-0.0410
1.0	0.35	0.0058	-0.0404
2.0	0.46	0.0060	-0.0398
3.0	0.56	0.0062	-0.0392
4.0	0.65	0.0066	-0.0386
5.0	0.76	0.0070	-0.0380
6.0	0.87	0.0075	-0.0374
7.0	0.97	0.0081	-0.0368
8.0	1.07	0.0088	-0.0362
9.0	1.16	0.0096	-0.0356
10.0	1.26	0.0105	-0.0350
11.0	1.35	0.0115	-0.0344
12.0	1.44	0.0126	-0.0338

On one graph, plot both the section lift coefficient and the section normal force coefficient as a function of angle of attack. On another graph, plot both the section drag coefficient and the section axial force coefficient as a function of angle of attack.

- 1.2. From the data presented in problem 1.1, on one graph, plot the location of the center of pressure, x_{cp}/c , and the aerodynamic center, x_{ac}/c , as a function of angle of attack.

- 1.3. As predicted from thin airfoil theory, the section lift and leading-edge moment coefficients for a NACA 2412 airfoil section are given by

$$\tilde{C}_L = 2\pi(\alpha + 0.03625) \quad \text{and} \quad \tilde{C}_{m_{le}} = -\frac{\pi}{2}(\alpha + 0.07007)$$

where α is in radians. On one graph, plot both the section lift and normal force coefficients as a function of angle of attack, from -6 to $+12$ degrees. On another graph, plot both the section drag and axial force coefficients as a function of angle of attack, from -6 to $+12$ degrees.

- 1.4. From the thin airfoil relations for the airfoil section presented in problem 1.3, on one graph plot the location of the center of pressure, x_{cp}/c , and the aerodynamic center, x_{ac}/c , as a function of angle of attack, from -6 to $+12$ degrees.
- 1.5. Write a computer subroutine to compute the geopotential altitude, temperature, pressure, and air density as a function of geometric altitude for the standard atmosphere that is defined in Table 1.2.1. The only input variable should be the geometric altitude in meters. All output variables should be in standard SI units. Test this subroutine by comparing its output with the results that were obtained in Example 1.2.1 and those presented in Appendix A.
- 1.6. Write a computer subroutine to compute the geopotential altitude, temperature, pressure, and air density as a function of geometric altitude for the standard atmosphere that is defined in Table 1.2.1. The only input variable should be the geometric altitude in feet. All output variables should be in English engineering units. Test the subroutine by comparison with Example 1.2.2 and the results presented in Appendix B. Since this standard atmosphere is defined in SI units, this subroutine could be written using simple unit conversion and a single call to the subroutine written for problem 1.5.
- 1.7. Show that the velocity distribution for the two-dimensional source flow, which is expressed in Eq. (1.5.4), is irrotational.
- 1.8. Show that the velocity distribution for the two-dimensional vortex flow, which is expressed in Eq. (1.5.6), is irrotational.
- 1.9. Show that the velocity distribution for the two-dimensional doublet flow, which is expressed in Eq. (1.5.8), is irrotational.
- 1.10. Show that the velocity distribution for the two-dimensional stagnation flow, which is expressed in Eq. (1.5.10), is irrotational.
- 1.11. Show that the velocity distribution for the two-dimensional vortex flow, which is expressed in Eq. (1.5.6), satisfies the incompressible continuity equation.

148 Chapter 1 Overview of Aerodynamics

- 1.12. The section geometry for a NACA 4-digit series airfoil is completely fixed by the maximum camber, the location of maximum camber, the maximum thickness, and the chord length. The first digit indicates the maximum camber in percent of chord. The second digit indicates the distance from the leading edge to the point of maximum camber in tenths of the chord. The last two digits indicate the maximum thickness in percent of chord. The camber line is given by

$$y_c(x) = \begin{cases} y_{mc} \left[2 \left(\frac{x}{x_{mc}} \right) - \left(\frac{x}{x_{mc}} \right)^2 \right], & 0 \leq x \leq x_{mc} \\ y_{mc} \left[2 \left(\frac{c-x}{c-x_{mc}} \right) - \left(\frac{c-x}{c-x_{mc}} \right)^2 \right], & x_{mc} \leq x \leq c \end{cases}$$

where y_{mc} is the maximum camber and x_{mc} is the position of maximum camber. The thickness about the camber line, measured perpendicular to the camber line itself, is given by

$$t(x) = t_m \left[2.969 \sqrt{\frac{x}{c}} - 1.260 \left(\frac{x}{c} \right) - 3.516 \left(\frac{x}{c} \right)^2 + 2.843 \left(\frac{x}{c} \right)^3 - 1.015 \left(\frac{x}{c} \right)^4 \right]$$

where t_m is the maximum thickness. For the NACA 2412 airfoil section, determine x/c and y/c for the camber line, upper surface, and lower surface at chordwise positions of $x/c = 0.10$.

- 1.13. Using the formulas given in problem 1.12, for the NACA 0012 airfoil section, determine x/c and y/c of the upper and lower surfaces at chordwise positions of $x/c = 0.00, 0.001, 0.10, 0.40, 0.50, 0.90,$ and 1.00 .
- 1.14. Using the formulas given in problem 1.12, for the NACA 4421 airfoil section, determine x/c and y/c of the upper and lower surfaces at chordwise positions of $x/c = 0.00, 0.001, 0.10, 0.40, 0.50, 0.90,$ and 1.00 .
- 1.15. Using the formulas given in problem 1.12, for the NACA 0021 airfoil section, determine the angle of the upper surface relative to the chord line in degrees at a chordwise position of $x/c = 0.10$.
- 1.16. Using the formulas given in problem 1.12, for the NACA 4421 airfoil section, determine the angle of the upper surface relative to the chord line in degrees at a chordwise position of $x/c = 0.10$.
- 1.17. The formulas for the geometry of a NACA 4-digit series airfoil are given in problem 1.12. For the NACA 2412 airfoil section, use thin airfoil theory to determine the zero-lift angle of attack, the lift coefficients at 0- and 5-degree angles of attack, and the quarter-chord moment coefficient. Also plot the center of pressure as a function of angle of attack from -5 to 10 degrees.

- 1.18. The formulas for the geometry of a NACA 4-digit series airfoil are given in problem 1.12. Using thin airfoil theory, for the NACA 4412 airfoil section, determine the zero-lift angle of attack, the lift coefficients at 0- and 5-degree angles of attack, the quarter-chord moment coefficient, and the center of pressure at the 0- and 5-degree angles of attack.

- 1.19. The NACA 23012 airfoil section has a camber line defined by the equation

$$\frac{y_c}{c} = \begin{cases} 2.6595\left(\frac{x}{c}\right)^3 - 1.6156\left(\frac{x}{c}\right)^2 + 0.3051\left(\frac{x}{c}\right), & 0.0 \leq \frac{x}{c} \leq 0.2025 \\ 0.02208\left(1 - \frac{x}{c}\right), & 0.2025 \leq \frac{x}{c} \leq 1.0 \end{cases}$$

Using thin airfoil theory, determine the zero-lift angle of attack, the lift coefficients at 0- and 5-degree angles of attack, the quarter-chord moment coefficient, and the center of pressure at the 0- and 5-degree angles of attack.

- 1.20. The NACA 24012 airfoil section has a camber line defined by the equation

$$\frac{y_c}{c} = \begin{cases} 1.1072\left(\frac{x}{c}\right)^3 - 0.9632\left(\frac{x}{c}\right)^2 + 0.2523\left(\frac{x}{c}\right), & 0.0 \leq \frac{x}{c} \leq 0.2900 \\ 0.02700\left(1 - \frac{x}{c}\right), & 0.2900 \leq \frac{x}{c} \leq 1.0 \end{cases}$$

Using thin airfoil theory, determine the zero-lift angle of attack, the lift coefficients at 0- and 5-degree angles of attack, the quarter-chord moment coefficient, and the centers of pressure at 0- and 5-degree angles of attack.

- 1.21. Write a computer program that uses the vortex panel method that was described in Sec. 1.6 to compute the pressure distribution on a NACA 4-digit series airfoil. Use the program to compute the lift coefficient of the NACA 2412 airfoil section. Compare the results of your program with those plotted in Fig. 1.6.6.
- 1.22. Use the computer program written for problem 1.21 to compute the lift coefficient of the NACA 2421 airfoil section. Compare the results of your program with those plotted in Fig. 1.6.7.
- 1.23. Use the computer program written for problem 1.21 to compute the lift coefficient of the NACA 0015 airfoil section. Compare the results of your program with those plotted in Fig. 1.6.8.
- 1.24. Using thin airfoil theory, plot the ideal section flap effectiveness as a function of flap chord fraction. Compare your results with those plotted in Fig. 1.7.3.
- 1.25. Using thin airfoil theory, plot the quarter-chord moment slope as a function of flap chord fraction. Compare your results with those plotted in Fig. 1.7.6.

150 Chapter 1 Overview of Aerodynamics

- 1.26. Consider an elliptic wing of aspect ratio 8 having no sweep or dihedral and no geometric or aerodynamic twist. The wing is constructed with a thin symmetric airfoil section. For an angle of attack of 5 degrees, estimate the lift and induced drag coefficients for the wing.
- 1.27. Consider a rectangular wing of aspect ratio 8 having no sweep or dihedral and no geometric or aerodynamic twist. The wing is constructed with a thin symmetric airfoil section. For an angle of attack of 5 degrees, estimate the lift and induced drag coefficients for the wing.
- 1.28. Consider a tapered wing of aspect ratio 8 and taper ratio 0.5 having no sweep or dihedral and no geometric or aerodynamic twist. The wing is constructed with a thin symmetric airfoil section. For an angle of attack of 5 degrees, estimate the lift and induced drag coefficients for the wing.
- 1.29. Write a computer program that uses the series solution to Prandtl's lifting-line equation to predict the lift and induced drag coefficients for an elliptic wing having linear geometric and aerodynamic twist. Use your program to rework problem 1.26 for a wing with 5 degrees of linear washout.
- 1.30. Use the computer program that was written for problem 1.29 to plot the lift and induced drag coefficients as a function of angle of attack for elliptic wings of aspect ratio 8 having 0 and 5 degrees of linear washout.
- 1.31. Write a computer program that uses the series solution to Prandtl's lifting-line equation to predict the lift and induced drag coefficients for a tapered wing having linear geometric and aerodynamic twist. Use your program to rework problems 1.27 and 1.28 for wings with 5 degrees of linear washout.
- 1.32. Use the program from problem 1.31 to plot lift coefficient as a function of angle of attack and induced drag coefficient as a function of lift coefficient for a rectangular wing of aspect ratio 8 and having 5 degrees of linear washout.
- 1.33. Use the program from problem 1.31 to plot lift coefficient as a function of angle of attack and induced drag coefficient as a function of lift coefficient for a tapered wing of aspect ratio 8 and taper ratio 0.5 having 5 degrees of linear washout.
- 1.34. Write a computer program that uses the series solution to Prandtl's lifting-line equation to predict rolling and yawing moment coefficients for a tapered wing with linear washout, aileron deflection, and roll. Use your program to rework Example 1.8.3 for wings with 0 and 4.5 degrees of linear washout.
- 1.35. Use the program written for problem 1.34 to plot the rolling and yawing moment coefficients as a function of the linear washout angle for the wing and aileron planform in Example 1.8.3. Use a 5-degree aileron deflection with no roll.

- 1.36. Write a computer program that uses the numerical lifting-line method presented in Sec. 1.9 to predict the lift and induced drag for a tapered wing with linear geometric and aerodynamic twist. Test your program by comparing results with those obtained in problems 1.27, 1.28, 1.32, and 1.33.
- 1.37. Use the computer program from problem 1.36 to compute the lift at 10 degrees angle of attack for a rectangular wing with a thin symmetric airfoil section and an aspect ratio of 6. The root chord is 5.5 ft. Use $V=176$ ft/sec at standard sea level.
- 1.38. Use the computer program that was written for problem 1.36 to compute the lift at 10 degrees angle of attack for a tapered wing having aspect ratio 4.0, taper ratio 0.5, and a thin symmetric airfoil section. The wing quarter chord is swept such that there is no sweep in the trailing edge and the planform area of the wing is 36 ft^2 . Use $V=176$ ft/sec at standard sea level.
- 1.39. The wing described in problem 1.38 is to be used as an aft horizontal stabilizer for the main wing described in problem 1.37. The root quarter chord of the horizontal stabilizer is 15 feet aft of the quarter chord of the main wing. Use the computer program from problem 1.36 to compute the lift at 10 degrees angle of attack for each lifting surface in this wing-tail combination. Use $V=176$ ft/sec at standard sea level. Compare the results obtained with those obtained in problems 1.37 and 1.38 for each lifting surface in isolation. Discuss your findings.
- 1.40. For the NACA 2412 airfoil section, which was described in problem 1.17, plot the lift slope and quarter-chord moment coefficient as a function of Mach number from 0.0 to 0.8.
- 1.41. For the NACA 2412 airfoil section described in problem 1.17, plot the derivative of lift per unit area with respect to airspeed as a function of flight Mach number from 0.0 to 0.8. Neglect the Reynolds number dependence and use a 5-degree angle of attack with standard conditions at sea level.
- 1.42. Using the panel code written for problem 1.21 and the Prandtl-Glauert compressibility correction, estimate the critical Mach number of the NACA 2412 airfoil section for angles of attack of 0 and 5 degrees.
- 1.43. Using the panel code written for problem 1.21 and the Prandtl-Glauert compressibility correction, estimate the critical Mach number of the NACA 2421 airfoil section for angles of attack of 0 and 5 degrees.
- 1.44. A symmetric supersonic airfoil section has a parabolic thickness distribution with the point of maximum thickness located at the half-chord. For a maximum thickness of 4 percent, plot the section lift, drag, and half-chord moment coefficients as a function of freestream Mach number from 1.2 to 3.0. Use a fixed angle of attack of 5 degrees.

152 Chapter 1 Overview of Aerodynamics

- 1.45. A symmetric supersonic airfoil section has a parabolic thickness distribution with the point of maximum thickness located at the half-chord. For a maximum thickness of 12 percent, plot the section lift, drag, and half-chord moment coefficients as a function of freestream Mach number from 1.2 to 3.0. Use a fixed angle of attack of 5 degrees.
- 1.46. A symmetric supersonic airfoil section has a parabolic thickness distribution with the point of maximum thickness located at the half-chord. For a maximum thickness of 4 percent, plot the section drag per unit area as a function of free-stream Mach number from 1.2 to 3.0 for a constant wing loading of 100 lbf/ft² and standard conditions at 30,000 feet.
- 1.47. A symmetric supersonic airfoil section has a parabolic thickness distribution with the point of maximum thickness located at the half-chord. For a maximum thickness of 12 percent, plot the section drag per unit area as a function of free-stream Mach number from 1.2 to 3.0 for a constant wing loading of 100 lbf/ft² and standard conditions at 30,000 feet.
- 1.48. A symmetric diamond-wedge airfoil section has a thickness distribution that increases linearly from the leading edge to the point of maximum thickness located at the half-chord. The thickness then decreases linearly from the half-chord to the sharp trailing edge. For a maximum thickness of 4 percent, plot the section lift and drag coefficients as a function of freestream Mach number from 1.2 to 3.0. Use a fixed angle of attack of 5 degrees.
- 1.49. A symmetric diamond-wedge airfoil section has a thickness distribution that increases linearly from the leading edge to the point of maximum thickness located at the half-chord. The thickness then decreases linearly from the half-chord to the sharp trailing edge. For a maximum thickness of 4 percent, plot the section drag per unit area as a function of Mach number from 1.2 to 3.0 for a constant wing loading of 100 lbf/ft² and standard conditions at 30,000 feet.
- 1.50. Consider a rectangular wing of aspect ratio 8.0 with a constant thin airfoil section having $\tilde{C}_{m_{ac}} = 0.053$ and $\tilde{C}_{L_{\max}} = 1.6$. Estimate $C_{L_{\max}}$, \bar{x}_{ac}/\bar{c} , and $C_{m_{ac}}$ for this wing planform with the following amounts of quarter-chord sweep and linear washout:

$$A = 0, \Omega = 0; \quad A = 0, \Omega = 4^\circ; \quad A = 30^\circ, \Omega = 0; \quad A = 30^\circ, \Omega = 4^\circ$$

- 1.51. Consider a wing with linear taper of aspect ratio 4.0 and taper ratio 0.5. The wing has a constant thin airfoil section with $\tilde{C}_{m_{ac}} = 0.053$ and $\tilde{C}_{L_{\max}} = 1.6$. Estimate $C_{L_{\max}}$, \bar{x}_{ac}/\bar{c} , and $C_{m_{ac}}$ for this wing with the following amounts of quarter-chord sweep and linear washout:

$$A = 0, \Omega = 0; \quad A = 0, \Omega = 5^\circ; \quad A = 30^\circ, \Omega = 0; \quad A = 30^\circ, \Omega = 5^\circ$$